Università degli Studi di Napoli Federico II

Neuromorphic organic electrochemical transistors for bio-inspired computation, learning and biological interfaces

Ph.D. Program in Industrial product and Process Engineering
XXXVI - cycle

Ugo Bruno, M. Sc.

Coordinator: Prof. Andrea D’Anna

Supervisor: Prof. Francesca Santoro

Tutor: Prof. Paolo Antonio Netti

Table of contents

List of figures

List of tables

List of equations

List of abbreviations

1. **[EMIM][TFSI]** – 1-ethyl-3-methylimidazolium bis(trifluoromethylsulfonyl)amide
2. **AC** – amacrine cells
3. **AFM** – atomic force microscopy
4. **AI** – artificial intelligence
5. **ANN** – artificial neural network
6. **AP** – action potential
7. **APTES** – 3-Aminopropyltriethoxysilane
8. **Azo-alkyne** – 4-Propargyloxyazobenzene
9. **BBL** – poly(benzimidazobenzophenanthroline)
10. **BC** – bipolar cells
11. **CGMP -** cyclic guanosine monophosphate
12. **CHOL** – cholesterol
13. **CMOS** – complementary metal-oxide-semiconductor
14. **CNS** – central nervous system
15. **CP** – conducting polymer
16. **CPU** – central processing unit
17. **CV** – cyclic voltammetry
18. **DA** – dopamine
19. **DFT/TD-DFT** – density functional theory and time-dependent density-functional theory
20. **DI** – deionized
21. **DNN** – deep neural network
22. **DQ** – dopamine o-quinone
23. **DRG** – dorsal root ganglion
24. **ECG** – electrocardiography
25. **ECM** – extracellular matrix
26. **ECoG** – electrocorticography
27. **EDL** – electrical double layer
28. **EDOT-N3** – 2-Azidomethyl-2,3-dihydrothieno[3,4-b]−1,4-dioxine
29. **EEG** – Electroencephalography
30. **EG** – ethylene glycol
31. **EGOFET** – electrolyte-gated organic field-effect transistor
32. **EIS** – electrochemical impedance spectroscopy
33. **EMG** – electromyography
34. **ENODe** – electrochemical neuromorphic organic device
35. **eRBP** – event-driven random backpropagation
36. **ET** – eligibility trace
37. **FeFET** – ferroelectric field-effect transistor
38. **FEM** – Finite element method
39. **FeRAM** – ferroelectric random-access memory
40. **FLOPS** – floating-point operations per second
41. **FRAP** – fluorescence recovery after photobleaching
42. **FTJ** – ferroelectric tunnel junction
43. **GC** – ganglion cells

44. **GCL** – ganglion cell layer
45. **GOPS** – 3-glycidyloxypropyl)trimethoxysilane
46. **HC** – horizontal cells
47. **HOMO** – highest occupied molecular orbital
48. **HRS** – high resistance state
49. **IF** – integrate-and-fire
50. **INL** – inner nuclear layer
51. **IPL** – inner plexiform layer
52. **ITO** – indium tin oxide
53. **LRS** – low resistance state
54. **LTD** – long term depression
55. **LTP** – long term potentiation
56. **LUMO** – lowest unoccupied molecular orbital
57. **MOSFET** – metal-oxide-semiconductor field-effect transistor
58. **MVM** – matrix-vector multiplication
59. **NMDARs** – N-methyl-d-aspartate receptors
60. **OEC-RAM** – organic electrochemical resistive access memory
61. **OECT** – organic electrochemical transistor
62. **OFET** – organic field-effect transistor
63. **OLED** – organic light-emitting diode
64. **OMIEC** – organic mixed ionic-electronic conductor
65. **ONL** – outer nuclear layer
66. **OPL** – outer plexiform layer
67. **OPV** – organic photovoltaics
68. **PAH** – polyallylamine hydrochloride
69. **PBS** – phosphate buffered saline
70. **PC** – Purkinje cell
71. **PCM** – phase-change memory
72. **PDMS** – polydimethylsiloxane
73. **PEDOT:PSS** – poly(3,4-ethylenedioxythiophene):poly(styrene sulfonate)
74. **PEI** – poly(ethylenimine)
75. **PI** – polyimide
76. **PM** – plasma membrane
77. **PMMA** – Poly(methyl methacrylate)
78. **PNS** – peripheral nervous system
79. **POPC** – 1-palmitoyl-2-oleoyl-glycero-3-phosphocholine
80. **PSP** – post synaptic potential
81. **PSSNa** – poly(sodium 4-styrenesulfonate)
82. **PTP** – post-tetanic potentiation
83. **PVDF-co-HFP** – poly(vinylidene fluoride-co-hexafluoropropylene)
84. **PW** – pulse width
85. **RA** – rapidly adapting
86. **RA1** – rapidly adapting type 1
87. **RA2** – rapidly adapting type 2
88. **RC** – reservoir computing
89. **RLL** – resistor-ladder logic
90. **RMS** – root mean square
91. **RNN** – recurrent neural network

92. SA – slowly adapting
93. SA1 – slowly adapting type 1
94. SA2 – slowly adapting type 2
95. SLB – supported lipid bilayer
96. SM – sphingomyelin
97. SMU – source measure unit
98. SNN – spiking neural network
99. SNR – signal-to-noise ratio
100. SRDP – spike-rate-dependent plasticity
101. STD – short term depression
102. STP – short term potentiation
103. STPD – spike timing dependent plasticity

Abstract

The rise of artificial intelligence and artificial neural networks revolutionized information technology and our daily lives. Such progress was inspired by the parallel organization and computation paradigm of the brain, allowing to build networks able to learn from experience and, very recently, actively process the natural language, to generate text and images, summarize content, translate text in different language and offer a human-like assistance.

This progress, though, comes with a price. While the software is inspired from the brain parallel and efficient computing, the supporting hardware is still based on classical von Neumann architecture, which, unlike the human brain, was designed to run simple operation in a linear succession. This mismatch between software and hardware causes an excessive energy consumption when training and operating such architectures.

In this framework, neuromorphic engineering aims to take inspiration from the brain, to design the hardware of the future. It harvests from all possible biological computational primitives, such as single synapses, ionic fluxed, plasticity and sparse coding to develop novel principles to design hardware. Material science, with the study of innovative materials, has been of utmost importance in continuously providing a wave of innovation, allowing researchers to demonstrate innovative brain-derived architectures.

Among the plethora of available materials, organic semiconductors emerged for easy processability, solution processing and easy processability, along with low voltage operations. Nonetheless, such materials can offer a mixed conduction mechanism, relying on both electrons and ions to modulate their conductivity. This last feature was indeed crucial in interfacing such materials with biology, where electronic signaling leaves space to ions moving in an electrolytic environment. Moreover, the soft nature of these materials minimized the mechanical mismatch between electronical devices and biological tissue, offering a seamless interface with the human body, and without eliciting any inflammatory response.

The thesis work here presented envisions the merging of these two concepts: the possibility to optimally interface with biology, while achieving brain-inspired computation. Organic electrochemical transistors were designed to demonstrate bio-inspired in loco computation of biologically relevant signals, as pressure, light, or neurotransmitters. By engineering the alternance of conducing and non-conducting thin films, a non-volatile pressure sensor, inspired by the sense of touch was designed. OECTs were subsequently endowed with light-sensitivity, through an ad hoc synthetic strategy. Here, the obtained transistors were able to emulate light-

processing of the human retina, while demonstrating memory compartmentalization, as formulated by classical neuroscience theories. Neurotransmitter-mediated synaptic plasticity was then demonstrated and exploited to build a closed-loop neuromorphic system, in which organic transistors could communicate and cooperate with standard CMOS technology to endow a well-established mechatronic system with brain-derived adaptive features, as autonomous reinforcement learning. Lastly, biomimicry was enforced in OECTs, by embedding bio-inspired membranes in the electrolytic environment of the transistors. Notably, while offering a seamless interface with biological tissue, the membranes were able to modulate both short- and long-term plasticity of the artificial synaptic device.

Chapter 1: Introduction

1.1. Brain and neurons

The nervous system is the complex system, organized in a highly interconnected network, and responsible for coordinating functions and conveying information throughout the whole body. It is divided into central nervous system (CNS) and peripheral nervous system (PNS). The former is composed by the brain and the spinal cord, while the latter comprehends all the nerves departing from the CNS, extending to other parts of the body[1].

The human brain deserves a special mention, as it represents one of the most powerful and complex system available in nature. It deals with complex tasks, sensing, computing and propagating information all at the same time, on an energy budget of ~ 20 W[2]. Such energy efficiency relies on billions of neurons, that communicate in an intricate and highly dynamic network. As a result, the whole computation does not depend on the activity of a single neuron, but rather on the whole network activation[1], in which each area is specialized to accomplish a different task. Still, all the neural cells feature the same basic structure (**Fig. 1.1-a**): a cell body (soma), several branches (dendrites) and an elongated structure (axon).

In addition, neurons are excitable cells, *i.e.*, cells able to generate and propagates electrical impulses, based on rapid changes of the membrane potential[3]. At rest, in fact, the cellular membrane composed of lipid bilayers acts as a barrier for ion diffusion[4].

This results in a separation of charges across the intra- and extracellular domains, leading to a difference of electrical potential across the membrane (**Fig. 1.1-b**): the membrane resting potential V_m, that usually sits in the range $[-70; -60]$ mV. Among all the ionic species present in the biological environment, Na^+ and Ca^{2+} are mostly found in the extracellular domain, while K^+ is found in the intracellular compartment[1,5] (**Fig. 1.1-b**).

A reduction in charge separation, leading to a less negative membrane potential, is called *depolarization* (**Fig. 1.1-c**). On the other hand, a more negative membrane potential, due to an increased charge separation, is defined as *hyperpolarization* (**Fig. 1.1-d**. Such perturbation of V_m, mainly due to cations and anions entering or exiting the cell, is responsible for the action potential (AP) generation and neural communication[1,6,7].

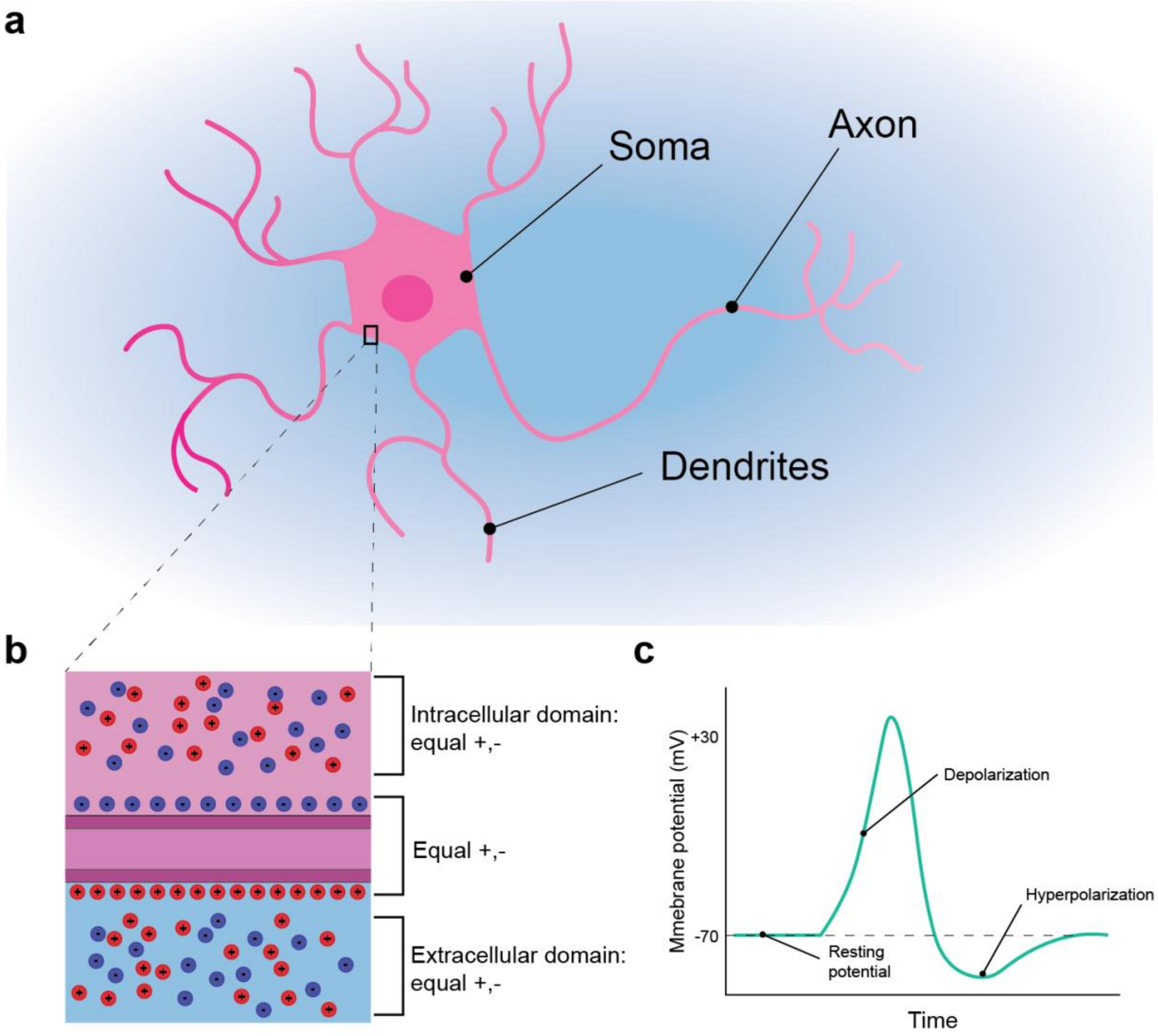

Figure 1.1 | **a**) Structure of a neuron. **b**) Intra- and extracellular charge equilibrium, with charge accumulation at the membrane. **c**) Schematic of depolarization and hyperpolarization of a neuron.

Neurons are not the only players in neural communication, as non-excitable cells *i.e.*, Glial cells may also be involved. Such cells can be divided into micro- and macroglia. The former are mainly responsible for acting in case of injuries and pathologies, the latter can serve various functions. There are three main types of macroglia: oligodendrocytes, Schwann cells and astrocytes[8]. Oligodendrocytes and Schwann cells form myelin sheath that insulates parts of the axon by wrapping around it in spiral (**Fig. 1.2**). The unmyelinated gaps between the regularly spaced myelinated portions of the axon are called nodes of Ranvier, that are pivotal in the efficient propagation of APs along the axon[9].

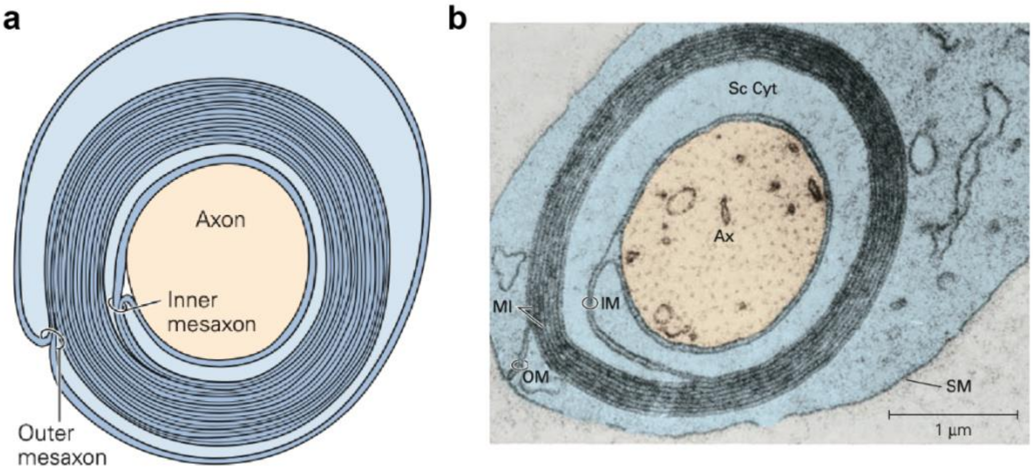

Figure 1.2 | **a**) Illustration of a Schwann cell wrapping around an axon; **b**) electron micrograph of a transverse section of an axon in a mouse nerve. Adapted from [1].

1.1.1. Plasma membrane

The cell membrane, also known as plasma membrane (PM), is the outpost of the cell, mediating all the communication between the intracellular domain and the extracellular matrix[10] (ECM). In particular, the PM is responsible for sensing for the external environment, providing the cell with biochemical, mechanical, and topological cues[11–13]. At the same time, it adapts and responds to environmental changes, regulating cell homeostasis and functions[14,15].

The main components of the PM are phospholipids[16], *i.e.*, molecules characterized by a hydrophilic head and two hydrophobic tails (**Fig. 1.3-a**). Such molecules assemble in a phospholipid bilayer (**Fig. 1.3-b**), where heads face to the outside (water-rich domain), while the tails face inward, away from the watery environment[17]. Moreover, the lipid composition endows the PM with specific curvature, fluidity and thickness, crucial parameters for several processes[18,19]. The neural cell membrane, for instance, is rich with lipid rafts[20,21], *i.e.*, microdomains rich in cholesterol (CHOL) and sphingomyelin (SM) that are pivotal in synapses formation[22,23]. Importantly, changes in neuronal PM, as a response to external stimuli, is pivotal in synaptic plasticity[24].

In addition, CHOL was demonstrated to interact with Na^+,K^+-pump, that is the enzyme responsible for pumping sodium out of the cell and potassium inside it, against their concentration gradient. It inhibited the pumping action when present in large quantities, while, when present in low concentration, it acted like a stimulating agent[4].

Importantly, one crucial feature of the PM is to offer selective permeability to some compounds, while blocking other. Passive diffusion of ions through the membrane, for instance, is deeply limited by the structure of the PM itself. Here, the hydrophobic inner portion of the bilayer does not allow for charged (and consequently hydrophilic) molecules as ions, to easily penetrate and cross the membrane. Small and uncharged molecules, on the contrary, can pass the membrane in an easier way[25]. When larger or polar molecules, or ions, need to be transported from one side to the other of the membrane, facilitated diffusion occurs. In this case, membrane proteins[26] provide a passageway through the membrane[27].

Membrane proteins can either be located inside or on the surface of the bilayer, absolving to various functions, as energy transport, transport of molecules, transmission of chemical signals or catalyse reactions[26] (**Fig. 1.3-c**). Such membranes can either be integrated inside the bilayer (integral proteins) or associated with the membrane (peripherals proteins). When integrated within the membrane, the transmembrane portion of the proteins is usually characterized by hydrophobic amino acids, making it compatible with the interior of the bilayer. As a result, such proteins are locked in the membrane by the hydrophobic effect. Conversely, other types of proteins can diffuse along the membrane or along portion of it[4].

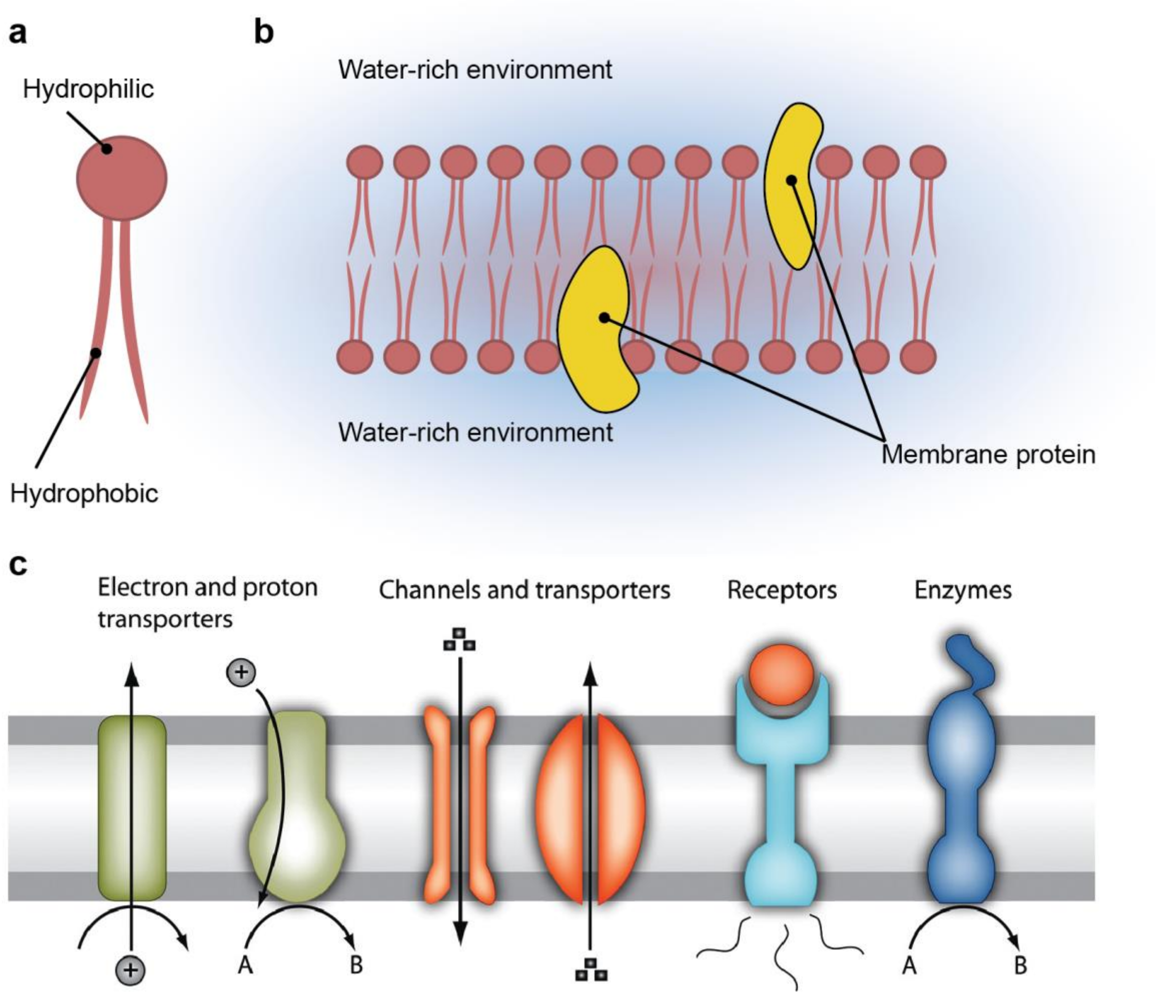

Figure 1.3 | **a**) Phospholipid molecule. **b**) Assembly of a phospholipidic bilayer with protruding membrane proteins. **c**) Several functions of membrane proteins. Adapted from [26].

Among the plethora of membrane proteins, ion channels[28] are particularly relevant for this thesis work. Such integral proteins can form pores in the cell's lipid bilayer, allowing for a selective passage of ions. A plethora of ion channels can be found in cells, offering selectivity to different ions, differing by gating mechanism or functional and structural diversity[7].

They can be divided into temperature-gated ion channels, opening or closing in response to change in temperature[29], ligand-gated ion channel, which opens in response to the binding of a chemical messenger, like a neurotransmitter, as glutamate[30], and voltage-gated ion channels, responding to the changes in the membrane potential[31]. Channels responsible for the transport of potassium, calcium, sodium and chloride belongs to this last category, making them particularly important in AP generation.

Given the importance of understanding the mechanisms underlying neural communication, an equivalent electrical circuit of the PM can be adopted (**Fig. 1.4**). Such models can provide an intuitive and yet quantitative description of electrical signal generation in nerve cells, as the one presented by Hodgkin and Huxley[6] in 1952. In brief, the cell's lipid bilayer endows the neuron with insulating and charge separation properties, *i.e.*, it acts as a capacitance (C_m). In addition, as this capacitance is not perfectly insulating, but it rather behaves like a leaky capacitor, such leakage of ions is modelled through a conductive element (g_r). Sodium and potassium ion channels, on the other hand, allow for ionic currents to flow through, acting as ohmic conductors (g_{Na} and g_K, respectively). Lastly, the resting membrane potential and concentration gradient of both cations and anions, that elicits an electrochemical force, can be modelled as batteries (E_r, E_{Na} and E_K). Several modifications and evolutions of this model are now available in literature[32–35].

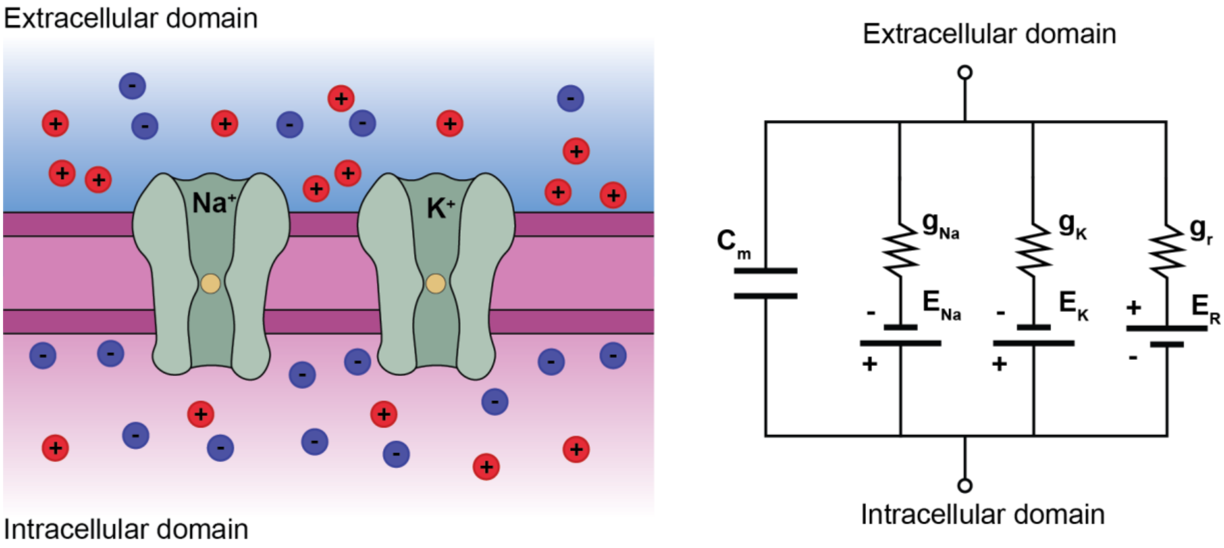

Figure 1.4 | Schematic of the plasma membrane, including calcium and potassium ion channels, along with the equivalent model formulated by Hodgkin and Huxley.

Finally, the PM is directly involved in cell-to-cell signalling and communication, as receptors exposed on the surface of the membrane can trigger a cascade of intracellular responses[36–38].

1.1.2. Action potential generation and synapses

The communication between neurons starts with the generation of an action potential at the soma[39]. Initially the cell is at the resting potential V_m, due to the large amount of Na^+ outside and K^+inside the neuron (**Fig 1.5-a**). Upon stimulation, either chemical, electrical or mechanical, the membrane potential starts to increase, slowly depolarizing it up to a certain level (firing threshold, usually –55 mV). Upon reaching such threshold, sodium ion channels open, allowing for a rush of Na^+ ions to enter the plasma membrane, furtherly and rapidly depolarizing the membrane[3] (**Fig 1.5-b**). Consequently, the polarity of the membrane potential is reversed, reaching the peak of the action potential (*i.e.*, electrical spike) in the range $[30; 40]$ mV. Here, sodium ion channels inactivate, while potassium ones open. As the intracellular domain is now more positive of the extracellular one, K^+ ions flow out of the neuron, restoring the resting potential state[1,6] (**Fig 1.5-c**, **i**). In addition, as potassium ion channels are slow in closing, the neuron hyperpolarizes (**Fig 1.5-c**, **ii**). Slowly, the membrane potential is restored to the resting level, by the sodium-potassium pump that restores the original concentrations of Na^+ and K^+ inside and outside the neuron. During this process, for a period of time, defined as refractory period, the sodium ion channels are inactivated, and the neuron is not able to generate a new AP[40].

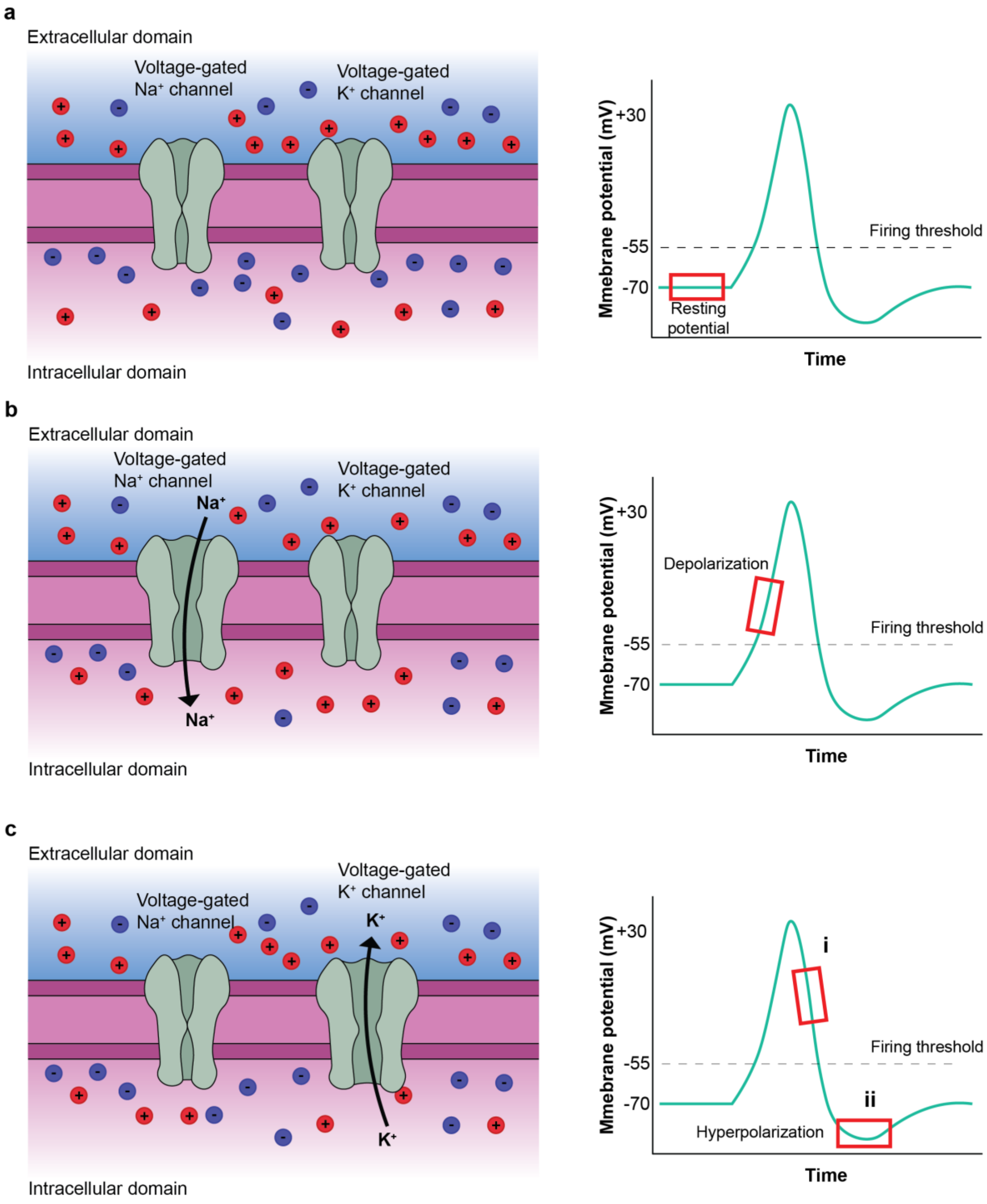

Figure 1.5 | **a**) Neuron at resting potential, with a more positive extracellular environment and a more negative intracellular one. **b**) Depolarization occurring after stimulation, with a flux of NA$^+$ ions entering the cell. **c**) K+ ions exiting the cell, initially recovering the resting potential and then hyperpolarizing the neuron (**i** and **ii**, respectively).

Some important considerations can be drawn by observing AP dynamics. First, an AP is generated only when a firing threshold is crossed. Second, it is an all-or-none event, meaning that the shape of the AP is not dependent on the applied stimulus, as it will have the same shape in case of a stimulus that largely crosses the firing threshold or barely reaches it. Lastly, every current spike is followed by a refractory period, in which the ability of firing a new AP is suppressed[1].

Importantly, Hodgkin and Huxley model can describe and predict such behaviour by independently modelling sodium and potassium dynamics[6], as previously explained (**Fig 1.6**).

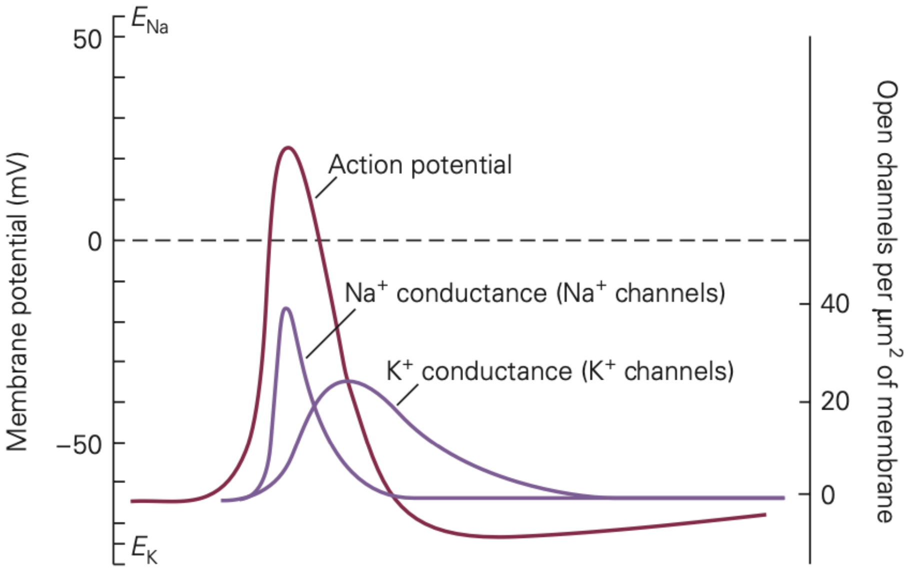

Figure 1.6 | Calcium and potassium dynamics during AP generation, according to Hodgkin and Huxley model. Adapted from [1].

Once an AP is generated, it travels along the axon. While propagating, the AP is supposed to decay with distance. Here, the presence of the nodes of Ranvier is crucial in the fast and efficient propagation of this signal, preventing the signal to die out. In fact, even if the area of membrane at each node is small, this membrane is rich in ion channels. Therefore, upon reaching a node, an intense depolarizing influx of Na^+ is passively generated, regenerating the action potential[9].

In addition, the AP travels slowly when crossing a node, as this area is characterized by a high membrane capacitance, while it rapidly spreads along the myelinated areas of the axon because of the low capacitance of the sheath. As a result, the AP is said to move by saltatory conduction, as it ‘jumps’ from a node of Ranvier to the following.

At its end, the axon is branched in several structures that connect to the dendrites of other neurons at specific zones, namely synapses[1]. Here, the neuron propagating the signal takes the name of presynaptic cell, while all the neural cells receiving such signal take name of postsynaptic neurons. The actual communication takes place when the AP reaches the terminals, eliciting the release of vesicles containing neuroactive molecules in the narrow space separating the pre- and postsynaptic cells, defined as synaptic cleft[41,42] (**Fig. 1.7**). Lastly, the released neurotransmitters will bond to specific receptors of the receiving cell, eliciting an inward current, that might potentially depolarize it[1].

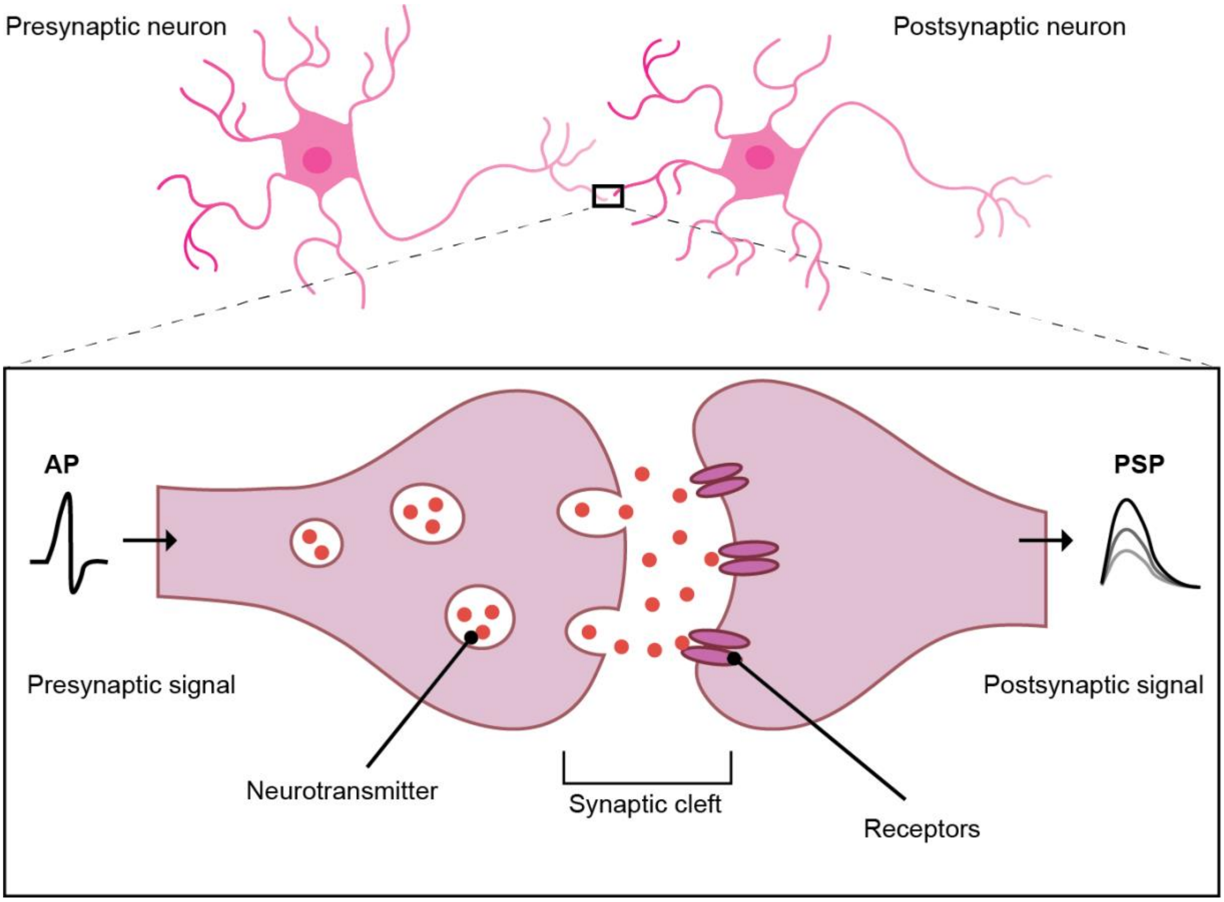

Figure 1.7 | Schematic of a synapse.

The neurotransmitters chemically bind to specific receptors exposed to the synapse on the pre-synaptic neuron, opening/closing ion channel, and eliciting an ionic influx/efflux. Such ionic current, *i.e.*, the transduction of a chemical stimulus into an electrical one, is defined as post synaptic potential[1] (PSP, (**Fig. 1.7**). Importantly, receptors are classified in two groups, based on the ability to directly or indirectly open/close ion channels. When a receptor directly drives the opening/closing of an ion channel, it is referred to as ionotropic receptor[43,44] (**Fig. 1.8-a**). Conversely, when the receptor elicits a series of metabolic reactions leading to the opening/closing of ion channels, it is defined as metabotropic receptor[43,44] (**Fig. 1.8-b**).

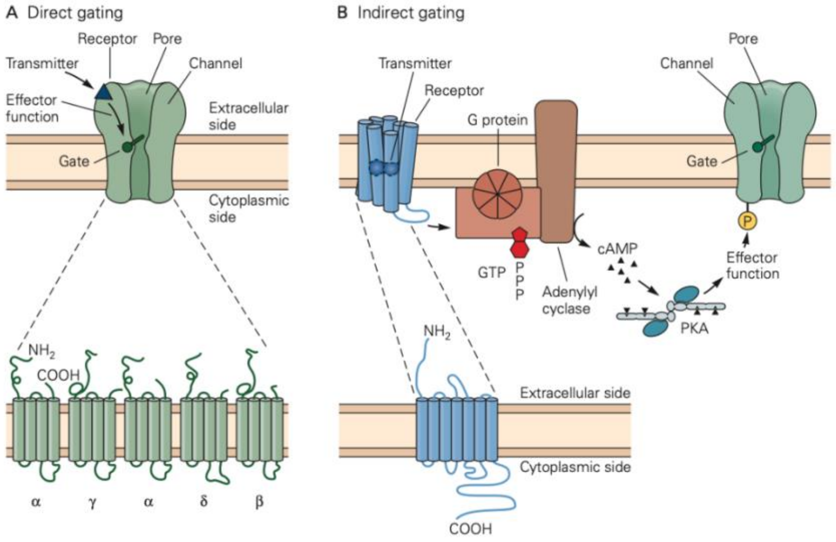

Figure 1.8 | **a**) Example of direct gating mechanism in an ionotropic receptor. **b**) Example of indirect gating in a metabotropic receptor. Adapted from [1].

1.1.3. Synaptic plasticity

As information propagates, correlated signals are enforced while the ones that result in a non-favourable output are depleted, continuously reshaping the countless synaptic connections. This ability of the brain to dynamically reshape to adapt to incoming stimulation is defined as synaptic plasticity and it is pivotal in several functions of the nervous system[1,45,46].

Such modifications can last from few milliseconds to hours. We refer to the former case as short term plasticity, while the latter is defined as long term plasticity. As both mechanisms can either strengthen or weaken a synapse, it is possible to define both short- and long-term potentiation (STP and LTP) and depression (STD and LTD)[45].

1.1.3.1. Short-term plasticity

Short term plasticity is a dynamic modulation of synaptic strength, resulting either in STP or STD. While several mechanisms underlying long term plasticity were deeply investigated, the functioning principle of short-term plasticity remains unclear[47].

What is clear is that both STD and STP relies on a modification at presynaptic level. In particular, the most prominent hypothesis is the so-called residual Ca^{2+} theory, stating that the dynamic potentiation/depression is caused by the presence of Ca^{2+} ions, remaining in the nerve terminals after stimulation[48].

Based on the timescale, it is possible to distinguish between three types of short-term plasticity. Facilitation occurs in the range of 10-100 ms. It occurs when two or more APs arrive in quick succession and following evoked PSPs grew in amplitude, up to ten times higher than the original PSP[49]. Facilitation often builds and then decays as an exponential function of the time (**Fig. 1.9**).

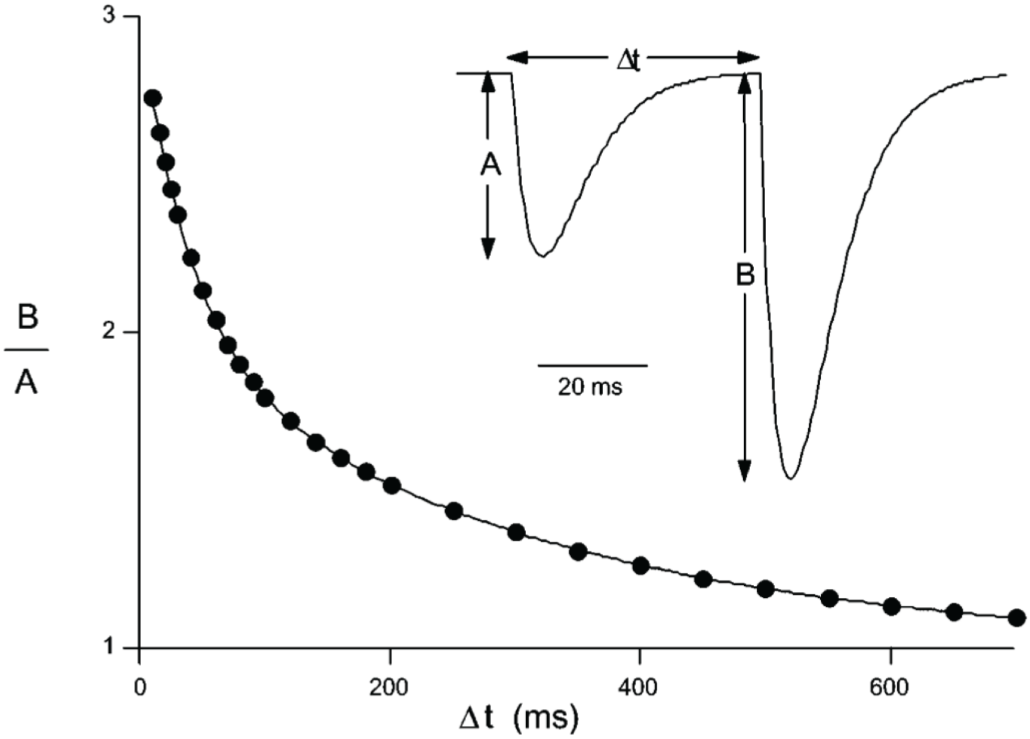

Figure 1.9 | Exponential decay of STP, in the form of paired pulse facilitation/depression. Adapted from [48].

Synaptic augmentation is an increase of the synaptic strength, lasting few seconds, that follows a train of high-frequency stimulation. Lastly, post-tetanic potentiation (PTP) can be observed after a tetanus, *i.e.*, a period of high-frequency stimulation, and can last from 30 s to several minutes. It is important to note that in some neurons, while there are cases in which it is easy to distinguish between synaptic augmentation and PTP, sometimes it is not possible to separate between the two phenomena, as they partially overlap[48].

1.1.3.2. Long-term plasticity

Long term synaptic plasticity defines a long-lasting change in the strength of synaptic connections. It is at the basis of learning and memory in the brain. Despite several types of long-term plasticity were theorized, modelled and experimentally demonstrated, it is possible to group them in broad categories as follows, to highlight some fundamental differences: Hebbian learning, neuromodulated plasticity, supervised plasticity and behavioural timescale plasticity.

1.1.3.2.1. Correlative Hebbian synaptic plasticity

The first category of synaptic plasticity is the so-called Hebbian learning. In late 1940s' Donald Hebb postulated that if cell A "repeatedly or persistently takes part" in firing cell B, their connection should strengthen[50]. Later, in early 1970s, synaptic plasticity was first reported in hippocampus: the near-synchronous activation of pre- and postsynaptic neurons resulted in a strengthening of the synaptic input only in the stimulated connections[51]. The mechanism is ascribable to N-methyl-d-aspartate glutamate receptors (NMDARs). The coincidence of glutamate binding and a depolarized membrane potential allowed for a temporal overlap of the presynaptic input and the AP, increased the postsynaptic intracellular Ca^{2+} levels[52].

As the coincidence of synaptic input and AP generation is seen as a correlation between pre- and postsynaptic signalling, most types of investigated synaptic plasticity fall into these self-correlative mechanisms, defined as Hebbian learning (**Fig. 1.10**).

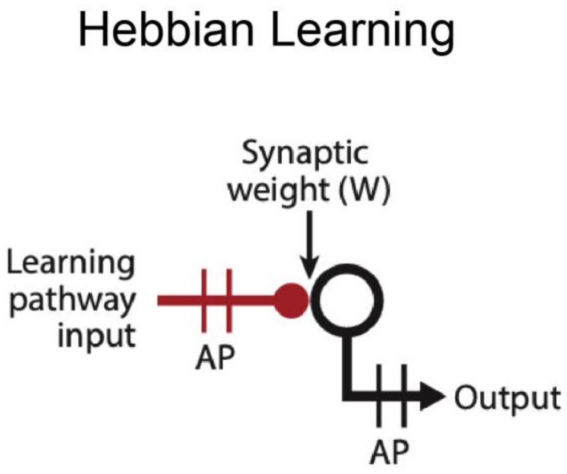

Figure 1.10 | Schematic of Hebbian learning, in which the presynaptic activity regulates the synaptic weight modulation. Adapted from [46].

Among the plethora of LTD/LTP mechanisms, spike timing dependent plasticity (STPD) represents the most prominent example of Hebbian learning[53,54]. STPD broadens the concept of correlation, introducing time. In brief, if a presynaptic input occurs just before a postsynaptic spike, that connection is strengthened. Conversely, if the presynaptic signal follows the postsynaptic one, the synapse is weakened. Four types of STPD are reported[55,56] as symmetric Hebbian/anti-Hebbian and asymmetric Hebbian/anti-Hebbian learning rules (**Fig. 1.11**).

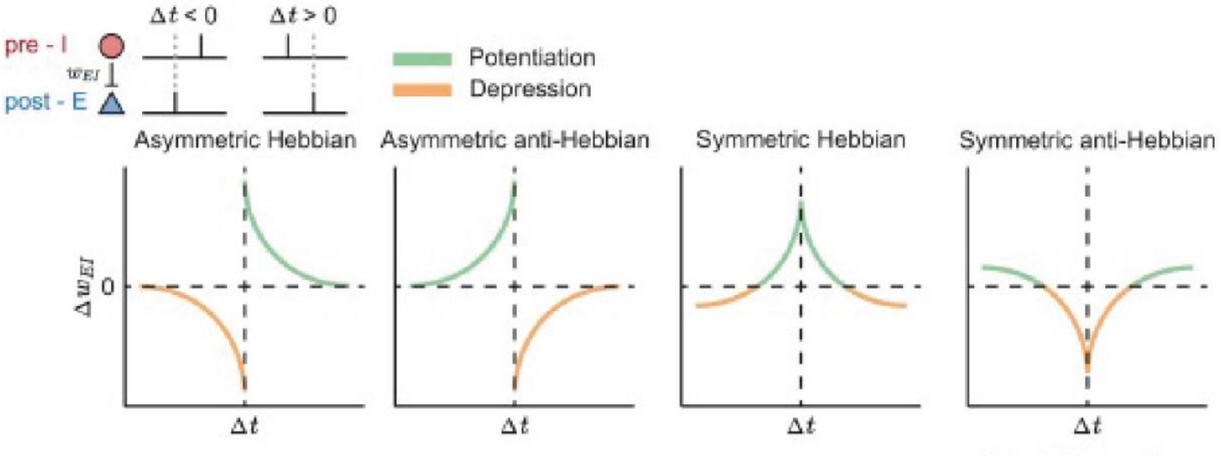

Figure 1.11 | Four types of STPD. In asymmetric Hebbian STPD potentiation occurs when the postsynaptic stimulus follows the presynaptic one, while depression occurs in the opposite case. Asymmetric anti-Hebbian is characterized by the opposite situation, *i.e.*, a presynaptic stimulus following a presynaptic one is depressed. In symmetric learning, on the other hand, potentiation/depression occurs when the time delay between pre- and postsynaptic stimuli tends to zero (Hebbian and anti-Hebbian, respectively). Adapted from [55].

Despite the simple correlative Hebbian synaptic plasticity correctly approximates synaptic strengthening/weakening mechanisms, it still presents some limitations. First, there is a timescale problem, as it is not clear how synaptic mechanisms operating on physiological timescales (tens of milliseconds) could influence behavioural[57] (in the range of seconds). A second problem is the locality of the synapses' modifications, *i.e.*, a given neuron can't know if it is useful to strengthen/weaken a certain synapse[58]. Lastly, without a clear regulation mechanism, synapses should change continuously, resulting in an overwriting of old memories[59].

1.1.3.2.2. Neuromodulated synaptic plasticity

Neurotransmitter and neuroactive molecules have been shown to modulate synaptic plasticity in a reward-motivated behaviour[60,61], in a concentration and receptor type dependent manner, leading to the idea that neurotransmitters could mediate Hebbian learning[62,63].

This neuromodulated model of synaptic plasticity may also overcome two limiting factors of the self-correlative Hebbian learning rule. Firstly, it introduces the idea of a behavioural-global message, overcoming the problem of the locality of the STPD. In addition, the presence of a neuromodulator may act as a regulating factor, avoiding undesired synaptic modifications.

Neuromodulated plasticity can be explained through the concept of eligibility traces[57] (ETs). ETs are defined as internal signals, related to a single synapse, that do not produce any electrical output, but they rather mark a synapse as eligible for modifications (**Fig. 1.12**). In addition, these signals operate on a timescale of few seconds.

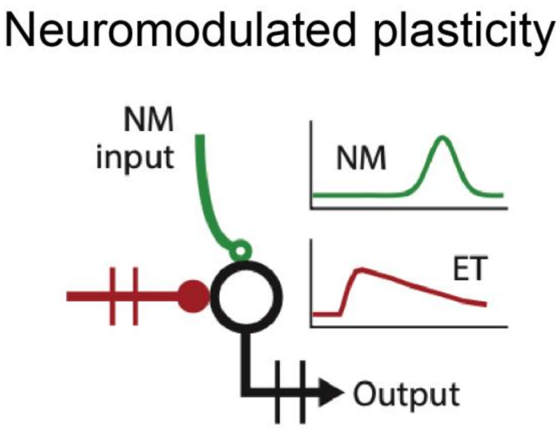

Figure 1.12 | Schematic of neuromodulated plasticity, in which neuroactive molecules generated ETs, marking the synapse as eligible for modification. Adapted from [46].

This approach is also referred to as three-factor STPD. In brief, Hebbian-like correlated signals (synchronous pre- and postsynaptic signals) do not induce synaptic weight modification, but they generate ETs, that are subsequently gated by the presence of neuromodulators[64,65].

The presence of neuromodulators clearly impacts synaptic plasticity, also correlating single synapses to behavioural outcomes. Still, the role of neuromodulators in plasticity remains unclear, suggesting that such molecules may be of a permissive nature, rather than an instructive one.

1.1.3.2.3. Supervised synaptic plasticity

The concept of supervised plasticity, or more in general, supervised learning refers to a process in which synaptic weights are iteratively changed to minimize an error, or a cost function, introducing the concept of a goal, both in biological and artificial neural networks[46].

Supervised synaptic plasticity includes three main actors (**Fig. 1.13**): first, there is a pattern to be achieved, *i.e.*, an objective often coming from another area of the brain. Then there is an instructive pathway, that is typically a non-local at the synapse that evokes dendritic spikes at presynaptic level. Lastly, there is a voltage signal within neural dendrites, involved in synaptic plasticity. This last signal is defined as instructive signal, as it triggers plasticity in the dendritic spikes evoked by the instructive pathway[46].

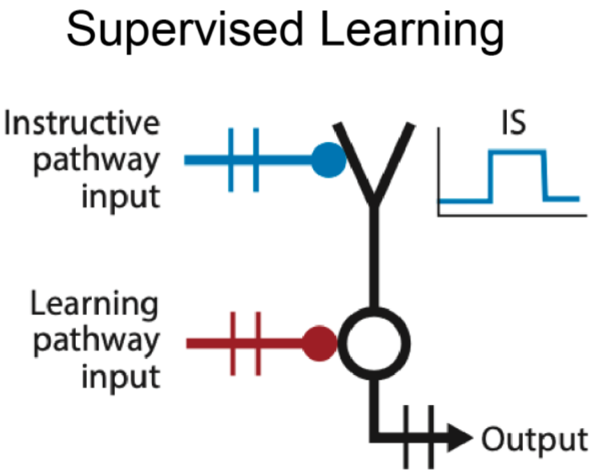

Figure 1.13 | Schematic of supervised learning, in which an instructive pathway evokes dendritic spines at presynaptic level, while a learning pathway triggers synaptic plasticity. Adapted from [46].

Supervised learning was observed and demonstrated in the cerebellar cortex, with a single-layer of adaptive neurons (**Fig. 1.14**), Purkinje cells (PCs). PCs receive a feedback input that evokes Ca^{2+} dendritic spikes (instructive pathway). Then, granule cells project feedforward synaptic signals, whose weights are adjusted by classical Hebbian STPD, modulating the AP output[66,67].

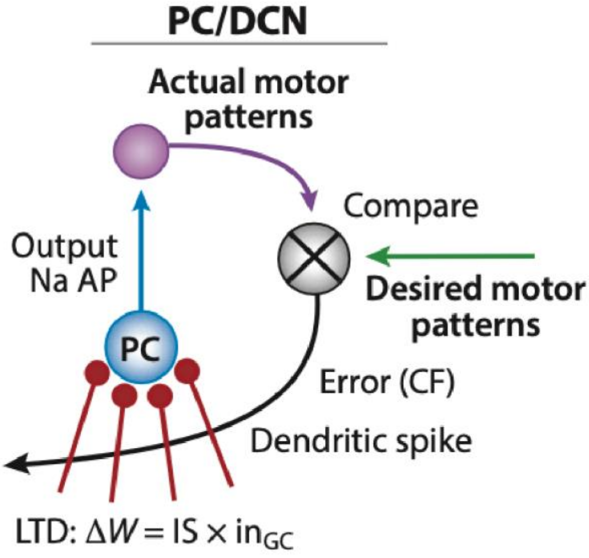

Figure 1.14 | Example of supervised learning in PCs, which receive a feedback from the comparison of a desired motor pattern and the actual produced one. Adapted from [46].

Supervised learning was also demonstrated in multilayer networks, implementing a strategy to update synaptic weights of hidden-layers. Here the instructive pathway guides the weight updates in the intermediate layer by projecting on the dendrites of the very same layer. Then, an internal comparison with feedforward input signals is performed to generate a local error[68]. Thereby, whenever the feedforward signal deviates from the target, synaptic plasticity occurs in this intermediate layer, locally[69]. Such strategy ensures that the overall output error is minimized by reducing the local-generated error.

Such mechanisms are found in the cortical areas of the brain, where pyramidal neurons form complex networks, receiving feedforward signals from the lower levels of the networks, and feedback synapses from other areas of the brain[70,71]. The feedforward signals are projected in the vicinity of the soma, in the so-called proximal compartment, eliciting APs[72]. The feedback signals, on the other hand, innervates the distal region, *i.e.*, far away from the output site of the neuron (**Fig. 1.15**). Such signals will elicit Ca^{2+} plateau potentials[73], that are known to promote synaptic plasticity[74–76].

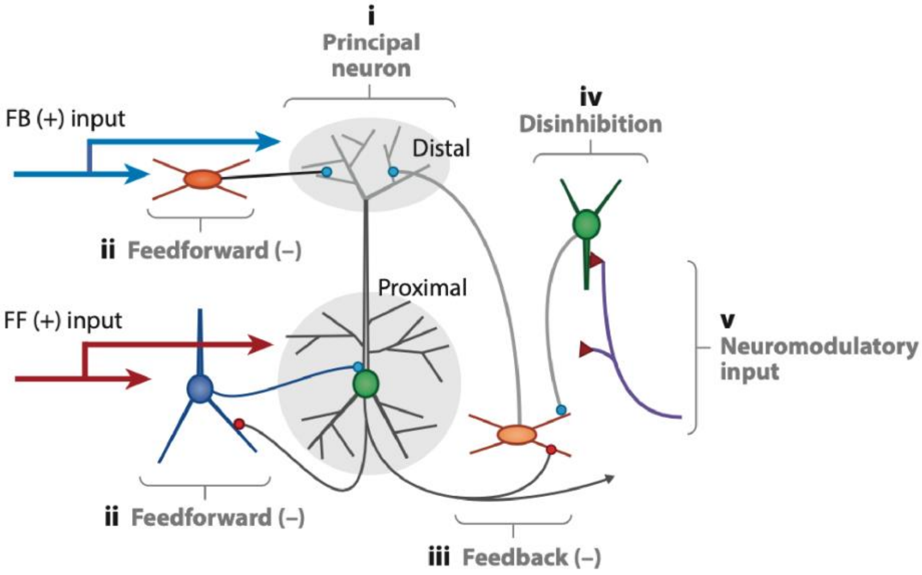

Figure 1.15 | Pyramidal neurons achieving multilayer supervised learning. Adapted from [46].

1.1.3.2.4. Behavioural timescale synaptic plasticity

Behavioural timescale synaptic plasticity can be seen as a combination of the above-mentioned learning rules[77,78].

1.2. Sensory coding

All the neural principles illustrated in the previous paragraphs are exploited by the CNS to allow for the execution of multiple functions. For instance, in humans and, more in general in animals, the sensory processing is originated in specific receptor cells spread all over the body[79,80]. These cells can sense a specific stimulus and transduce into an electrical signal, that, in accordance with the nomenclature used for synapses, is defined as receptor potential[81,82].

Importantly, there is a difference between APs and receptor potentials. While the former are all-on-none events whose shape and amplitude do not depend on the type of stimulation (**Paragraph 1.1.1** for details), the latter are characterized by a graded response, *i.e.*, with duration, shape and amplitude directly dependant on the type of stimulation[83]. Here, touching objects at different temperatures, like 50 and 100 ˚C, will cause the same receptors to react differently. For this reason, one can model APs as digital signals, while receptor potentials are analog signals. Typically, the analog-to-digital transduction of sensory information is carried out by means of the afferent neurons, *i.e.*, neural cells connected to receptors, that will transduce the analog intensity of receptor potentials into a digital train of pulses (APs), whose frequency mirrors the amplitude of the original stimulus[79,84]. Lastly, the peripheral nervous system (PNS) transmits these APs to the central nervous system (CNS), composed by the brain and the spinal cord (**Fig. 1.16)**.

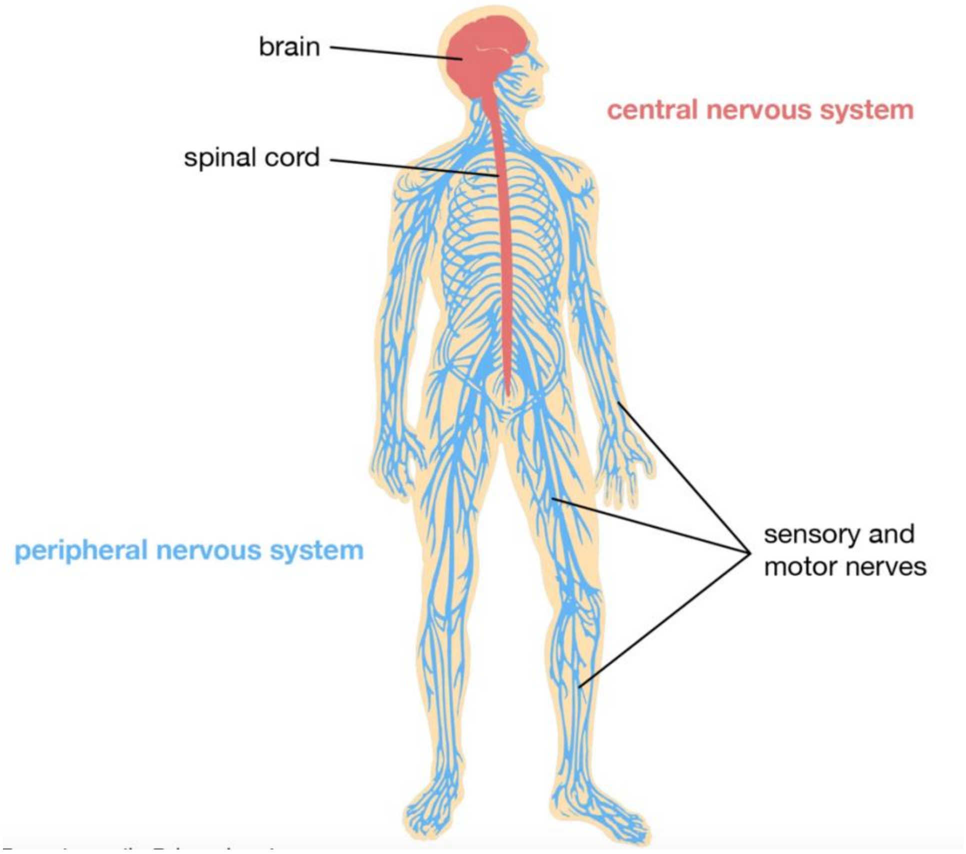

Figure 1.16 | **a**) Schematic of the communication between nerves, PNS and CNS. Courtesy of Encyclopaedia Britannica [85].

Human sensory receptors are grouped as photoreceptors, mechanoreceptors, chemoreceptors and thermoreceptors[1,86]. The former are responsible for vision, and they can be found in the retina. The sense of touch is mediated by different types of mechanoreceptors. Chemoreceptors are responsible for olfaction and gustation. Lastly, thermoreceptors can sense cooling and warming.

1.2.1. Touch

The sense of touch is crucial in everyday life. It comprises several sensations, like pressure, vibration, temperature and pain. It relies on mechanoreceptors spread throughout the body.

Notably, the mechanoreceptors of the glabrous skin[87] represented a source of inspiration for this thesis work. They can be divided into: Meissner corpuscles, Merkel cells, Pacinian corpuscles and Ruffini endings (**Fig. 1.17-a**). They differ in size and depth within the skin, and they can be grouped into rapidly adapting (RA), responding to motion on the skin, and slowly adapting (SA), that keep on firing in response to a steady pressure.

Merkel cells and Ruffini endings are type 1 and type 2 SA cells, respectively (SA1, SA2). The former are particularly sensitive to edges and corners, while the latter are specialized to response to stretch, *i.e.*, they are particularly sensitive to the shape of the object.

Meissner corpuscles are rapidly adapting type 1 (RA1) cell, and they are responsible to detect the initial contact with a surface. Lastly Pacinian corpuscles are rapidly adapting type 2 (RA2), capturing high-frequency vibrations. To summarize, these four receptors differ in the receptive field (**Fig. 1.17-b**). Consequently, the same stimulus elicits very diverse spike trains[1] (**Fig. 1.17-c**).

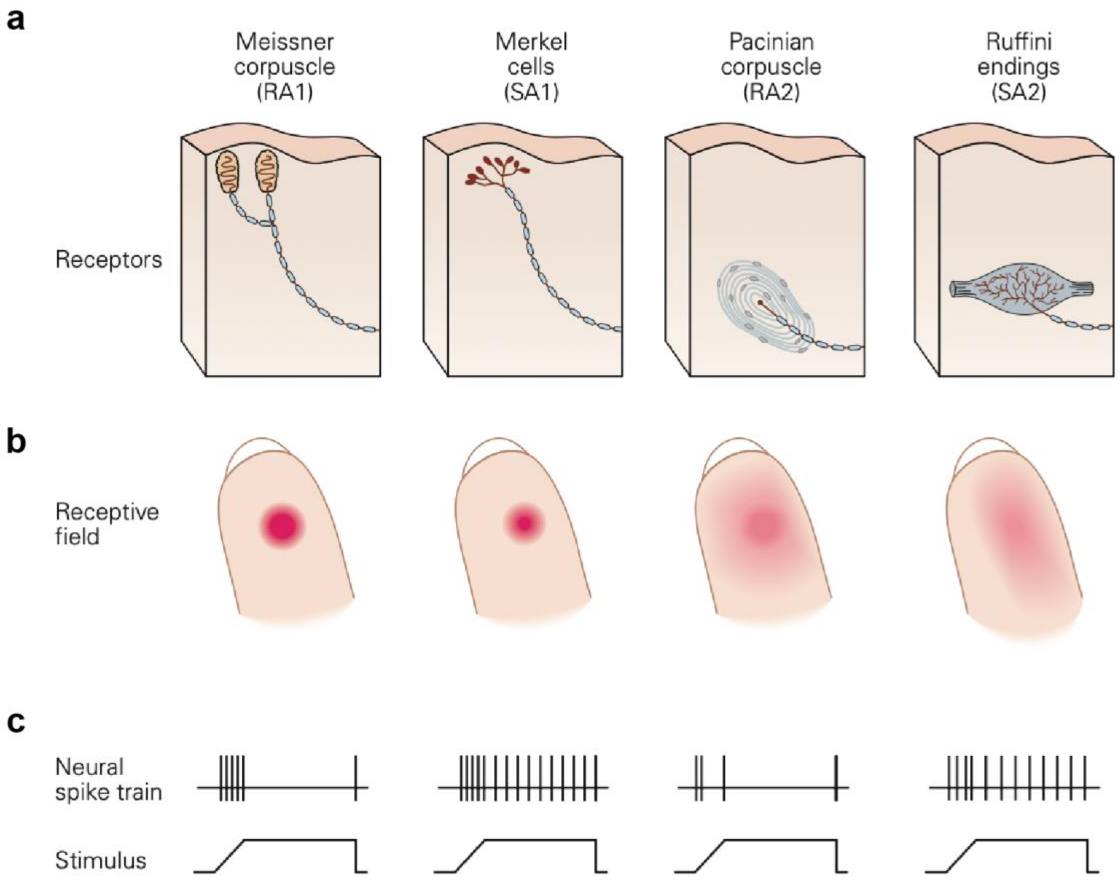

Figure 1.17 | **a**) Mechanoreceptors of the human glabrous skin. **b**) Receptive field of each mechanoreceptor. **c**) Elicited neural spike train of different mechanoreceptors, as a response to the same stimulus. Adapted from [1].

These receptors are contained in specific neurons, called dorsal root ganglion (DRG) neurons[88]. Such neurons are characterized by an axon with two branches, one projecting to the periphery and one projecting to the CNS.

1.2.2. Vision

The sense of vision represents the largest source of information for humans, that can perceive the environment through the usage of light.

The transduction of light into electrical signals takes place in the retina[89], that acts as the brain's window on the world. The retina contains several types of cells: photoreceptors (rods and cones), bipolar cells (BCs), horizontal cells (HCs), amacrine cells (ACs) and ganglion cells (GCs).

Such cells are organized in layers[89,90] (**Fig. 1.18**). The outer nuclear layer (ONL) hosts the cell bodies of the photoreceptors. The inner nuclear layer (INL) contains the soma of BCs, HCs and ACs, while the ganglion cell layer (GCL) hosts GCs. In addition, two more layers composed of fibers and synapses separate the first three layers, namely outer plexiform layer (OPL) and inner plexiform layer (IPL).

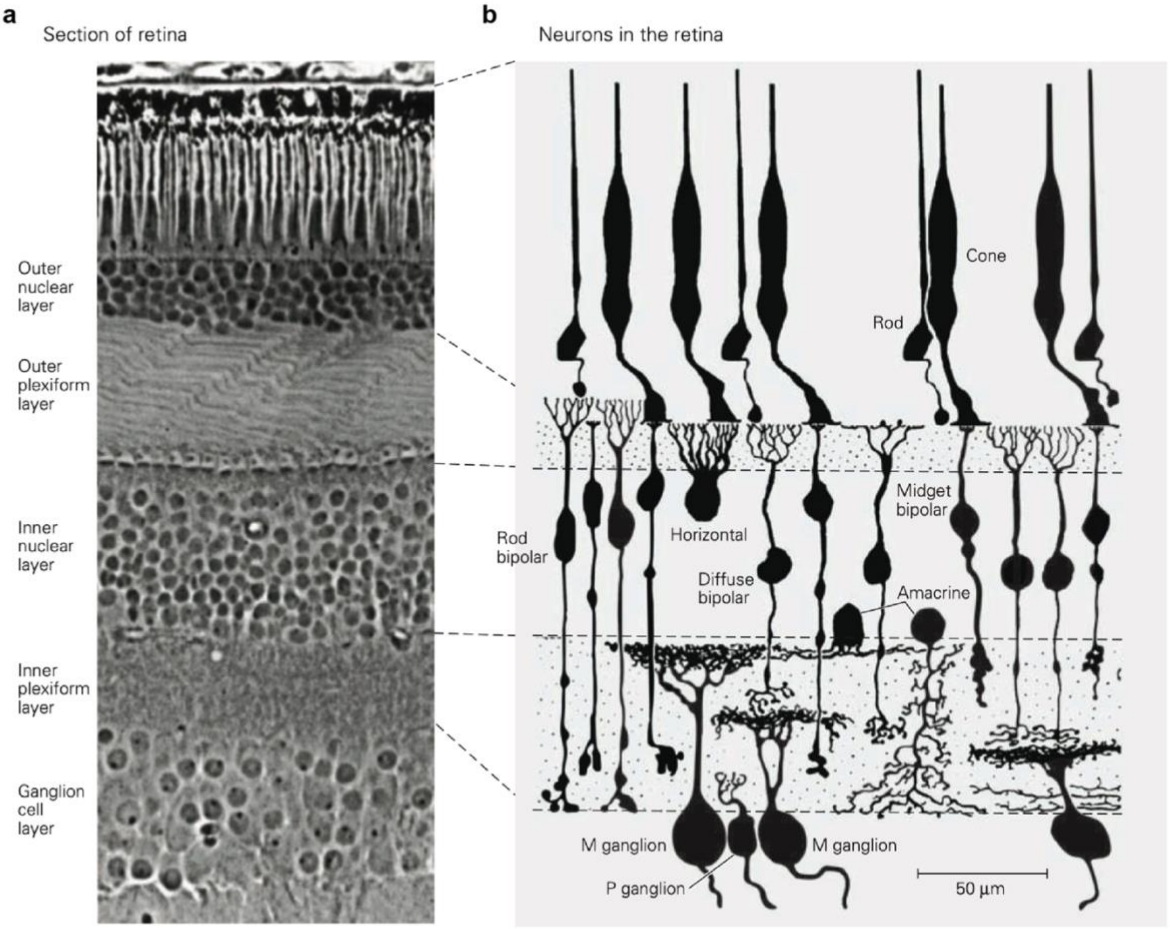

Figure 1.18 | **a**) Section of human retina, showing the division in layers. **b**) Schematic of the retina layers and structure. Adapted from [1].

The visual information is not simply delivered from the retina to the brain, but the optical signal is transformed at each layer of synapses, making calculations before leaving the eye and reaching the brain. The information streams in two directions at the same time. There is a main or vertical pathway, propagating the information from photoreceptors to BCs and from BCs to GCs. A secondary, or lateral pathway, goes from photoreceptors to HCs and back again to photoreceptors, providing local feedback. While the former pathway delivers the signal from the eye to the brain, the latter provides an adjustment of the gain of the photoreceptors, to optimize vertical signal transmission[90,91].

Of particular importance in this work is the vertical pathway. The phototransduction starts with rods and cones. They differ in morphology and sensitivity to light. Rods have a long cylindrical shape, while cones are shorter. The former are responsible for vision under dim light, *i.e.*, night vision, while latter are less sensitive to intensity of light, but they are responsible for daylight vision, as they can distinguish different wavelengths[90].

In dark conditions, both types of receptors are depolarized ($V_m \cong$ -45 mV). As a result, a continuous release of neurotransmitter (glutamate) occurs. Such phenomenon is the consequence of the opening of cyclic guanosine monophosphate (cGMP) gated cation channels that are held open in absence of stimulation, allowing for an inward depolarizing current. In presence of light, on the other hand, cGMP-gated cation channels close, hyperpolarizing the cell and decreasing the release of glutamate[91].

Unlike photoreceptors that solely hyperpolarize in presence of light, BCs can undergo either depolarization or hyperpolarization. BCs that hyperpolarize with light are call OFF BCs, while the ones that depolarize with light are called ON BCs. The difference between these cells, both exploiting the decrease of glutamate, lies in the nature of the receptors they expose at the synaptic domain. The former (OFF BCs) are equipped with ionotropic receptors (in particular, iGluRs) that are keep membrane pores open in presence of glutamate, allowing for an inward current of ions. These pores are closed when glutamate concentration decreases. Conversely, ON BCs feature metabotropic receptors that do not form pores in the membrane. They are G-protein-coupled receptors that bind to glutamate and close non-specific cation channels in dark conditions, hyperpolarizing the cell at rest. When light stimulation decreases the glutamate rate, cation channels can open, depolarizing the cell[91].

Lastly, the processed signal is transmitted to GCs that are the first retinal neurons featuring all-or-none signalling, *i.e.*, they produce APs that propagate through their axon to reach the brain[90,91].

To summarize, a photoreceptor can either be connected to an OFF BC (OFF vertical pathway) or to an ON BC (ON vertical pathway). In the former case, light stimulation leads to the termination of APs generation. In the latter, upon light exposure, APs are generated (**Fig. 1.19**).

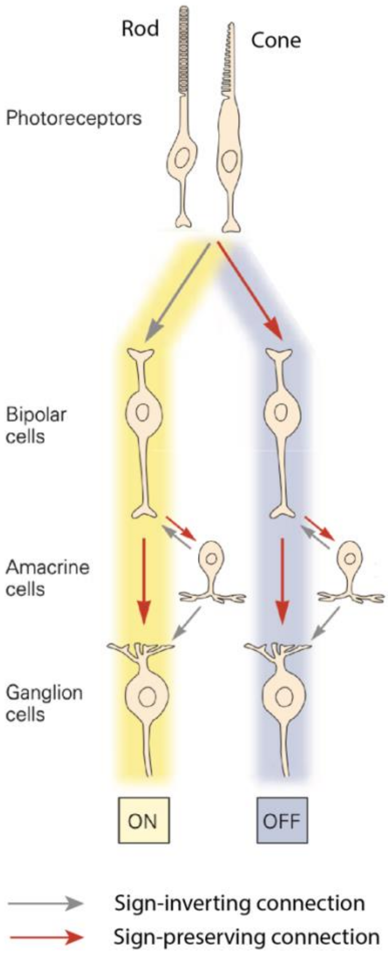

Figure 1.19 | Schematical illustration of the OFF vertical pathway of the human retina. Adapted from [1].

1.3. Closed-loop communication in the brain

Another important feature of the brain is the active exploitation of numerous feedback loops to effectively transmit information and perform computations. Indeed, closed-loop processing is vital at every level of neural activity, ensuring accurate behavioural responses[1].

For instance, when executing a simple movement, a feedforward dynamic model is used to command the muscles of the body to move a limb. In addition, the information coming from the sensory systems provides feedback signals that are exploited to adjust the "gain" of the movement[1]. Such protocol is then iterated until the final desired state is reached (**Fig. 1.20**).

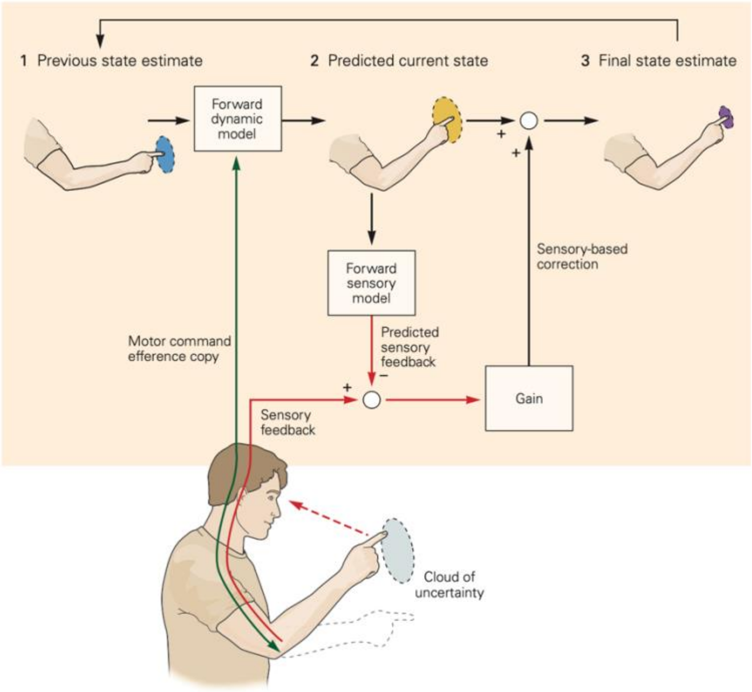

Figure 1.20 | Example of closed-loop processing occurring between several organs and several areas of the brain, in order to accomplish a task, such as moving a finger. Adapted from [1].

Feedback loops of the brain usually involve different areas that cooperate to accomplish a certain task. For instance, the motor generation in the human body requires the closed-loop dopamine (DA) mediated communication of three different areas of the brain: motor cortex, basal ganglia and striatum [92]. The basal ganglia motor processing starts with an input signal of the planned movement from the cortex to the striatum. A DA enhanced and movement-promoting direct pathway, and a DA suppressed, and movement-inhibiting indirect pathway take place within the basal ganglia. The output of the basal ganglia is then projected to the thalamus and then back to the motor cortex. To summarize, in this circuit knows as nigrostriatal pathway, DA signals from the midbrain modulate the integration of descending control signals from the motor cortex in the striatum to generate motor output, in a closed-loop fashion[93,94] (**Fig. 1.21**).

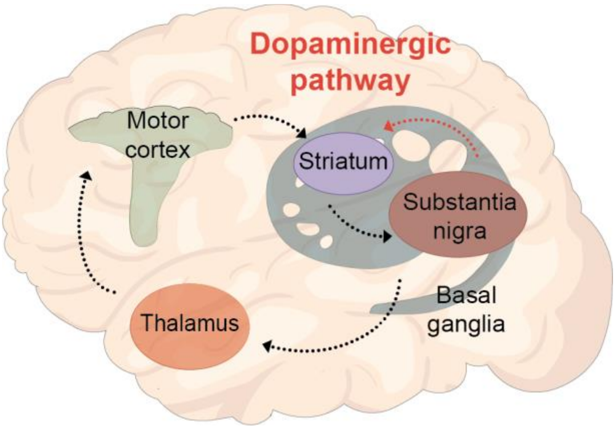

Figure 1.21 | Basal ganglia closed-loop circuity, involved in motor generation. Here, DA acts as a reward, enforcing positive outcomes.

1.4. Neuromorphic engineering

The word “neuromorphic” was introduced in the 1990s by Carver Mead, to define mixed analog/digital very large-scale integration computing systems, taking inspiration from the way in which the brain is organized[95]. Then neuromorphic engineering has emerged as a new research field, combining knowledge of different disciplines to create electronic systems able to recapitulate neural computational primitives[96,97].

The field rapidly developed, including either the implementation of neural circuits, or spike-based systems that leverage on computational neuroscience models. Consequently, some approaches are focused on the strict recapitulation of neural dynamics, others focused on the implementation of brain-inspired principles to perform calculations, as matrix multiplications.

1.4.1. Energy consumption and von Neumann architecture

State-of-the-art artificial neural networks (ANNs) and artificial intelligence (AI) systems are revolutionizing information technology and our daily lives. These intelligent systems are now able to perform decision-making tasks[98], image[99,100] and speech recognition[101] and, very recently, natural language processing with the rise of the famous OpenAI’s GTP model that is now able to handle context and sequence-dependent information[102].

The training of such architectures is a data-driven process, relying on the availability of huge amount of data to generate output. Conversely, handling this amount of information requires an always increasing number of floating-point operations per second (FLOPS). While the demand of FLOPS in brain-inspired architecture doubles every two months[103], available computational architectures based on graphic processing unit (GPU) and tensor processing unit (TPU) “only” double their FLOPS every two years[104,105] (**Fig. 1.22**).

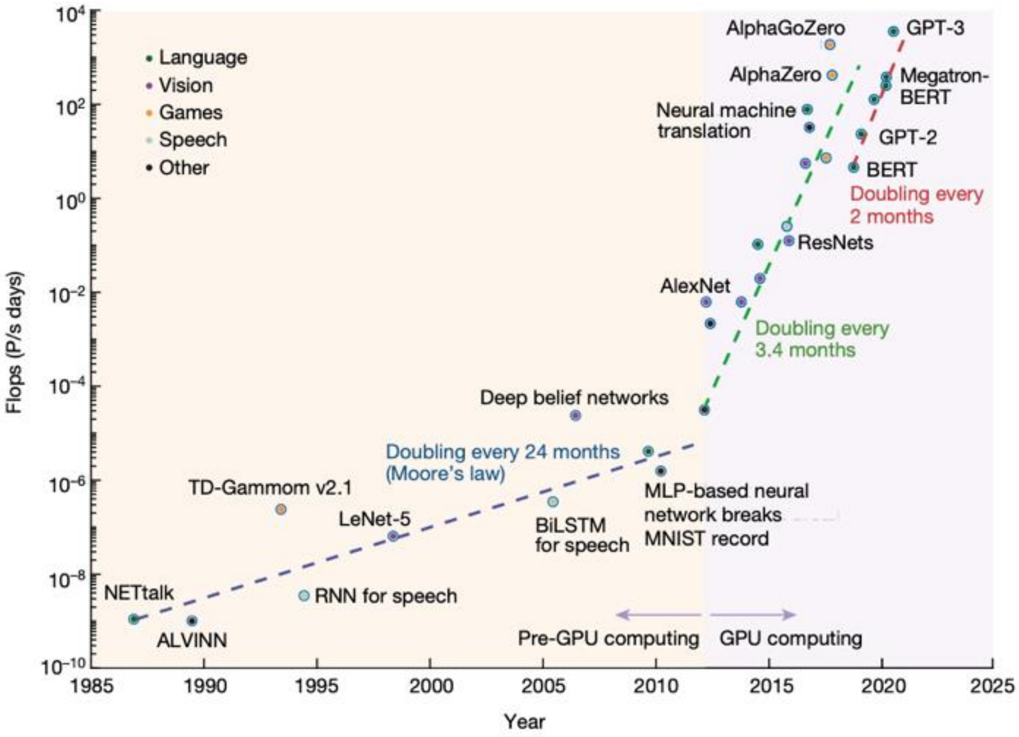

Figure 1.22 | Flops evolution as a function of the time, and of the computing architecture. Adapted from [96].

Here, the training of such architectures is performed on the cloud. For instance, training GPT-3 required 9200 GPUs for two weeks[102], consuming as much carbon as 1300 cars in the same amount of time[106]. Indeed, it's estimated that 5%-15% of global energy consumption is utilized in various data-related activities[107], such as data processing and transmission.

Indeed, data movement is the primarily source of energy dissipation. While executing a multiplication between two 16-bit-floating-point numbers consumes less than 1 pJ, transmitting the result of such operation in a chip consumes about 50 pJ[108].

In addition, data transmission introduces another relevant problem, formally known as von Neumann bottleneck. The traditional computer architecture (von Neumann architecture) is characterized by a central processing unit (CPU) that is physically separate from a memory unit. CPU and memory unit share the same bus, and, as the CPU is much faster than the transfer data rate, the processor often wait for data to be delivered, resulting in data congestion.

Considering this, neuromorphic devices are emerging as ideal candidates to solve the above-mentioned problem. Regarding the von Neumann bottleneck, the human brain and brain-inspired devices foresees co-localization of memory and processing unit. In addition, from an energetic point of view, the energy dissipation of traditional chips scales with the power of N (number of transistors), while 3D-sparse architectures could result in a linear scaling with number of neurons, as it happens in the mammalian brain[96] (**Fig. 1.23**).

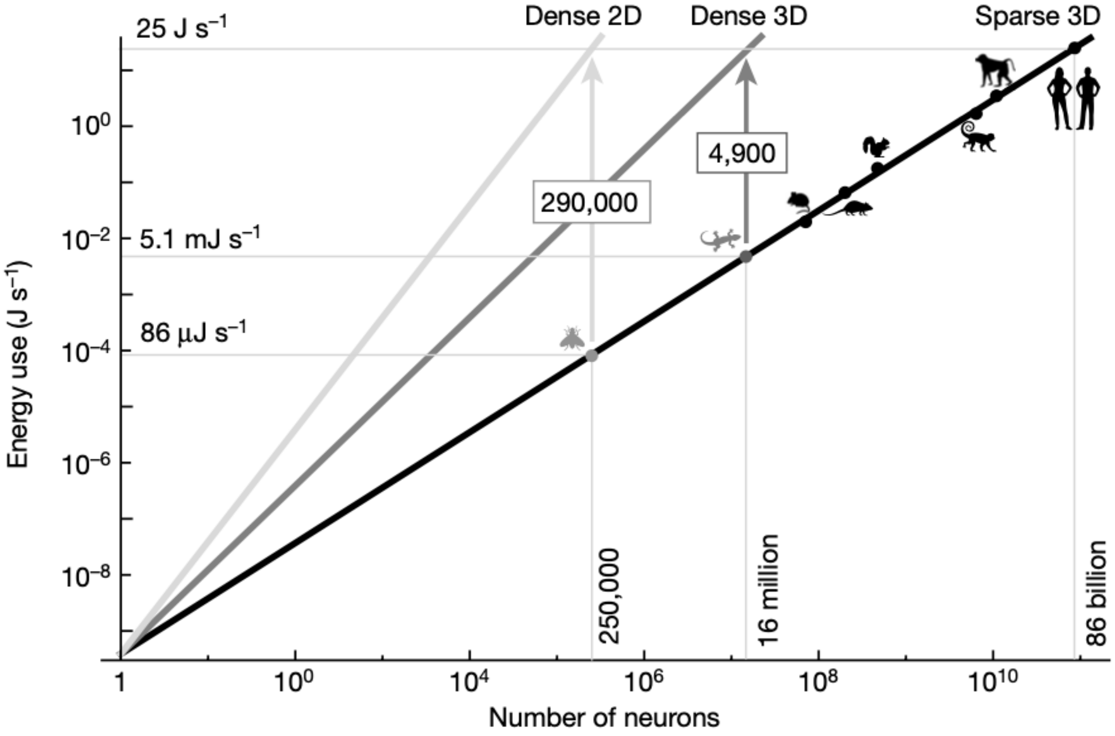

Figure 1.23 | Dependency of the energy consumption on the number of neurons, in different architectures, *i.e.*, 2D, dense 3D and sparse 3D. Adapted from [96].

In this section the working principle of several inorganic (*i.e.*, based on silicon, metal, oxides etc) neuromorphic devices, material and circuits will be shown.

1.4.2. Neuromorphic devices and materials

The combination and the recent advancements in material science and technology processes led to the development of a plethora of neuromorphic devices, exploiting several physical properties to emulate relevant features of the human brain.

1.4.2.1. Memristors

The principle of a memristor was introduced by Chua[109] in 1971. It is a passive and non-linear electrical device with two terminals (anode and cathode), interspaced by a resistive layer. Such structure allows the device to change its electrical resistance upon electrical stimulation, computing and storing information at the same time, mimicking the brain in-memory computation[110,111].

Commonly, upon applying a voltage stimulus, memristors undergo a reversible switching between two separate conducting states: high resistance state (HRS) and low resistance state (LRS) (**Fig. 1.24-a**). The underlying mechanism is the formation/rupture of conducing pathways between the two-terminals of the device. The resistive change is usually retained over time, without the application of any voltage, drastically reducing energy consumption. In addition, it is possible to divide memristors in two broad categories, unipolar and bipolar[112]. In the former case, the switching between HRS and LRS is not dependant on the direction of the voltage/current sweep. In the latter, two different electrical signal polarities are required to switch from HRS to LRS, and vice versa. Another broad categorization is based on the two main physical processes involved in the switching: valence change mechanism (VCM) and electrochemical metallization (ECM).

In VCM the resistive layer is usually a metal oxide film (HfO_2, Ta_2O_5, TiO_2, etc.). Applying an electrical potential at the cathode results in an electrical field, that pushes oxygen atoms out from the lattice of the metals oxides to the anode. The oxygen vacancies lead to the formation of a sub-oxide phase as a conductive filament, connecting anode and cathode[113,114] (**Fig. 1.24-b**).

In ECM the conductive path connecting anode and cathode is the result of the migration of metal ions. The usual structure of this type of device is metal/electrolyte/metal. A first active electrode is usually made of Ag, Ni or Cu, while the counter electrode is made of Pt, Pd or TiN. Electrochemical reactions are triggered by an applied voltage, that drives ionic transport within the device, causing the creation of a metallic filament[115] (**Fig. 1.24-c**).

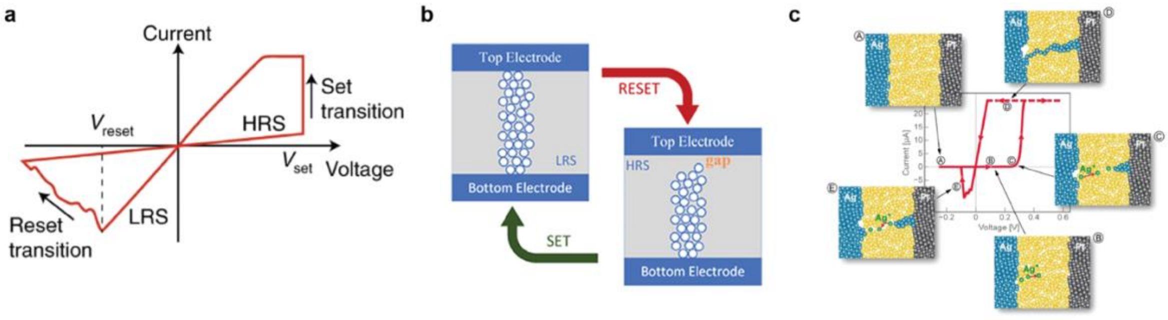

Figure 1.24 | a) Switching mechanisms of memristive device. Adapted from [111]. **b**) Formation of a conductive filament in VCM memristors, upon set transition, and disruption of the conductive pathway, which follows a reset stimulus. Adapted from [114]. **c**) Schematic of the creation and disruption of metallic filaments in ECM, during different phases of switching. Adapted from [115].

1.4.2.2. Ferroelectric devices

Ferroelectricity describes the ability of a material (usually a crystalline material) to be permanently electrically polarized, because of the formation of stable electric dipoles[116]. Exploiting this principle, ferroelectric random-access memories (FeRAM) were demonstrated[117], where the information is stored as the polarization state of the ferroelectric material.

The building block of neuromorphic ferroelectric devices is the ferroelectric tunnel junction (FTJ). It usually comprises two electrodes and an ultrathin ferroelectric barrier (3-4 nm) separating them. The change in the polarization direction leads to charge modulation, increasing or decreasing the potential barrier between the two electrodes, in a continuous manner[118,119]. Several brain-inspired features were demonstrated in such devices, as LTP/LTD induced by changing amplitude/width/number of applied voltage pulses, along with STPD curves[120] (**Fig. 1.25-a**).

Ferroelectric neurons were also demonstrated with leaky ferroelectric field-effect transistor[121] (FeFET), *i.e.*, three terminal devices in which a ferroelectric material is employed as gate dielectric (**Fig. 1.25-b**).

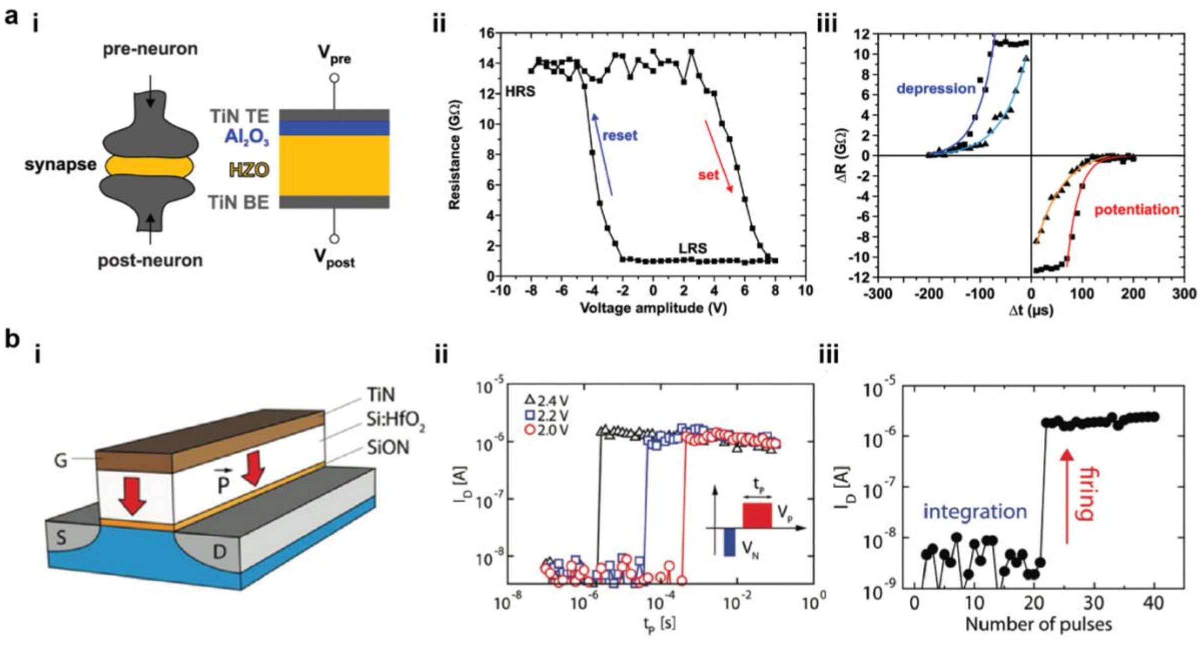

Figure 1.25 | **a**) Ferromagnetic neuromorphic two-terminal device. **i**) Schematic of the device. **ii**) Switching between HRS and LRS. **iii**) Emulation of PPF and PPD. Adapted from [120]. **b**) Neuromorphic ferroelectric three-terminal device. **i**) Schematic of the device. **ii**) Switching-on of the device upon pulse application **iii**) Emulation of the neural input integration and firing. Adapted from [121].

1.4.2.3. Phase-change memory

Phase-change memory (PCM) are non-volatile memory devices that rely on materials (typically compounds of Ge and Sb) able to switch between amorphous and crystalline phases upon the application of voltage pulses, leading to different resistive states[122] (**Fig. 1.26-a**). Despite these devices can switch between a high and a low resistive state like memristors, they differ from the latter in possibility of continuously tuning their resistance. This feature is enabled by intermediate phase configurations[122] (**Fig. 1.26-b**). Indeed, when applying a low and wide voltage pulse a gradual growth of nanocrystals occurs. Conversely, the application of a very high but short voltage melts the phase change materials, that quickly cools down, restoring the amorphous region.

PCM-based devices are mainly employed in in-memory computing and logical operations[111,123].

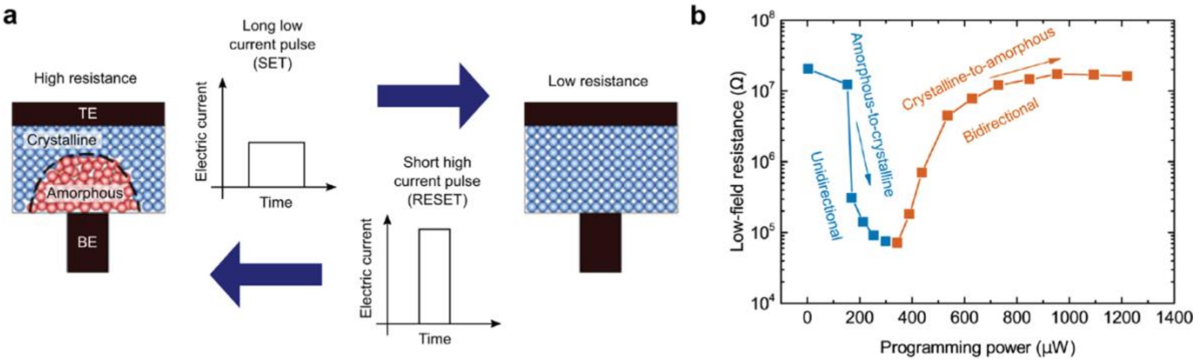

Figure 1.26 | **a**) Working principle of a PCM device. **i**) Gradual switching between amorphous-to-crystalline and vice versa. Adapted from [122].

1.4.3. Neuromorphic circuits

Neuromorphic devices can be integrated either into conventional complementary metal-oxide-semiconductor (CMOS) circuitry or in hybrid platforms made of several synaptic devices to develop fully neuromorphic circuits. Several different architectures and applications were developed, all grouped by a non-von Neumann structure.

1.4.3.1. Crossbar arrays and matrix-vector multiplication

Given the importance of neural networks in the modern society, the endeavour of several researchers is focused on technological solutions to improve energy-efficiency while accelerating neural networks, by exploiting in-memory computing[111,124]. For instance, neuromorphic hardware arrays were shown to accelerate matrix-vector multiplication[125] (MVM).

To this end, several hardware structures were implemented exploiting the concept of a crossbar array. It consists of a network of perpendicular wires. At each junction a resistive device connects the two wires (**Fig. 1.27**). Each input voltage (each row) is multiplied via Ohm's low at each column intersection. The resulting currents along the columns are then summed up via Kirchhoff's law. This physical matrix multiplication consumes far less power that its digital counterpart[126].

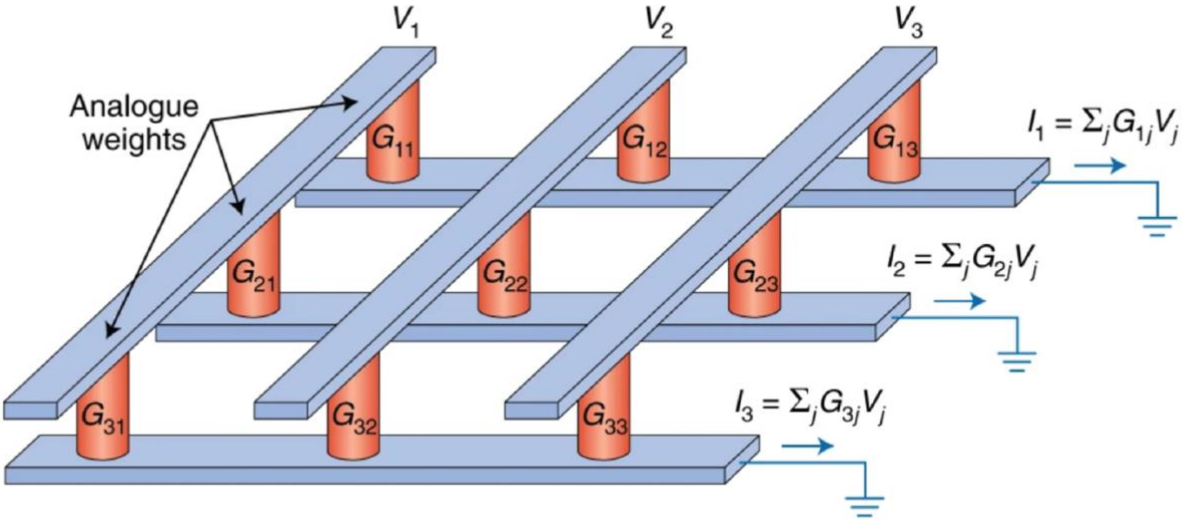

Figure 1.27 | Exemplary schematic of a crossbay array, in which devices at intersections between feedlines are the analogue synaptic weights. Currents are generated and summed up, as described by Ohm's and Kirchhoff's laws. Adapted from [111].

In addition, in-memory computing can easily be implemented using these structures by substituting the resistive elements at each intersection with neuromorphic devices (*e.g.*, memristors, FTJ, etc.). In this way, crossbar arrays can be programmed by finely tuning the conductance of the neuromorphic devices, allowing for active programming of the array.

However, the implementation of such architecture using only a single memristive element at each intersection (1R) poses some severe limitations in the actual use of these devices, as leakage current will hinder the correct reading of the network output. For this reason, more complicated structures were implemented, using like one-transistor-one memristor (1T1R), one diode-one memristor (1D1R) or one selector-one memristor[127,128] (1S1R) (**Fig. 1.28**). Such addition, while requiring for a more complex circuitry, improves energy efficiency during the programming of the array, while also enhancing synaptic features of the whole architecture[129].

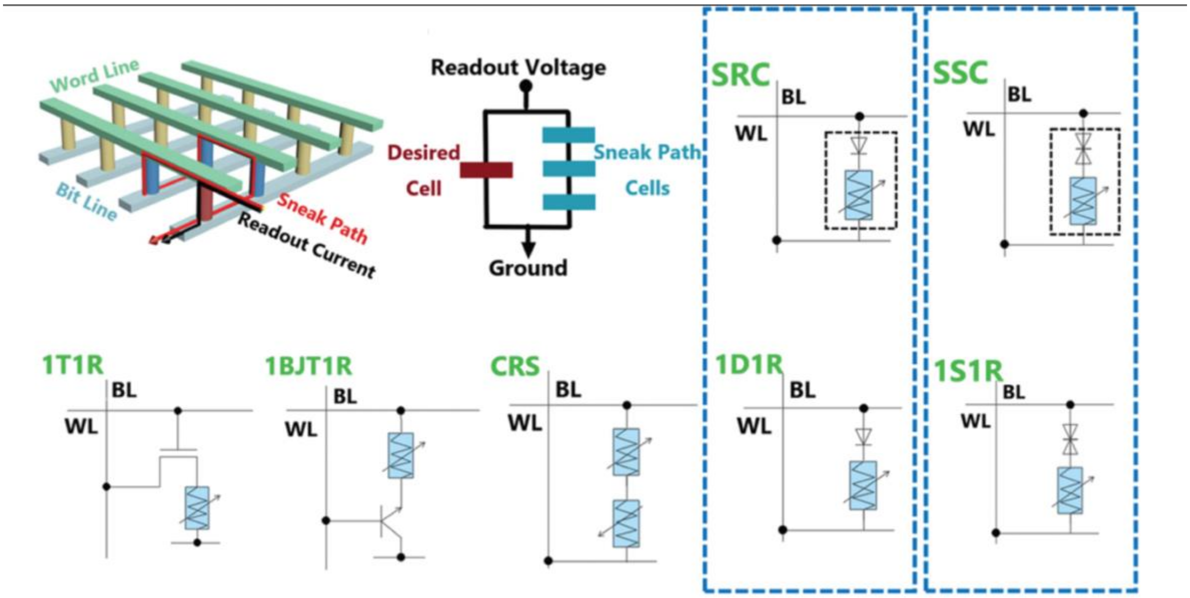

Figure 1.28 | Schematic of sneak path forming in crossbar arrays featuring a simple resistive element at intersection. Several architectures are proposed to dampen this phenomenon. Adapted from [124].

1.4.3.2. Spiking neurons

Biological neurons communicate through spikes, they mix analog and digital signaling, while relying on a sparse and distributed representation of the data, colocalizing memory and computation. On the other hand, digital computing architectures are based on logic operations, precise representation of the data and synchronous operations. The difference in the information representation leads to a mismatch in energy efficiency[130].

To fill this gap, silicon implementations of biological neurons were developed over the years[131,132]. Starting from the cornucopia of models available in neuroscience, silicon neurons can strictly reproduce all sorts of biological dynamics, allowing to group them into some broad categories[132]:

- Biologically-plausible: Models that closely mirrors biological neural systems.
- Biologically-inspired: models that replicate biological behaviours, but not necessarily in a biologically-plausible way.

- Integrate-and-fire (IF): A simpler category of biologically-inspired spiking neuron models that are designed to integrate incoming electrical signals and generate an output, or 'fire,' when a certain threshold is reached. They are very simple, while basic compared to more complex neuron models, but still useful for studying neural networks and creating efficient computational architectures, because of their low computational demands.
- McCulloch-Pitts: Neuron models that are derivatives of the original McCulloch-Pitts neuron where the output of the neural cell is a simple logical operation[133].

These models present a clear trade-off between biological plausibility and complexity, *i.e.*, computational feasibility (**Fig. 1.29-a**). An exemplary IF silicon neuron is shown in **Fig. 1.29-b**.

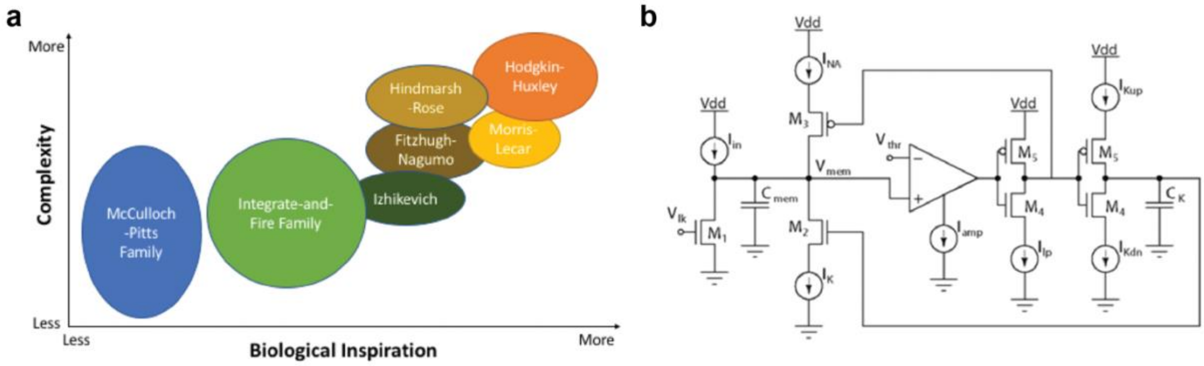

Figure 1.29 | **a**) Trade-off between computational complexity and biological plausibility. Adapted from [131]. **b**) Exemplary circuit implementing an IF spiking neuron. Adapted from [132].

1.4.4. Neuromorphic algorithms

Inspiration from the brain also involves software development, that can benefit too from neural computation primitives. Biologic spiking data is sparse and embedded with noise. Still, the brain can handle all that, gathering information from the environment and making the computation robust[134]. For this reason, algorithms tend to emulate how the information is encoded, as the high energy efficiency of the brain resides in the maximization of information per unit spike[135].

1.4.4.1. Spiking neural networks

Spiking neural networks (SNNs) are referred to as the third generation of artificial neural networks[136] (ANNs). They consist of spiking neurons, interconnected by synapses, modelled as adjustable scalar weights. They encode information taking inspiration from the brain, *i.e.*, they encode analog signals into spike trains. Different strategies can be adopted to encode information, based on the neural mechanisms they emulate, like rate-based[137], population coding[138] or temporal coding[139]. The advantage of this encoding resides in the fact that few spike trains sparse in time may convey high information, reducing power consumption[140], making SNNs suitable to handle large volumes of data with using train of spikes[141].

To consider the computational complexity of actual neurons, SNNs usually uses a simpler version of the models available in literature, implementing a pure threshold dynamic. Here, the activity of a presynaptic neuron directly modulates the membrane potential of a postsynaptic neuron, that will eventually fire when these potential crosses a threshold. Indeed, Izhikevich model[142] and leaky integrate-and-fire[143] (LIF) neurons are extremely popular, as they can capture several biological dynamics, while being not demanding computationally.

Learning-wise, SNNs allow for a bio-inspired learning, that can depend on relative timings between spikes, like in STPD. In addition, the information for the weight update is locally available, mirroring the learning that occurs in several areas of the brain[144–146].

On the other hand, the nature of the spiking signalling poses a problem in the learning process. In SNNs spikes are represented as sum of Dirac delta functions, that have no derivatives. Therefore, derivative-based approaches, widely used in ANNs, can’t be implemented.

Several strategies were developed over the years to be able to train SNNs. Unsupervised learning, based on STPD rule was achieved on both a single neuron[147] and multiple neuron architectures[148], to recognize spatial-temporal spike patterns.

Supervised learning in introduced by SpikeProp[149], the first algorithms to extend backpropagation technique in SNNs. Over the years, this approach was extended and improved, leading to the implementation of backpropagation with spatial-temporal gradient descent in multi-layer SNNs[150]. More recently, deep SNNs were developed using a modified version of the backpropagation algorithm, that treats the neuron’s membrane potential as the differentiable signal, that, in analogy with standard deep neural networks (DNNs), will trigger a non-linear activation function[151] (*i.e.*, the spiking output). Lastly, event-driven random backpropagation (eRBP) was proposed to reduce computational cost of learning in deep SNNs, also introducing synaptic plasticity[152].

1.4.5. Reservoir computing

Reservoir computing (RC) is a computational framework that can either be used in software or hardware[153]. It is born as an evolution of recurrent neural networks (RNNs), that can deal with dynamical systems and, therefore, temporal data processing[154].

The working principle of RC is that a RNN in the reservoir transforms an input into a spatiotemporal pattern in a high-dimensional space. The so-obtained spatiotemporal pattern is then read outside the reservoir for further computation (**Fig. 1.30**). The role of the reservoir is basically to nonlinearly transform an input into a high-dimensional space, that can be easily processed by a simple learning algorithm.

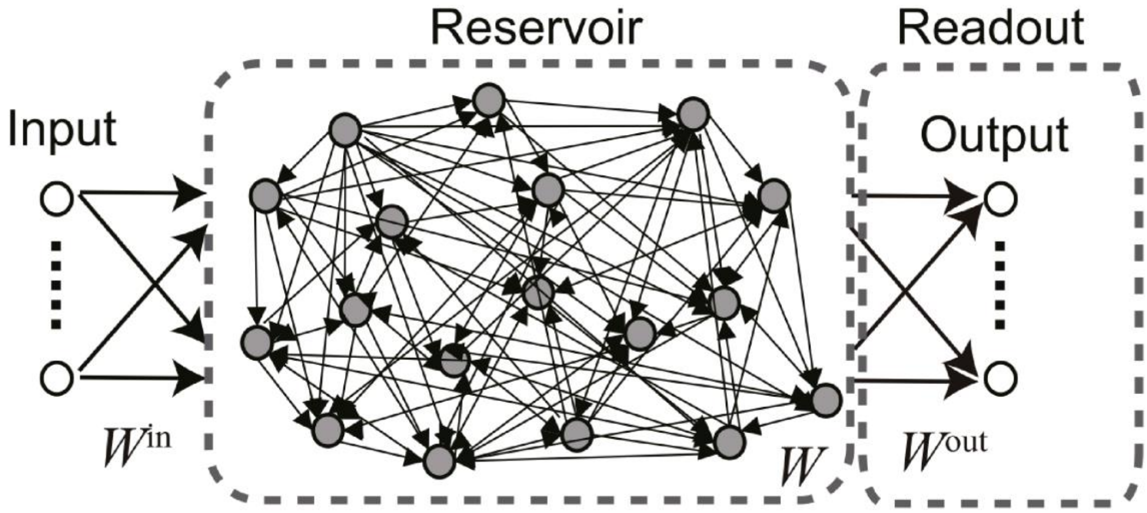

Figure 1.30 | Schematic representation of reservoir computing framework, in which the input is non-linearly transformed into a high dimensional space, to be classified through a simple algorithm, such as a linear classifier. Adapted from [153].

The main difference between RC and RNNs is that input weights (W_{IN}) and weights of the reservoir (W) do not need any training, while only the weights of the output layer (W_{OUT}) are trained with a simple algorithm, like linear regression.

For this reason, either software or physical reservoir are of easy implementation. Given the simplicity of the training method in RC, several applications were demonstrated over years, such as pattern classification[155,156], adaptive control[157] and time series forecasting[158].

Further evolutions of the single reservoir structure were also demonstrated with multiple reservoirs[159,160], and evolving reservoirs[161].

Regarding the physical implementation of RC, any dynamical system can, in principle, be used as reservoir: one interesting example of the first physical RC is a fluidic reservoir, *i.e.*, some bucket with water, used in pattern recognition[162]. Here an electrical input was transduced into vibration that formed waves on the surface of the water. Such waves were recorded by a camera and used to perform XOR and spoken digit recognition. Still, few requirements are needed to efficiently solve computational tasks[153]. First, high-dimensionality is required to be able to map inputs into an high-dimensional space. Then, nonlinearity is essential to map non-linearly separable input, into linearly separable ones. Short-term memory, in addition, is required to grant that the reservoir state is only dependant on recent-past states.

Lastly, reservoirs can be grouped into several categories. First, one can discern among different physical principles[153], *i.e.*, mechanical reservoir, photonic reservoir, electrical reservoir etc. Another useful classification can be based on the type of non-linear dynamic system employed as reservoir, like coupled oscillators[163,164], cellular automata[165] and delayed dynamical systems[166]. This last type of reservoir is appealing as it is possible to build single-node reservoir with delayed feedback[167–169]. Lastly, biological tissue can be used as reservoir[170,171].

1.5. Organic electronics

Organic electronics refers to the development of organic materials, *i.e.*, carbon-based molecules or polymers, exhibiting electronic properties. In particular, the field focuses on organic semiconductors, that are π-conjugated materials, in which carbon atoms reside in the backbone of the materials, while molecular orbitals are delocalized over conjugated segments[172]. As such segments may vary in size, they have a different energy for the highest occupied molecular orbital (HOMO) and lowest unoccupied molecular orbital (LUMO). These variation in energy creates localized electronic states, *i.e.*, electronic disorder. Notably, HOMO and LUMO in organic semiconductors represent the equivalent of valence of conduction bands of solid-state semiconductors, respectively. Here, the possibility of a charge carrier to flow strictly depends on the possibility of the carrier to flow from valence to conduction band[173]. Thus, in case of overlapping level, the conductivity of the material will be high. On the other hand, semiconductors are characterized by a small gap between such levels, resulting in a flow of charge carriers only when energy is supplied.

Notably, the band gap of organic materials (energy difference between HOMO and LUMO) is rather large, making them naturally insulators[172]. Therefore, different mechanisms as doping or carrier injection are required to increase the intrinsic carrier density of these materials, allowing for semiconducting properties, *i.e.*, reducing the band gap.

The beginning of the field dates to 1950, when electronic conduction in violanthrone and isoviolanthrone (two organic materials, was demonstrated[174]. Fifty years later, the Nobel Prize in chemistry was awarded to Shirakawa, Heeger, and MacDiarmid, recognizing the importance of conducting polymers. From that moment on, several devices were developed with particular focus on thin-film transistors, organic photovoltaics (OPVs) and organic light-emitting diodes (OLEDs).

Particularly relevant for this work are organic thin-film transistors, which can be divided into organic electrochemical transistors (OECTs) and organic field-effect transistors.

1.5.1. Organic field effect transistors

Organic field-effect transistors (OFETs) can be divided into OFETs and EGOFETs share the same architecture, with two electrodes (source and drain) that are connected through an organic semiconductor, defining the channel of the transistor, while a third electrode, the gate, is physically and electrically separated from the channel, by means of a dielectric. In case of a solid dielectric, we refer to OFET, while when the insulation is achieved by means of an electrolyte solution, we refer to EGOFET.

In an OFET, in analogy to a MOSFET, a capacitor is formed between gate, dielectric and semiconducting channel. Therefore, upon the application of a voltage bias at the gate terminal with respect to the source (V_{GS}), a field-effect is formed at channel/dielectric interface, modulating the density of charge carriers[175], and changing the current flowing through the channel I_{DS} (**Fig. 1.31-a**).

In EGOFETs the application of a gate voltage bias causes ions to drift towards gate/electrolyte and channel/electrolyte interfaces, forming two electrical double layers (EDLs). Given that the channel material is ion-impermeable, ionic-electronic interactions occur at the surface of the channel, causing accumulation or depletion of charges[176] (**Fig. 1.31-b**).

Importantly, while the working principles of OFETs and EGOFETs are similar, they differ in the voltage range they can be operated. While the former requires tens of volts to operate, the latter exploits EDLs as a capacitor with thickness of few nanometers[177]. Consequently, such devices can achieve large IDS modulation, with low working voltages (< 1 V).

Both OFETs and EGOFETs have been largely used in biosensing for detection of biologically relevant analytes[176,178–182], like proteins, ions and metabolites.

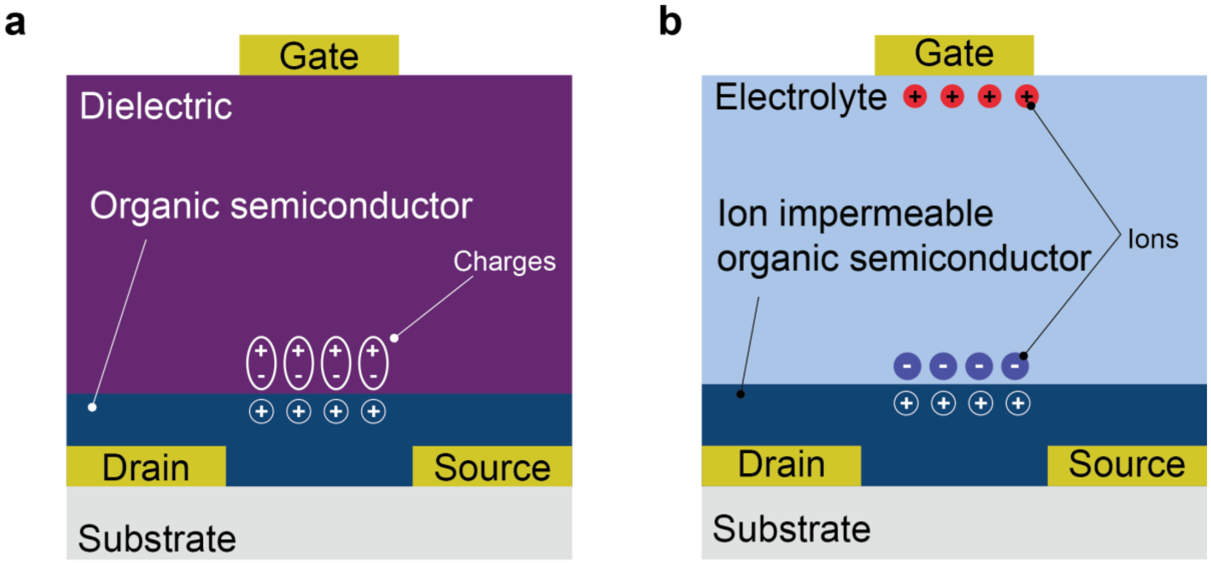

Figure 1.31 | **a**) Schematic of an OFET, in which the potential applied at the gate terminal elicits an accumulation of charges at the dielectric/channel interface, generating a field effect that modulates the channel conductance. **b**) Schematic of an EGOFET, in which the application of a potential at the gate terminal causes the movement of ions in the electrolyte, that will accumulate at the electrolyte/channel interface, generating a field-effect that allows for charges to flow through the transistor channel.

1.5.2. Organic electrochemical transistors

Since the first demonstration[183] that dates to mid-1980s, OECTs gained a lot of attention due to low-voltage operation, low-cost processibility, broad tuneability and biocompatibility[184]. They share the same architecture with EGOFETs, but they use organic mixed ionic-electronic conductors (OMIECs) as channel material, usually conducting polymers (CPs). As such materials are ion-permeable, when applying a gate voltage bias V_{GS}, ions are pushed from the electrolyte to the bulk of the channel material, changing its doping state, and thus its conductivity[185] (**Fig. 1.32-a**).

In addition, the application of a source-drain voltage bias V_{DS}, induces a current I_{DS} that is proportional to mobile holes/electrons in the channel, *de facto* probing its doping (and hence conducting) state.

As in conventional MOSFET, based on the mobile charge carriers in the channel OECTs can be divided into p-type and n-type (holes and electrons, respectively). In addition, another important distinction must be made in OECTs, as they can work either in accumulation or depletion mode[186]. In the former case, in absence of V_{GS}, the CP is in the OFF state, *i.e.*, there is a small number of mobile charge carriers in the channel, and I_{DS} is close to zero, independently from the applied V_{DS}. The application of a gate voltage bias, on the other hand, causes electrochemical doping, increasing the number of carriers, taking the CP to the ON state (**Fig. 1.32-b**). Conversely, depletion mode OECTs work in a complementary fashion. They are normally in the ON state, while the application of VGS depletes the number of charge carriers in the channel, taking the device in the OFF state (**Fig. 1.32-c**).

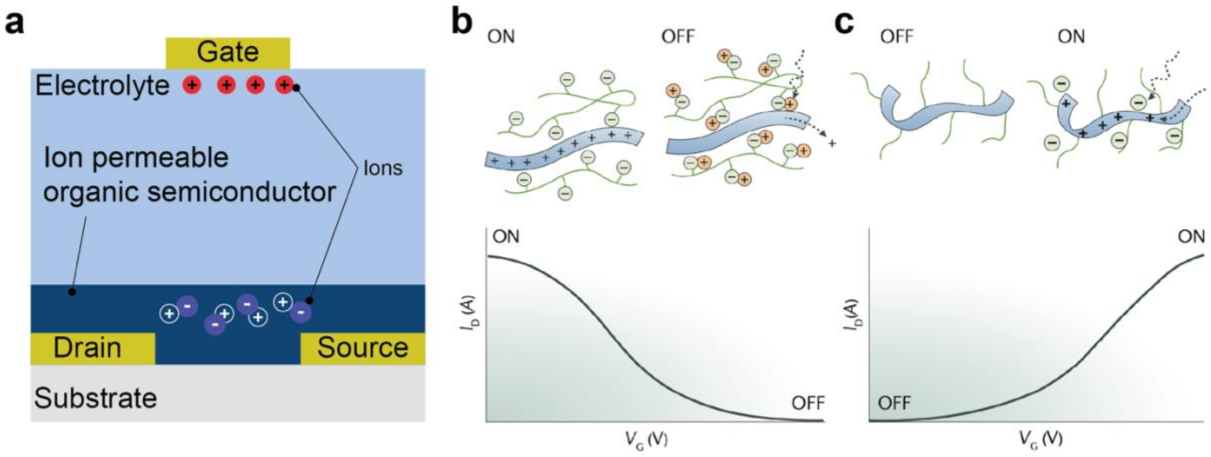

Figure 1.32 | **a**) Schematic of an OECT, in which the application of a potential at the gate terminal causes the injection of ions from the electrolyte to the channel, causing the chemical doping/de-doping of the polymer, changing its conductance. **b**) Exemplary transfer curve of a depletion mode OECT, in which the device is at ON state when the gate is biased with 0 V. By increasing the gate voltage bias the channel current decreases and the device transits to the OFF state. Adapted from [186]. **c**) Exemplary transfer curve of an accumulation mode OECT, which is turned on upon gate bias application. Adapted from [186].

OECTs featuring poly(3,4-ethylenedioxythiophene):poly(styrene sulfonate) (PEDOT:PSS) as channel material are the basis of the presented thesis work. They are depletion mode, p-type OECTs: in absence of a gate voltage, and hole current flows in the polymeric channel (ON state). The application of a positive V_{GS}, cations are injected from the electrolyte to the bulk of the CP, compensating for anions[187]. This ion injection depletes the number of holes in the channel decreases, leading to a decrease in I_{DS}, taking the device to the OFF state.

1.5.2.1. Device physics

OECTs profoundly differ from conventional MOSFET, as they do not rely on a 2D inversion layer to form at the interface with the channel, caused by an applied gate voltage. In OECTs, the very same gate voltage bias causes the accumulation of ionic charges in the 3D bulk of the material[186,187]. This difference is particularly as the oxide capacitance in MOSFET (surface capacitance), is now replaced by the polymeric channel volumetric capacitance. Hence, unlike MOSFETs, the thickness of the channel *d* is an active parameter, influencing the transistor performance.

Starting from this consideration, Daniel Bernards and George Malliaras formulated the Bernard-Malliaras (BM) model[185], that describes the electronic charge in the OECT channel (based on PEDOT:PSS, *i.e.*, p-type and depletion mode), with the same set of equations used to model long-channel MOSFETs, yielding:

$$I_D = \begin{cases} \mu C^* \dfrac{Wd}{L}[(V_{GS} - V_T) - \dfrac{1}{2}V_{DS}^2] & V_{GS} > V_T, V_{DS} \leq V_{GS} - V_T \\ \dfrac{1}{2}\mu C^* \dfrac{Wd}{L}(V_{GS} - V_T)^2 & V_{GS} > V_T, V_{DS} > V_{GS} - V_T \end{cases} \quad (1.1)$$

Where I_D is the drain current, μ is the hole mobility, C^* is the volumetric capacitance of the channel's polymer, V_T is the threshold voltage and V_{GS} and V_{DS} are the applied gate-source and drain-source voltages. Notably, the usual capacitance of the oxide in MOSFET (C_{ox}) is replaced by the product *dC** (thickness of the polymer, multiplied by the volumetric capacitance). *W, L* and *d* are width, length and thickness of the polymeric channel, respectively.

From equation (1.1), it is easy to get the expression of the transconductance g_m, by computing the derivative of the drain current, with respect to the gate voltage. Transconductance is a figure of merit in OECTs, as it describes how much a voltage signal at the gate can be amplified[186,187].

$$g_m = \begin{cases} \mu C^* \frac{Wd}{L} V_{DS}] & V_{GS} > V_T, V_{DS} \leq V_{GS} - V_T \\ \mu C^* \frac{Wd}{L} (V_{GS} - V_T) & V_{GS} > V_T, V_{DS} > V_{GS} - V_T \end{cases} \tag{1.2}$$

In addition, BM model also includes the ionic transport inside the electrolyte, which correlates to the OECT transient response and switching speed. The complete model combines an equivalent electronic circuit (**Fig. 1.33-a**) and an equivalent ionic circuit (**Fig. 1.33-b**).

The former is modelled as a variable resistance, describing the steady-state behaviour of the device, by implementing equations (1.1) and (1.2), whereas the latter models the drift-diffusion of ions at gate, electrolyte and channel domains, introducing temporal dependence in the model. The equivalent ionic circuit consists of two capacitances C_G and C_{CH}, modelling gate/electrolyte and channel/electrolyte interfaces, respectively. In addition, a resistor R_E models the resistivity of the electrolyte, along with other parasitic contributions.

While coupling these two systems, BM model relies on two assumptions. First, no electrochemical reactions occur at the gate electrode. Second, the model is limited to thin-film transistors, *i.e.*, all the charge densities are uniform across the channel thickness.

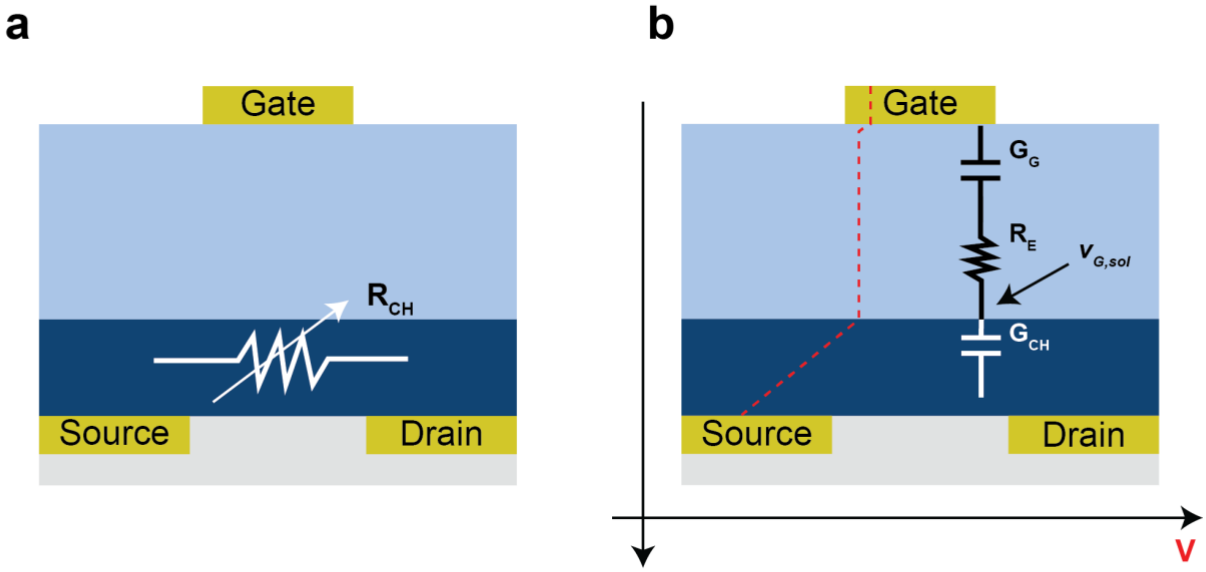

Figure 1.33 | **a**) Electronic circuit of the OECT model, in which the channel is modelled as a variable resistance. **b**) Ionic circuit of the OECT model, along with potential profile inside the electrolyte (red curve).

Lastly, potential distribution across the OECT is shown in **Fig. 1.33-b**. In analogy to a well-designed MOSFET, where the poly-silicon gate is heavily doped to limit depletion inside of it, in a properly designed OECT, the gate capacitance C_G should much larger than the channel capacitance C_{CH}, so that the applied gate voltage would drop at the channel-electrolyte interface. To achieve this behaviour, there are two possible solutions. First, it is possible to use a non-polarizable gate electrode, such as Ag/AgCl electrodes, commonly used in electrochemistry. Second, it is possible to cover the gate electrode with the same polymer used to define the channel, but with a much larger footprint, increasing C_G.

BM model predicts that the OECT response is linked to an ionic RC time constant, defined as follows:

$$\tau_i = R_E C_{CH} \tag{1.3}$$

Where the channel capacitance is computed as $C_{CH} = C^* WdL$, while the resistance of the electrolyte may show different proportionalities, based on the OECT architecture. In case of a metal electrode coated with PEDOT:PSS, if the gate terminal is covered by a much broader volume of electrolyte, the resistance scales as $R_E = r^* \frac{1}{\sqrt{WL}}$, where $r*$ has the unit of a resistivity[188]. Eventually, by combining such laws, one can conclude that the ionic time constant scales with the channel dimensions $\tau_i \propto d\sqrt{WL}$.

The contribution of the gate electrodes needs to be taken into account. The time response is limited by the equivalent capacitance, *i.e.*, C_G and C_{CH} connected in series: $C_{eq} = \frac{1}{1/C_G + 1/C_{CH}}$. When the condition for a good gating is matched ($C_G \gg C_{CH}$), the following approximation yields: $C_{eq} \approx C_{CH}$.

BM model also includes the transient response of the OECT, when source and drain voltage are fixed, while the gate voltage bias varies with time. In this section, quantities that change with time will be denoted with lower-case names.

In analogy to the steady-state case, one can compute the channel current, *i.e.*, the electronic transport current, as follows:

$$i_{CH}(t) = \begin{cases} \mu C^* \frac{Wd}{L}[\left(v_{G,sol}(t) - V_T\right) - \frac{1}{2}V_{DS}^2] & v_{G,sol}(t) > V_T, V_{DS} \leq v_{G,sol}(t) - V_T \\ \frac{1}{2}\mu C^* \frac{Wd}{L}\left(v_{G,sol}(t) - V_T\right)^2 & v_{G,sol}(t) > V_T, V_{DS} > v_{G,sol}(t) - V_T \end{cases} \quad (1.4)$$

Where V_{GS} was replaced by $v_{G,sol}$ (**Fig. 1.33-b**), that is the gate-source voltage after the propagation through the channel, *i.e.*, the actual voltage difference that is applied at the channel.

In addition, the ionic transport current through the ionic RC circuit, related to the doping/dedoping of the polymer induced by the gate voltage bias yields:

$$i_G(t) = C_{CH}\frac{d}{dt}v_{G,sol}(t) \quad (1.5)$$

Lastly, as formulated in the BM model, the drain current is computed as a sum of the channel current and a displacement current. In case of a square voltage pulse, it showed an exponential dependence with time, given by:

$$i_D(t) = I_{SS}(V_{GS}) + \Delta I_{SS}\left[1 - f\frac{\tau_e}{\tau_i}\right]\exp\left(-\frac{t}{\tau_i}\right) \quad (1.6)$$

Where $I_{SS}(V_{GS})$ is the steady-state drain current when the gate voltage is V_{GS}. ΔI_{SS} is the difference between the initial and the final steady-state currents, while $\tau_I = \frac{L^2}{\mu V_{DS}}$ represents the electronic transit time along the channel. Lastly, *f* is a weighting factor.

Equation (1.6) predicts two different working regimes of the OECT (**Fig. 1.34**). In a first regime, electronic transport is faster than ionic charging, the drain current relaxes monolithically (**Fig. 1.34-b**). In the second regime, the ionic charging is faster than the electronic transport, and the drain current spikes to then relax to the final value of current (**Fig. 1.34-c**).

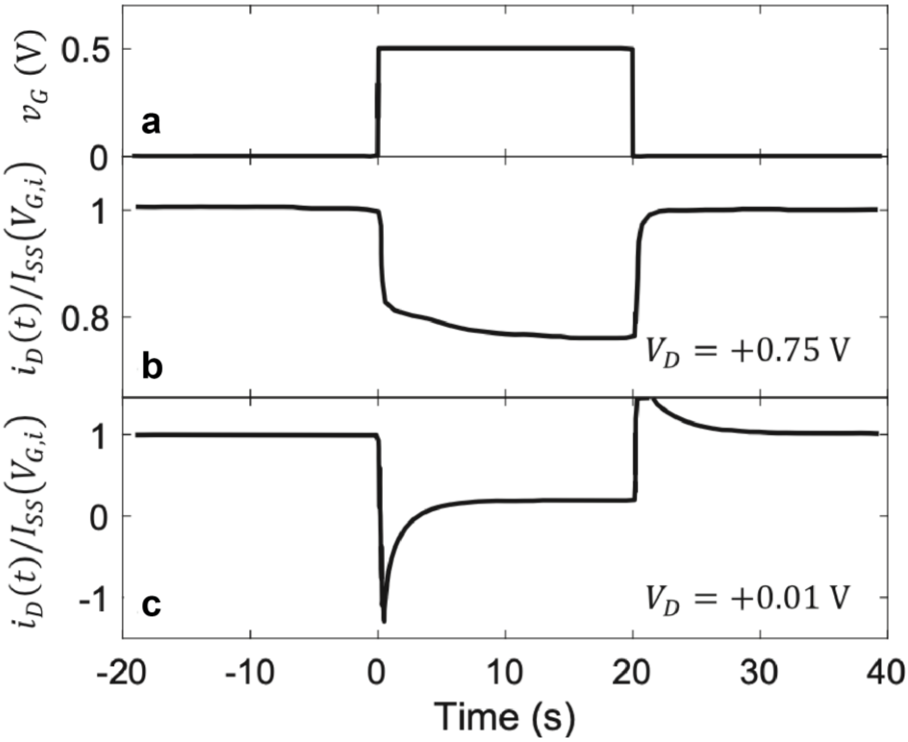

Figure 1.34 | **a**) Square voltage pulse applied at the gate terminal. **b**) First OECT conduction regime, in which the electronic transport is faster than ionic transport. **c**) Second OECT regime, in which the ionic transport is faster than the electronic one. Adapted from [185].

Several modifications to BM model are available in literature, focusing on several modifications of the weighting factor *f*, to overcoming several limitations of the presented model[189–191].

1.5.2.2. 2D modelling

As discussed above, BM model describes the OECT steady-state and transient response as a thin-film transistor, assuming that all the charge carrier densities are uniform along the channel thickness. Basically, they assume an average of ion and hole concentration along the transistor channel, instead of a full distribution, reducing the complexity of the problem to one dimension.

One important consideration is that BM model does not consider possible lateral migration of ions, that occurs in planar-gated OECTs. In addition, as the transistor channel is usually several orders of magnitude longer then thicker, such contribution is not negligible[192].

These considerations lead to the development of more complex models, like a 2D drift-diffusion model of OECTs, enabling the study of the transient response without any *ad hoc* assumptions about ion and hole distribution along the channel[193].

The model is based on Poisson's and two continuity equations (holes and cations), that are solved using the Gummel scheme in 2D. The OECT is modelled as a layer of electrolyte, a layer of organic semiconductor and three electrodes (**Fig. 1.35**). Hole concentration is set to zero in the electrolyte domain, while in the semiconducting layer they are mobile, as cations are. Lastly, anion concentration is kept constant, and their movement is not included. The gate electrode is placed on the top of the device, and it is simplified as ohmic contact for cations, meaning that any possible redox reaction occurring at the gate/electrolyte interface is fast enough to retain cation equilibrium. Source and drain contacts are modelled as reflecting for cations, and as ohmic contacts for holes. Lastly, interaction between ions and holes in the semiconducting layer are treated as electrostatic. A p-type, depletion mode OECT is simulated (e.g., PEDOT:PSS).

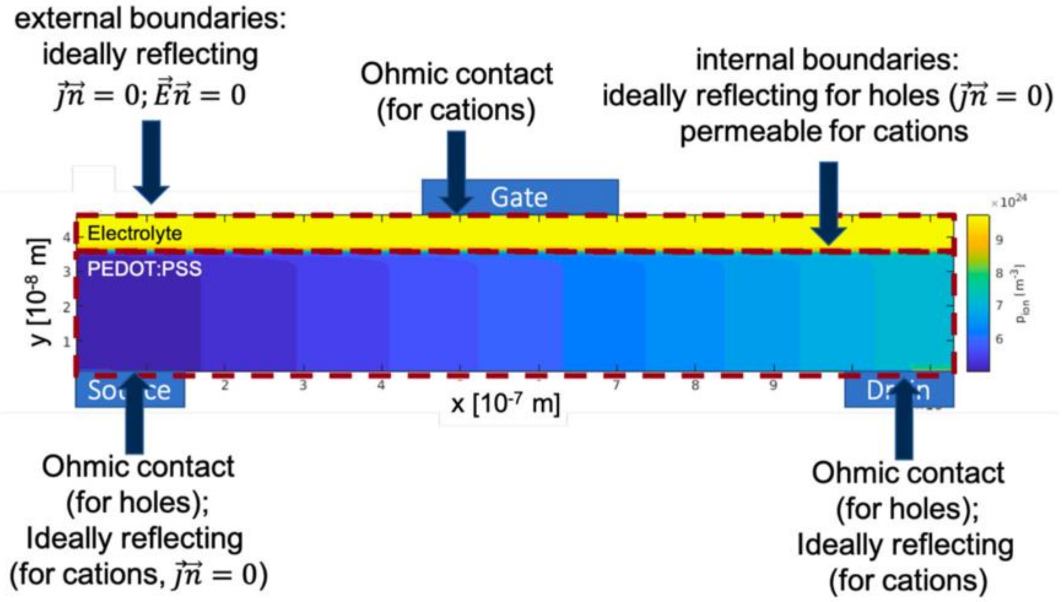

Figure 1.35 | Geometry of the 2D drift-diffusion model, along with boundary conditions. Adapted from [193].

During the OFF switching (**Fig. 1.36**), ion concentration is almost constant in the electrolyte region, while it varies in the polymer layer. After few microseconds (50 µs), the cation concentration is constant along the y-axis, while it forms a gradient along the x-axis. The conclusion one can draw from this simulation is that cations are pushed inside the channel (vertical current), but then they are pulled towards the drain electrode, generating a horizontal current.

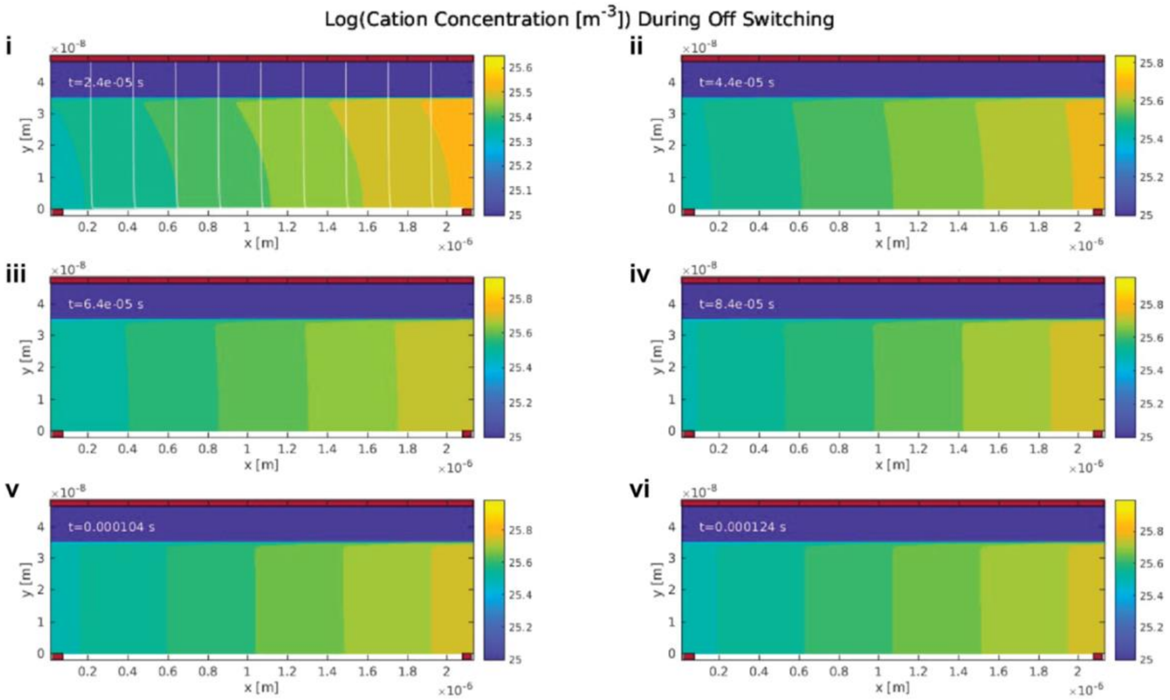

Figure 1.36 | Concentration of cations during an OFF switching of a PEDOT:PSS OECT, monitored in time (**i** to **vi**). Movement of cations along the x-axis direction is much slower that the y-axis direction. Adapted from [193].

This phenomenon is not observed during an ON switching (**Fig. 1.37**), where cations are uniformly pulled towards the gate terminal.

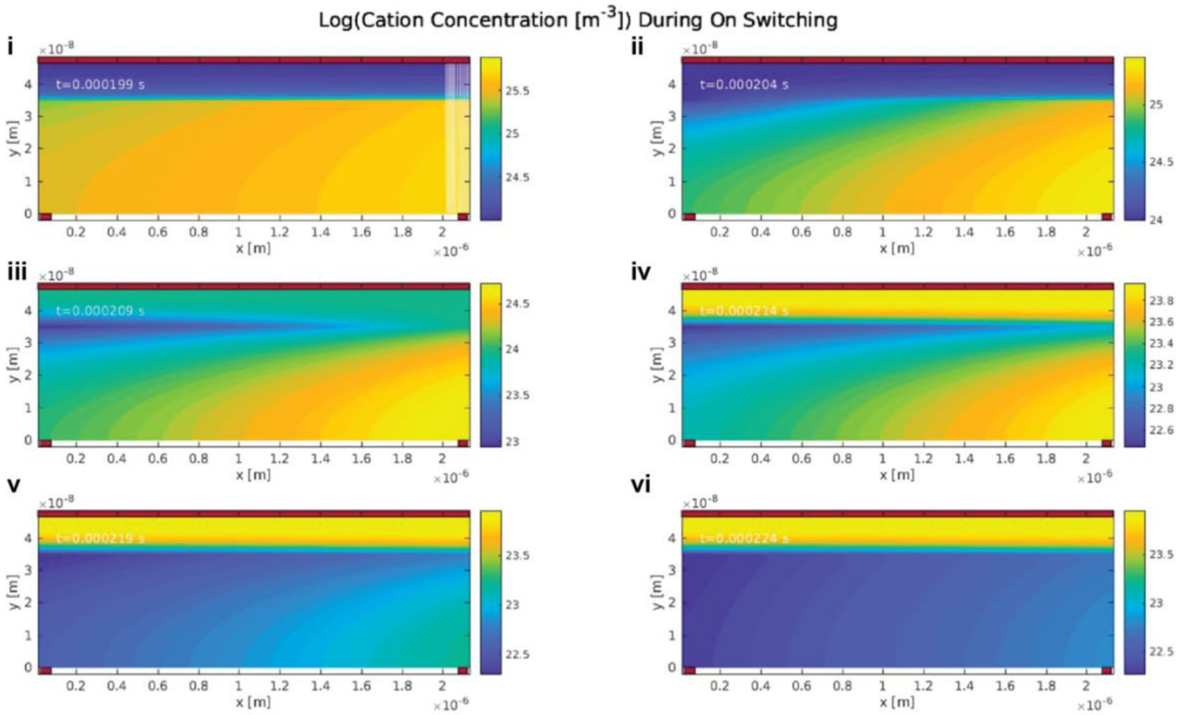

Figure 1.37 | Concentration of cations during an ON switching of a PEDOT:PSS OECT, monitored in time (**i** to **vi**). Here cations uniformly move towards the gate terminal. Adapted from [193].

A quantification of horizontal and vertical currents is shown in **Fig. 1.38**. While during the ON switching horizontal current is almost absent, the OFF switching is dominated by the horizontal contribution of the current. These simulations lead to the conclusion that, cations quickly enter the polymeric channel of the OECT (50 µs), leading to a quick drop in drain current. However, while such vertical component is quickly dampened, the contribution of a lateral ionic current increases. Such lateral currents drop to zero slowly, and the OECT reaches the steady-state.

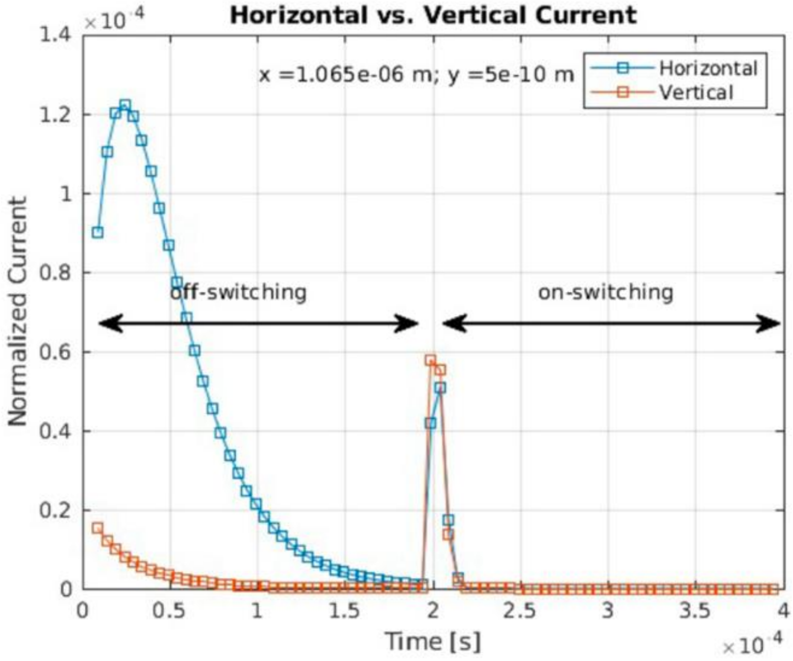

Figure 1.38 | Horizontal and vertical components of the current, during both ON and OFF switching events. Adapted from [193].

1.5.2.3. Applications

OECTs bloomed over the last decade, leading to the development of several applications, ranging from logical circuits to biointerfacing. As OECTs can either work in depletion/accumulation, while featuring p- and n-type materials, complementary circuits, logic arrays and digital electronics can be developed.

For example, organic inverters have been demonstrated, as they represent the elementary building block of any digital circuits. The simplest organic inverter architecture was based on the resistor-ladder logic[194–196] (RLL, **Fig. 1.39-a**), where a resistor ladder is coupled to a p-type depletion mode OECT, switching the circuit between low and high logic level. Exploiting these architectures, NAND and NOR logic gates can be developed [194], along with ring oscillators[195]. In addition, basic memory units, like flip-flops or shift registers based on OECTs were demonstrated[197].

Integrating NOT and NAND gates on the same substrate, several structures were demonstrated, as a 2-to-4 decoder, a 4-to-1 multiplexer and a 7-bit shift register[196]. Lastly, a binary-coded decimal 4-to-7 encoder was employed to drive an organic electrochromic display with only four data bits[196] (**Fig. 1.39-b**).

The implementation of complementary logic-like inverters, based on both p- and n-type OECTs integrated on the same structure was recently shown. For instance, poly(benzimidazobenzophenanthroline) (BBL) was used to fabricate a complementary NOT gate exhibiting high gain at low voltage supply[198,199] (0.7 V, **Fig. 1.39-c)**.

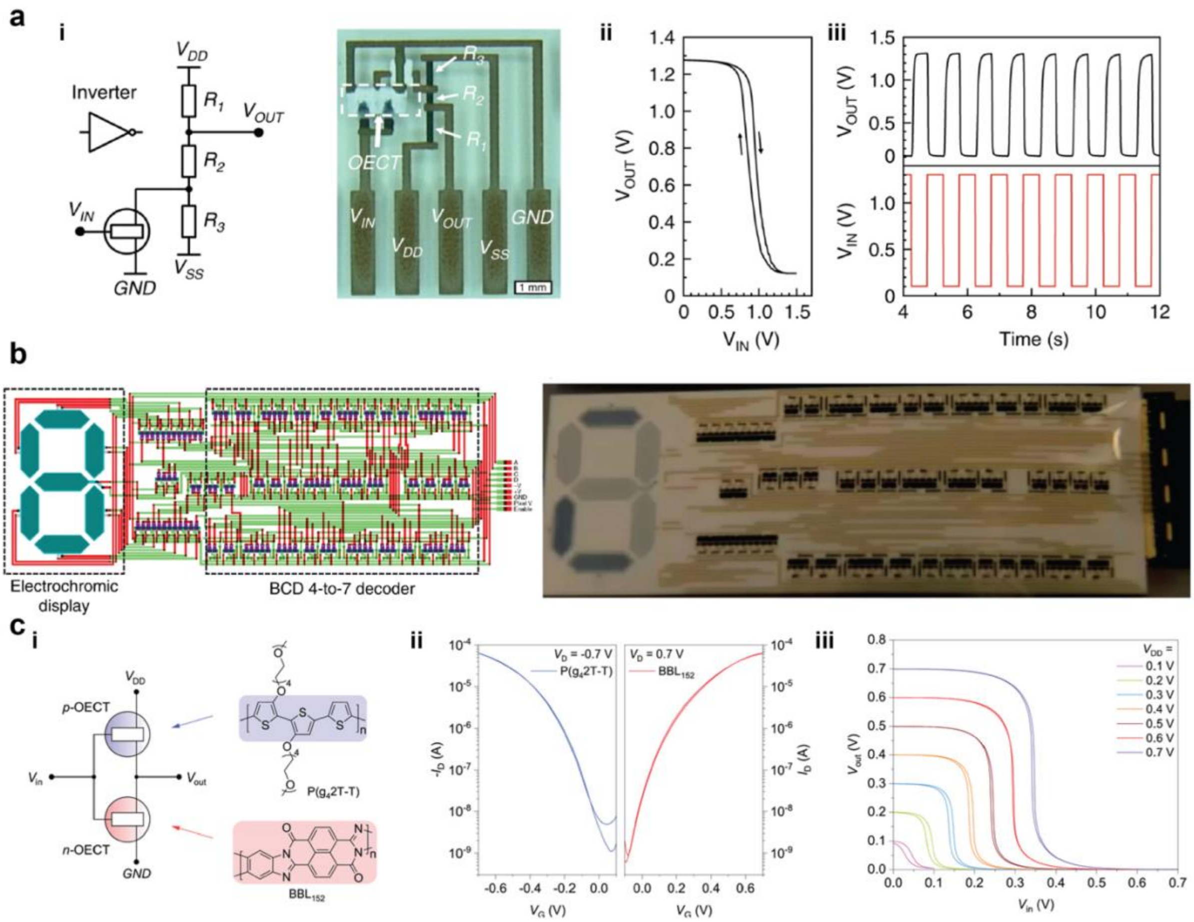

Figure 1.39 | **a**) RLL inverted build using PEDOT:PSS-based OECTs. **i**) Circuit schematic and physical prototype. **ii**) Voltage transfer characteristic of the inverter. **iii**) Switching characteristic of the inverter. Adapted from [196]. **b**) Fully organic 4-to-7-bit decoder, driving and organic electrochromic display. Adapted from [196]. **c**) Complementary logic inverted based on BBL n-type OECT and p(g42T-T) p-type OECT. **i**) device schematic and polymer chemical structure. **ii**) transfer curves of p- and n-type OECTs. **iii**) Organic inverted voltage transfer characteristic. Adapted from [199].

In addition, OECTs were broadly exploited in bioelectronics, where the mixed conduction property of OMIECs allows such devices to directly interact with biological tissue and fluids. For instance, OECTs, emerged in biosensing, *i.e.*, recognition of biologically relevant signals and substances. Indeed, in OECTs the channel current is influenced by the voltage balance at the gate/electrolyte and channel/electrolyte interfaces. Thus, when biomolecules induce changes at either of these interfaces, the OECT can effectively detect and respond to these alterations. Therefore, several strategies of functionalization were developed, in which functional groups able to react/bond to bioactive molecules are immobilized either on the gate or on the channel of the OECT. For instance, detection of E. coli was demonstrated by modifying a PEDOT:PSS channel with 3-glycidoxypropyl-trimethoxysilane[200]. Electrostatic interactions can be exploited to anchor biorecognition elements, like acetylcholinesterase that was electrostatically anchored on the channel made of a PEDOT:TOS/polyallylamine hydrochloride (PAH) composite for acetylcholine sensing[201]. In addition, due to the high transconductance, a slight change in the gate properties, due to a biorecognition event, leads to a significant change in the channel current. Exploiting this principle, several biorecognition elements were immobilized on the gate electrode of OECTs, as proteins[202], DNA[203], enzymes[204] and ion-selective polymers[205]. Furthermore, an OECT featuring a Pt gate electrode was used to detect neurotransmitters in real-time, proving high selectivity in a complex environment[206,207] (*e.g.*, dopamine detection in ascorbate).

Another advantage of CPs, with respect to conventional electronics, is the possibility to pattern such material on flexible substrates, allowing for a class of devices that are particularly suited for wearable application, in which in situ amplification and low working voltages are a strict requirement[208,209]. Indeed, OECTs have been used for wearable devices able to monitor several physiological signals. For instance, electrocardiography (ECG) measurements[210,211] were demonstrated (**Fig. 1.40**). Thus, long-term monitoring was achieved by using an hydrogel electrolyte, enabling recording over several hours[212].

Electroencephalography (EEG) was shown too, by using internal-ion-gated OECTs[213], while an ultrathin and ultraflexible devices were comfortably attached to the human skin to record electromyography[210] (EMG, **Fig. 1.40**).

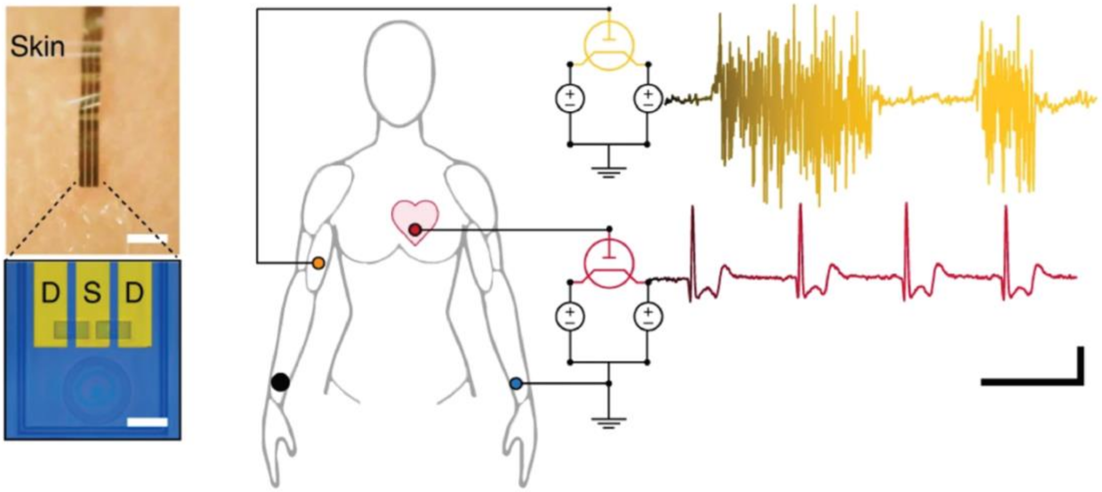

Figure 1.40 | OECT used to record EMG and ECG traces, shown on the right hand side. Scale bar is 1 s, 200 µA. Adapted from [210].

Flexibility and stretchability, together with the possibility to work in an aqueous environment, also makes OECTs particularly suited in electrophysiological recordings both *in vivo* and *in vitro*[10]. Almost 10 years ago, the first implementation of brain activity monitoring with an OECT was demonstrated[214], exploiting the high transconductance of the device to record electrocorticography (ECoG) signals with a much higher signal-to-noise ratio (SNR) with respect to surface electrodes. More recently, devices were shown to record local field potential from freely moving rats over two weeks, without eliciting any inflammatory response[210]. Furthermore, arrays of organic transistors enabled an *in vivo* mapping of electrophysiological signals such as EMG[215] and ECoG[216] (**Fig. 1.41**). The soft nature of OECTs also enabled stimulation of excitable tissue, while reducing the risk of inflammatory response and scarring during chronical implantation[217]. For instance, flexible neural probes for localized stimulations were implanted, showing no formation of scars in 1 month of implantation[218] (**Fig. 1.41-b**).

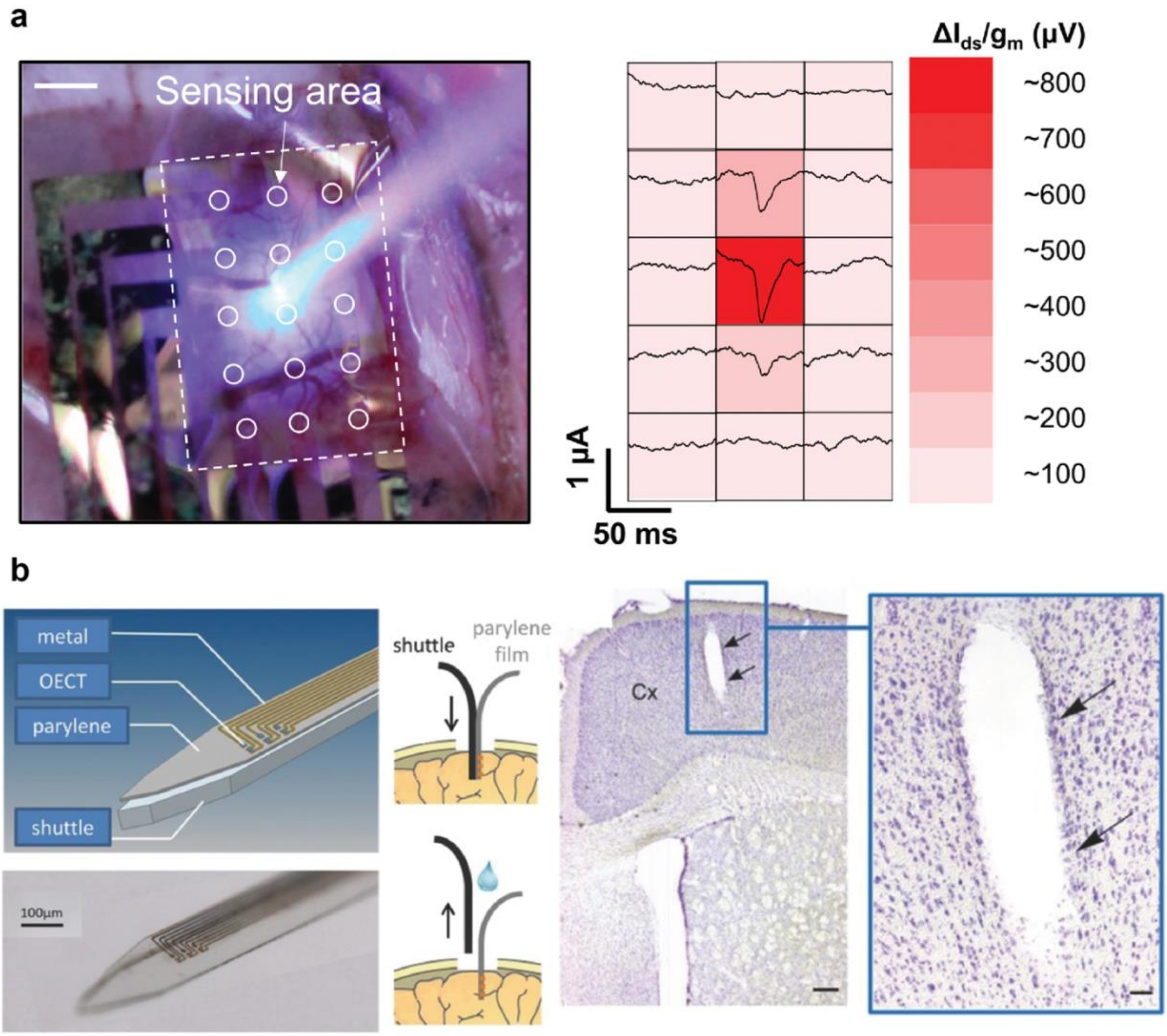

Figure 1.41 | a) Implanted flexible OECTs and spatial mapping of the ECoG. Adapted from [216]. **b**) Implantable OECT on a flexible substrate, along with histology, showing no scarring effect after 1 month of implantation. Adapted from [218].

Notably, pressure sensing is particularly relevant to this thesis work. It was demonstrated in several OECT-based platform, relying on different mechanisms[219–221]. A widely spread approach, that is adapted in the presented work, is to use a solid electrolyte that could be compressed upon the application of a pressure, gating (or not) the transistor[222]. In such devices the solid electrolyte presents a pyramidal shape pattern, to modulate the equivalent circuit (CRC) that connects gate and channel (**Paragraph 1.3.2.1**). Without the application of any pressure (**Fig. 1.42-a**), the pattern induces a minimal contact area, limiting the charging because of the gate capacitance ($C_G << C_{CH}$). Conversely, upon the application of pressure (**Fig. 1.42-b**), the contact area between electrolyte and channel increases. As a result, the gate capacitance increases too, allowing for ion movement and transistor gating, now $C_G > C_{CH}$.

Electrical measurements are shown in **Fig. 1.42-c** and **d**. In the former, the transfer curve of the OECT changed upon pressure application, up to 15 kPa. The latter shows examples of low-pressure sensing, as the channel current of the OECT changed when a flower or a grain of rice are used to apply pressure (1.1 and 2 Pa, respectively).

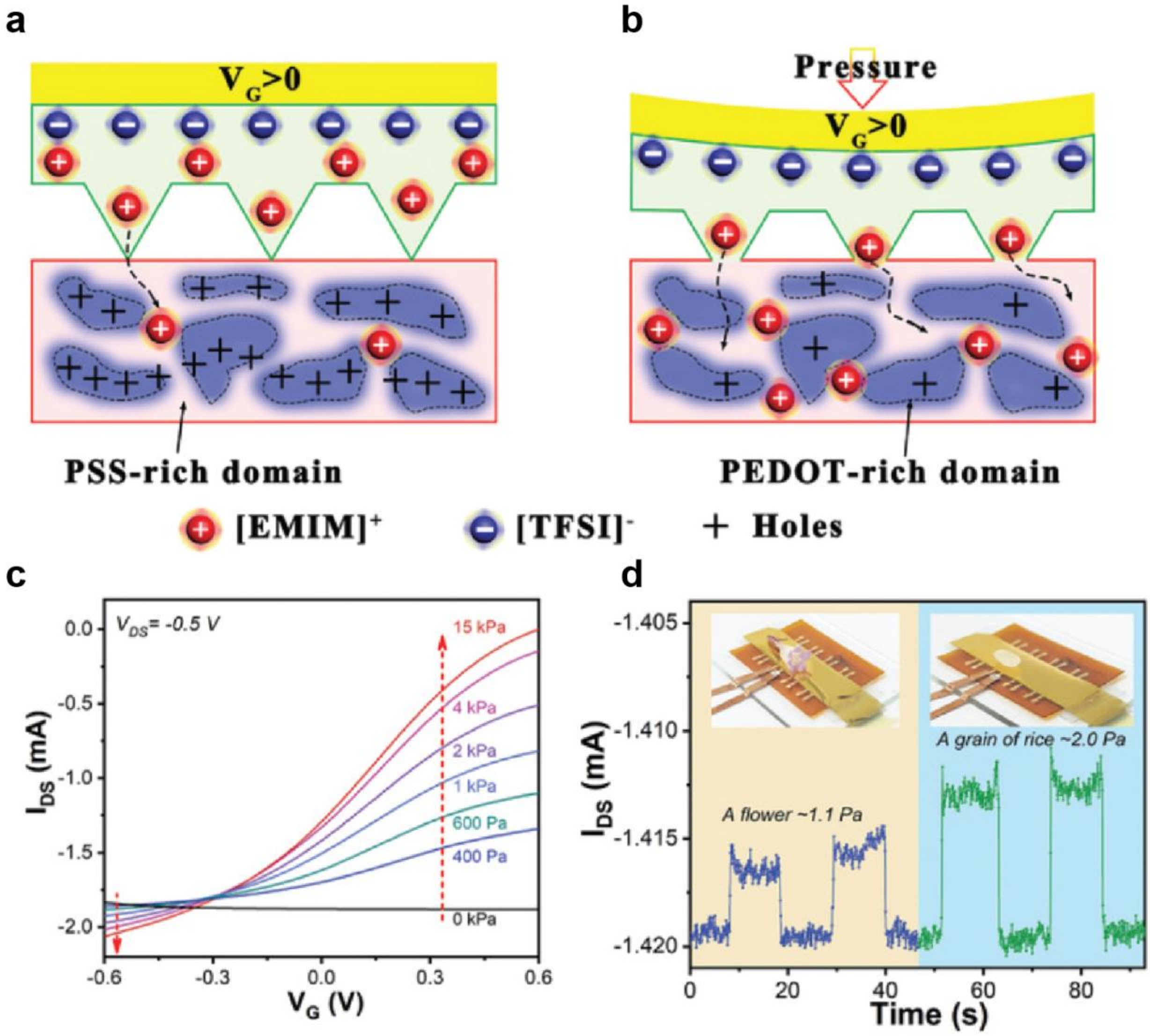

Figure 1.42 | Pressure sensing in OECTs. **a**) When no pressure is applied, the small contact area between electrolyte and channel limits the OECT gating. **b**) Upon the application of pressure, the contact area increases, allowing for ion migration. **c**) Transfer curve as a function of the applied pressure. **d**) Examples of low-pressure sensing (1.1 Pa and 2 Pa). Adapted from [222].

1.6. Organic neuromorphic devices and systems

Neuromorphic engineering, as discussed above, represents a promising approach to integrate energy-efficient brain-inspired devices into systems that we use every day. Silicon and, more in general, inorganic materials are still far away from biological computational power, that relies on stochastic mechanisms and different carriers of information, like ions and neurotransmitters[223].

For this reason, OMIECs and organic electronic devices emerged as ideal candidates in neuromorphic applications, as they can leverage on ions, liquid environment and electrochemical reactions to process signals, closely resemble biological primitives. In addition, the soft nature of these materials makes them particularly suited for interfacing with biology[10], paving the way towards integrated system in which artificial and biological neurons could cooperate[224].

For a clear and smooth presentation of the architecture and applications of organic neuromorphic devices, in this discussion they are categorized into two- and three-terminal devices.

1.6.1. Neuromorphic two-terminal devices

With organic neuromorphic two-terminal devices we mainly identify organic memristors. In analogy to their inorganic counterpart, organic memristors generally consist of two terminal devices, with two metal layers interspaced by an insulating material, showing stable and tuneable conductance states. Several resistive switching mechanisms have been demonstrated, such as conductive filament generation, redox reaction and charge trapping.

In case of conductive filament generation, upon the application of an electric field, oxidation of active metal ions (usually Ag or Cu) into cations occurs, which migrate towards the cathode. Here, they're reduced back into metals, forming a conducting filament (**Fig. 1.43-a**). Continuous application of electric field leads to the progressive formation of conductive paths, eventually tuning the conductance of the device[225].

These paths may be instable, *i.e.*, they degrade and rupture after the removal of the electrical field, or they can be dissolved through a reverse voltage[226]. Notably, an Ag/PEDOT:PSS/Ta memristor was demonstrated[227]. Here, the conductive capacity of the commercially available and biocompatible PEDOT:PSS layer could provide a conducting path for the Ag movement.

The charge trapping mechanism refers to the process of modulating the trapping and release of charge carriers in the memristive layer[228]. In such devices, charge carriers can be trapped in defects or impurities of the insulating layer, resulting in a conductance change of the memristor[229]. In addition, the action of a continuous electric field increases the number of charge carriers captured by these foreign components, and eventually lead to a permeation network that serves as an effective carrier hopping path[229] (**Fig. 1.43-b**). Conversely, the opposite polarity may reverse the trapping, restoring the original level of conductance.

Lastly, redox based memristors consist of two electrodes interspaced by electrolyte and an organic material[230]. Here, a voltage-induced redox reaction in the electrolyte is balanced by a counter-redox reaction of the organic material, changing its conductive state[231,232] (**Fig. 1.43-c**).

These devices were able to mirror important synaptic features, as STP, LTP, STDP and spike-rate-dependent plasticity[227,231,233–237] (SRDP).

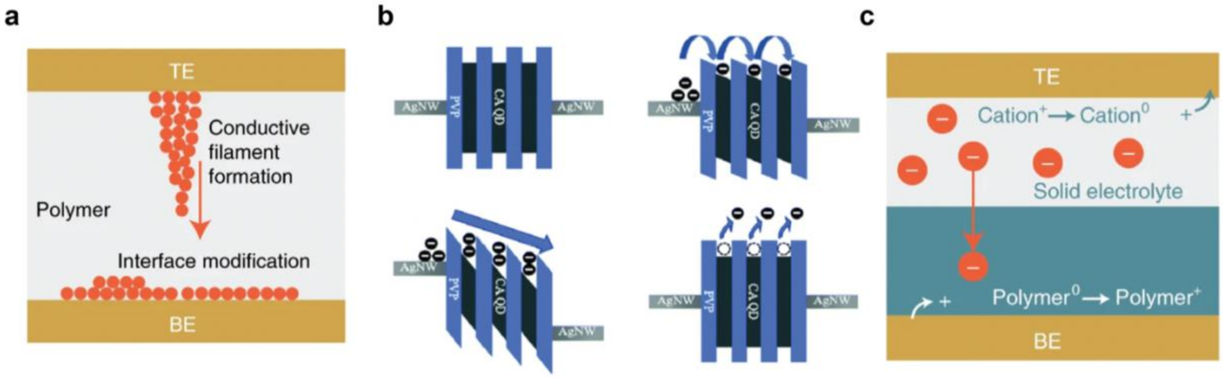

Figure 1.43 | Physical mechanisms of two-terminal organic neuromorphic device. **a**) Conductive filament generation. Adapted from [230]. **b**) Charge trapping mechanism. Adapted from [229]. **c**) Redox-based memristors. Adapted from [230].

1.6.2. Neuromorphic three-terminal devices

Leveraging on the in-built suitability of organic materials to interface with biology, several neuromorphic architectures were developed as neuromorphic biosensors, processing sensory stimuli as the brain does[238–241], *i.e.*, featuring PPF, STDP, STP and STP.

Of particular interest are organic FeFET. They share the same architecture of OFETs, while featuring a ferroelectric material as dielectric. Here, upon the application of an electric field, electric dipoles in the ferroelectric material align, gating the semiconducting channel[239]. Notably, such alignment is maintained even in absence of the external electric field, exhibiting excellent LTP[242].

Furthermore, while field-effect transistors do not allow for ionic penetration in the semiconducting channel, OECTs, closely resemble synapses, as ions are physically mediating the conductance of the channel. A comparison is shown in **Fig. 1.44**. Here, a square voltage pulse applied at the gate terminal mirrors the biological presynaptic stimulus. Such voltage bias causes ions to migrate from the electrolyte to the polymeric channel, mimicking the electrochemical signal transduction of biological synapses, in which APs cause the release of the neurotransmitter in the synaptic cleft. Therefore, the transistor channel is de-doped, changing its conductance level, and resulting in a modulation of the channel current, that represents a PSP. If, on the one hand, this mechanism allows to easily recapitulate STP and PPF[243], the communication is volatile, as the removal of the voltage bias at the gate causes ions to migrate back to the electrolyte, restoring the initial charge equilibrium. Finally, OECTs requires further modifications to improve LTP.

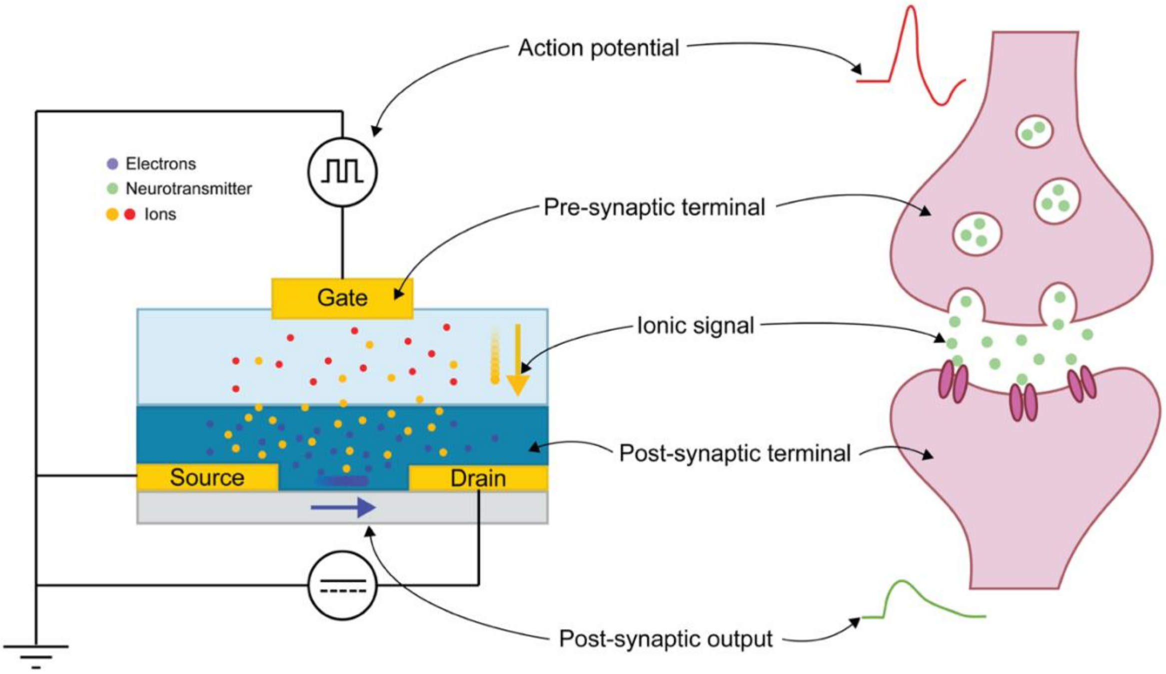

Figure 1.44 | Comparison between OECT and biological synapse. Adapted from [224].

Indeed, non-volatility was demonstrated in organic electrochemical resistive access memories (OEC-RAMs). An OEC-RAM is a particular type of OECT, where the gate electrode is functionalized with a CP (**Fig. 1.45-a**). This modification makes the device redox-reactable. Here, when a positive (or negative) signal is applied at the gate terminal, electrons are removed (or injected) from the CP covering it, consequently releasing (or absorbing) cations in the electrolyte, *de facto* maintaining charge neutrality. At this point, a surplus of cations breaks the electroneutrality of the electrolyte, that will push them to (or pull them from) the transistor channel, changing its doping state, and thus the charge carrier concentration and conductivity[244,245]. To summarize, a redox reaction occurring at the gate terminal is balanced by a counter-redox reaction of the channel, that will restore electroneutrality, changing its conductance, in turn. The first demonstration of this concept was achieved by van de Burgt, et al., that presented the first realization of an electrochemical neuromorphic organic device (ENODe). Here, the gate electrode was functionalized by a layer of PEDOT:PSS, while the semiconducting channel of the transistor was made of PEDOT:PSS partially reduced with poly(ethylenimine)[244] (PEI). This device was able to emulate LTP, displaying more than 500 independent non-volatile conductance states, while operating at low voltage (1 V) (**Fig. 1.45-b**).

Furthermore, exploiting the same architecture the first biohybrid synapse was demonstrated[246], showing how the ENODe can directly communicate with neural cells. Here dopaminergic cells were plated directly on the gate electrode of the transistor, spontaneously releasing DA (**Fig. 1.45-c**). The application of a gate bias, matching the neurotransmitter's oxidation potential[247], favours an oxidation reaction and a consequent release of protons and electrons in the electrolyte [REF]. Cations generated in such reaction will elicit a charge-transfer process to both gate and channel of the organic transistor, reducing the PEDOT:PSS and finally decreasing the device's conductance (**Fig. 1.45-d**).

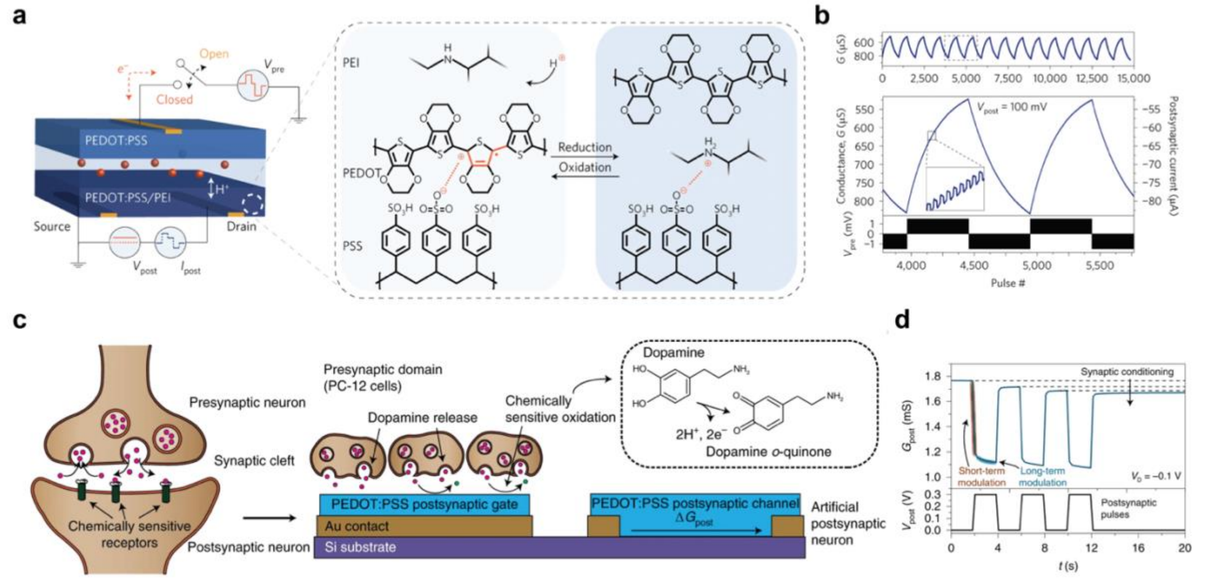

Figure 1.45 | **a**) Schematic of the ENODe platform demonstrating conductance modulation through PEDOT:PSS oxidation and reduction. **b**) Stable independent conductance states. Adapted from [244]. **c**) Schematic of the biohybrid synapse with dopaminergic cells releasing DA and oxidation schematic. **d**) Non-volatile conductance modulation achieved through DA oxidation. Adapted from [246].

In addition, multiple neurotransmitters modulation was demonstrated, along with optical monitoring strategies that rely on electrochromic properties of CPs[248]. In particular, a mixture of DA and serotonin (5-HT) were introduced in the electrolyte of a PEDOT:PSS-based OECT. By tuning a pattern of square voltage pulses applied at the gate terminal, selectivity in the oxidation of the neurotransmitter was demonstrated (**Fig. 1.46**).

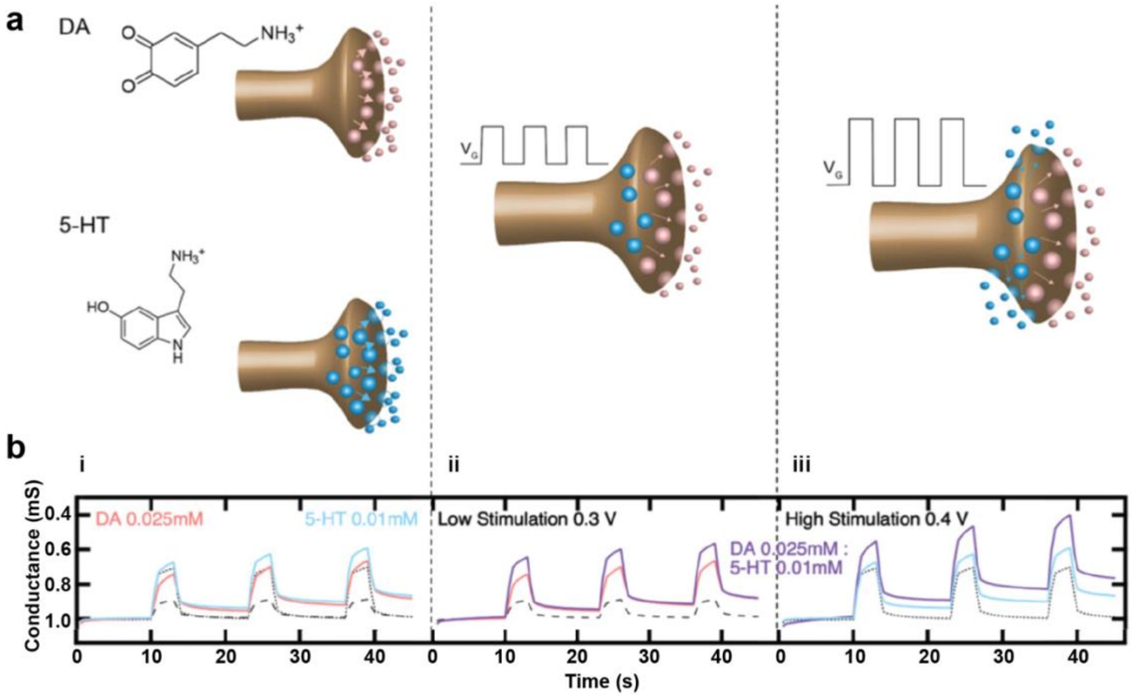

Figure 1.46 | **a**) Neurotransmitter co-modulation schematic, in which co-expression of both DA and 5-HT is expressed only in case of high stimulation (square voltage pulse train with amplitude 0.4 V). In case of low stimulation (square voltage pulse train with amplitude 0.3 V) only DA response is elicited. **b**) OECT response at high and low stimulation expressed as conductance, *i.e.*, ratio between channel current I_{DS} and drain-source voltage V_{DS}. Adapted from [248].

1.6.3. Applications of organic neuromorphic devices

Organic devices not only emerged for single synapse/neuron recapitulation, but they were also integrated into more complex systems, as electronic or mechanical systems. For instance, leveraging on the easy-processability of organic devices, 3D crossbar arrays featuring organic resistive elements at each intersection, were demonstrated[249] (**Fig. 1.47-a**). Such architectures showed STDP mechanisms and simultaneous potentiation and depression of different nodes[250].

Notably, while crossbar arrays can either be implemented by using either organic or inorganic materials, the electrolyte-gated device structure allowed for the fabrication of distributed neuromorphic platforms, that could not be trivially reproduced by any inorganic counterparts. Either a multi-channel/single-gate architecture[251] or a single-channel/multi-gate architecture[252] were demonstrated (**Fig. 1.47-b** and **c**, respectively). The former was the first example of recapitulation of the homeoplasticity of the neural environment and global synchronization, while the latter proved hardware discrimination of stimuli orientations and ion-based multiplexing of spatial distributed input signals.

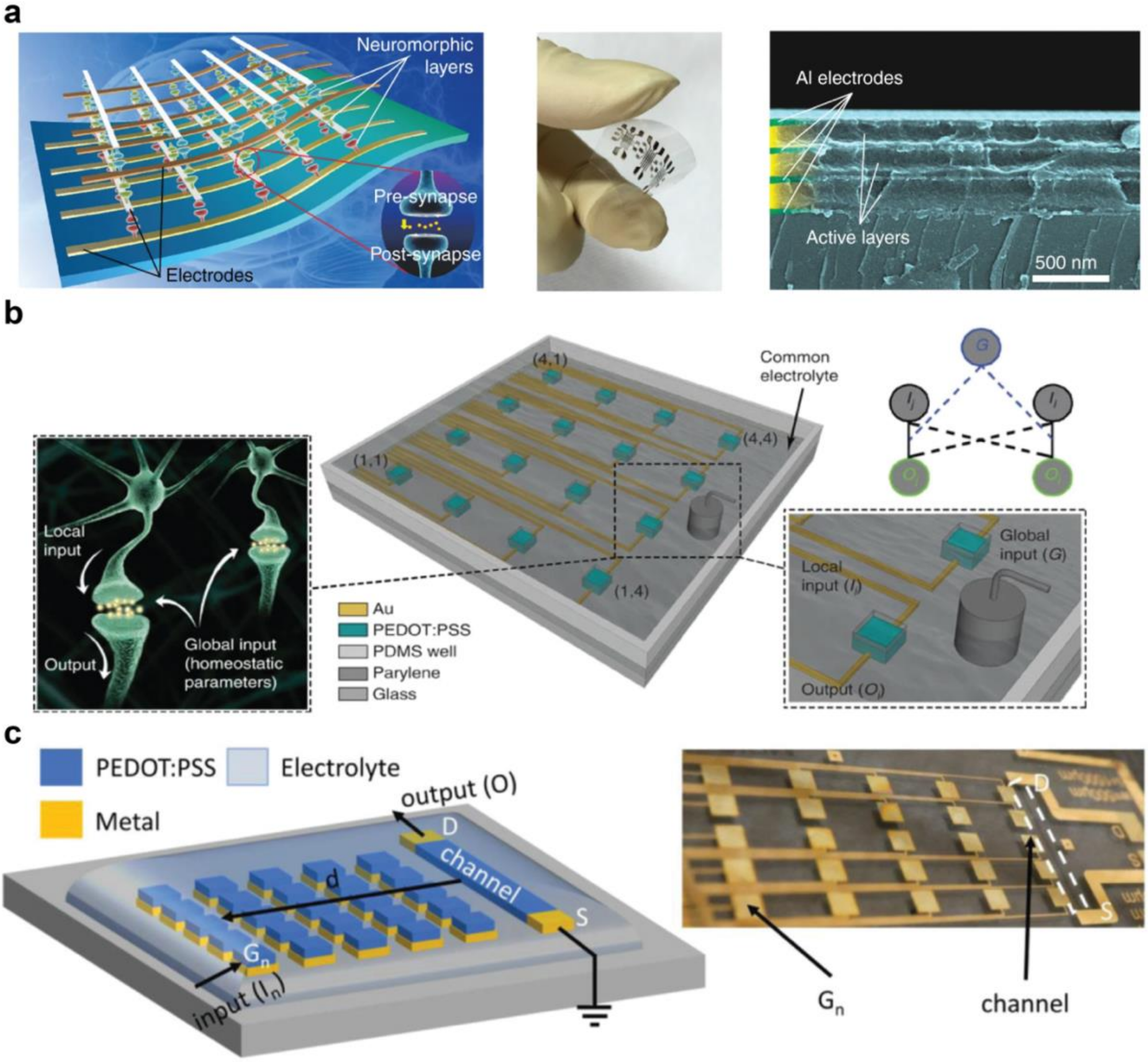

Figure 1.47 | **a**) Neuromorphic 3D crossbay array made of organic materials. Adapted from [249]. **b**) Distributed neuromorphic OECT structure, featuring single gate/multi channel architecture. Adapted from [251]. **c**) Distributed neuromorphic OECT structure, featuring multi gate/single channel architecture. Adapted from [252].

Moreover, hardware reservoir computing was demonstrated in organic platforms. The non-linear transformation of the input signal was achieved in an electropolymerized network of PEDOT:PF6[253] (**Fig. 1.48-a**), in which both excitatory and inhibitory connections can be created (bridges and dead ends, respectively). Such architecture was able to perform classification, time series prediction and arrhythmic heartbeat classification with an accuracy of 88% (**Fig. 1.48-b**).

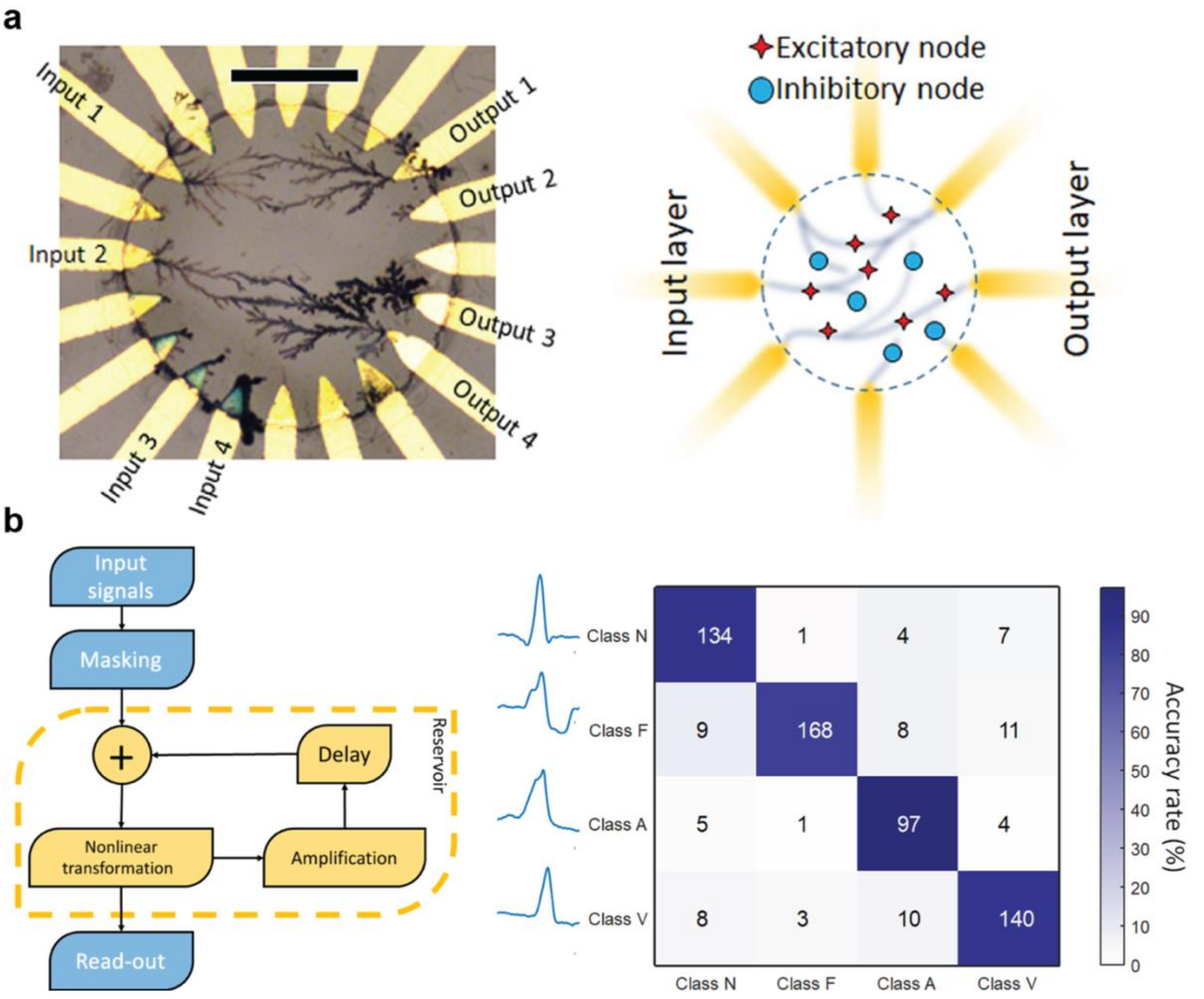

Figure 1.48 | **a**) Physical reservoir made of PEDOT:PF6 electropolymerized fibers, featuring inhibitory and excitatory nodes. **b**) Classification of heartbeat series through the reservoir. Adapted from [253].

Furthermore, by exploiting the possibility of OECTs of working in aqueous environment, organic spiking neurons, closing mirroring neuronal dynamics, were demonstrated. The first fully organic spiking neuron was shown to emulate the axon-hillock model, while being able of modulating spiking frequency based on ionic concentration of the electrolyte used to gate several p- and n-type OECTs[254] (**Fig. 1.49-a**). Later, the same group could develop a spiking neuron that could reproduce sodium and potassium ion-channels dynamics, while spiking at bio-plausible frequency (*i.e.*, almost 100 Hz) and demonstrating ion-based spiking modulation in *in vivo* nerve stimulation[255] (**Fig. 1.49-b**). Lastly, by exploiting non-linear features of organic devices, organic oscillators where build with minimal circuital complexity, demonstrating spiking neurons able to operate in biologically relevant ionic environments, and exhibiting DA-mediated synaptic excitability[256].

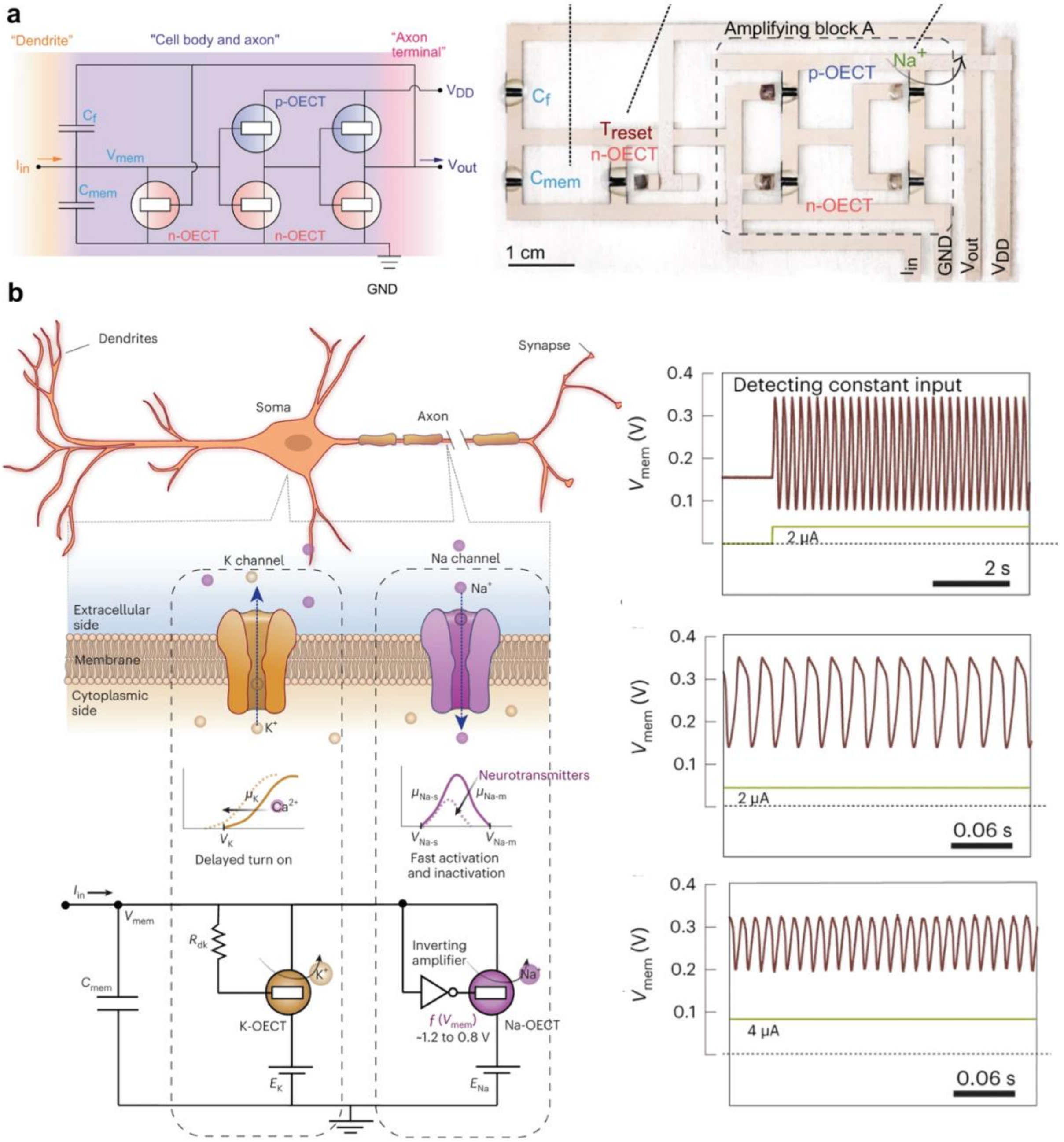

Figure 1.49 | **a**) Organic spiking neuron implementing Axon-Hillock model. Adapted from [254]. **b**) Organic spiking neuron implementing sodium and calcium dynamics, along with spiking at different frequencies, up to 80 Hz. Adapted from [255].

Lastly, as the goal of organic neuromorphic platforms is to embed brain-inspired intelligence into electronic systems, an example of autonomous reinforcement learning was demonstrated in a mobile robot[257] (**Fig. 1.50-a**). Here, the mobile robot followed a track, performing turns at every intersection, with the aim of exiting a maze. Whenever it took the wrong direction, a punishment signal was sent to an organic circuit, made up of a volatile and a non-volatile OECT coupled together (**Fig. 1.50-b**), conditioning it, *i.e.*, changing the conductance of the non-volatile OECT. The voltage drop on the volatile OECT was then used to determine the direction of the next turn. Eventually, after some failed trials, the organic devices were correctly conditioned so that the robot can execute all the correct turns, exiting the maze (**Fig. 1.50-c**).

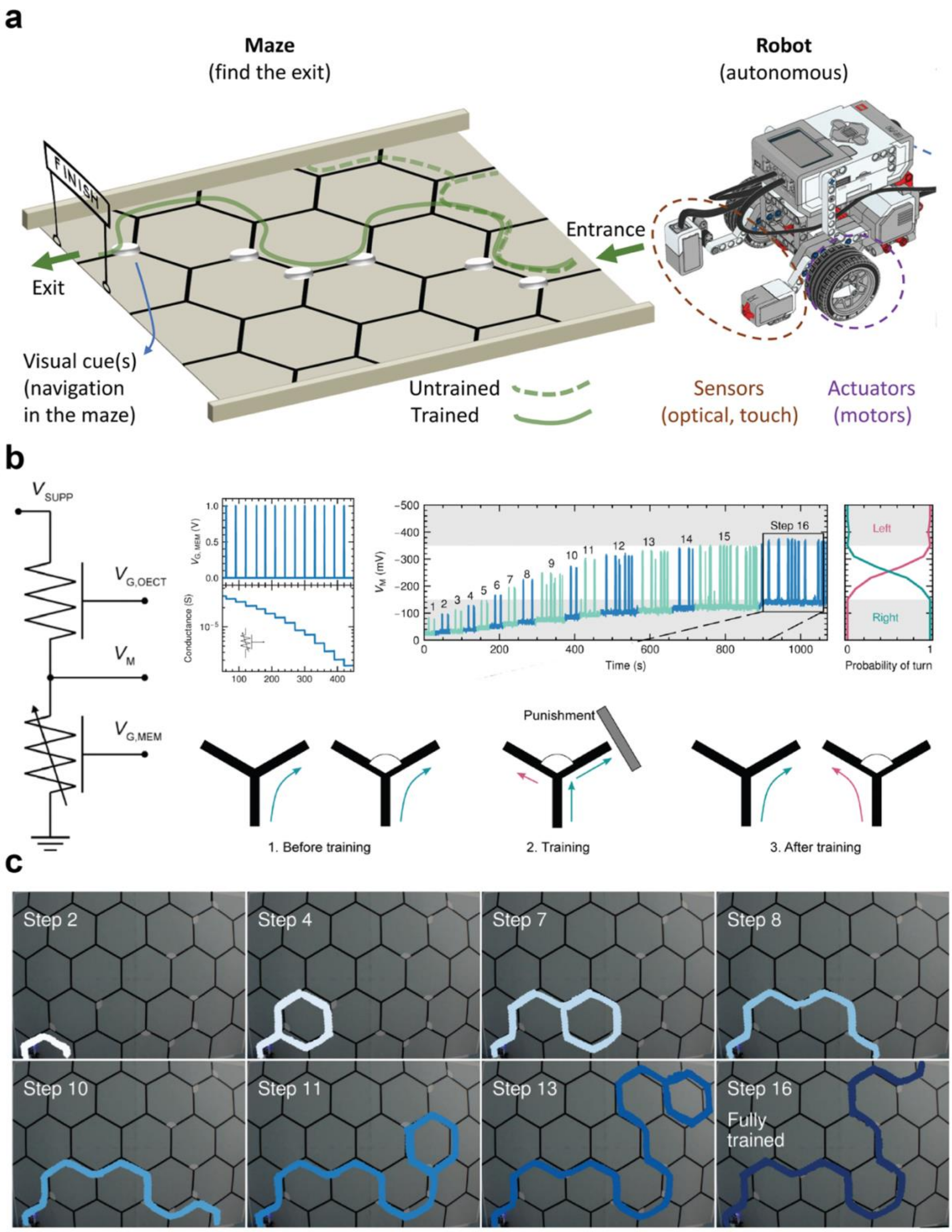

Figure 1.50 | **a**) Schematic of the mobile robot that learns to navigate through the maze. **b**) Volatile and non-volatile OECT coupled to achieve an adaptive neuromorphic circuit, that change its conductance as a consequence of a punishment, *i.e.*, failed trial. The conductance of the device decreases upon the application

of a pulse at the gate terminal. **c**) Robot navigating through the maze, learning how to find the exit after 16 trials. Adapted from [257].

1.7. Challenges

Neuromorphic devices and, in particular, organic neuromorphic devices have been shown to recapitulate several features of neural communication, to improve energy efficiency in a novel generation of hardware.

A fundamental challenge, yet to be addressed, is the possibility to easily integrate such devices with complementary metal-oxides semiconductors (CMOS) technology, to leverage on the maturity of such platforms to endow existing electronics with innovative and bio-inspired features.

In addition, closed-loop operations in a neuromorphic system were not demonstrated yet, fatally failing in the recapitulation of the computational approach of the in brain, in stand-alone applications.

Lastly, while a seamless integration with biological tissue was demonstrated, a smart and adaptive neuromorphic interface was not developed. Here, such device might be able to interact with a biological tissue, while adapting to comply with the continuously evolving biological environment.

1.8. Our study

The aim of this PhD thesis is to leverage on the versatility of OECTs to build fully-organic neuromorphic systems that can interface and interact with biological systems to accomplish several tasks, such as biosensing, stimulation, emulation and learning.

First, by engineering some modifications of a PEDOT:PSS-based OECT, the possibility the possibility to endow such neuromorphic platform with LTP and, at the same time biosensing capabilities, to replicate the way in which the brain processes vision and touch.

A chemical functionalization of the OECT gate allowed to induce light-gating properties to the device. Interestingly, upon the light exposure the gate underwent a faradic charge transfer process, ultimately changing the transistor conductance in a non-volatile way, emulating LTP. In addition, a fully organic circuit was designed and built to emulate the OFF vertical pathway of the human retina.

The sense of touch was implemented by using a solid-state electrolyte. Upon pressure, a strong contact between gate and channel was ensured, gating the device, while upon release, the gate bias was removed. In addition, by including a dedicated patterned insulating layer, ionic migration could be stopped, inducing charge trapping, resulting in LTP.

Then, neurotransmitter-mediated LTP is exploited to demonstrate learning in robotics. In particular, the redox reaction-induced conductance modulation of PEDOT:PSS-based OECTs was characterized electrically and optically, demonstrating LTP. Reversibility was achieved by oxidizing the CP used as semiconducting channel. In addition, as the brain uses closed-loop circuitry to enforce positive behaviours and deplete non-advantageous ones, we introduced a closed-loop structure. Here, by controlling flowrates of different electrolyte solutions, LTP of a neuromorphic OECT was finely controlled. In addition, leveraging on this concept, the neuromorphic device was used to perform autonomous reinforcement learning, in which it learned how to correctly drive a robotic hand to grasp objects of different sizes.

Despite recapitulating several aspects of neurons, neuromorphic OECTs are still far from structurally recapitulating their biological counterpart. Therefore, to fill this gap and structurally mimic biological synapses, we engineered a biomimetic artificial synapse coupling OECT with optimal models of neural PM. The impact of the PM on the electrical properties of the OECT was evaluated in different conditions, such as membrane positioning, confinement and composition. Notably, the presence of the PM, working as a barrier for ions, induced a reversible charge-trapping mechanism, allowing to tune STP in OECTs.

Chapter 2: Materials and Methods

2.1. Pressure-sensitive OECTs

2.1.1. Numerical simulation of pressure application

Simulations of the solid electrolyte deforming and touching the channel of the transistor were carried out through COMSOL Multiphysics software. Structural mechanics was the physics employed in the simulation with solid mechanics interface. The OECT channel and the spacer were modelled as rigid bodies using glass as material (imported from COMSOL library).

The solid electrolyte was approximated as an elastic linear body using silicon as material (properties of the material imported from COMSOL library). Constrains were applied to the rigid bodies and to the side of the solid electrolyte which was free to move along the z-axis. Lastly, the applied pressure was implemented with a triangular function progressively applying and removing the load from the surface of the solid electrolyte.

2.1.2. OECTs fabrication

The fabrication of the OECT was carried out in cooperation with Lussem group, at Institute for Microsensors, -actuators and -systems (IMSAS), UniBremen. A schematic of the fabrication is shown in **Fig. 2.1**.

A double polished silicon wafer with a 500 µM thick silicon oxide layer was cleaned and used as substrate for the fabrication. Initially, a 300 nm thick gold layer was sputtered on the substrate (100 W, DC magnetron). A 1.8 µM thick photoresist was then spin coated onto the substrate (AZ 1518, MicroChemicals GmbH, 89079 Ulm, Germany). UV light exposure was performed, and the photoresist was developed, defining the contact pad geometry. Subsequently, the gold layer was etched (Au Etch 200, NB Technologies GmbH, 28359 Bremen, Germany) and the photoresist is removed (AZ 100 Remover, MicroChemicals GmbH, 89079 Ulm, Germany). The adhesion promoter 3-Aminopropyltriethoxysilane (APTES, 0.1 vol.%, Sigma-Aldrich Chemie GmbH, 82024, Taufkirchen, Germany) was applied and polyimide (PI, U-Varnish-S, UBE Europe GmbH, Germany) was spin coated onto the substrate at 3000 RPM, yielding for a layer of 5 µM. Subsequently, PI was cured on a vacuum hotplate, stepping the temperature of 5 ºC/min, up to 450 ºC. A second PI layer was then deposited, using the same procedure of the first one. Notably, after crosslinking, the second layer will not adhere to the former one, allowing for a manual peel-off. Another lithography step was then performed to define the active areas of the OECT, *i.e.*, gate and channel. A thicker photoresist was employed in this step (20 µM, AZ 9260, MicroChemicals GmbH, 89079 Ulm, Germany). Both PI layers were etched using a O_2/CF_4-reaction ion etching, and the remaining photoresist was stripped.

Subsequently, a PEDOT:PSS dispersion was prepared by mixing a commercially available PEDOT:PSS aqueous solution (Hereaus, Clevios PH1000) with 5 vol% ethylene glycol (Sigma-Aldrich) and 1 vol% 3-glycidyloxypropyl)trimethoxysilane (Sigma-Aldrich). The prepared solution was spun coated onto the devices, 1000 RPM, 100 RPM/s, 60 s. Thermal annealing was performed on hotplate at 120 ºC, 1h. Lastly, the upper PI layer was manually peeled-off. Gate and channel had same sizes: 500 x 500 µM^2.

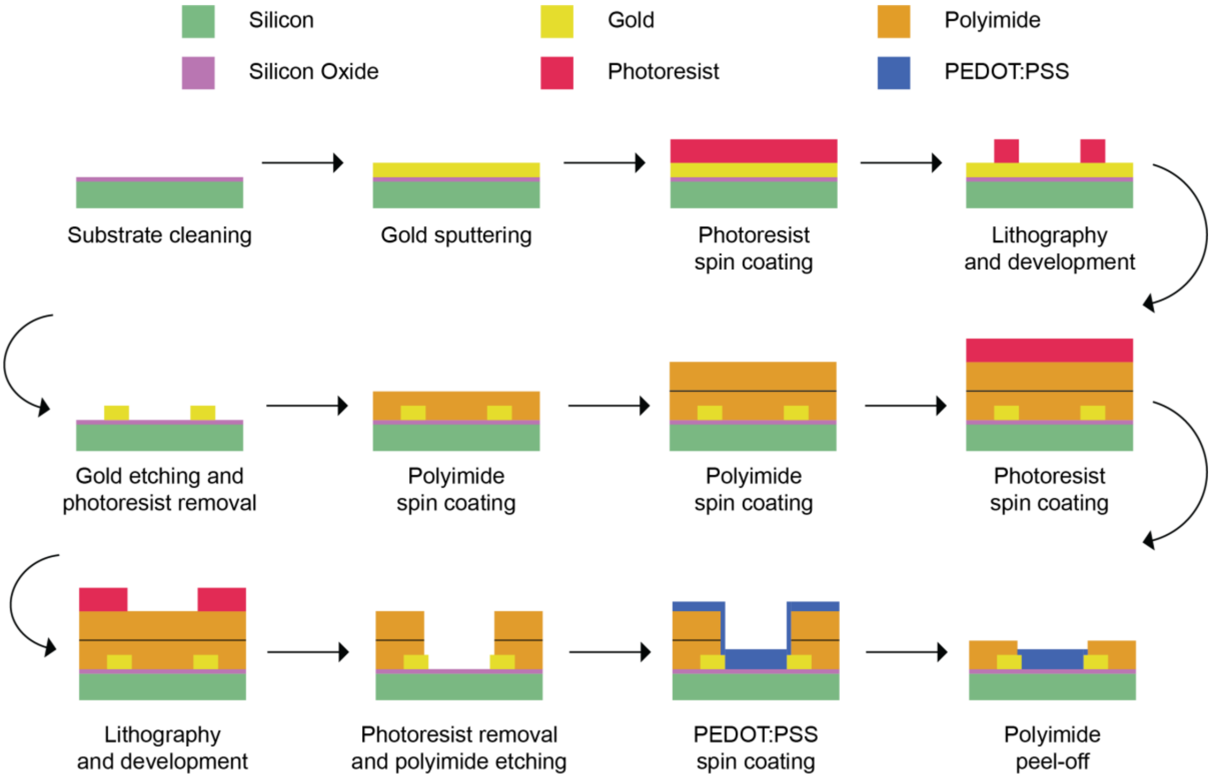

Figure 2.1 | Schematics of the fabrication of PEDOT:PSS OECTs.

2.1.3. Electrolyte preparation

A sodium chloride (NaCl) 100 µM liquid electrolyte was used to characterize the fabricated OECTs. Such solution was prepared by dissolving NaCl (Sigma-Aldrich GmbH) in deionized (DI) water.

A solid electrolyte was prepared to perform pressure sensing. Initially, poly(vinylidene fluoride-co-hexafluoropropylene) (PVDF-co-HFP, Mw = 400 000 g mol−1, Sigma-Aldrich GmbH) was dissolved in acetone at a final concentration of 110 mg/ml. The obtained solution was stirred for 12 on a magnetic stirrer (250 RPM). Subsequently, the ionic liquid 1-ethyl-3-methylimidazolium bis(trifluoromethylsulfonyl)amide ([EMIM][TFSI]) was added into the solution in a weight ration 1:2. The obtained solution was vigorously stirred initially through vibrations and then on a magnetic stirrer for 1 h (250 RPM). The obtained electrolyte was spun coated onto a clean silicon wafer (1500 RPM, 60 s), and transferred into a vacuum over (70 ºC, 24h). After curing, the electrolyte was manually peeled and positioned on the transistor channel.

2.1.4. Flexible gate electrode fabrication

A flexible gate electrode was prepared by using a PI film as substrate (Kapton, DuPont). Initially the film was cleaned by means of acetone, isopropanol and DI water. Subsequently, chromium/gold layers were deposited (Cr/Au, 10/100 nm) by means of thermal evaporation. Lastly, a solution of PEDOT:PSS was prepared and deposited onto the substrate (**Paragraph 2.1.3**).

2.1.5. OECTs steady state characterization

Steady state characterization of the fabricated OECTs was carried out in Salleo Lab at Stanford University. Measurements were carried out by coupling two source measure units (SMUs, Keithley 2400, Tektronix), through a custom LABVIEW routine. Transfer curves were obtained by sweeping the gate potential V_{GS} (from 0 to 0.6 V, with voltage steps of 50 mV), while measuring the channel current I_{DS}, at a fixed drain-source voltage V_{DS} (-0.1, -0.2, -0.3 and –0.4 V). Output curves were recorded by sweeping the drain-source voltage V_{DS} (from –0.1 to –0.6 V, with a voltage step of –50 mV), while fixing the gate potential V_{GS} (-0.15, -0.30, -0.45 and –0.60 V), and measuring the channel current I_{DS}.

2.1.6. OECTs pressure measurements

Pressure measurements were carried out by coupling two SMUs Keithley 2400, Tektronix), through a custom LABVIEW routine. Here, V_{DS} was set to –0.2 V, while the gate electrode was biased either with 0.5 V or 0 V (write and erase mode, respectively).

Pressure was applied by placing scale calibration weights on the gate of the transistor. By knowing the mass of the weights (5 g, 10 g, 50 g and 100g) and measuring the diameter (5 mm, 5.5 mm, 9.5 mm and 12 mm), the applied pressure was assessed, yielding 624.5 Pa, 1032.3 Pa, 1730.0 Pa and 2168.5 Pa, respectively.

2.2. Optoelectronic neuromorphic OECTs

2.2.1. Synthetic procedure

The fabrication of the azo-tz-PEDOT:PSS was carried out by first synthetizing 2-Azidomethyl-2,3-dihydrothieno[3,4-b]−1,4-dioxine (EDOT-N3), which was subsequently electrodeposited onto a conductive substrate, defining an N3-PEDOT:PSS film. Lastly, an ad hoc synthetized molecule, 4-Propargyloxyazobenzene (azo-alkyne), was used to functionalize the obtained film, through click-chemistry. The whole synthetic procedure was carried out in cooperation with Federica Corrado, Tissue Electronics lab at the Italian Institute of Technology, Naples.

2.2.1.1. EDOT-N3 synthesis

2-chloromethyl-2,3-dihydrothieno[3,4-b]−1,4-dioxine, EDOT-Cl (Merck Life Science S.r.l., Italy) (50 mg, 0.262 mmol, 1 eq) was dissolved in 3 mL of N,N-dimethylformamide (DMF) (Merck Life Science S.r.l., Italy) and stirred at room temperature under inert atmosphere until complete dissolution. After the addition of sodium azide (NaN3) (TCI chemicals, Belgium) (34 mg, 0.524 mmol, 2 eq), the reaction mixture was refluxed for 3 h. The reaction mixture was extracted with ethyl acetate (EtOAc) (Merck Life Science S.r.l., Italy) and the resulting combined organic layers were washed with water to remove DMF (Merck Life Science S.r.l., Italy). The obtained crude product was dried over sodium sulfate (Na2SO4) (Merck Life Science S.r.l., Italy) and concentrated under vacuum giving the EDOT-N3 as a colourless oil (48 mg, 0.243 mmol, 93%).

2.2.1.2. Azo-alkyne synthesis

4-(Phenylazo)phenol (TCI chemicals, Belgium) (50 mg, 0.252 mmol, 1 eq) was dissolved in previously degassed acetone (3 mL) (Merck Life Science S.r.l., Italy). Potassium carbonate (K2CO3) (Thermo Fisher Scientific Inc., Germany) (174 mg, 1.26 mmol, 5 eq) was added to the organic solution and the reaction mixture was stirred at room temperature under inert atmosphere for 90 min. Then, propargyl bromide (TCI chemicals, Belgium) (150 mg, 1.26 mmol, 5 eq) was added, and the reaction mixture was refluxed overnight, under inert atmosphere. Removal of the acetone under vacuum provided the solid crude product. It was then re-dissolved and extracted with EtOAc (Merck Life Science S.r.l., Italy) and the combined organic solution was washed with water and dried over Na2SO4 (Merck Life Science S.r.l., Italy). Removal of the solvent under vacuum was employed to yield the alkyne as an orange powder (56.5 mg, 0.239 mmol, 95%).

2.2.2. OECTs fabrication

A schematic of the fabrication is shown in **Fig. 2.2**. An indium tin oxide (ITO, surface resistivity 20 Ω cm^{-2}, 25 mm × 25 mm, Kintec, Hong Kong) patterned glass substrate was washed with DI water, acetone and isopropanol in an ultrasound bath (10 min per solvent). Two squares of ITO will be used as source and drain terminals, while the remaining ITO rectangle will host the azo-tz-PEDOT:PSS gate electrode. Indeed, a N3-PEDOT:PSS film was electrodeposited onto the ITO substrate (**Paragraph 2.2.2.1**). The two ITO squares are protected by use of kapton tape (DuPont).

Then, the previously synthesised azo-alkyne (141 mg, 0.6 mmol, 1 eq) was dissolved in tetrahydrofuran (THF) (Merck Life Science S.r.l., Italy) (30 mL), before the addition of 30 mL of an aqueous solution of CuSO4•5H2O (Merck Life Science S.r.l., Italy; 150 mg, 0.64 mmol, 1.07 eq) and sodium ascorbate (Merck Life Science S.r.l., Italy; 118.9 mg 0.53 mmol, 0.89 eq). The electropolymerized N3-PEDOT:PSS film was then put in the resulting mixture and maintained under gentle stirring for 24 h. The obtained functionalized film was repeatedly washed with deionized water to remove the excess of catalyst and with THF to remove the excess of unreacted azo-alkyne. The kapton tape was removed from the ITO squares, while a polydimethylsiloxane (PDMS, Silgard 184) mask was used to cover the azo-tz-PEDOT:PSS gate electrode. PDMS was mixed in ratio 10:1 wt/wt with a crosslinker, and cured at 80 °C, 1 h in oven. A commercially available PEDOT:PSS solution (**Paragraph 2.1.2)** was spun coated onto the substate (2000 RPM, 400 RPM/s, 2 min) and thermally annealed for 1 h on a hotplate at 140 ºC. Lastly, a second PDMS mask is positioned onto the spin coated PEDOT:PSS and O_2 plasma etch is performed (RIE, 15 min, 100 W), to define the transistor channel. The size of the gate electrode was 13 x 10 mm^2, while the channel had dimensions 15 x 7 mm^2. The obtained devices were rinsed in DI water overnight, to allow for PEDOT:PSS swelling.

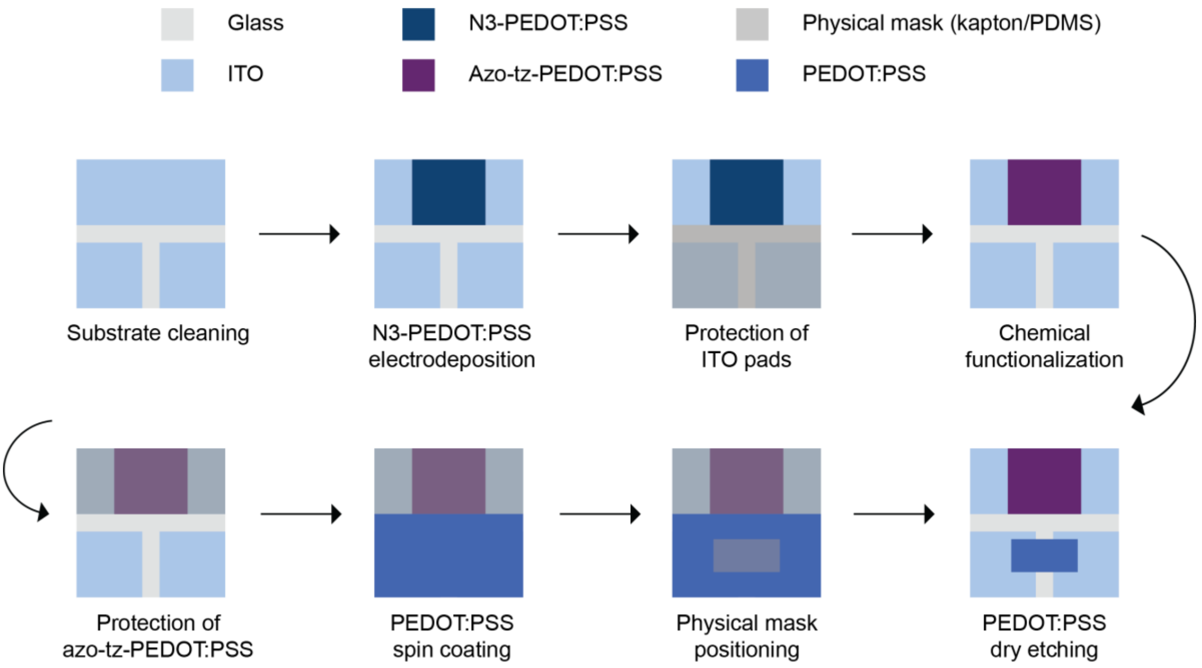

Figure 2.2 | Schematics of the fabrication of the OPECT, featuring gate electrode made of azo-tz-PEDOT:PSS and channel made of commercially available PEDOT:PSS.

2.2.2.1. Electrodeposition

The electrodeposition of N3-PEDOT:PSS was carried out with Autolab PGSTAT302N potentiostat (Metrohm Italiana S.r.l., Italy), through a cyclic voltammetry (CV), sweeping the potential from 0 V to 1.5 V, with a scan rate of 50 mV/s, in a three electrode configuration: ITO substrate (working electrode), platinum wire (counter electrode, Merck KGaA, Germany) and a reference Ag/AgCl NaCl (3 M) electrode (reference electrode, Redox.me, Sweden).

The ITO substrates were cleaned in an ultrasonic bath with DI water, acetone and isopropanol before the electropolymerization procedure. A suspension of 7.5 mg mL−1 of poly(sodium 4-styrenesulfonate) (PSSNa) containing 0.01 M of N3-EDOT monomer was employed. Ten CV cyles were performed. After electrodeposition, the films were washed with water to remove both the PSSNa and the unreacted monomer excess. Finally, the substrates were dried on hot plate at 120 °C for 1 h.

2.2.2.2. Organic resistor

The patterning of the organic resistor was carried out by following the same procedure explained for the patterning of the OPECT channel: spin coating, dry etching and swelling (**Paragraph 2.2.2**).

2.2.3. Morphological characterization

A Dimension Icon® AFM (Bruker Corporation, USA) with Scan Assyst, operating in tapping mode (the cantilever vibrates near its resonance frequency causing the tip to oscillate up and down), was used in dry conditions and under ambient atmosphere to measure films surface topography and roughness. The cantilevers (Bruker, Model: SCANASYST-FLUID) were characterized by spring constant 0.7 N/m, resonance frequency 150 Hz, Thickness = 600 nm, Width = 10 nm, Length = 70 nm. The scanned area was $5 \times 5\ \mu m^2$ with a scan rate of 2 Hz. Nanoscope 2.0 software was used to evaluate the root mean square (RMS or Rq) roughness for each acquired area.

2.2.4. Electrochemical characterization

Cyclic voltammetry (CV) analyses were carried out with Autolab PGSTAT302N potentiostat (Metrohm Italiana S.r.l., Italy). The films were characterized on an ITO-coated square acting as working electrode, an Ag/AgCl NaCl (3 M) electrode as reference electrode and a platinum wire as counter electrode. Phosphape buffered saline (PBS) solution (Merck Life Science S.r.l., Italy), with pH = 7.4 (100 μL) was employed as electrolyte and the voltage was swept from –0.4 V to +1.0 V at a scan rate of 50 mV/s.

Electrochemical impedance spectroscopy (EIS) was carried out with Autolab PGSTAT302N potentiostat (Metrohm Italiana S.r.l., Italy), in a two-electrode configuration: the films deposited on an ITO-patterned glass acter as reference and sense electrode, while an Ag/AgCl NaCl (3 M) electrode acted as both reference and counter electrode. Impedance was recorded using PBS as electrolyte solution, in a frequency range spanning from 0.1 Hz to 10 kHz. The applied signal was a sinusoidal wave with amplitude ±10 mV, around 0 V.

2.2.5. OECTs steady state characterization

Transistor steady state characterization was carried out using a commercially available platform (ARKEO, Cicci Research, Italy). In both output and transfer curves, the azo-tz-PEDOT:PSS electrode was used as gate terminal, while the spin coated PEDOT:PSS acted as transistor channel. PBS was used as electrolyte solution. Output curves were recorded by sweeping V_{DS} from 0 V to –0.8 V with a voltage step of – 50 mV, at different values of V_{GS} (0.2, 0.4, 0.6 and 0.8 V). Transfer curves were obtained by sweeping the gate voltage from −0.2 V to 0.8 V with a scan rate of 50 mV/s while the drain voltage (both versus the source potential) was held at different values (0.1 V to –0.6 V with a voltage step of –0.1 V).

Light exposition was carried out through a UV lamp (λ = 365 nm) at three different power levels (20% = 0.56 W/cm^2, 60% = 1.7 W/cm^2 and 100 % = 2.8 W/cm^2). After 5 min of light exposition, the lamp was turned off and output and transfer curves were recorded again.

2.2.6. OECTs transient measurements

Transient measurements were carried out using a commercially available platform (ARKEO). PBS was employed as electrolyte. Drain-to-source voltage bias was held at –0.2 V, while the gate terminal was held at 0 V against source potential. The azo-tz-PEDOT:PSS electrode, acting as gate, was exposed to 60 s of UV light (λ = 365 nm) and 60 s of dark condition. Light intensities employed were: 20% = 0.56 W/cm^2, 60% = 1.7 W/cm^2 and 100 % = 2.8 W/cm^2.

2.2.7. Retina emulation

An organic resistor made of PEDOT:PSS was connected in series to the channel of the OPECT by means of a tin-based soldering wire, along with conductive silver paint (RS Components). Arkeo commercial platform was used to carry out the measurements, using PBS as electrolyte. A pulsed voltage supply was applied during the whole duration of the measurement (V_{DD} = 0.4 V/ 0 V, PW = 3 s, Δt = 3 s). The gate voltage bias of the OPECT was held to 0 V during the first part of the measurement and ramped up to 0.3 V, such value was kept constant for 60 s. Light illumination was supplied by a UV lamp (λ = 365 nm) with an intensity of 2.0 W/cm^2.

2.2.8. Neuromorphic measurements

Neuromorphic measurements were carried out using a commercial platform (ARKEO). PBS was employed as electrolyte. Neuromorphic measurements were carried out by pulsing the gate terming with a square voltage pulse (V_{GS} = 0.3 V) with different PWs (0.5 s, 1 s and 5 s), while keeping the drain terminal biased at –0.2 V, with respect to the source electrode. The intensity of the UV light (λ = 365 nm) was: 20% = 0.56 W/cm^2, 60% = 1.7 W/cm^2 and 100 % = 2.8 W/cm^2.

The emulation of PPF was carried out by keeping V_{DS} at –0.2 V, while applying two consecutive voltage pulses at the gate terminal of amplitude 0.3 V, while varying the delay between the two pulses (Δt). In this case, Δt was chosen as: 0.1 s, 0.5 s, 1 s, 3 s, 5 s, 8 s, and 11 s.

Current and/or conductance modulations were computed through a MATLAB script. In particular, the script allowed to select two data points of current raw data (typically starting and ending points) and compute the difference between the two. Subsequently, such difference was converted into a percentage variation, using the value of the first data point (starting point of the raw current data) as reference, *i.e.*, 100%

2.2.9. Optoelectronic memory measurements

The optoelectronic memory was characterised using ARKEO commercial setup and employing PBS as electrolyte solution. V_{DS} was held constant at –0.2 V. Initially, the gate potential V_{GS} was held at 0V while light pulses were applied: $\lambda = 365$ nm, 2.8 W/cm^2 of light intensity, PW = 2 s, and $\Delta t = 10$ s. After the illumination, negative voltage pulses were applied at the gate terminal: PW = 2 s, $\Delta t = 10$ s and amp = −0.3 V.

2.3. OECTs for electrolyte potential monitoring

OECTs for electrolyte potential monitoring were fabricated as discussed in **Paragraph 2.1.2**, in cooperation with Lussem group, at UniBremen. The potential of the electrolyte was monitored in a four-electrode configuration. Two SMUs (Keithley 2400, Tektronix) were used to bias the drain electrode with –0.2 V, and the gate terminal with 0.3 V, both with respect to the source terminal. In addition, an oscilloscope (name of oscilloscope) was coupled to the two SMUs (common ground), using an Ag/AgCl pellet to monitor the potential of the electrolyte.

2.4. OECTs for neurotransmitter-mediated plasticity

2.4.1. OECTs fabrication

The fabrication of the OECTs is schematically shown in **Fig. 2.3**. OECTs were fabricated on 5x25 mm square glass substrate, with 10x10 mm^2 (ITO) square at each corner (Xinyan Technology Ltd.). Substrates were washed with DI water, acetone and isopropanol. Then, a PEDOT:PSS solution was prepared as discussed in **Paragraph 2.1.2,** and was spun coated onto the substrates at 2000 RPM, 400 RPM/s, 2 min. O_2 plasma treatment (20 W, 2 min) was performed prior to the PEDOT:PSS deposition, to enhance adhesion. Thermal annealing was then performed on hotplate for 1 h, 140 °C. PEDOT:PSS gate and channel were patterned through O_2 plasma dry etching technique for 15 min, at 100 W. Physical masks were used to define the transistor geometry, made from PDMS, mixed in ratio 10:1 wt/wt with a crosslinker, and cured at 80 °C, 1 h. Finally, through the etching process two symmetrical PEDOT:PSS stripes 7x17 mm wide were deposited 2 mm apart. Then the devices were immersed in milliQ water for 1 h to allow for the complete swelling of the PEDOT:PSS.

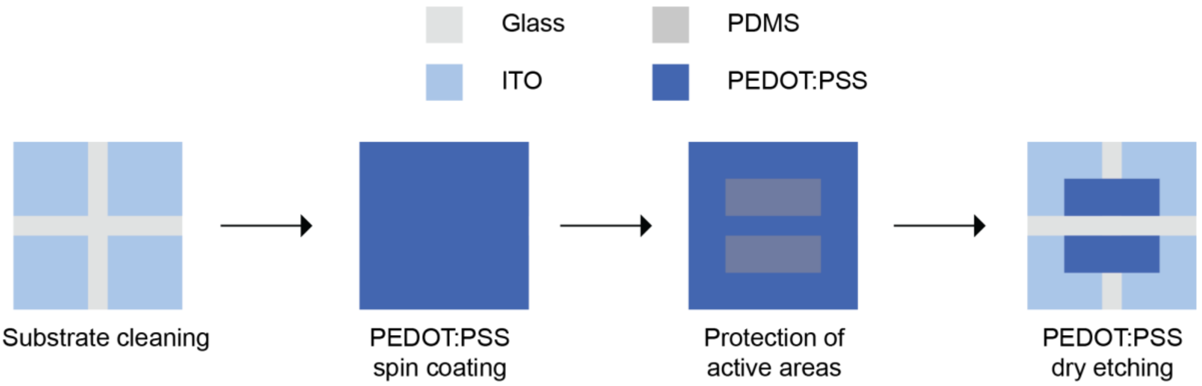

Figure 2.3 | Schematics of the fabrication of the PEDOT:PSS-based OECT.

2.4.1.1. Microfluidic module fabrication and in-flow measurements

To allow the electrolyte to connect and flow between the channel and the gate of the neuromorphic OECT, a microfluidic channel, made of PDMS, was attached on the device. The channel was made by pouring uncured PDMS into a mould made of Poly(methyl methacrylate) (PMMA). The mould was created by subtractive manufacturing, by means of a micromilling machine (Minitech, USA). The module was attached to the OECT by means of uncured PDMS, placed on the edges of the channel, and subsequently cured at 80 °C for 1h.

The microfluidic channel had a rectangular shape (17x4 mm^2, 1 mm in height) with a y-shaped junction at one end. Three holes were created with the use of a 1.2 mm punch at the ends of the y-shaped channel.

In case of static measurements, electrolytes were manually injected inside the module by means of a micropipette. During in-flow measurements the holes on the y-shaped side of the channel were connected through PTFE tubes to two programmable syringe pumps. The outlet, was connected to a waste container.

2.4.2. Electrolyte solutions preparation

Several electrolyte solutions were employed to characterize PEDOT:PSS oxidation and reduction. PBS without Ca^{2+} and Mg^{2+} buffer solution was purchased from Life Technologies. Dopamine (DA) and serotonin (5-HT) solutions were obtained by dissolving dopamine hydrochloride and serotonin hydrochloride in powder (Sigma-Aldrich, USA) in PBS. A stock H2O2 (30% in water, Sigma-Aldrich, USA) was diluted in PBS to obtain H_2O_2 solutions.

2.4.3. OECTs steady state characterization

Steady state characterization of the OECTs was carried out using a commercially available setup (Arkeo, Cicci Research, Italy) featuring two independent SMUs. Output curves were obtained by sweeping the drain-source potential from 0.1 V to -0.6 V, with a step of 100 mV, while three different gate voltage bias were employed (-0.2 V, +0.3 V and +0.8 V).

2.4.4. OECTs transient measurements

Transient measurements of OECTs were carried out using a commercially available setup (Arkeo) featuring two independent SMUs. Square voltage pulses were applied at the gate terminal, while keeping a fixed bias voltage V_{DS} = -0.2 V. Each measurement consisted of 6 pulses with PW = 3 s and delay between pulses Δt = 9 s. The amplitude of the pulses was 0.3 V in all cases, except for the electrolytic solutions containing 5-HT, where it was set to 0.4 V, to match the neurotransmitter oxidation peak potential[247].

2.4.5. Synaptic potentiation/depression extraction

Synaptic potentiation was achieved by inserting 100 µl DA/5-HT solution in the microfluidic module coupled to the OECT. Each measurement consisted of 6 voltage pulses applied at the gate terminal. After each measurement three washes were performed with 100 µl of fresh PBS solution. The channel conductance was calculated by dividing the channel current by V_{DS}. Then conductance variation (difference between values before and after the application of V_{GS} pulses) was represented as percentage.

Three consecutive measurements were performed (for a total of 18 applied voltage pulses) and conductance variations were computed and averaged for each device.

Synaptic depression was characterized in the same way of synaptic potentiation but employing an H_2O_2 solution as electrolyte. In addition, as synaptic depression was only achieved as an inversion of synaptic potentiation, one measurement with DA (6 voltage pulses) was performed before the application of H_2O_2.

In addition, in case of in-flow measurements the procedure was the same, but the electrolyte solutions were inserted using programmable syringe pumps.

2.5. Biomimetic neuromorphic OECTs

2.5.1. OECTs fabrication

OECTs were fabricated as discussed in **Paragraph 2.3.1**. A microfluidic channel was created and glued on the OECTs as discussed in **Paragraph 2.3.1.1**, with a rectangular shape, 17 mm long, 4 mm wide, and 0.4 mm high.

2.5.2. SLB preparation and formation

The lipid mixture consisted of 100 mol% of POPC (Avanti Polar Lipids), and 0.5% (mol/mol) of Texas Red 1,2-dihexadecanoyl-sn-glycero-3-phosphoethanolamine triethylammonium (Thermo Fisher, USA) salt as a fluorescent probe. The lipids were mixed in chloroform at a desired concentration. The chloroform was evaporated using nitrogen, and then under vacuum for 2 h. The resulted lipid thin film was rehydrated with a mixture of 70% v/v of water a 30% v/v of isopropanol to obtain 5 mg/mL as final concentration. The solution was vortexed and then sonicated on ice for 25 min. Finally, the suspension was extruded 15 times through a 100 nm pore polycarbonate membrane (Sigma-Aldrich, USA). Subsequently, a supported lipid bilayer (SLB) was obtained using the solvent-assisted lipid bilayer (SALB) method, where the SLB was formed into a microfluidic channel (**Paragraph 2.4.1**) by means of a solvent exchange procedure[258].

Prior the membrane formation, the OECT was treated with oxygen plasma (Diener electronic, Germany) at a pressure of 1 mbar (20 W, 2 min). The liposome solution was diluted with isopropanol/water mixture (3:7 v/v) to a final concentration of 0.5 mg/mL and incubated for 30 min inside the chamber. A buffer solution ($10 \times 10{-}3$ m Tris, $100 \times 10{-}3$ m NaCl, pH 7.5) was delivered into the microfluidic channel with a flow rate of 50 µL/min for 2 h to remove excess vesicles while forming the bilayer. SLB formation and characterization were carried out in cooperation with Chiara Ausilio and Claudia Lubrano, Tissue Electronics lab at the Italian Institute of Technology, Naples.

2.5.2.1. Fluorescence recovery after photobleaching

The fluidity of the bilayer was evaluated using the FRAP technique with a Leica TCS SP5 gated with stimulated emission depletion (STED) microscope (Leica Microsystems, Germany) equipped with a 25× water immersion objective. A 20 µm wide circular spot was bleached by 114 mW 592 nm laser beam for 1.3 s. The recovery of the photobleached spot was then monitored for 5 min. The fluorescence intensity of the spot was measured and normalized to a reference spot in each image. The normalized fluorescence intensity was fit with a Bessel function. The images were analyzed with ImageJ Radial profile tool which allowed the quantification of the fluorescence intensity along the radius of a selected area. The fluorescence intensity profiles at three different time points after bleaching (0 s, 60 s, and 5 min) were obtained by drawing a circle around the bleached area. The diffusion coefficient was obtained from the following equation: $D = \omega/4\tau 1/2$, where ω is the radius of the bleached spot and $\tau 1/2$ is the time required to achieve half of the maximum recovery intensity.

2.5.2.2. Atomic force microscopy

AFM measurements were carried out on Bruker Dimension Icon microscope (Bruker Corporation, USA) in tapping mode in hydrated condition both on bare OECT and on POPC bilayer. The ScanAsyst-Fluid probe (Bruker Corporation, USA) with a spring constant of 0.7 N/m, a tip radius of 5–20 nm, and resonance frequency of about 150 kHz was used. The average roughness parameters were calculated over 2 µm × 2 µm areas, using the built-in Nanoscope software.

2.5.3. Electrochemical characterization

EIS measurements were carried out with Autolab PGSTAT302N potentiostat (Metrohm Italiana S.r.l., Italy), in a two-electrode configuration, where the fabricated OECT was employed as working and sense electrode, while an Ag/AgCl was employed as reference and counter electrode. Measurements were performed by applying a sinusoidal signal with amplitude of 50 mV around a voltage offset of 0 V. The frequency range analysed spanned from 0.1 Hz to 1 MHz. A buffer solution (10 × 10−3 m Tris, 100 × 10−3 m NaCl, pH 7.5) was used as electrolyte.

EIS data fitting to a circuital model was performed by means of a custom Python script, relying on the ScyPy package to perform least square optimization algorithm, minimizing the error between the recorded data and the impedance response of the defined circuital model.

2.5.4. Gate current analysis

Gate current was analysed to extract the number of charges injected from the electrolyte to the polymeric channel, and the amount of charged retained inside the channel. The estimation of the charges was obtained by numerically integrating gate current over time. In particular, the gate current generated by a square voltage pulse at the gate terminal is characterized by two spikes, corresponding to the raising and to the falling edge of the gate bias. Such spikes are due to the gate-to-channel capacitive coupling. The first portion of the signal was integrated, allowing to obtain the injected charges (during pulsing), while the remaining part of the signal allowed to compute the charges returning from the channel to the electrolyte (**Fig. 2.4**). The difference between the two represented the number of charges retained inside the channel.

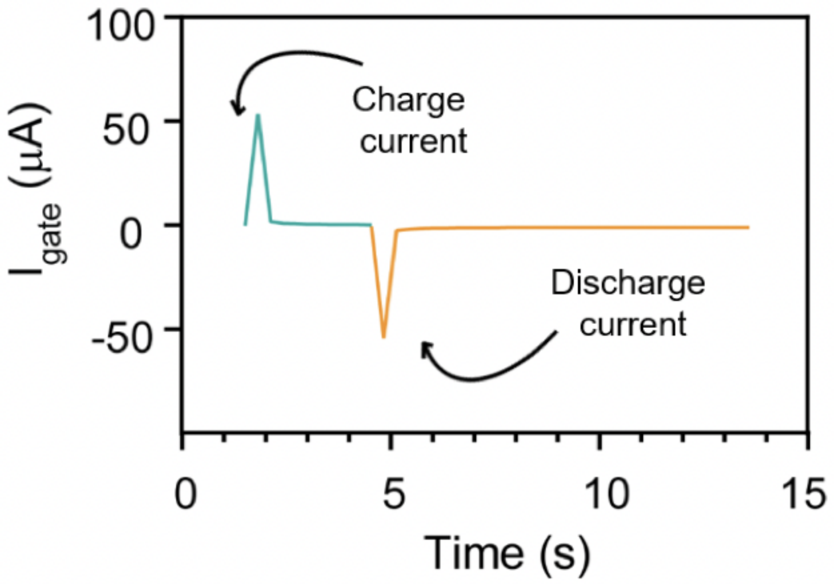

Figure 2.4 | Charge and discharge gate currents, used to compute injected and retained charges.

2.6. Biomimetic neuromorphic OECTs for LTP

2.6.1. OECTs fabrication

OECTs were fabricated as discussed in **Materials and Methods 2.5.1**.

2.6.2. SLB formation and confinement

Lipid preparation and formation was carried out as discussed in **Materials and Methods 2.5.2**. In addition, a new lipidic composition was introduced, consisting of POPC, cholesterol (chol, Avanti Polar Lipids, USA) and brain sphingomyelin (SM, Avanti Polar Lipids, USA) at a molar ratio of 1:1:1. SLB formation and characterization were carried out in cooperation with Chiara Ausilio and Claudia Lubrano, Tissue Electronics lab at the Italian Institute of Technology, Naples.

In addition, a protocol to confine the SLBs solely on the channel of the transistor was implemented as schematically shown in **Fig. 2.5**.

Here a microfluidic module was assembled by glueing two separate parts of the PDMS onto the OECT (**Fig. 2.5**, **i**). A protruding element of the second PDMS component divided the channel in two areas: SLB chamber and a second one, physically isolated (**Fig. 2.5**, **ii**). The protruding element (PDMS wall) was manually removed (**Fig. 2.5**, **iii**) and then glued (**Fig. 2.5**, **iv**) onto the substrate by use of biphasic glue (Picodent Twinsil), insulating the two chambers again. Subsequently, the SLB was formed (**Fig. 2.5**, **v**) as previously discussed (**Materials and Methods 2.5.2**). Lastly, the PDMS wall was manually and carefully removed, connecting the two chambers (**Fig. 2.5**, **vi**).

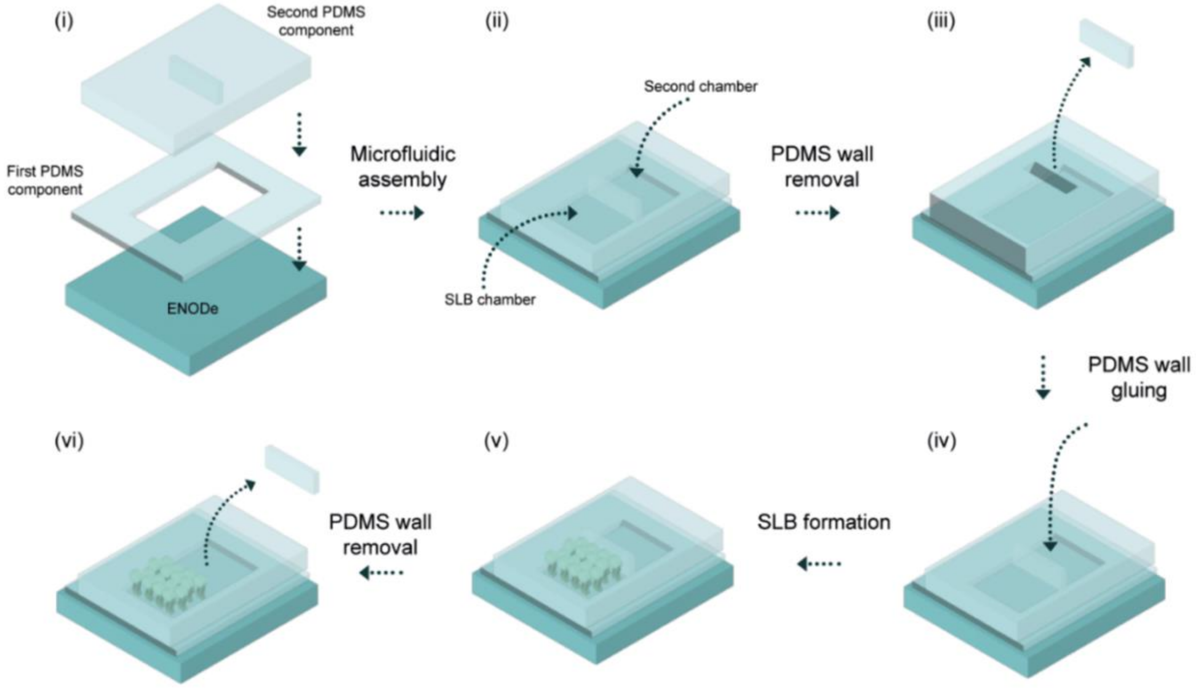

Figure 2.5 | SLB confinement protocol.

2.6.3. SLB characterization

Characterization was carried out by means of FRAP, AFM and EIS, as discussed in **Materials and Methods 2.5.2.1**, **2.5.2.2** and **2.5.3**.

2.6.4. Pavlov associative learning experiment

The Pavlov conditioning measurements were performed by implementing two different procedures. The first one was the learning, in which a neurotransmitter solution (DA, 5-HT or DA:5-HT) was used as electrolyte. In this case 3 square pulses were applied at the gate terminal with amplitude either 0.3 V or 0.4 V, to match the neurotransmitter oxidation potential[247]. In the second procedure, (washing) H_2O_2 was present in the electrolyte solution, and 6 voltage pulses (0.3 V amplitude) were applied at the gate terminal. PW was equal to 3 s, while the delay between pulses was set to 9 s, in all cases (DA, 5-HT, DA:5-HT and H_2O_2). V_{DS} was set to –0.2 V.

2.7. Closed-loop neuromorphic system

2.7.1. OECT fabrication

OECTs were fabricated as discussed in **Paragraph 2.4.1**, furtherly equipped with a y-shaped microfluidic channel (**Paragraph 2.4.1.1**). Closed-loop operations were carried out in cooperation with Daniela Rana, Tissue Electronics lab at the Italian Institute of Technology, Naples.

2.7.2. Robotic hand printing and driving

The hand was 3D printed using an open-source cable-driven design (InMoov, https://inmoov.fr/) using a commercially available 3D printer (Prusa MKS3+, https://www.prusa3d.com/). Hand closure and opening was achieved by driving servomotors (one per fingers), connected to cables, which were mounted on the motors so that the 0-degree position corresponds to completely open hand, while 90-degree position corresponds to a fully closed one. Commands were sent to the servomotors through a commercial microcontroller board (Arduino Uno board, https://www.arduino.cc/). A custom-made Arduino script was used to read data through serial interface from the electrical measurement setup and drive the servomotors.

The connection of all the parts composing the system is shown in **Fig. 2.6**. Here the channel current of the transistor was recorded and based on the output of the PID control system, a signal was sent to the actuators, *i.e.*, syringe pumps. After the application of each voltage pulse, the channel current value was sent to Arduino Uno board, which controlled five servomotors, assembled in the robotic hand. To this end, Arduino was connected to customized PID software (Arkeo Cicci Research srl) and the different motors were connected to the five analogic outputs of Arduino through a board. Each motor was connected through nylon thread to a single finger. When an electrical signal was applied, the angle of the motors varied, resulting in the wire pulling of the fingers. The servomotors were powered by a 7V supplier.

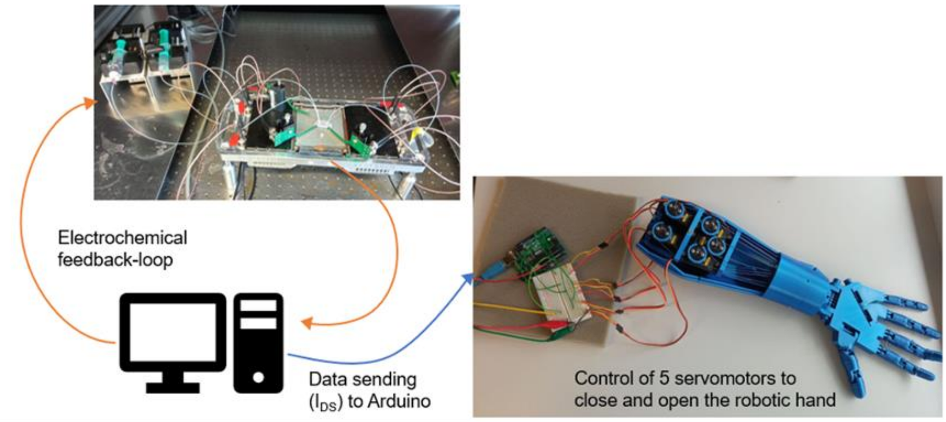

Figure 2.6 | Hand connection with the neuromorphic OECT and closed-loop schematic.

2.7.3. Control-loop execution

The variable controlled by the feedback-loop control system was the channel current of the neuromorphic OECT after the application of a square voltage pulse at the gate terminal. The workflow of the customized software based on lab view is the following:

1) Prior to the initiation of the experiment, these parameters were set as follows: the value of the drain constant voltage V_{DS} was 0.2V. The shape of the pulse to be applied as voltage gate was defined with 2s of ON time, 6s of OFF and 0.3V amplitude. The microfluidic pump that should work depending on the status of the controller was chosen by selecting the sign of the error. For positive errors, the pump with DA solution was activated whereas for negative errors the other pump would be activated. The maximum flow rate that the pumps can reach was set to 1 mL/min. The first desired value for channel current ISET was chosen in the tolerance regime of the device (known from the electrical characterization of the OECT, prior to the experiment) and the range of error was set in the order of µA.

2) As the experiment started the microfluidic channel of the OECT contained PBS solution only. The first pulse was applied to the gate and the channel current I_{DS} was measured after the removal of the pulse.

3) The error was calculated as: $e(t) = ISET - I_{DS}$, where both I_{DS} and ISET had negative values. If ISET > I_{DS}, a positive error resulted and the pump for DA solution was initiated with a flow rate that depended on the amplitude of the error and the set values for the proportional, integrative and derivative constants of the PID. If ISET < I_{DS}, a negative error was measured and the pump for the H_2O_2 solution was activated with a flow rate depending on the error value and the set values for the proportional, integrative and derivative constants of the PID.

Depending on the OFF time selected of the gate voltage, a new pulse was applied at the gate terminal of the transistor, inducing a variation of I_{DS} associated with the oxidation of DA or the action of H_2O_2. The workflow was then repeated starting from point (2), considering that ISET could be modified any time during the experiment.

Chapter 3: Results and Discussion

3.1. Neuromorphic sensing

Neuromorphic sensing refers to the design and characterization of sensors able to replicate some of processes occurring in the nervous system, when acquiring sensory information[259]. The advantage of such approach is to endow sensors with computation capabilities, mirroring what happens in the human body, that locally processes the sensory information at receptor level, before it is sent to the PNS, or to the CNS[260].

3.1.1. OECT-based neuromorphic pressure sensing

This thesis work first aimed at engineering a neuromorphic pressure sensor, exploiting a PEDOT:PSS-based OECT as transducing element. The sensor was designed and built starting from previous work[222], where a solid electrolyte was exploited as sensing element, connecting gate and channel of the transistor only upon pressure application (**Paragraph 1.3.2.3**).

This architecture was further optimized as it would typically feature a non-volatile behaviour, *i.e.*, the conductance state reached upon receiving a stimulus was not retained after the removal of the very same stimulus. Here, non-volatility was enforced, as a pressure stimulus induced the device to change its conductance state and retain it even after the removal of the stimulus, emulating LTP. To do that, an insulating layer (spacer) was designed to be embedded into the OECT architecture, as shown in **Fig. 3.1-a**. Such insulating layer was designed as a pored membrane, separating the solid electrolyte from the transistor channel. Each pore had hexagonal shape (**Fig. 3.1-b**) to densely fill the surface.

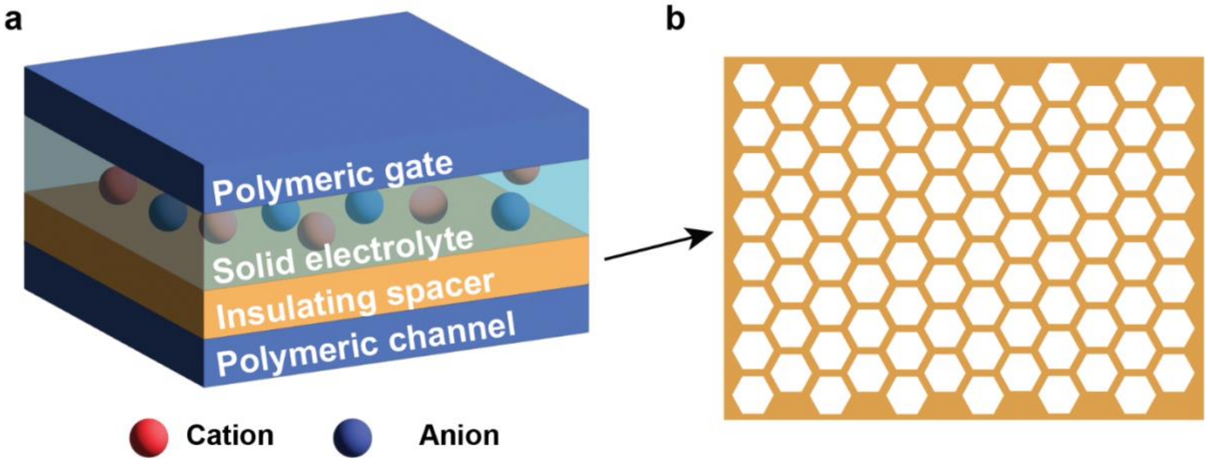

Figure 3.1 | **a**) Structure of the neuromorphic pressure sensor, made of four layers: transistor channel, insulating spacer, solid electrolyte and flexible gate. **b**) Design of the insulating spacer (front-view).

The working principle of the presented design can be divided into two phases: write mode and erase mode. Write mode ($V_{GS} > 0$ V) is shown in **Fig. 3.2**. Here, initially the OECT channel was free of ions and even by applying a potential at the gate terminal, gating will not occur, as the insulating spacer would behave like an open circuit, preventing physical contact between the electrolyte and the channel of the transistor (**Fig. 3.2-a**). Conversely, the application of a pressure will push the electrolyte through the pores of the insulating spacer (closed circuit), allowing for physical contact and, therefore, the gating of the transistor, with ion migrating from the electrolyte to the channel (**Fig 3.2-b**). Lastly, upon pressure removal, the insulating spacer would physically separate the channel and the electrolyte, resulting in an open circuit and achieving ion trapping in the channel of the transistor (**Fig. 3.2-c**). As a result, the conductance of the device would change in a non-volatile manner in response to an input stimulus, emulating LTP.

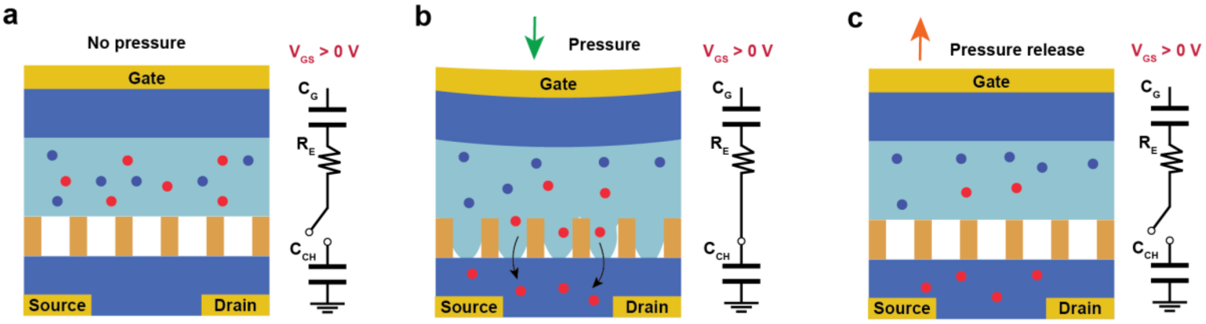

Figure 3.2 | Write mode of the neuromorphic pressure sensor. **a**) Initially no ions are present in the channel, and the insulating spacer results in an open circuit in the gate-to-channel equivalent circuit. **b**) Upon pressure application, the gate-to-channel circuit is closed, and transistor gating occurs. **c**) Upon pressure removal, ions are trapped in the polymeric channel as the insulating spacer physically separates the electrolyte from the channel.

In erase mode the gate voltage is held at 0 V. (**Fig. 3.3**). Here the solid electrolyte was physically separated from the channel and ions could not leave the polymer (**Fig. 3.3-a**). Upon the application of pressure, the gate-to-channel circuit was closed, allowing for ions to migrate back to the electrolyte (**Fig. 3.3-b**). Finally, upon stimulus removal, the spacer separated again electrolyte and channel, restoring the initial state of the device (**Fig. 3.3-c**).

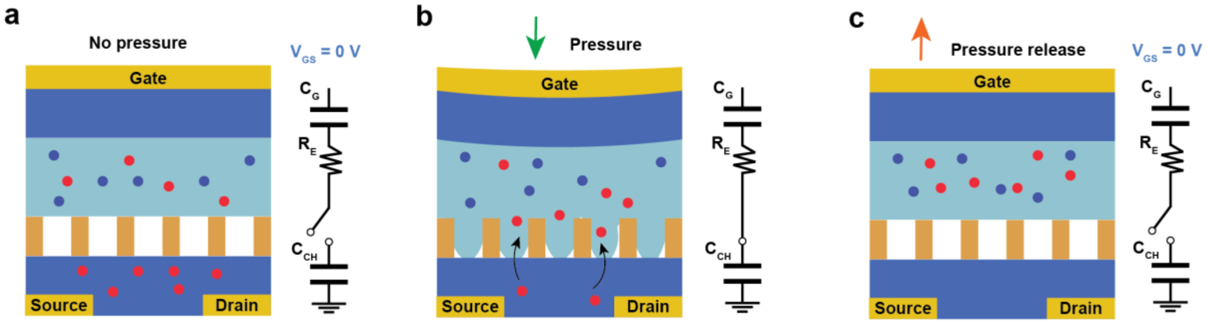

Figure 3.3 | Erase mode of the neuromorphic pressure sensor. **a**) Initially ions are trapped in the channel, and the insulating spacer results in an open circuit in the gate-to-channel equivalent circuit. **b**) Upon pressure application, the gate-to-channel circuit is closed, and ion migrate back to the electrolyte. **c**) Upon pressure removal, the initial state of the device is restored.

Before fabrication, numerical simulations exploiting finite elements method (FEM) were carried out (**Materials and Methods 2.1.1**), to confirm whether the solid electrolyte could penetrate through the pores of the insulating spacer, gating the transistor. Only the mechanical part of the device was simulated, in which both spacer and channel are modelled as rigid body, while the electrolyte was designed as an elastic linear body (**Fig. 3.4-a**). In addition, to preliminary modelling was performed using an axisymmetric design to simulate a 3D device with a 2D approximation. The amount of surface of the electrolyte in contact with the channel of the transistor was extracted from the simulations, allowing to compute the contact surface as a function of the applied pressure (**Fig. 3.4-b,** spacer size 1000 µm, uniform pressure).

In addition, different hole sizes and different pressure areas were simulated (**Fig. 3.4-c** and **d**, respectively).

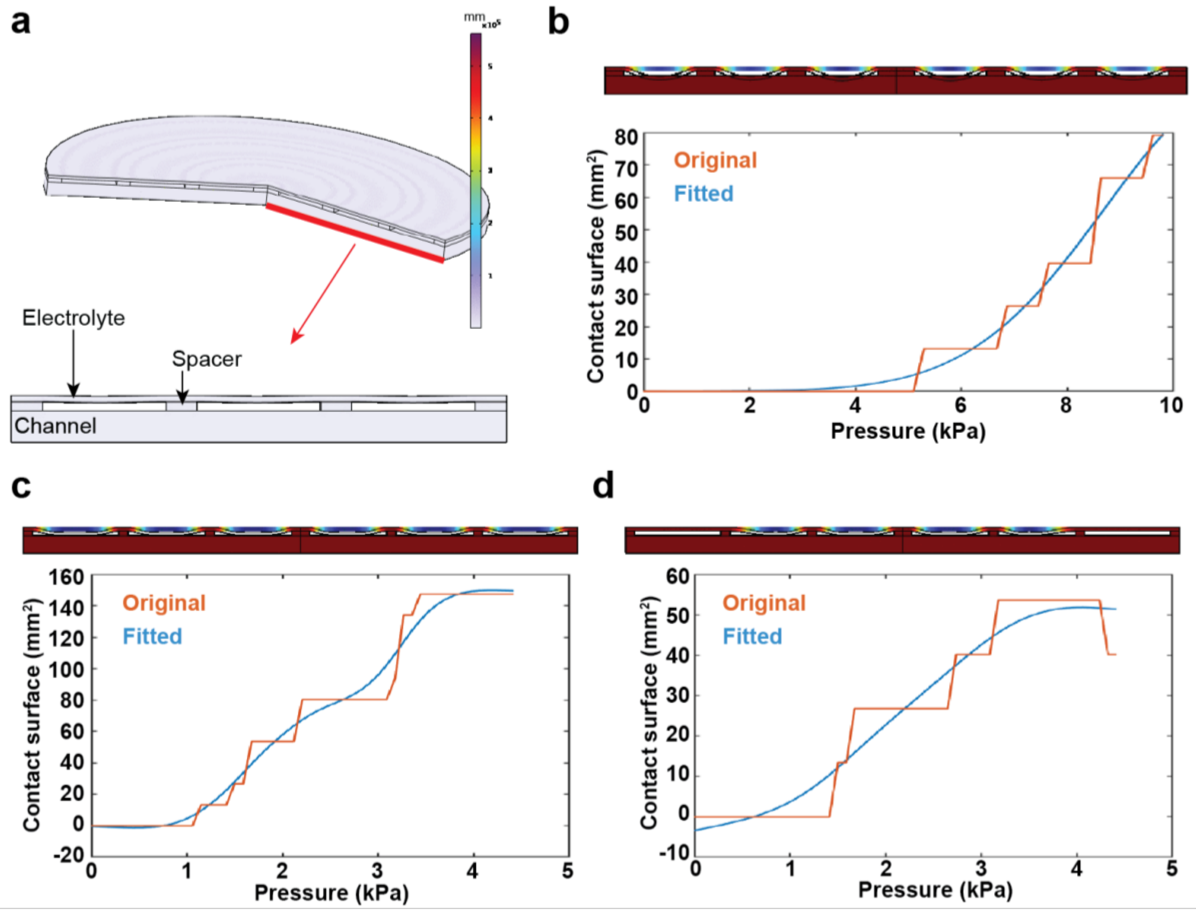

Figure 3.4 | FEM simulations of pressure application. **a**) Simulated geometry. **b**) Pressure application and electrolyte deformation simulation using an insulating spacer with 1000 µm holes and 300 µm height. In addition, contact area as function of the applied pressure is shown. **c**) Numerical simulation with an insulating spacer with 500 µm hole size, and equivalent surface contact area. **d**) Numerical simulation of a pressure applied only in the middle of the device using an insulating spacer with 500 µm holes and 300 µm height, and area contact.

As expected, the size of the pores influenced the amount of contact surface and thus the channel capacitance that would eventually charge the transistor channel. On the one hand, a larger pore size would result in larger channel capacitance, increasing the switching speed of the transistor. On the other hand, the dynamic range of pressure that could be sensed with the transistor would decrease with increasing pore size. Eventually, pore size was set to 40 µm, while spacing between holes was set to 20 µm.

Then, the OECT for pressure sensing was fabricated as discussed in **Materials and Methods 2.1.2**, in cooperation with the Lussem group, at UniBremen. In brief, the transistor channel was made of PEDOT:PSS, with dimensions 500x500 µm^2 (L x W). Static characterization was carried out, *i.e.*, transfer and output curve (**Materials and Methods 2.1.5**), in the Salleo group at Stanford University. A planar electrode made of PEDOT:PSS (same size of the channel) was employed as gate. Transfer curves were obtained by sweeping the gate potential V_{GS} (from 0 to 0.6 V, with voltage steps of 50 mV), while measuring the channel current I_{DS}, at a fixed drain-source voltage V_{DS} (-0.1, -0.2, -0.3 and –0.4 V). Output curves were recorded by sweeping the drain-source voltage V_{DS} (from –0.1 to –0.6 V, with a voltage step of –50 mV), while fixing the gate potential V_{GS} (-0.15, -0.30, -0.45 and –0.60 V), and measuring the channel current I_{DS}. **Fig. 3.5-a** displays a typical output curve of the above-mentioned devices. Here, the absolute value of I_{DS} decreased when increasing V_{GS}, as the cations were being pushed from the electrolyte to the channel. The same behaviour was observed in transfer curves (**Fig. 3.5-b**) and the ratio between the current in the ON and OFF states (ON/OFF ratio) was barely reaching one order of magnitude ($< 10^1$). Such limited switching efficiency was expected, as the gate and the channel had same physical dimension whereas an efficient gating can occur only when the surface of the gate is greater than the channel's one as discussed in **Paragraph 1.3.2.1**. Measurements were carried out in NaCl [100 mM] liquid electrolyte (**Materials and Methods 2.1.3**).

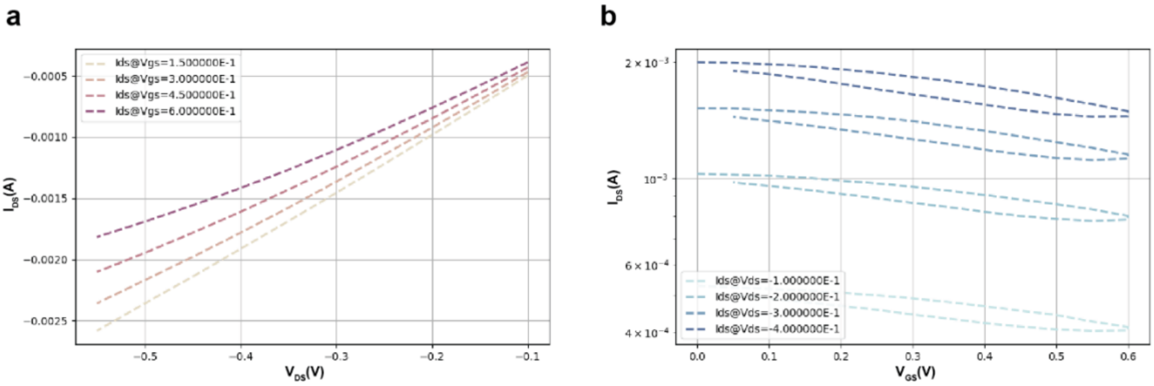

Figure 3.5 | **a**) Exemplary output curve of an OECT, featuring both channel and gate electrode of PEDOT:PSS, and size 500x500 μm^2. Drain-source voltage bias was swept from –0.1 to –0.6 V, while gate voltage was fixed at 0.15, 0.30, 0.45 and 0.6 V (light to dark pink). **b**) Transfer curve of the same PEDOT:PSS-based OECT, at different V_{DS} values (-0.1, -0.2, -0.3 and –0.4, light to dark blue).

Subsequently, a solid electrolyte consisting of poly(vinylidene fluoride-co-hexafluoropropylene) (PVDF-co-HFP) ionic conductive polymer and ionic liquid, 1-ethyl-3-methylimidazolium bis(trifluoromethylsulfonyl)amide ([EMIM][TFSI]) was fabricated as discussed in **Materials and Methods 2.1.3**. The gate electrode employed in this case was a PEDOT:PSS-coated gold electrode deposited on a flexible polyimide film (**Materials and Method 2.1.4**).

The application of a pressure stimulus in write mode is shown in **Fig. 3.6**. Here, V_{DS} was set to –0.2 V, while the gate electrode was biased with 0.5 V. Notably, before applying any pressure, the insulating spacer behaved as an open circuit (**Fig. 3.6-i**, yellow trace). As a result, despite the applied gate voltage bias, the channel current was stable (no gating of the OECT). Then, a weight of 10 g (yielding for 1032.3 Pa) was positioned on the gate electrode. As observable, the equivalent circuit was closed and the transistor gated (**Fig. 3.6-ii**, orange trace), and therefore ions penetrated the channel of the OECT, thus decreasing I_{DS}. Lastly, when the weight was removed, the insulating spacer behaved as an open circuit again (**Fig. 36-iii**, yellow trace) and ions were trapped in the channel, achieving a non-volatile conductance change.

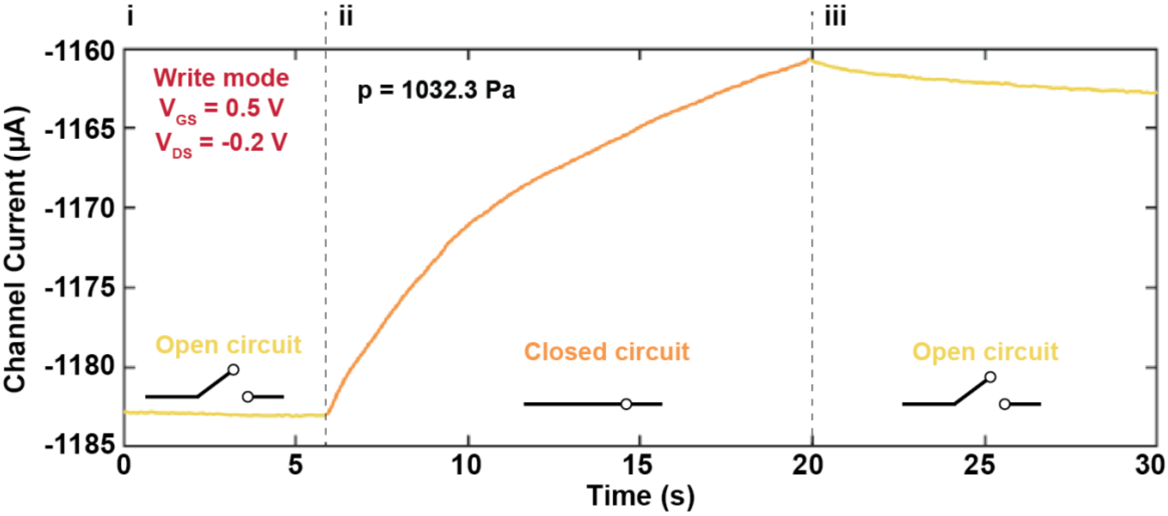

Figure 3.6 | Measurement performed in write mode (V_{GS} = 0.5 V). **i**) The insulating spacer behaves like an open circuit, preventing any gating. **ii)** Upon pressure application, the gate-to-channel circuit is closed, and ion injection occurs. **iii**) Upon pressure removal, the ions are trapped in the channel, as the gate-to-channel to circuit is open again, not allowing for ions to migrate back to the electrolyte.

Subsequently, erase mode measurements were performed (**Fig. 3.7**): here ions were already trapped into the channel because of the previously achieved writing operation. Initially, even if the gate voltage bias was held at 0 V, ions could not migrate back to the electrolyte as the insulating spacer physically opened the gate-to-channel circuit (**Fig. 3.7-i**, yellow trace). Upon application of pressure (1032.3 Pa), gating occurred and ions could migrate back from the channel to the electrolyte, restoring the initial state of the device (**Fig. 3.7-ii**, orange trace).

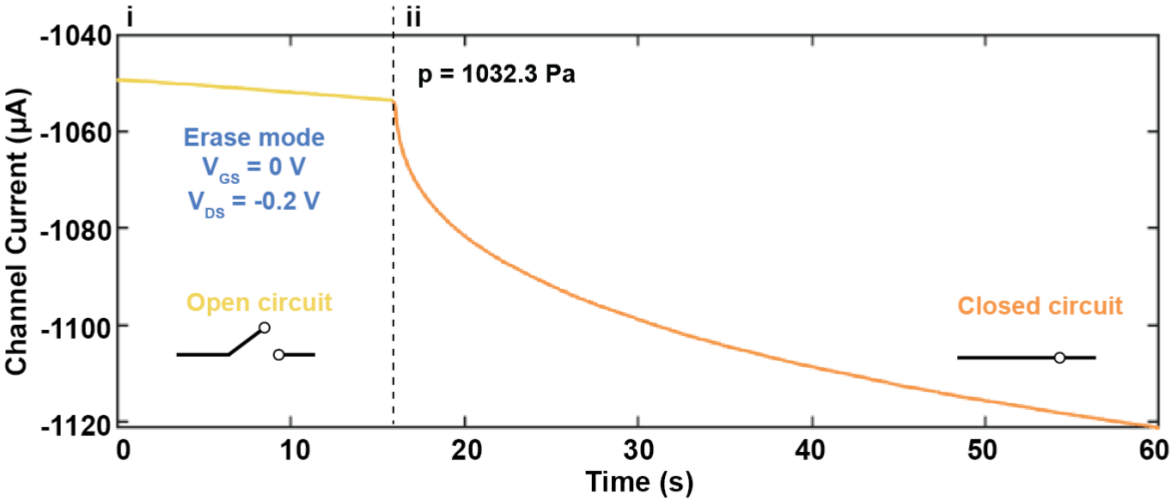

Figure 3.7 | Measurement performed in erase mode (V_{GS} = 0 V). **i**) The insulating spacer behaves like an open circuit, preventing the discharge of the channel. **ii**) Upon pressure application, the gate-to-channel circuit is closed, and ion migrate back to the electrolyte.

Lastly, measurements alternating write and erase modes were performed (**Fig. 3.8**). Initially, writing operation was performed ($V_{GS} > 0$ V) by applying different pressures (624.5, 1032.3, 1730.0 and 2168.5 Pa) alternated with by 60 s of no pressure (**Fig. 3.8-i**). Every time a pressure stimulus was applied, the gate-to-channel circuit was closed (**Fig. 3.8-i**, orange trace) effectively gating the transistor. On the contrary, when no pressure was applied, the equivalent circuit was open thus stabilizing the conductance level of the device (**Fig. 3.8-i**, yellow trace). In erase mode (V_{GS} = 0 V), the opposite behavior could be observed: ions previously trapped could migrate back to the electrolyte upon pressure application (**Fig. 3.8-ii**).

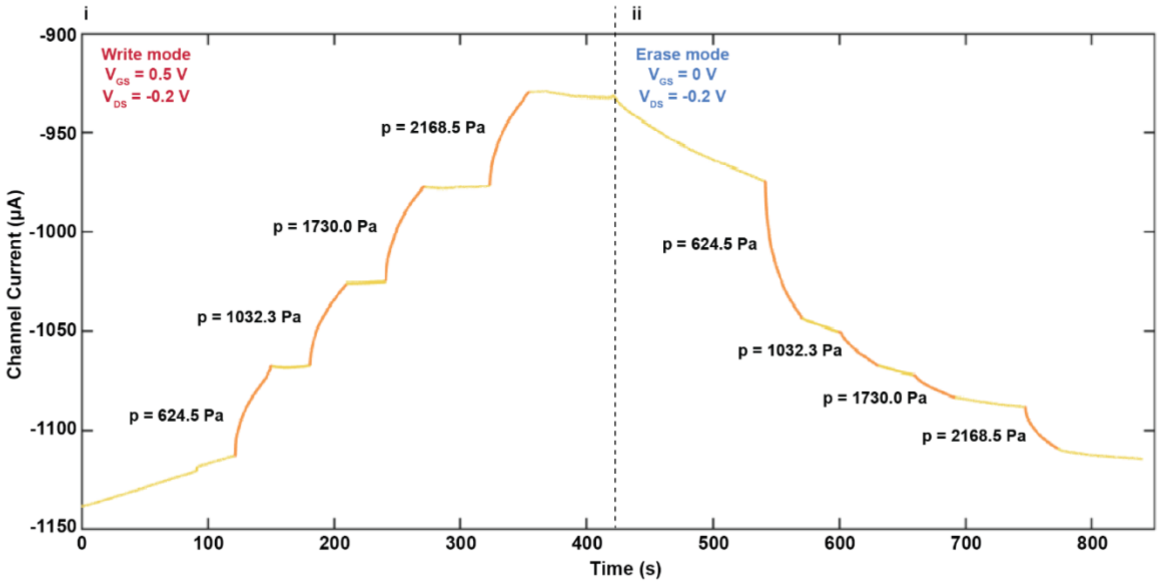

Figure 3.8 | Continuous measurement alternating write ($V_{GS} > 0$ V) and erase mode ($V_{GS} = 0$ V). **i**) Write mode. Here ions migrate from the electrolyte to the channel every time pressure is applied. Charge trapping occurs upon pressure removal. **ii**) Erase mode. Upon pressure application, the transistor channel can discharge.

Further details on pressure-driven measurements can be found in **Materials and Methods 2.1.6**.

The neuromorphic pressure sensor exhibited non-volatile sensing, emulating LTP, as upon stimulus application the conductance of the device was changed. The device did not demonstrate high sensitivity as there was no difference in gating when the different pressures were applied. Such low sensitivity was ascribed to the flat solid electrolyte (**Materials and Methods 2.1**), however this could be increased by patterning the solid electrolyte with protruding microstructures[220,221]. Notably, the low sensitivity was due to limited contact area upon pressure application and this might be advantageous in neuromorphic applications, as the conductance of the device slowly changed, achieving an analogue modulation as in biological synapses, synaptic weights are updated in analogue fashion, *i.e.*, they change with continuity. A trade-off must be sought between sensitivity (*i.e.*, tuning the size of the protruding microstructures) and analogue conductance modulation.

3.1.2. Optoelectronic neuromorphic OECTs

Light perception is pivotal in humans, as most of the sensory information we use comes from the sense of vision, that is processes as discussed in **Paragraph 1.1.3.2**. To build a neuromorphic light sensing platform, an OECT was modified through chemical functionalization. By endowing a PEDOT:PSS-based transistor with a photosensitive material, a neuromorphic organic photoelectrochemical transistor (OPECT) was demonstrated[261].

The photosensitive material was azo-tz-PEDOT:PSS (synthetized as discussed in **Materials and Methods 2.2.1**) and was employed as gate electrode material in a planar OECT (**Fig. 3.9-a**, **Materials and Methods 2.2.2**). The whole synthetic procedure was carried out in cooperation with Federica Corrado, Tissue Electronics lab at the Italian Institute of Technology, Naples. The peculiarity of this material was a surface coating with azobenzene moieties, *i.e.*, molecules able to switch between two physical conformations (namely cis and trans) upon stimulation. In this case, azo-tz-PEDOT:PSS could switch from trans to cis conformation upon stimulation with UV light ($\lambda = 365$ nm, **Fig. 3.9-b**).

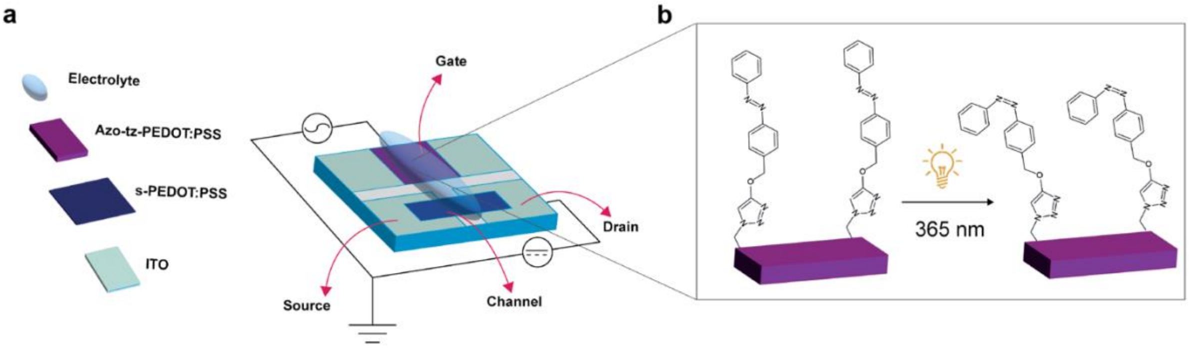

Figure 3.9 | Schematic of the fabricated OPECTs. **a**) Three-terminal device structure with channel made of commercially available PEDOT:PSS, and gate made of the synthetized azo-tz-PEDOT:PSS. **b**) Schematic of trans-cis isomerization of the azobenzene moieties of the obtained film. Adapted from [261].

The functionality of the trans-cis isomerization upon light exposure was evaluated after the embedding of the moieties on the surface of the film through UV-visible spectroscopy (**Fig. 3.10-a**). Here the spectrum showed an adsorption peak at 347 nm, typical of the trans-azobenzene isomer, and a smaller peak at 434 nm, related to the azobenzene in cis configuration (**Fig. 3.10-a**, solid line). Upon light exposure ($t = 5$ min, $\lambda = 365$ nm, 6 W), a decrease in the trans-isomer related peak was observed, while the peak at 434 nm slightly increased (**Fig. 3.10-a**, dashed line), in accordance with literature[262].

Furthermore, as PEDOT:PSS was chemically treated to achieve azobenzene functionalization, morphological characterization through AFM was carried out before and after the functionalization procedure (**Fig. 3.10-b**, **Materials and Methods 2.2.3**). The typical globular structure of the PEDOT:PSS surface can be observed before functionalization in **Fig. 3.10-b**, **i**, while a minor smoothening was observed after the surface functionalization (**Fig. 3.10-b**, **ii**). In particular, the root mean square (RMS) roughness of the surface changed from 15.7 ± 2.0 nm (pristine PEDOT:PSS) to 10.5 ± 3.1 nm (azo-tz-PEDOT:PSS).

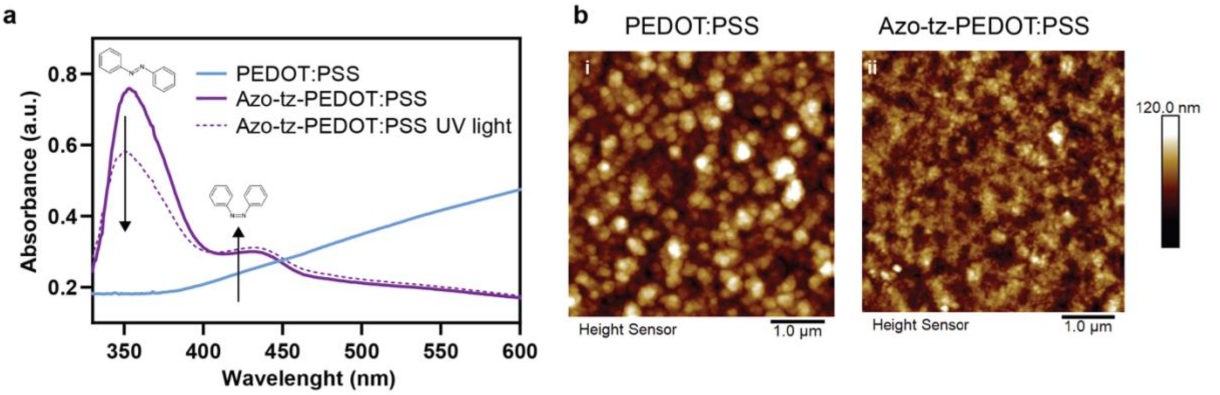

Figure 3.10 | **a**) UV-Visible spectrum of azo-tz-PEDOT:PSS before and after light irradiation (solid and dashed line, respectively). Trans-azobenzene isomer peak is found at 347 nm, while cis-related peak is found at 434 nm. **b**) Morphological characterization of pristine PEDOT:PSS (**i**) and azo-tz-PEDOT:PSS (**ii**) through AFM. Adapted from [261].

Subsequently, electrochemical characterization (**Materials and Methods 2.2.4**) was carried out by means of cyclic voltammetry (CV) and electrochemical impedance spectroscopy (EIS). The former (**Fig. 3.11-a**) showed a characteristic peak at –0.12 V, ascribable to the oxidation of the azobenzene N=N bond and second one at 0.57 V, that may be correlated to the oxidation of the azobenzene[263]. Upon light irradiation (**Fig. 3.11-a**, dashed line), the hysteresis of the azo-tz-PEDOT:PSS film showed a significant decrease, due to. the trans-to-cis isomerization, as the cis-azobenzene created an additional impediment to charge flow. In addition, a control measurement was carried out with a pristine PEDOT:PSS film (**Fig. 3.11-a**, solid and dashed blue lines).

Later, EIS measurements were employed to evaluate the capacitance of both PEDOT:PSS and azo-tz-PEDOT:PSS films (**Fig. 3.11-b**, blue and violet lines, respectively). The capacitance of the latter was characterized by a lower value, as the layer of azobenzene molecules acted like a spacer between the CP and the electrolyte reducing the existing EDL[264].

Lastly, the output curves of the transistor were recorded using an azo-tz-PEDOT:PSS film as gate electrode (**Fig. 3.9-a**) with and without UV light irradiation (**Figure 3.11-c**, solid and dashed lines, respectively), by sweeping V_{DS} from 0 V to –0.8 V with a voltage step of – 50 mV at different values of V_{GS} (0.2, 0.4, 0.6 and 0.8 V). Interestingly, the channel current I_{DS} was lower when the transistor was irradiated with UV light ($t = 5$ min, $\lambda = 365$ nm, 6 W), suggesting that the light exposure elicited a non-reversible de-doping of the transistor channel. Further details on OPECT steady state characterization can be found in **Materials and Methods 2.2.5**.

The proposed mechanism was that a charge transfer between azobenzene molecules and PEDOT:PSS, upon light stimulation. Density functional theory and time-dependent density-functional theory (DFT/TD-DFT) computation were performed (in collaboration with Pavone group, UniNa), predicting the energy diagram (cis conformation) shown in Fig. **3.11-d**. The HOMO is localised on the PEDOT backbone, while the LUMO is localised on the azo-tz moiety. Here, upon UV light irradiation, the photoexcited electron can be transferred from the LUMO (on the azo-tz) to the HOMO on the PEDOT backbone. As a result, spatial charge separation would occur, trapping positive charges on the azobenzene side and positively polarizing the gate electrode (transistor gating). In addition, the charge transfer mechanisms were found to be light-intensity dependent, as shown in **Fig. 3.11-e** and **f**, where output and characteristic curves of the azo-tz-PEDOT:PSS-based transistors are shown as a function of the light intensity (100% = 2.8 W/cm^2, 60% = 1.7 W/cm^2, 20% = 0.56 W/cm^2, violet, red and yellow lines, respectively).

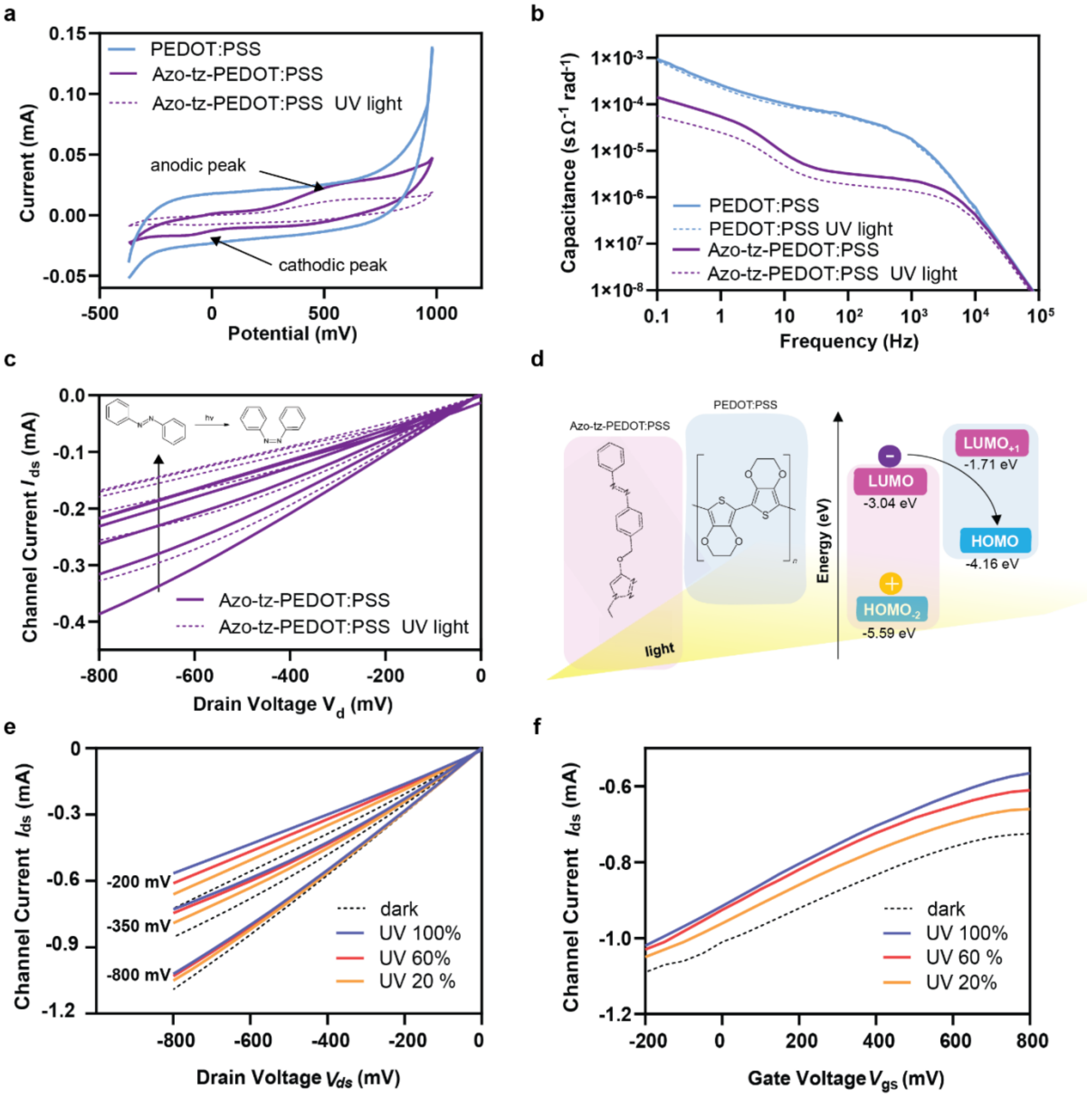

Figure 3.11 | **a**) Cyclic voltammetry of azo-tz-PEDOT:PSS film, before and after light exposition (solid and dashed lines, respectively). In addition, a control measurement performed on pristine PEDOT:PSS is reported (blue lines). **b**) Film capacitance extracted from EIS measurements on both azo-tz-PEDOT:PSS and PEDOT:PSS (Violet and blue lines, respectively). Measurements were performed before and after light exposure (solid and dashed lines, respectively). **c**) Transistor output curves measured using azo-tz-PEDOT:PSS as gate electrode material, before and after UV light irradiation (solid and dashed lines, respectively). **d**) Chemical structure and energy levels of the azo-tz-PEDOT system obtained from DFT/TDDFT calculations **e-f**) Output and transfer curves as a function of the UV light intensity. Adapted from [261].

To clarify such mechanism, transient measurements were carried out (**Materials and Methods 2.2.6**), decoupling electrical and optical stimuli (**Fig. 3.12**). Light pulses were employed (60 s ON, 60 s OFF), while keeping V_{GS} = 0 V and V_{DS} = -0.2 V. Both the channel current I_{DS} (**Fig. 3.12-a**) and the gate current I_{GS} (**Fig. 3.12-b**) were recorded. Upon light irradiation, the gate current increased (**Fig. 3.12-a**, violet solid line) to then decay back upon stimulus removal (**Fig. 3.12-a**, black dashed line). Therefore, in agreement with the previously proposed mechanism, photoexcitation occurred causing a positive polarization of the gate electrode, gating of the OPECT, with the subsequent injection of cations from the electrolyte to the channel. The flow of cations induced by the positive gate polarization, reflected into channel current (conductance) decrease (**Fig. 3.12-b**), *i.e.*, PEDOT:PSS de-doping[185]. Notably, the gating mechanisms induced by electrical and optical stimuli were independent. Indeed, in OECTs electrical gating induces a capacitive gate current with a capacitive peak and fast decay towards zero. Conversely, the light exposure generated a faradic current, as charges were continuously transferred from the gate to the electrolyte during the whole stimulation without showing a significant decay (**Fig. 3.12-a**).

Such current generation was in agreement with the mechanism previously elaborated by DFT/TDDFT calculations (**Fig. 3.11-d**): upon light exposure, negative charges were transferred from the LUMO (azo-tz) to the HOMO (PEDOT backbone) while holes were kept in the azo-tz. As a result, the gate/electrolyte interface potential decreased inducing a faradic current in the electrolyte. To preserve electroneutrality, the channel/electrolyte potential increased then de-doping the polymeric channel[206].

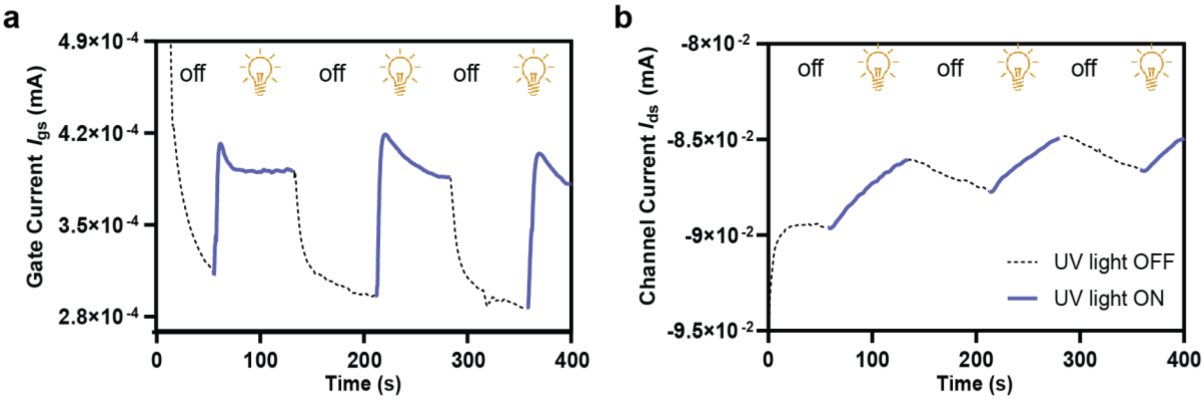

Figure 3.12 | **a**) Transient measurement of the gate current of the OPECT, while applying UV light pulses (60 s on, violet solid line and 60 s off, black dashed line). V_{GS} = 0 V and V_{DS} = -0.2 V. **b**) Channel current versus time, recorded while applying UV light pulses (60 s on, violet solid line and 60 s off, black dashed line). V_{GS} = 0 V and V_{DS} = -0.2 V. Adapted from [261].

Exploiting the presented photoexcitability, the OPECT was coupled to an organic resistor (connected in series) to emulate the OFF vertical pathway of the human retina (**Paragraph 1.1.3.2**). A comparison between the obtained circuit and the retina structure is provided in **Fig. 3.13-a**. Here, the gate electrode of the OPECT, acted as photoreceptors, the electrolyte/channel interface as the bipolar cells (BCs) layer, and the organic resistor (spin coated PEDOT:PSS,

Materials and Methods 2.2.2.2) mimicked ganglion (CGs). The output voltage of the circuit (V_{GC}) was determined by the conductance of the OPECT channel.

Under dark condition, the artificial GCs fired continuously (output voltage V_{GC}), as it happens in the biological counterpart where depolarization is induced by continuous glutamate release (vertical OFF pathway, **Paragraph 1.1.3.2**). The lateral pathway (photoreceptor gain adjustment) was reproduced by the application of a voltage bias (V_L) at the gate terminal of the OPECT. Indeed, by increasing VL up to 0.3 V (**Fig. 3.13-b**, **i** green box), the output voltage VGC decreases (- 15%, **Fig. 3.13-b**, **ii** green box) and the amplitude of the output voltage so reached was defined as firing threshold (**Fig. 3.13-b**, **ii** horizontal black solid line).

Upon light exposure the equivalent CGs stopped firing (**Fig. 3.13-b**, **iii**, voltage amplitude variation -18 %), as the threshold was not crossed anymore. Such process resembled the hyperpolarization of GCs, induced by the absence of glutamate release in the OFF vertical pathway. Moreover, further regulation was granted by introducing the equivalent lateral pathway (V_L = 0.3 V) and reducing the output voltage of -20% (total variation –43%, **Fig. 3.13-b**, **iii**).

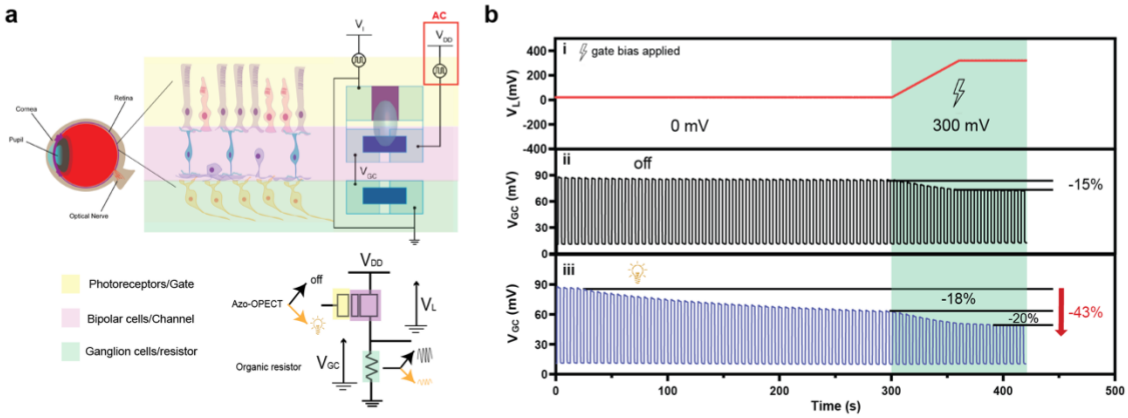

Figure 3.13 | **a**) Retina schematics and visual pathways, along with the equivalent artificial circuit, proposed to emulate the OFF vertical pathway. **b**) Emulation of the OFF vertical pathway. **i**) retina lateral pathway emulation, with the application of a regulation voltage (up to 0.3 V). **ii,iii**) OFF vertical pathway, with electrical train pulses application in dark and light conditions, respectively. Adapted from [261].

Further details on the measurements can be found in **Materials and Methods 2.2.7**.

After bio-emulation, neuromorphic features of the developed OPECT were investigated. Firstly, the combined effect of light and voltage were evaluated (**Fig. 3.14-a**). The electrical input was chosen as a train of positive square voltage pulses (amplitude 0.3 V, pulse width (PW) = 5s), while the drain-source bias was held at –0.2 V. Light stimulus was applied for 6 min ($\lambda = 365$ nm), eliciting a conductance decrease of $\Delta G\% = 12.5 \pm 3.1$ (**Fig. 3.14-a**, blue arrow).

After the removal of the light stimulus, the channel conductance increased ($\Delta G\% = -2.7 \pm 3.1$, **Fig. 3.14-a**, red arrow), but without recovering the initial state of the device. The first variation (conductance decrease) was identified as conditioning (LTP), while the second was identified as extinction (LTD).

To check a possible correlation between the two types of stimuli, the neuromorphic behaviour was investigated by varying voltage pulse width (PW) and light intensity (**Fig. 3.14-b**, **i**, **ii** and **iii**, **Materials and Methods 2.2.8**). Conductance variation was then computed and plotted both as a function of either the light intensity (**Fig. 3.14-c**) or the PW (**Fig. 3.14-d**). Interestingly, while ΔG showed a linear relationship with light intensity, no dependence on PW was found. Here, we could conclude that there was no correlation between electrical and optical stimulation, and that the OPECT was decoupling the two mechanisms.

Therefore, while light stimulation could be used to reproduce LTP/LTD (**Fig. 3.14-a**), the electrical input could be exploited to recapitulate STP, as shown in Fig. **3.14-e**, where PPF was achieved (**Materials and Methods 2.2.8**) without any significant difference between light and dark conditions.

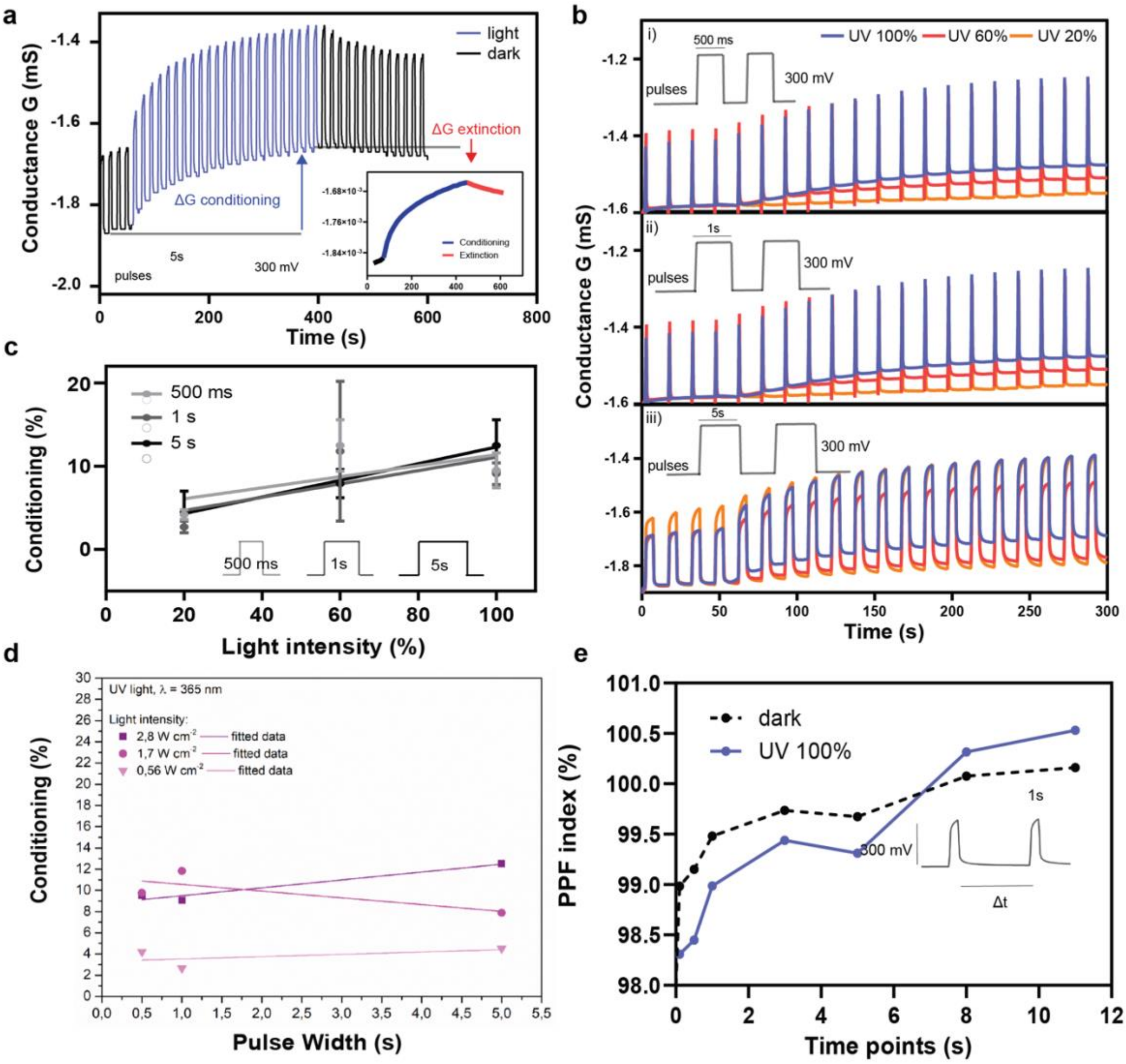

Figure 3.14 | **a**) Combined light and optical stimulation of the OPECT, with definition of conditioning and extinction. **b**) Variation of PW and light intensity: **i**) PW = 0.5 s and amplitude 0.3 V, light intensities 100%, 60% and 20%. **ii**) PW = 1 s and amplitude 0.3 V, light intensities 100%, 60% and 20%. **iii**) PW = 5 s and amplitude 0.3 V, light intensities 100%, 60% and 20%. **c**) Conditioning as function of the light intensity. **d**) Conditioning as function of the PW. **e**) PPF index computed in both light and dark conditions. Adapted from [261].

Lastly, the possibility of reverting the light-induced current decrease was investigated. It was found that the application of a negative electrical pulse at the gate terminal, could (almost) restore the initial level of conductance of the device (**Fig. 3.15-a**, V_{GS} = -0.3 V, 10 min).

To properly explain the underlying mechanism, a series of consecutive pulses with increasing negative amplitude were supplied (from –20 to –120 mV, with a voltage step of 20 mV, **Fig. 3.15-b**, **i**). Under dark conditions (**Fig. 3.15-b**, **ii**), the photo-induced non-volatile conductance modulation was not observed, and the effect of negative gate voltage bias was completely reversed. Conversely, under light irradiation (**Fig. 3.15-b**, **iii**), the photo-induced conductance modulation was observed only when the electrical negative bias was negligible (-20 mV and –40 mV). Indeed, when the voltage bias became more negative (from –80 mV to –120 mV), the photo-induced effect could not be observed anymore. Such measurements highlighted that there was a competing effect between light stimulation and negative voltage. In particular, the latter was predominant when the stimulation amplitude increased.

A mechanism is proposed in **Fig. 3.15-c**. Azobenzene reduces to hydrazobenzene when a voltage between –20 mV and –350 mV is applied, as shown by CV measurements (**Fig. 3.11-a**). In such reaction, two protons are required. Therefore, such negatively charged azobenzenes, to keep electroneutrality, attracted protons from the channel. On the other hand, PSS- counterions stripped of a proton, could restore the former interaction with PEDOT+, doping it again and restoring the former channel conductance.

Exploiting the antagonistic mechanism of light- and negative voltage-induced modulation, a synaptic optoelectronic memory was envisioned and built. Information, *i.e.*, a stable conductance state, could be written with light while it could be erased with negative voltage, as shown in **Fig. 3.15-d** (**Materials and Methods 2.2.9**).

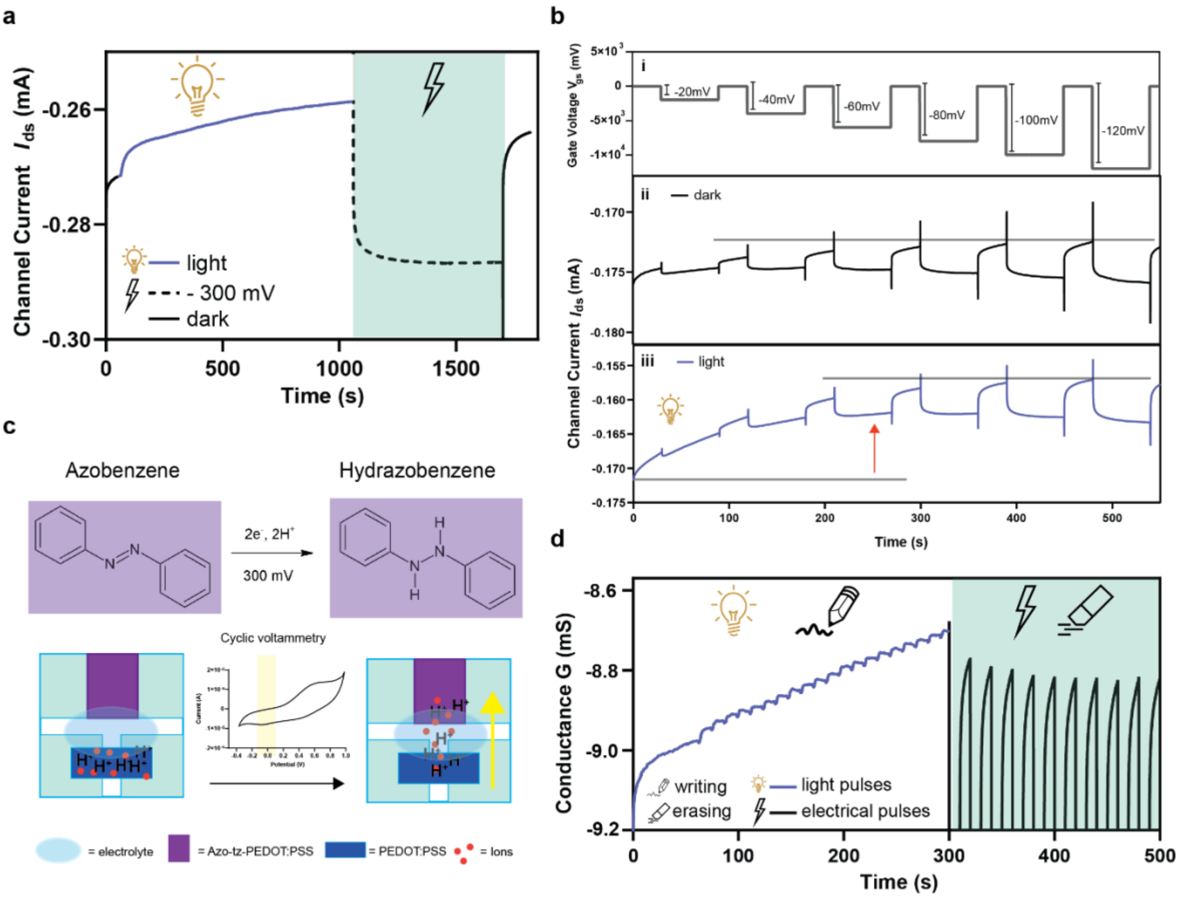

Figure 3.15 | **a**) Conditioning achieved with 500 light pulses (λ = 365 nm, PW = 1 s, Δt = 1 s, blue solid line) and extinction induced by negative voltage pulse (black dashed line, green box). **b**) Competing effect of light and negative voltage: **i**) Applied negative voltage pulses **ii**) Channel current under dark condition (V_{DS} = -0.2 V). **iii**) Channel current under light irradiation (λ = 365 nm, V_{DS} = -0.2 V). **c**) Proposed mechanism for negative voltage-mediated PEDOT:PSS doping. **d**) Optoelectronic memory measurement. Write operation with 20 light pulses (λ = 365 nm, PW = 2 s, Δt = 10 s, blue solid line) followed by an erase operation with a negative voltage pulses train (VGS = -0.3 V, PW = 3 s, Δt = 10 s, black solid line, green box). Adapted from [261].

Lastly, by exploiting write/erase operations, Atkinson-Shiffrin brain memory model[265] was demonstrated, in which the human memory is organized into three separate components: sensory, short- and long-term memory.

When a sensory information is received, it is stored in the sensory memory, where it would persist for a very short period, before being forgotten. By paying attention to such stimulus, the stimulus can be moved to the short-term memory. Lastly, through a rehearsal process, *i.e.*, iteration of the stimulus, the short-term memory can become a long-term one. Atkinson-Shiffrin theory was emulated in **Fig. 3.16**. The sensory information input (positive electrical pulse at the gate terminal, V_{GS} = 0.2 V, PW = 3 s, and Δt = 15 s) was applied and rapidly forgotten without rehearsal process (purple boxes), and the channel current did not reach the memory threshold (**Fig. 3.16**, **i**). The process of attention was emulated by a low intensity light stimulus (20% = 0.56 W/cm^2): here, the channel current crossed the memory threshold and the information was shifted from sensory to short-term. However, it was forgotten after the application of negative voltage pulses ($V_{GS} = -0.3$ V, PW = 5 s, and Δt = 12 s)(**Fig. 3.16**, **ii**). Lastly, transition from short- to long-term memory through rehearsal was emulated by applying a = 2.8 W/cm^2 high intensity light stimulus (100%). After such stimulus, a negative voltage pulse could not erase the information, proving long-term memory (**Fig. 3.16**, **iii**).

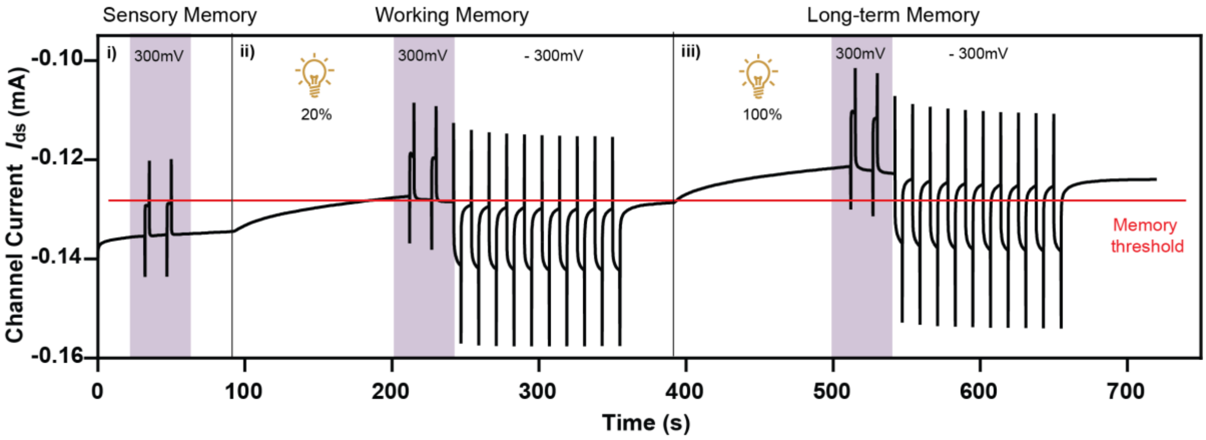

Figure 3.16 | Atkinson-Shiffrin memory model emulation. **i**) sensory memory: the sensory information was rapidly forgotten. **ii**) working memory: a low intensity light stimulus (20%) was applied, and the channel current overcame the memory threshold. By applying a negative square voltage pulse at the gate terminal, the current returned below threshold, emulating short-term memory. **iii**) Long-term memory: using a high intensity light stimulus (100%) that emulates the rehearsal process, an information is held even after the forgetting process, achieving long-term memorization. Adapted from [261].

3.2. Neurotransmitter-mediated plasticity in neuromorphic OECTs

As discussed in **Paragraph 1.4.2**, OECTs may leverage on redox reactions at the gate terminal, balanced by a counter reaction at the channel[230] to achieve sensing and polymer doping/de-doping. This approach was indeed exploited to prove the first biohybrid synapse, *i.e.*, a direct communication between a biological and an artificial neuron[246]. Here, dopaminergic cells were seeded on the gate terminal of a PEDOT:PSS-based OECT releasing DA which was oxidized inducing a conductance change in the device in a non-volatile manner.

In particular, the application of the voltage bias at the gate terminal elicited the oxidation of DA to dopamine o-quinone (DQ), as follows:

$$DA \rightarrow DQ + 2e^{-} + 2H^{+} \tag{3.1}$$

The cationic species from the electrolyte and the protons produced from the oxidation compensated the anions of the PSS- group, while the electrons eliminated the holes in the PEDOT+. This reaction resulted in the depletion of the organic layer and the consequent de-doping (**Fig. 3.17**):

$$PEDOT^{+}{:}PSS^{-} + e^{-} + Cat^{+} \rightarrow PEDOT^{0} + PSS^{-}{:}Cat^{+} \tag{3.2}$$

where $PEDOT^{+}$ indicated the pristine state of the polymer and $PEDOT^{0}$ the de-doped state of the polymer.

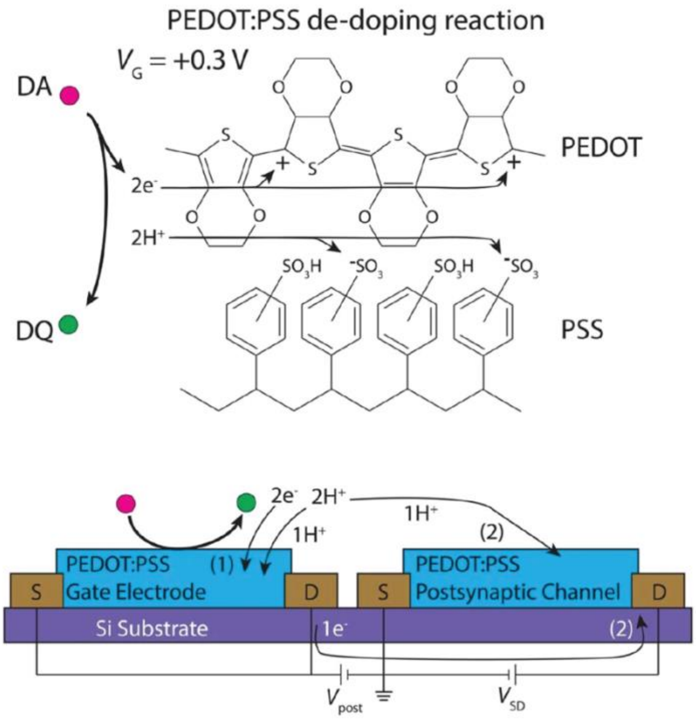

Figure 3.17 | Mechanism of PEDOT:PSS reduction, due to DA oxidation at the gate electrode. Adapted from [ref].

3.2.1. 2D Drift-diffusion-reaction model

Given the pivotal importance of this reaction in several OECTs processes, a 2D drift-diffusion-reaction model was developed in cooperation with the Lussem group, at IMSAS, UniBremen. A previous version of the model implemented a 2D drift-diffusion model[193] and was here further modified to include the presence of reactive species and their consequent faradic reactions.

The original model was based on the Poisson equation for electrical conduction (electrons, ions and holes) in the polymeric channel and two continuity equations (for ions and holes, respectively), as follows:

$$\begin{gathered}\nabla\varepsilon\nabla\phi(\mathrm{x},\mathrm{y}) - \mathrm{e}(\mathrm{C}(\mathrm{x},\mathrm{y}) - \mathrm{p}(\mathrm{x},\mathrm{y}) - \mathrm{p}_{\mathrm{ion}}(x,y)) = 0 \\ \nabla\vec{J}_{ion} - \frac{\partial p_{ion}}{\partial t} = 0 \\ \nabla\vec{J}_{p} - \frac{\partial p}{\partial t} = 0\end{gathered} \tag{3.3}$$

Where ε is the permittivity, ϕ is the electrical field, *e* is the elementary charge, *C* is the concentration of immobile charges (as polymer film counterions), p and p_{ion} are holes and ion concentrations, respectively. Lastly j_p and j_{ion} are holes and ionic current densities. The geometry used for the model was introduced in **Paragraph 1.3.2.2**.

To model the faradic reaction, two more species were included in the model: DA and cations produced in the faradic reaction. Furthermore, two continuity equations were added and Poisson equation was modified to include the electrical contribution of such cations:

$$
\begin{gathered}
\nabla\varepsilon\nabla\phi(\mathrm{x,y}) - \mathrm{e}(\mathrm{C}(\mathrm{x,y}) - \mathrm{p}(\mathrm{x,y}) - \mathrm{p_{ion}}(x,y) - p_{H^+}(x,y)) = 0 \\
\nabla\vec{j}_{ion}(\mathrm{x,y}) - \frac{\partial p_{ion}(\mathrm{x,y})}{\partial t} = 0 \\
\nabla\vec{j}_{p}(\mathrm{x,y}) - \frac{\partial p(\mathrm{x,y})}{\partial t} = 0 \\
\nabla\vec{j}_{DA}(\mathrm{x,y}) - \frac{\partial p_{DA}(\mathrm{x,y})}{\partial t} = R_{DA}(\mathrm{x,y}) - G_{DA}(\mathrm{x,y}) \\
\nabla\vec{j}_{H^+}(\mathrm{x,y}) - \frac{\partial p_{H^+}(\mathrm{x,y})}{\partial t} = R_{H^+}(\mathrm{x,y}) - G_{H^+}(\mathrm{x,y})
\end{gathered}
\tag{3.4}
$$

Where p_{DA} and p_{H+} are DA and redox-generated cations concentrations while j_{DA} and j_{H+} are the relative current densities. Lastly, R_{DA} and G_{DA}, along with R_{H+} and G_{H+}, are generation and recombination rates of the above-mentioned species. Such terms included the kinetics of the redox reaction.

Notably, continuity equations had to be solved for DA that is considered a neutral molecule. The numerical resolution of the continuity equation for a non-charged particle was carried out and it is presented in **Annex A**.

The redox reaction of a given species *M* could be written as follows:

$$M^+ + e^- \rightarrow M \tag{3.5}$$

and:

$$M + H^+ \rightarrow M^+ \tag{3.6}$$

describing reduction (3.5) and oxidation (3.6), respectively. The equilibrium (electrochemical) potential of the reaction is described by the Nernst equation:

$$\phi_{eq} = \phi_{eq}^{0} + \frac{RT}{F}\ln\left(\frac{[M^{+}]}{[M^{-}\,]}\right) \tag{3.7}$$

where ϕ_{eq} is the equilibrium potential of the reaction, ϕ^{0}_{eq} is the standard potential of the reaction, *$[M^{+}]$* and *$[M]$* are the concentration of the species involved. Additionally, T is the temperature, while R and F are the gas and Faraday constants, respectively.

Given the oxidized species M^{+}, the total reaction rate (production of oxidized species) could be simply computed as the difference between the generation (G_{M+}) and recombination (R_{M+}) rates:

$$\frac{d[M^{+}]}{dt} = G_{M^{+}} - R_{M^{+}} \tag{3.8}$$

In addition, the kinetics of such redox reaction, which allows to compute both generation and recombination rates, could be calculated through Butler-Vomler equations. Therefore, the generation rate G_{M+} can be written as:

$$G_{M^{+}} = k^{0}[M]e^{\left(-\frac{\alpha F}{RT}(\phi_{eq}-\phi_{eq}^{0})\right)}e^{\left(-\frac{\alpha F}{RT}\eta\right)} \tag{3.9}$$

By defining:

$$k_{ox}^{0} = k^{0}e^{\left(-\frac{\alpha F}{RT}(\phi_{eq}-\phi_{eq}^{0})\right)} \tag{3.10}$$

It was possible to write a more compact version of the generation rate:

$$G_{M^{+}} = k_{ox}^{0}[M]e^{\left(-\frac{\alpha F}{RT}\eta\right)} \tag{3.11}$$

Where k^0_{ox} is the standard rate of oxidation, which depends on the specific redox reaction, a is the charge transfer coefficient of the oxidation while η is called overpotential of the redox reaction, computed as:

$$\eta = E_F - (\phi_{eq} + \Delta\phi) \tag{3.12}$$

Where E_F indicates the Fermi Energy of the electrode, while Δϕ is the electrochemical voltage drop at electrode/electrolyte interface, which drove the redox reaction.

Similarly, the recombination rate could be expressed as:

$$R_{M^+} = k^0_{red}[M^+]e^{(\frac{(1-\alpha)F}{RT}\eta)} \tag{3.13}$$

Notably, the overpotential represented the electrochemical voltage driving the redox reaction. Indeed, when the energy level of the electrode and the equilibrium potential of the reaction are aligned, *i.e.*, $(\Delta\phi - \phi_{eq}) = E_F$, the overpotential is zero:

$$G_{M^+} = R_{M^+} \tag{3.14}$$

which described the steady-state condition. Lastly, Δϕ could be approximated by considering a linear potential drop over the electrode/electrolyte interface, allowing for the estimation of this parameter as:

$$E_{e,e} = \frac{\Delta\phi}{d_{e,e}} \rightarrow \Delta\phi = E_{e,e}d_{e,e} \tag{3.15}$$

where $E_{e,e}$ and $d_{e,e}$ are the electrical field at the electrode/electrolyte interface and the length of such interface, respectively.

Exploiting equations (3.11) and (3.13), the 2D drift-diffusion-reaction model (3.4) could be solved. Numerical parameters related to DA oxidation reaction were taken from literature[266,267].

The model was simulated using the geometry shown in **Fig. 3.18-a**. As in the reference model[193], holes concentration was set to zero in the electrolyte. Holes could move in the semiconducting channel whereas cations could move in both domains (electrolyte and CP). Source and drain contact were reflecting for cations while they offered ohmic contacts for holes. In addition, the gate electrode was an ohmic contact for cations. Lastly, H+ and DQ would be produced during DA oxidation and their starting concentration was set to 0, whereas DA concentration was set to be a custom value at gate/electrolyte interface, and 0 everywhere else. The CP chosen in the simulations was PEDOT:PSS and the electrolyte is NaCl.

A first simulation (**Fig. 3.18-b**, **c** and **d**) was carried out to evaluate that the DA oxidation reaction was correctly implemented in the 2D drift-diffusion model. Notably, a positive gate voltage bias was applied (V_{GS} = 0.3 V), eliciting DA oxidation, whose concentration available at the gate terminal decreased over time (**Fig. 3.18-a**), going from 30 µM (initial condition) to 29 µM. At the same time, H^+ was generated at the gate/electrolyte interface (**Fig. 3.18-b**). Unlike DA which is neutral, *i.e.*, not interacting with the generated electrical field, H^+ was accelerated by the applied gate voltage, resulting in an ionic current, that could be monitored by integrating such charges over time and over space, (**Fig. 3.18-d**).

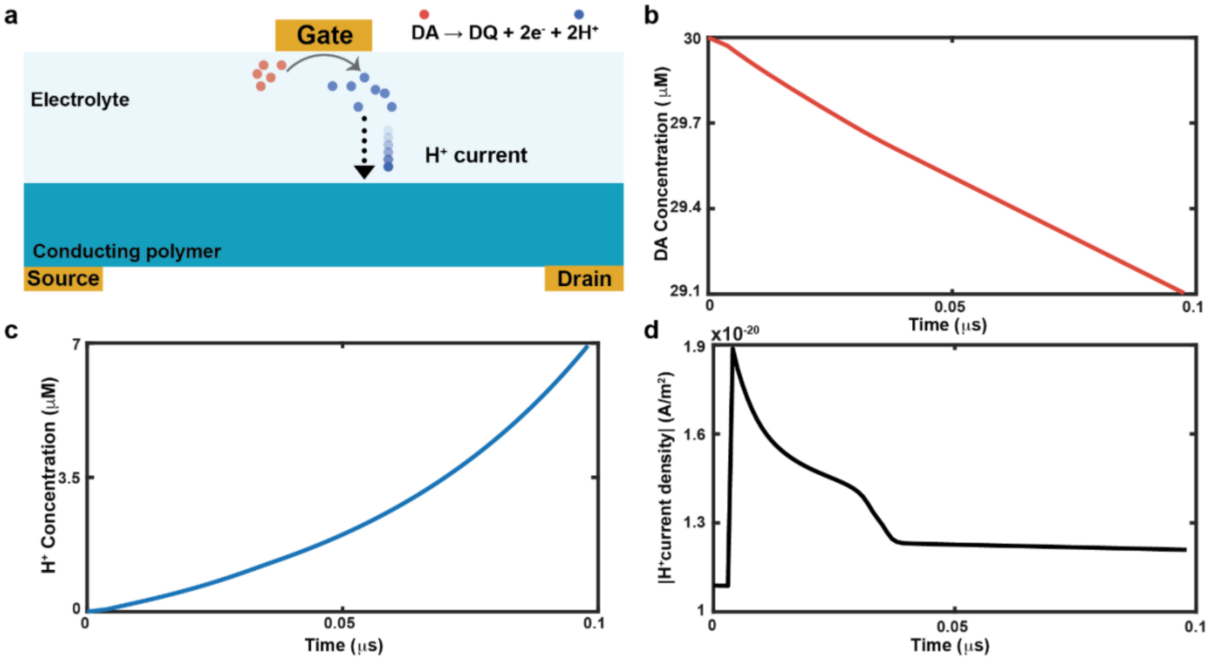

Figure 3.18 | **a**) Geometry used in the 2D drift-diffusion-reaction model. **b**) DA average concentration at the gate terminal throughout the whole simulation. **c**) H^+ average concentration at the gate terminal throughout the whole simulation. **d**) H+ current density.

According to (3.11) and (3.13), the redox reaction was driven by the overpotential h, *i.e.*, the voltage drop between (gate) electrode and electrolyte. Therefore, it was pivotal to investigate how h was influenced by the conductivity of the electrolyte. The voltage distribution in the simulated geometry is shown in **Fig. 3.19**.

When the equivalent resistance of the electrolyte is low (**Fig. 3.19-a**, high NaCl concentration [100 µM]), the voltage applied at the gate terminal (V_{GS} = 0.3 V) was equally distributed in the whole electrolyte domain, then dropping at the electrolyte/channel interface. Surprisingly, in case of a high electrolyte resistance (**Fig. 3.19-b**, low NaCl concentration [1 µM]), V_{GS} dropped at the gate/electrolyte interface.

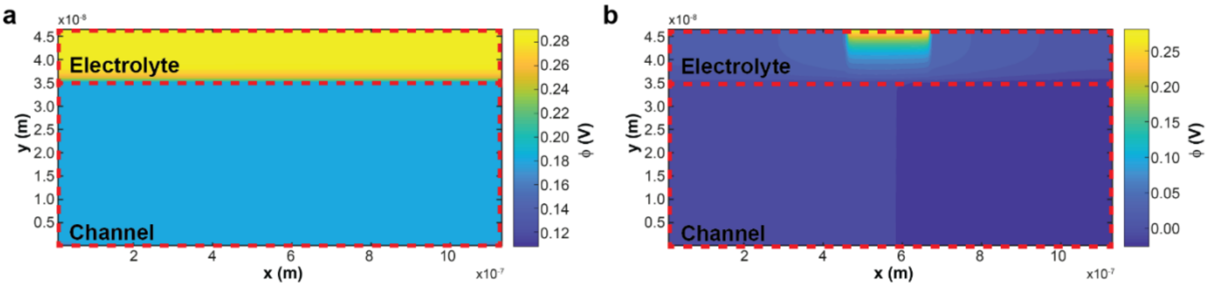

Figure 3.19 | **a**) Potential distribution in the simulated OECT when NaCl concentration is 100 µM. The gate electrode is positioned at the centre of the geometry, while source and drain electrodes can be found in left and right low corners, respectively (**Fig. 3.18-a**). **b**) Potential distribution in the simulated OECT when NaCl concentration is 1 µM. The gate electrode is positioned at the centre of the geometry, while source and drain electrodes can be found in left and right low corners, respectively (**Fig. 3.18-a**).

Subsequently, the overpotential and the H^+ current density were simulated using both high and low resistance electrolyte solutions (NaCl 1 µM and 100 µM, respectively). The H^+ current density revealed a much larger value in case of high resistance (**Fig. 3.20-a**), mirroring a larger number of ions generated in the redox reaction. Such finding was in accordance with the obtained overpotential curves (**Fig. 3.20-b**), as the overpotential of the high resistive solution was close to applied gate voltage (V_{GS} = 0.3 V) and much larger than the low resistive case.

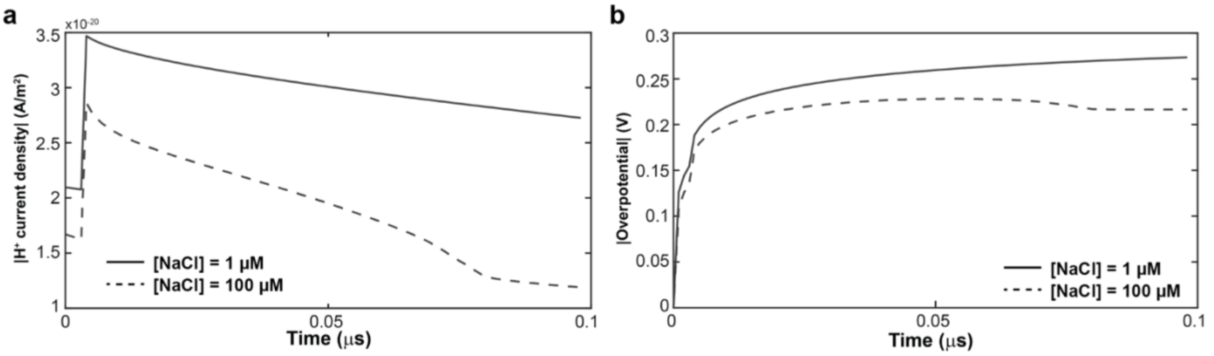

Figure 3.20 | **a**) H+ current density obtained using a high resistance solution (solid line, [NaCl] = 1 µM) and a low resistance solution (dashed line, [NaCl] = 100 µM). **b**) Overpotential obtained using an high resistance solution (solid line, [NaCl] = 1 µM) and a low resistance solution (dashed line, [NaCl] = 100 µM).

In addition, measurements were performed in a 4-electrode configuration, as discussed in **Materials and Methods 2.3**. **Fig. 3.21** displays the potential of the electrolyte as a function of the concentration of NaCl aqueous electrolyte a PEDOT:PSS OECT. In agreement with simulated data, the potential of the electrolytic solution decreased exponentially with increasing concentration of NaCl.

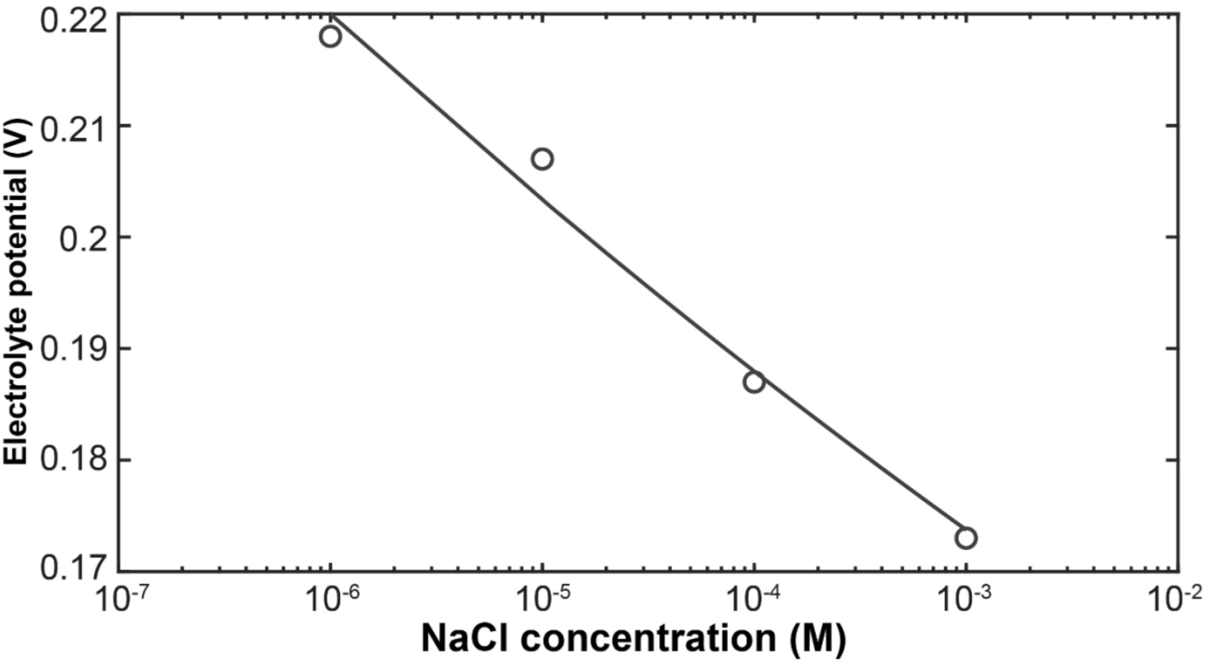

Figure 3.21 | Electrolyte potential as a function of the electrolyte solution ion concentration. Measurements are performed in a 4-electrode configuration, using a quasi-reference Ag/AgCl electrode to probe the potential of the aqueous electrolyte, while biasing the OECT with V_{GS} = 0.3 V, and V_{DS} = -0.2 V.

Once the DA oxidation was implemented, the effect on the channel, *i.e.*, PEDOT:PSS reduction had to be included in the model. Here the reduction of the polymer was simplified with a trapping mechanism. Upon reaching the OECT channel, H^+ ions were generated during the DA redox reaction and had a certain probability of being trapped in the polymer, depleting a counterion (PSS^-).

Trapping was implemented as the balance of two phenomena: capture and emission. The total trapping rate was:

$$\frac{dp_t}{dt} = C_p - E_p \tag{3.16}$$

where p_t is the density of trapped particles, while Cp and E_p are capture and emission rates, respectively. The trapping rate was calculated as:

$$C_p = cp(P_t - p_t) \tag{3.17}$$

where c is a capture coefficient, going from 0 to 1, mirroring the probability of a particle to get trapped. P_t is the density of available traps and p is the density of free particles. Such capture rate expression was completely general, *i.e.*, it did not dependent on the physics under study. It was proportional to both total amount of all available particles (p) and to the number of free traps (the difference (P_t - p_t)). When the number of trapped particles was equal to the number of traps ($P_t = p_t$), the trapping rate dropped to zero.

On the contrary, the emission rate was calculated as a probability that a given occupied trap was released, yielding:

$$E_p = ep_t \tag{3.18}$$

where e is an emission coefficient, going from 0 to 1. To mirror the non-volatility of the PEDOT:PSS reduction, the emission coefficient was set to 0, while the probability of trapping (capture rate) was set as 0.5 (50% probability that a free particle gets trapped when interacting with an available trap). The trapping mechanism was included in the 2D drift-diffusion-model as follows:

$$\begin{gathered}
\nabla\varepsilon\nabla\phi(\mathrm{x,y}) - \mathrm{e}(\mathrm{C}(\mathrm{x,y}) - \mathrm{p}(\mathrm{x,y}) - \mathrm{p_{ion}}(x,y) - p_{H^+}(x,y)) = 0 \\
\nabla\vec{J}_{ion}(\mathrm{x,y}) - \frac{\partial p_{ion}(\mathrm{x,y})}{\partial t} = 0 \\
\nabla\vec{J}_{p}(\mathrm{x,y}) - \frac{\partial p(\mathrm{x,y})}{\partial t} = 0 \\
\nabla\vec{J}_{DA}(\mathrm{x,y}) - \frac{\partial p_{DA}(\mathrm{x,y})}{\partial t} = R_{DA}(\mathrm{x,y}) - G_{DA}(\mathrm{x,y}) \\
\nabla\vec{J}_{H^+}(\mathrm{x,y}) - \frac{\partial p_{H^+}(\mathrm{x,y})}{\partial t} = \left(R_{H^+}(\mathrm{x,y}) - G_{H^+}(\mathrm{x,y})\right) + (E_{H^+}(\mathrm{x,y}) - C_{H^+}(\mathrm{x,y}))
\end{gathered} \tag{3.19}$$

A simulation of the model (3.19) is shown in **Fig. 3.22**. Here, holes of the CP were traps while H^+ generated in the redox reaction were the available particles. A square voltage pulse was applied at the gate terminal. The hole density was uniform in the initial state of the device within the polymeric channel (**Fig. 3.22**, **i**). Then, holes were depleted by cations (chemical doping induced by both Na^+ and H^+) entering the channel of the OECT (**Fig. 3.22**, **ii**) upon voltage application. Notably, the trapping occurred when H+ reached the channel. Therefore, the hole density was lower than the initial state even after the removal of the pulse, implying that PEDOT:PSS was de-doped in a non-volatile manner (**Fig. 3.22**, **iii**).

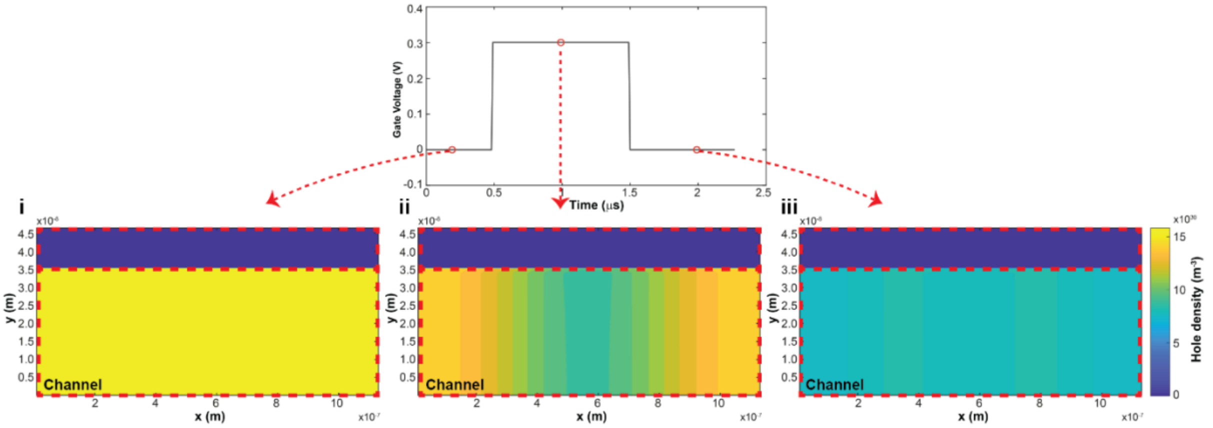

Figure 3.22 | Trapping of H+ in the PEDOT:PSS channel, observed as holes depletion. **i**) In the initial state, the device has uniform hole density. **ii**) During the application of the voltage at the gate terminal, chemical doping occurs, and holes are depleted by cations. **iii**) Upon the removal of the voltage bias, a fraction of the holes was still depleted, as cations were trapped in the polymeric channel.

The charge trapping was also observed by the simulation of the channel current, as shown in **Fig. 3.23**. Here, the baseline of channel current changed in a non-volatile manner after the oxidation of DA (30 µM).

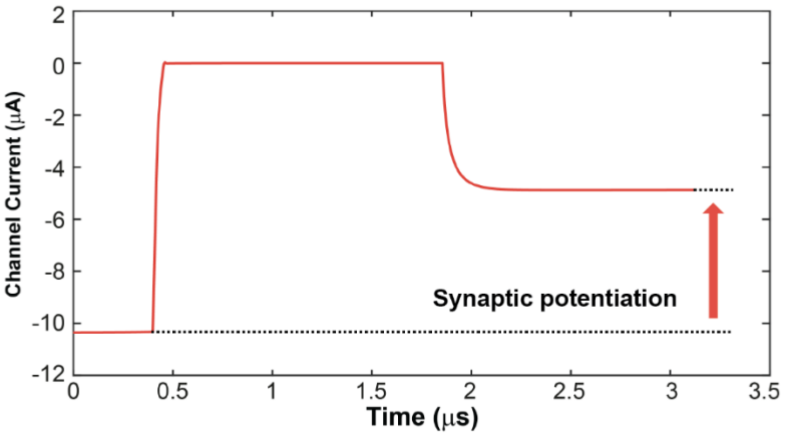

Figure 3.23 | Channel current of the OECT simulated through model (3.19). The oxidation of the neurotransmitter induces a non-volatile channel de-doping, reducing the amount of current that can flow in the polymeric channel.

3.2.2. Neurotransmitter-mediated synaptic potentiation

The model shown in **Paragraph 3.2.1** could reproduce the neuromorphic effect demonstrated in literature[246] with PEDOT:PSS-based OECTs. An experimental characterization was then carried out. PEDOT:PSS-based OECTs were fabricated as discussed in **Materials and Methods 2.4.1**. The preparation of the electrolytic solutions employed in this characterization are described in **Materials and Methods 2.4.2**.

Fig. 3.24-a displays a typical OECT output curve which was obtained by sweeping the drain-source potential from 0.1 V to -0.6 V, with a step of 100 mV. Three different gate voltage bias were selected: -0.2 V, +0.3 V and +0.8 V (**Fig. 3.24-a**, dark blue, blue and light blue, respectively). The typical depletion mode transistor behaviour was observed, in which the depletion of the channel current was a consequence of the increasing the gate voltage because of cations migrating from the electrolyte to the polymer. Transient measurements were carried out by applying subsequent square voltage pulses at the gate terminal (PW = 3 s, amp = 0.3 V, Dt = 9 s), while recording the channel current with VDS = -0.2 V (**Fig. 3.24-b**). Cations entered the polymeric channel upon voltage application when only PBS was employed as electrolyte solution (**Fig. 3.24-b**, top plot) and then they returned to the electrolyte as the voltage bias was removed, showing a volatile behaviour[187]. On the contrary, the presence of DA induces the above-mentioned redox reaction, de-doping the OECT channel in a non-volatile manner. Indeed, the channel current decreased after the application of each voltage pulse at the gate terminal (bottom plot, **Fig. 3.24-b**). The variation of the channel current was expressed as a percentage with respect to the initial current value and in this way defined the synaptic potentiation of the neuromorphic OECT.

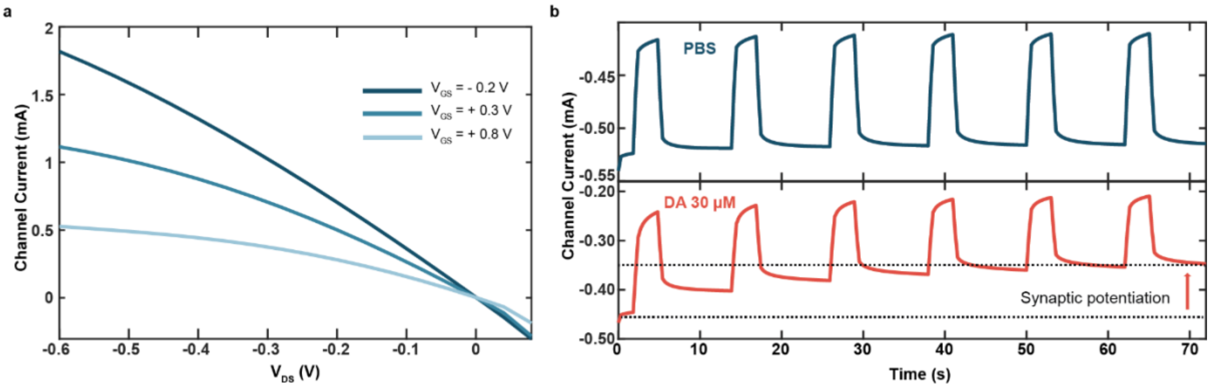

Figure 3.24 | **a**) Steady-state characterization of the OECT. The output curve was obtained sweeping V_{DS} in the range [-0.6, 0.1] V, at several valued of V_{GS} (-0.2 V, +0.3 V and +0.8 V, dark blue, blue and light blue, respectively). **b**) Transient measurements of the OECT, applying a square voltage pulse train at the gate terminal (PW = 3 s, amp = 0.3 V, Dt = 9 s). In presence of DA (bottom plot), the PEDOT:PSS of the channel is de-doped in a non-volatile manner. On the contrary, in case of PBS (top plot) such effect could not be observed.

The dependency of the synaptic potentiation on the concentration of DA was then characterized (**Fig. 3.25-a**). Three subsequent measurements consisting of 6 voltage pulses, were carried out on each neuromorphic device and then averaged to compute the synaptic potentiation of each OECT (**Materials and Methods 2.4.5**). Notably, a linear relationship between synaptic conditioning and DA concentration was found between 5 µM and 30 µM DA solutions. At higher concentrations (50 to 100 µM), the potentiation was showing no further increase with DA concentration. In addition, measurements at higher concentrations resulted in higher variability, *i.e.*, larger standard deviation. The non-dependency on DA concentration along with high variability were ascribed to a saturation effect: the high concentration of neurotransmitter almost completely de-doped the polymer with the first measurement.

The comparison between synaptic potentiation computed by three subsequent measurements of 6 pulses and a single measurement of 6 pulses is shown in (**Fig. 3.25-b**). Here, the synaptic potentiation of the single measurement (**Fig. 3.25-b**, blue circles) showed a quasi-linear dependency on DA concentration up to 100 µM, with a lover device-to-device variability. Such finding corroborated the saturation hypothesis.

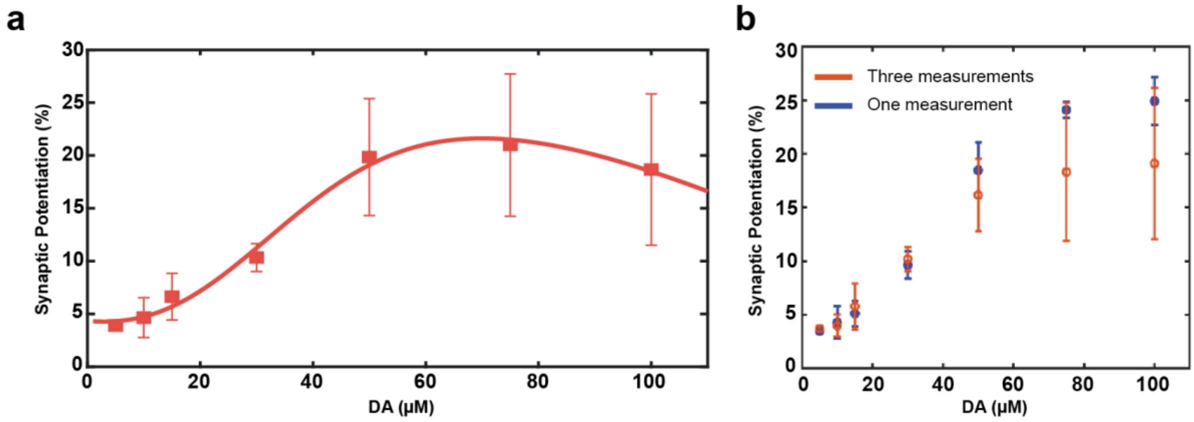

Figure 3.25 | **a**) Synaptic potentiation as function of DA concentration. Data points are extracted by averaging three subsequent measurements on each device. **b**) Comparison between data points extracted using three measurements or only one (orange and blue circles, respectively).

In addition, as it is known that oxidation of DA may cause electrode fouling[248], a microfluidic channel was coupled to the device (**Materials and Methods 2.4.1.1**) and further measurements were performed while the electrolyte solution would continuously flow and wash the surface of the electrodes. Indeed, measurements at different flowrates were performed (**Fig. 3.26**), revealing that synaptic potentiation linearly increased with the flowrate as the flow increased the number of fresh species available for oxidation.

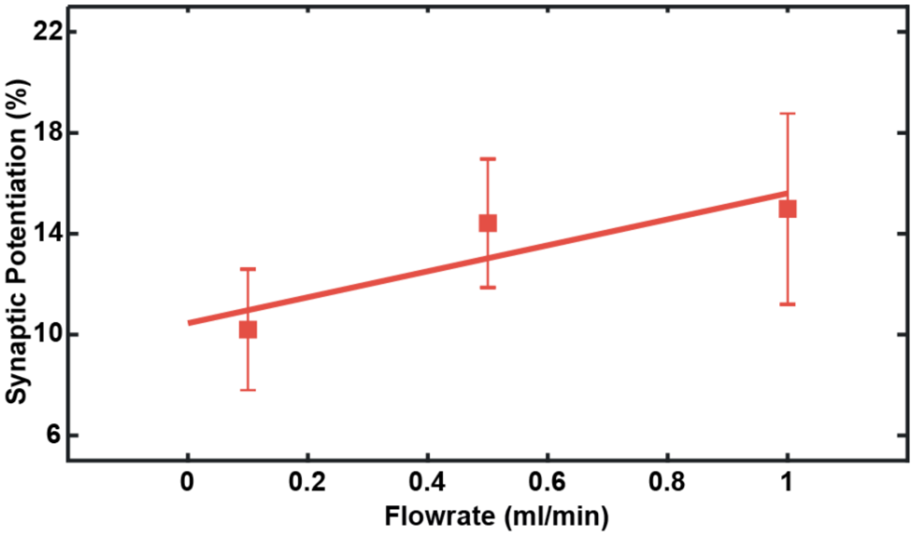

Figure 3.26 | Synaptic potentiation at different flowrates of the electrolyte solution. DA concentration employed these measurements is 30 μM.

3.2.3. Oxygen-induced synaptic depression

As discussed in **Paragraph 3.2.1**, the oxidation of neuroactive molecules, as DA or 5-HT, induced non-reversible PEDOT:PSS reduction at the channel of the OECT, allowing to emulate synaptic plasticity.

Such reaction can be inverted by introducing oxygen, that oxidizes the PEDOT:PSS, yielding:

$$2PEDOT^{0} + 2PSSH + O_2 \rightarrow 2PEDOT^{+}:PSS^{-} + H_2O_2 \qquad (3.20)$$

Indeed, such reaction leaves PEDOT in its conductive state (oxidized state). Transient measurements were carried out (**Fig. 3.27-a**) applying square voltage pulses at the gate terminal (amp = 0.3 V, PW = 3 s, Dt = 9 s) while a hydrogen peroxide (H_2O_2) solution was employed as electrolyte. As formulated by (3.20), the introduction of oxygen oxidized the PEDOT:PSS. Thus, the absolute value of current increased with time, recovering the original conductance state of the device. Such variation was defined as synaptic depression, as it reverted the DA-mediated synaptic potentiation previously discussed.

The dependence of synaptic depression on H_2O_2 concentration was then investigated (**Fig. 3.27-b**). Here, two solutions of DA (30 µM and 50 µM, light and dark blue circles, respectively) were employed prior to the introduction of H_2O_2, as PEDOT:PSS needed to be reduced, to assess the subsequent oxidation (**Materials and Methods 2.4.5**). As in case of synaptic potentiation (**Fig. 3.25-a**), six voltage pulses were applied at the gate terminal (amp = 0.3 V, PW = 3 s, Dt = 9 s) and the variation of the channel current was expressed as percentage with respect to the initial current value (synaptic depression). Notably, synaptic depression did not depend either on H_2O_2 concentration and DA concentration employed prior to H_2O_2. The hypothesis formulated to explain this finding was that, while the reduction of PEDOT:PSS driven by the oxidation of a neuroactive molecule occurred in the bulk of the polymeric film, the H_2O_2-mediated oxidation of PEDOT:PSS was a surface interaction. Therefore, such independence of synaptic depression from the concentration of the analyte may imply that the H_2O_2-mediated oxidation of PEDOT:PSS was elicited by a reaction occurring at the surface of the material.

In addition, in-flow measurements were performed supplying H_2O_2 30 mM at different flowrates (**Fig. 3.27-c**). The obtained results showed a slight increase of the synaptic depression with increasing flowrates, possibly implying an increased amount of solution that actively washed the surface of the channel.

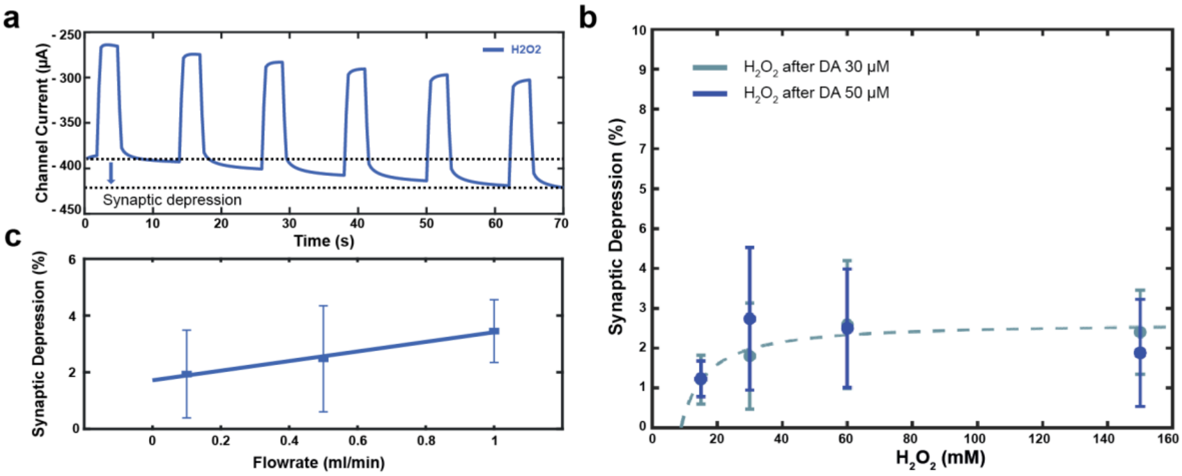

Figure 3.27 | **a**) Transient measurements of the OECT, applying a square voltage pulse train at the gate terminal (PW = 3 s, amp = 0.3 V, Dt = 9 s), in presence of H_2O_2. Here, the PEDOT:PSS of the channel is oxidized (doped), reversing the previous DA-mediated de-doping (reduction of the polymer, due to neurotransmitter oxidation). **b**) Synaptic depression as a function of H_2O_2 concentration, when previously exposed with DA 30 µM and 50 µM (light and dark blue, respectively). **c**) Synaptic depression induced by H_2O_2 30 mM, at different flowrates, after exposure to DA 30 µM.

3.3. Biomimetic neuromorphic OECTs

After dealing with the functional emulation of a feature of neural cells (LTP/LTD), the possibility of endowing OECTs with biomimetic potential was investigated by integrating a model of the cell membrane in the electrolyte solution of the transistors. Such integration was made possible by compatibility of CPs with the biological environment. Supported lipid bilayers (SLBs) were chosen as optimal model, to provide a structural, and yet functional, emulation of neural cells.

SLBs are artificial biomembranes consisting of lipid molecules, organized as a double phospholipidic layer, assembled on a rigid substrate[268]. The composition of such membranes can be easily tuned by embedding commercially available lipids, or by integrating the layer with proteins or analytes of interest. The ability of such membranes to modulate both STP and neurotransmitter-mediated LTP was demonstrated. SLB formation and characterization were carried out in cooperation with Chiara Ausilio and Claudia Lubrano, Tissue Electronics lab at the Italian Institute of Technology, Naples.

3.3.1. SLB-mediated STP

PEDOT:PSS based OECTs were fabricated on a planar glass substrate, creating two symmetric PEDOT:PSS areas, working either as channel or gate of the transistor (**Materials and Methods 2.5.1**). Subsequently, a SLB was assembled from made of 1-palmitoyl-2-oleoyl-glycero-3-phosphocholine (POPC), which is one of the major components of the cell PM[4]. The formation of the bilayer was carried out by means of a solvent-assisted lipid bilayer (SALB) technique[258], allowing to position the membrane inside the microfluidic channel of the OECT from the gate to the channel (**Fig. 3.28-a**, **Materials and Methods 2.5.2**).

Initially, the mechanical properties of the SLB were investigated by means of fluorescence recovery after photobleaching (FRAP, **Materials and Methods 2.5.2.1**), allowing to characterize the lateral mobility of the membranes (**Fig. 3.28-b**). In this technique, a fluorophore embedded in the membrane was bleached by a laser and the recovery of the fluorescence intensity profile was monitored over 5 min (**Fig. 3.28-b**). Later diffusivity of the bilayer was then calculated considering different substrates and the corresponding values are summarized in **Table 3.1**. Interestingly, the bilayer had a higher mobility when seated onto the CP (on gate and channel of the OECT) rather than when formed on the glass substrate (region between gate and channel) as previously shown literature[269]. Such variation was resulting from the interaction with the soft interface of the polymer reducing a possible frictional coupling between the membrane and the rigid substrate.

Morphological characterization of the SLB was then carried out by means of AFM (**Materials and Methods 2.5.2.2**) and the root-mean-square surface roughness (R_q) of the SLB was measured **Table 3.1**), suggesting that the membrane had a smoothening effect on the peculiar fuzzy surface morphology of PEDOT:PSS (**Fig. 3.28-c**).

SURFACE	**Diffusion coefficient [µM^2/s]**	**Rq [nm]**
Glass	-	1.7 ± 0.6
POPC on glass	1.3 ± 0.2	2.2 ± 0.5
PEDOT:PSS	-	2.3 ± 0.2
POPC on PEDOT:PSS	1.6 ± 0.2	1.6 ± 0.2

Table 3.1 | Diffusion coefficients and surface roughness of POPC SLBs on glass and PEDOT:PSS.

Lastly, as the phospholipidic membrane was theoretically ion impermeable, the electrical characteristics of the SLB-coated PEODT:PSS electrodes were investigated by means of EIS (**Fig. 3.28-c**). A two-electrode configuration was adopted using one PEDOT:PSS stripe as working and sense electrode, while a non-polarizable Ag/AgCl electrode was used as reference and counter electrode (**Fig. 3.28-d**, **i**). A typical Nyquist plot is shown in **Fig. 3.28-d**, **i**, comparing the impedance response of a POPC-coated (pick curve) and of a bare PEDOT:PSS (blue curve) electrode. Here, the formation of the bilayer increased the real part of the impedance, shifting the curve along the x-axis and forming a semicircle at high frequency. Such phenomena were the result of an increase resistance in the ionic pathway, causing a slower charge accumulation at the electrode/electrolyte interface[270]. An equivalent electrical circuit was used to fit the EIS data (**Fig. 3.28-d**, **ii** and **Materials and Methods 2.5.3**). The resistance R_S modelled the electrolyte solution resistance while R_{DL} and C_{DL} described the membrane/electrode interface. Lastly, the Warburg element Z_W was used to include all the non-idealities of polymeric films[271].

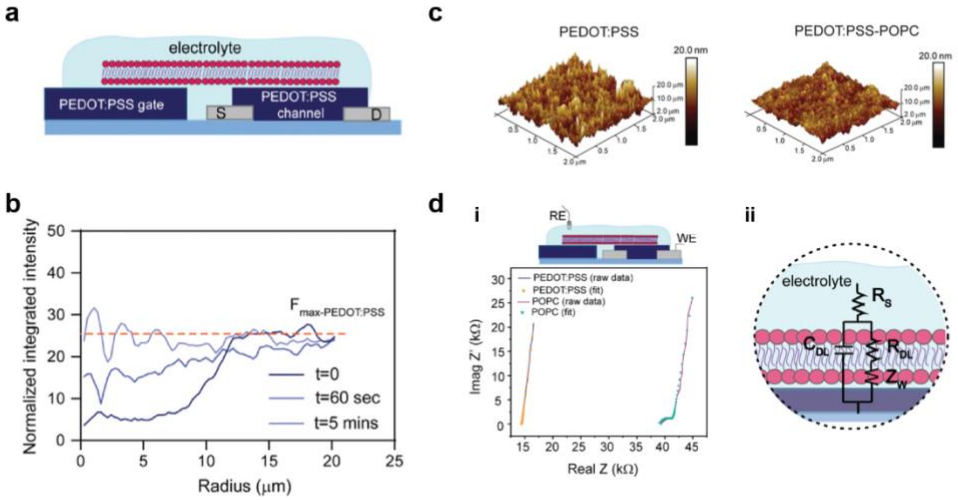

Figure 3.28 | **a**) Schematic of the PEDOT:PSS-based OECT, coated with a POPC SLB. **b**) Fluorescence intensity profile monitored over 5 min after photobleaching in FRAP technique. **c**) AFM 3D images of surface morphology of bare PEDOT:PSS and POPC-coated PEDOT:PSS. **d**) EIS measurements. **i**) EIS measurement schematic and measured data of bare PEDOT:PSS (blue curves) and SLB functionalized PEDOT:PSS electrodes (pink curves). **ii**) Equivalent electrical circuit used to fit the EIS data.

Numerical values obtained through fitting (**Materials and Methods 2.5.3**) are reported in **Table 3.2**. Notably, the capacitance C_{DL} decreased, denoting the passage from the bulk capacitance of the PEDOT:PSS to the surface capacitance of the SLB[272] while the resistance R_{DL} increased, describing the hindering effect of the bilayer on passage of ions (*i.e.*, ion impermeability).

	PEDOT:PSS	**POPC on PEDOT:PSS**
R_S [kΩ]	15.8 ± 2.1	27.1 ± 10.5
R_{DL} [Ω]	356.3 ± 197.9	2230.0 ± 208.8
C_{DL} [μF]	8.1 ± 0.6	4.8 ± 2.3

Table 3.2 | Equivalent electrical circuit parameters, assessed from EIS measurements, of both bare and POPC-coated PEDOT:PSS electrodes.

While the bilayer was positioned between gate and channel of the OECTs, transient measurements were carried out to assess the influence of the biomembrane on the gate-to-channel equivalent circuit. Such ionic circuit could be modelled as a capacitance C_{CH}, modelling the CP constituting the channel and a resistance R_S, describing electrolyte resistance connected in series (**Fig. 3.29-a** and **Paragraph 1.3.2.1**). A square voltage pulse (amplitude 0.3 V, PW = 3 s) was applied to the gate terminal in two different measurement configurations. In the first, the PEDOT:PSS patterned onto the substrate was used as gate electrode (**Fig. 3.29-b**, planar configuration). in the second, a PEDOT:PSS stripe patterned onto a different glass substrate was employed as gate terminal (**Fig. 3.29-c**, top configuration). Planar and top configurations were used to assess either or not the presence of the SLB affected the ionic pathway. The normalized current responses, upon the application of the voltage pulse at the gate terminal, are shown in Fig. **3.29-b** and **c**, before and after the formation of the bilayer (blue and pink in planar configuration, and green and orange in top configuration, respectively). The time needed to reach the 63% of the maximum charged state of the equivalent ionic circuit was identified as the time constant τ of the ionic circuit. Numerical values of the time constants (before and after the formation of the SLB, in both configurations) are shown in Fig. **3.29-d**.

Notably, the presence of the bilayer increased the time response in both configurations. The largest variation could be found in the top configuration in which τ almost doubled the one computed after the formation of the membrane. Therefore, gate configuration might elicit different ionic pathways. In the planar case, lateral ion currents could flow through the aqueous cushion between the SLB and PEDOT:PSS. In the other case, ions were forced to cross the bilayer, causing a significant delay in the gating of the device.

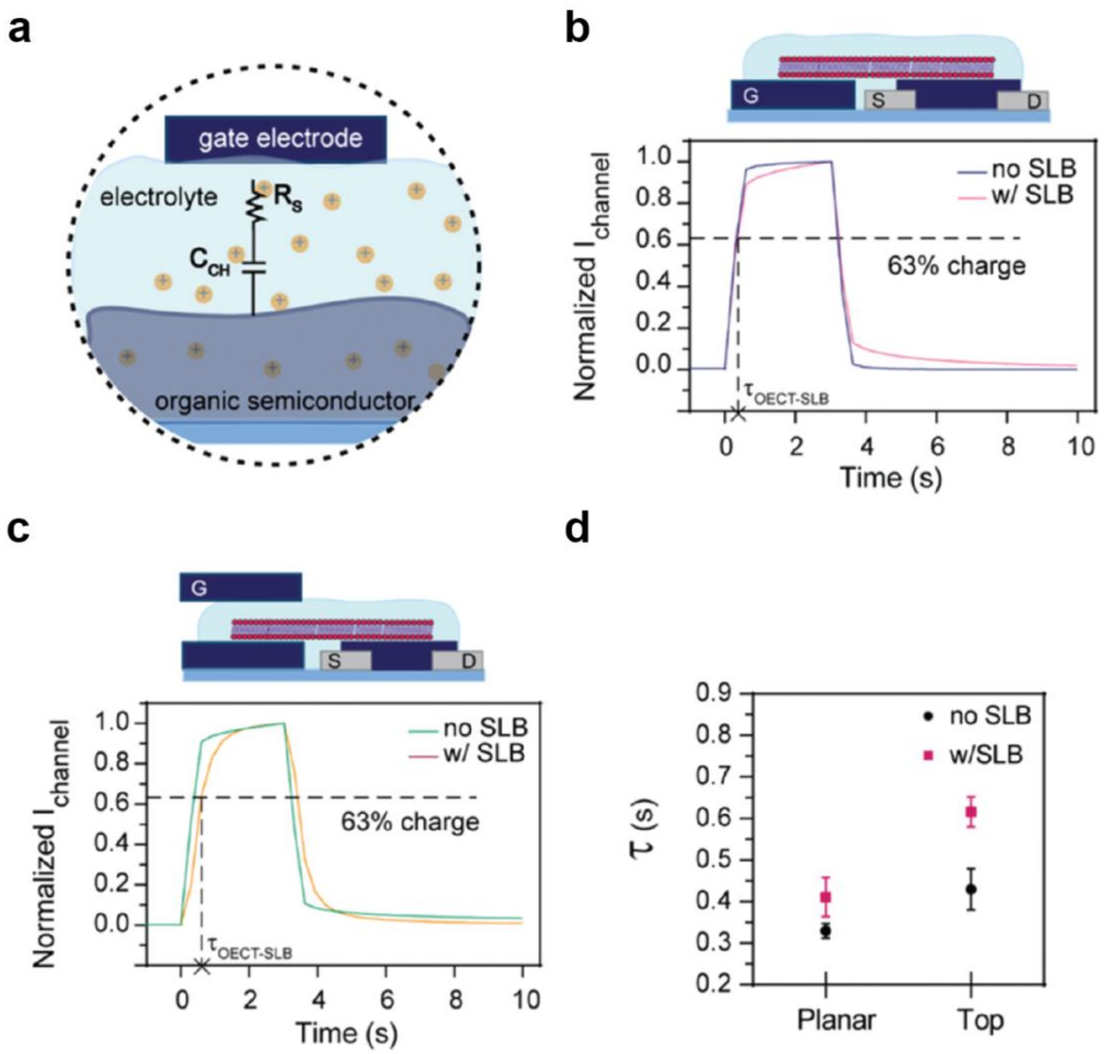

Figure 3.29 | **a**) Schematic of ionic circuit coupling the gate electrode to the channel of the OECT. **b**) planar configuration of the OECT, along with normalized channel current measured while biasing the gate terminal with a square voltage pulse (amplitude 0.3 V, PW = 3 s and Δt = 9 s). **c**) top configuration of the OECT, along with normalized channel current measured while biasing the gate terminal with a square voltage pulse (amplitude 0.3 V, PW = 3 s and Δt = 9 s). **d**) Comparison of time constants extracted before and after the formation of the bilayer (black and red squares, respectively), in both planar and top configurations.

Subsequently, neuromorphic measurements were performed to consider the capabilite of the SLB-OECT platform to emulate STP (**Fig. 3.30**). Here, a train of square voltage pulses was applied at the gate terminal to resemble APs of a presynaptic neuron. As the delay between two presynaptic stimuli plays a pivotal role in STP (**Paragraph 1.1.4.2**), the role of delay between the pulses on plasticity emulation was investigated by setting Δt as multiples of τ . The channel current was monitored by applying a drain-source voltage bias V_{DS} = -0.2 V. In addition, the conductance (ratio between I_{DS} and V_{DS}) was computed and plotted (**Fig. 3.30**). **Fig. 3.30-a** displays the conductance of the neuromorphic OECT in planar configuration when applying a train of square voltage pulses and setting Δt equal to τ and 5τ (**Fig. 3.30-a**, **i** and **ii**, respectively). Such values were chosen as upper and lower limit of Δt asthe equivalent RC circuit should be completely discharged in case of $\Delta t = 5\tau$, while it should be discharged of about 37% when $\Delta t = \tau$. **Fig. 3.30-b** reports the same measurements conducted in top configuration. In both cases the STP was evaluated as conductance variation ΔG before and after the application of the square voltage pulses, expressed as a percentage of the initial conductance value.

From the numerical quantification of ΔG (**Fig. 3.30-c**) it is possible to conclude that the highest conductance variation (highest STP) was elicited by when $\Delta t = \tau$. In addition, no significant variations could be observed in planar configuration.

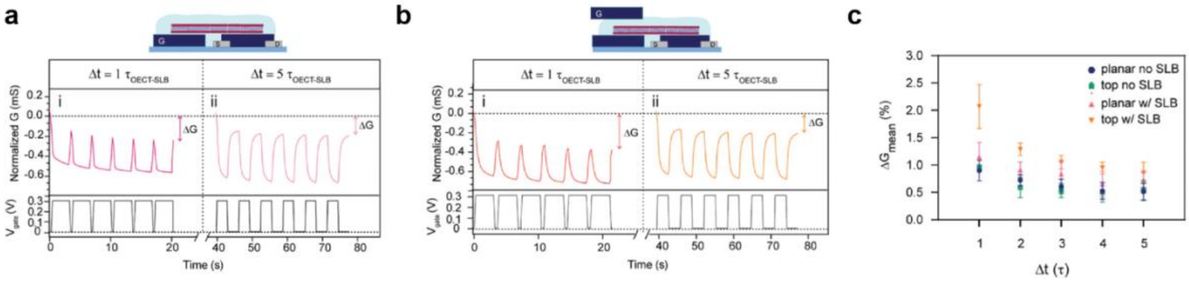

Figure 3.30 | **a**) Conductance variation in planar configuration (top plot) and applied voltage pulses at the gate terminal (bottom plot). **i**) $\Delta t = \tau$. **ii**) $\Delta t = 5\tau$. **b**) Conductance variation in top configuration (top plot) and applied voltage pulses at the gate terminal (bottom plot). **i**) $\Delta t = \tau$. **ii**) $\Delta t = 5\tau$. **c**) Comparison of conductance variation extracted by setting Δt as multiples of τ . Both configurations are compared, before and after the formation of the bilayer.

Such conductance variation was not compatible with the proposed RC model, as Δt = 1τ should have elicited a discharge of the polymeric channel of 37%, with and without the bilayer, and in both configurations. However, a significant difference was observed in ΔGfor the biomembrane-functionalized OECTs. To investigate this behaviour, the gate current was analyzed, to estimate the number of charges injected from the electrolyte to the polymeric channel, and subsequently retained in the OECT channel, after the removal of V_{GS} (**Materials and Methods 2.5.4**).

Notably, no significant differences could be observed in the number of charges injected in both POPC-coated and bare PEDOT:PSS cases (**Fig. 3.31-a** and **b**, respectively). Conversely, the analysis of the charge retained inside the channel after the removal of the voltage pulses revealed that in a POPC-coated transistor measured in the top configuration a high percentage of the charge injected could not return to the electrolyte. Such analysis further confirmed that the presence of the bilayer hindered the ionic discharge, enhancing neuromorphic behaviour (STP).

It was possible to conclude that the SLB favoured a charge trapping mechanism, which could not be explained by the RC model approximation.

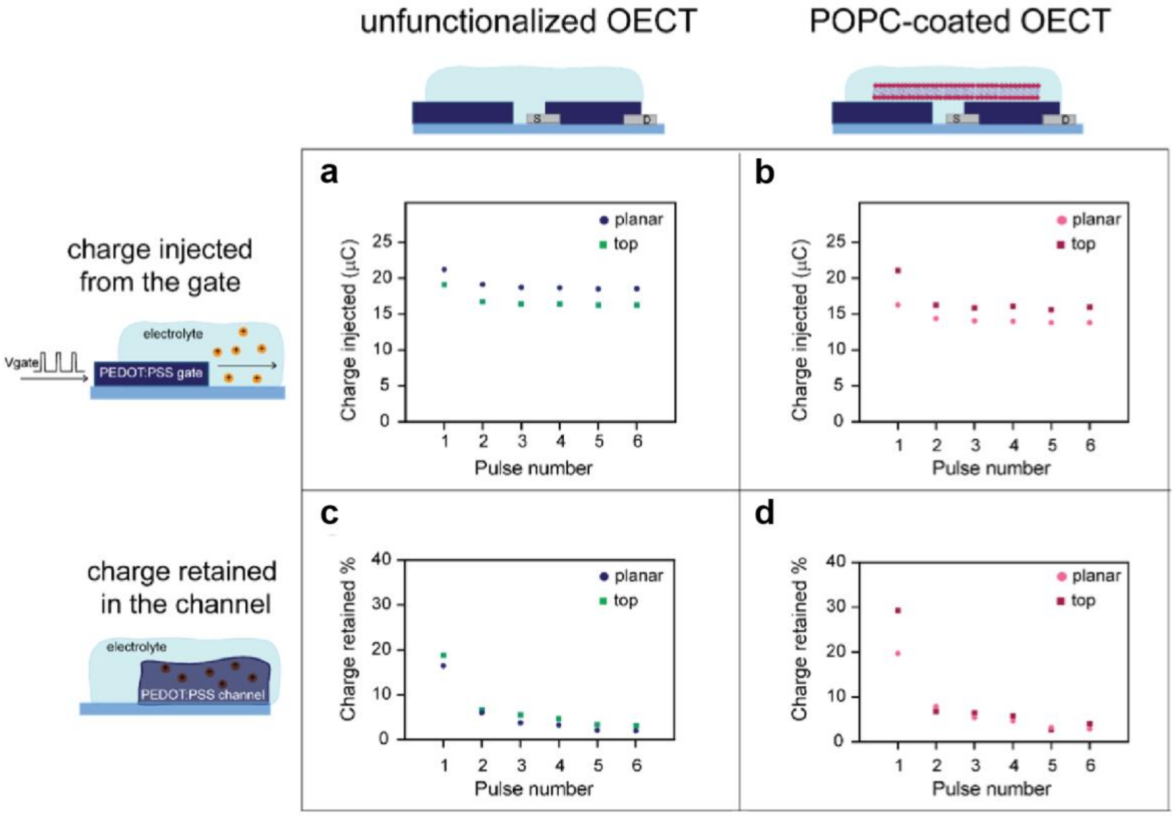

Figure 3.31 | **a**) Charge injected from the electrolyte to the OECT channel, in both planar and top configuration (blue circles and green squares, respectively), in a bare PEDOT:PSS transistor. **b**) Charge injected from the electrolyte to the OECT channel, when functionalized with POPC-SLB, in both planar and top configurations (pink circles and red squares, respectively). **c**) Percentages of charge retained inside the polymeric channel of the OECT, after the removal of the gate-to-source voltage bias, in both planar and top configurations (blue circles and green squares, respectively), in a bare PEDOT:PSS transistor. **d**) Percentages of charge retained inside the polymeric channel of the OECT, after the removal of the gate-to-source voltage bias, in both planar and top configurations (pink circles and red squares, respectively), in POPC-coated PEDOT:PSS transistor.

3.3.2. SLB-mediated LTP

A biomimetic neuromorphic platform, made by the integration of OECTs and SLBs was demonstrated (**Paragraph 3.3.1**). To further enhance the neuromorphic features of the obtained device, the possibility of including the neurotransmitter-mediated LTP with the biomimetic OECTs was investigated. An SLB formation protocol was developed, to confine the biomembrane only on the channel of transistor **(Fig. 3.32)**.

In brief, the lipidic membrane was confined on the post-synaptic terminal of the OECT, (channel) through the usage of a removable PDMS barrier. Following the formation of the membrane through SALB technique[258], the PDMS barrier confining the SLB was removed allowing for gate-to-channel ionic communication. Details on the OECT fabrication, along with a detailed procedure of the SLB formation can be found in **Materials and Methods 2.6.1** and **Materials and Methods 2.6.2**. Notably, two SLB compositions were formed and compared. The former is a solely POPC composed membrane, while the latter was assembled from POPC with the addition of cholesterol (Chol) and sphingomyelin (SM) (1:1:1 in mixture). Such composition was chosen as it characterized by the major constituents of neuronal lipid rafts[2021], and it will be referred to as brain-SLB.

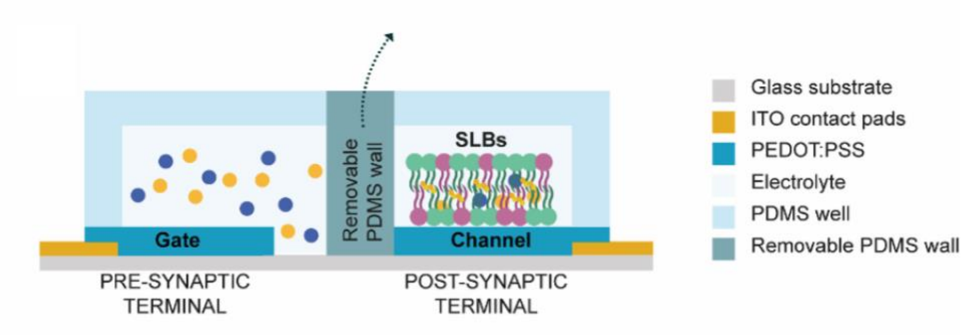

Figure 3.32 | a) Side view of the neuromorphic OECT and schematic of confinement of the SLB.

Morphological and structural properties of the obtained SLBs were investigated by means of FRAP and AFM, whereas the electrical properties of the membranes were evaluated by means of EIS.

Average roughness (R_a, **Table 3.3**) was extracted from AFM measurements (**Fig. 3.33-a**) revealing that, as previously discussed, a POPC-coated PEDOT:PSS electrode (**Fig. 3.33-a**, **i**) presented a smoother surface with respect to bare PEDOT:PSS (**Fig. 3.33-a**, **ii**). Conversely, the brain-SLB functionalized surface (**Fig. 3.33-a**, **iii**) was characterized by a higher surface roughness (**Table 3.3**). Such divergence from the previous results may be ascribed to the formation of liquid ordered domains of SM and Chol, protruding from the surface of the SLB[273,274].

Lateral diffusivity (**Table 3.3**) was calculated from FRAP measurements that were conducted by bleaching a fluorophore embedded in the membranes and monitoring the recovery of the fluorescence intensity profile over 5 min, for both POPC (**Fig. 3.33-b**) and brain (**Fig. 3.33-c**) biomembranes. Interestingly, the POPC-bilayer showed higher diffusivity with respect to the brain counterpart. The difference was mainly due to the presence of Chol and SM domains that were shown to hinder movements of lipids within the membrane[275].

SURFACE	**R_a [nm]**	**Diffusion coefficient [μM^2/s]**
PEDOT:PSS	1.45 ± 0.02	-
POPC on glass	1.37 ± 0.03	1.93 ± 0.15
POPC on PEDOT:PSS	1.62 ± 0.03	1.25 ± 0.04

Table 3.3 | Surface roughness and diffusion coefficients of POPC and brain SLBs on PEDOT:PSS.

EIS measurements were carried out and an equivalent electrical model was used to fit the data (**Fig. 3.33-d)**. The model consisted of a capacitance C, modelling either the SLB or the PEDOT:PSS volume, connected in series with a resistance R, accounting for both electrolyte and bilayer resistance. Such simple RC circuit was often employed to model EIS of polymeric electrodes[276]. Notably, while additional circuital elements are usually required to model a biomembrane completely coating an electrode[277], the confined SLB did not induce any significant variation of the EIS data (**Fig. 3.33-d**). Therefore, the simple RC circuit could properly fit the data suggesting that the confined membrane did not completely hinder passage of ions, which were able to laterally drift towards the polymeric electrode.

The parameters extracted by curve fitting before and after the formation of both membrane (**Fig. 3.33-e**) were in a comparable range, further corroborating the hypothesis of a non-complete hindrance of the ionic pathways. On the other hand, a slight difference could be observed between the two lipidic compositions. The capacitance of the brain-SLB was higher than the POPC-SLB, possibly due to different bilayer fluidity that influenced membrane dielectric constant, and, consequently, the capacitive properties[278]. Indeed, brain-SLBs were characterized lipid rafts domains, influencing the fluidity of the biomembrane, introducing local changes in the dielectric[279]. Further details on the characterization can be found in **Materials and Methods 2.6.3**.

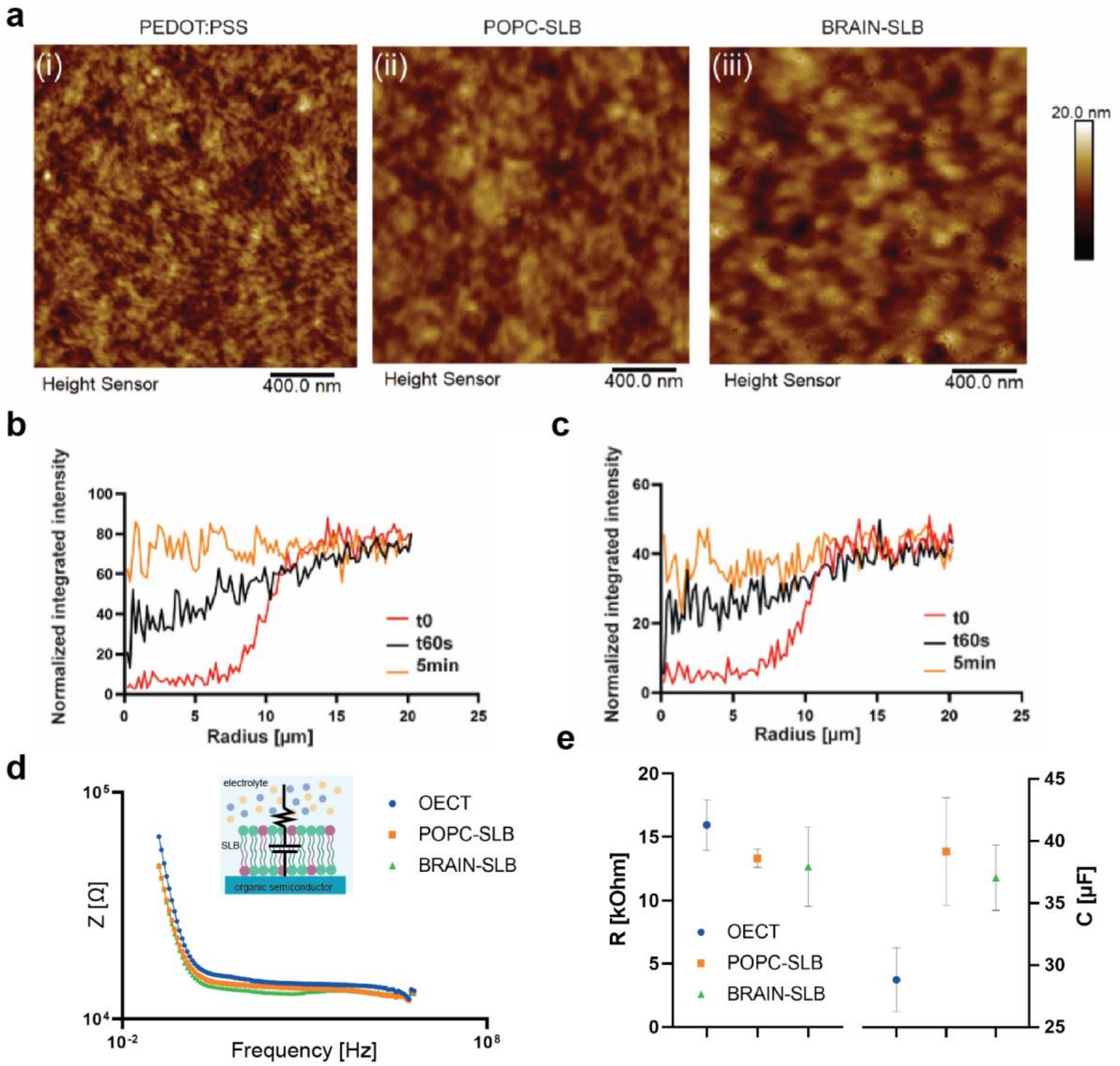

Figure 3.33 | **a**) Surface morphology of PEDOT:PSS, POPC-SLB and brain-SLB (**i**, **ii** and **iii**, respectively), extracted from AFM measurements. **b**) Fluorescence intensity profile of a POPC-SLB during FRAP experiments, right after the bleaching (t0, red curve), after 60 s (black curve) and after 5 min (yellow curve). **c**) Fluorescence intensity profile of a brain-SLB during FRAP experiments, right after the bleaching (t0, red curve), after 60 s (black curve) and after 5 min (yellow curve). **d**) Bode plot (modulus) of a bare PEDOT:PSS electrode (blue curve), a POPC-coated PEDOT:PSS electrode (orange curve) and a brain-SLB-coated PEDOT:PSS electrode (green curve). In addition, a schematic of the equivalent circuit used to fit the data is provided. **e**) Electrical parameters extracted from EIS data of bare, POPC-coated and brain-SLB-coated PEDOT:PSS electrodes (blue circles, orange squares and green triangles, respectively).

Subsequently, transient measurements were carried out to evaluate the influence of the confined SLBs on the time response of the OECTs. A square voltage pulse was applied at the gate terminal (amp = 0.3 V, PW = 3 s) while biasing the drain electrode with respect to the source with –0.2 V and recording the channel current I_{DS}. The extracted conductance is shown in **Fig. 3.34-a**. As discussed in **Paragraph 3.3.1**, by fixing a threshold at 63% of the maximum current response, it was possible to extract the time constant of the OECT ionic circuit. Notably, while no differences could be observed between the bare OECT and the brain-SLB coated one (**Fig. 3.34-b**, blue circle and green triangle, respectively), the presence of the POPC membrane introduced a delay in the gate-to-channel ionic communication. Notably, the bilayer confined on the channel of the OECT did not introduce a significant delay in the ionic circuit. These results agreed with the hypothesis of a non-complete ionic hindrance, induced by the confined SLB.

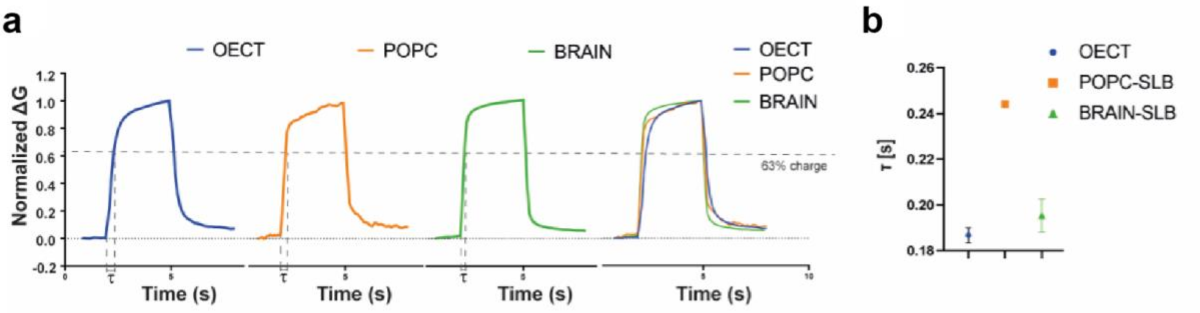

Figure 3.34 | **a**) Normalized conductance of bare, POPC-functionalized and brain-SLB-functionalized OECTs (blue, orange and green curves, respectively), during the application of a square voltage pulse at the gate terminal (amp = 0.3 V, PW = 3s). The drain electrode was biased with –0.2 V, and an overlap of all the curves is provided. **b**) Fluorescence intensity profile of a POPC-SLB during FRAP experiments, right after the bleaching (t0, red curve), after 60 s (black curve) and after 5 min (yellow curve).

Moreover, neuromorphic measurements were carried out by applying a train of square voltage pulses at the gate terminal (amp = 0.3 V, PW = 3 s), to evaluate STP. As discussed in **Paragraph 3.3.1**, the delay between pulses Δt was set to τ (**Fig. 3.35-a**) and 5τ (**Fig. 3.35-b**). Conductance profiles of the bare, POPC functionalized and brain-SLB functionalized OECTs are shown in **Fig. 3.35-a** and **b** (blue, orange and green curves, respectively). The conductance variation ΔG was computed as difference between the conductance value before and after the application of V_{GS}, expressed as a percentage with respect to its initial level. As expected, the highest conductance variation was achieved when Δt was set as τ, without any significant differences between the two lipidic compositions (**Fig. 3.35-c**). Such result agreed with the by analysis of the gate current in which the number of charges injected into the channel of the transistor (**Fig. 3.35-d**) and retained after the removal of the gate-source bias (**Fig. 3.35-e**) were extracted. Injection of charge did not show any dependence on either the presence of the bilayers or the delay between pulses (**Fig. 3.35-d**), whereas the amount of charge retained was increased in case of Δt = τ, without any difference between lipidic composition or presence.

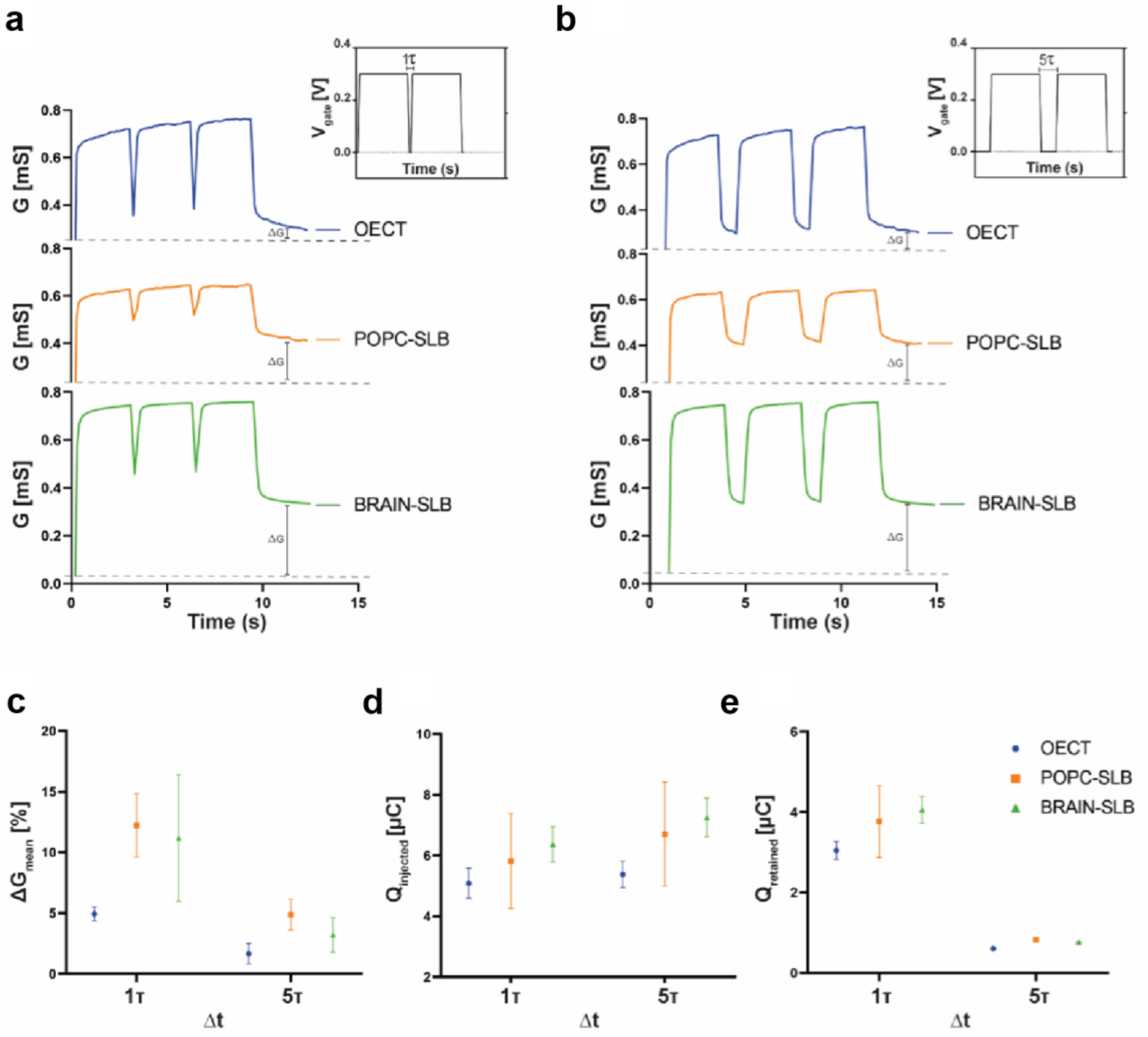

Figure 3.35 | **a**) Conductance of bare, POPC-functionalized and brain-SLB-functionalized OECTs (blue, orange and green curves, respectively), during the application of a train of square voltage pulses at the gate terminal (amp = 0.3 V, PW = 3 s, Δt = τ). VDS = -0.2 V. **b**) Conductance of bare, POPC-functionalized and brain-SLB-functionalized OECTs (blue, orange and green curves, respectively), during the application of a train of square voltage pulses at the gate terminal (amp = 0.3 V, PW = 3 s, Δt = 5τ). VDS = -0.2 V. **c**) Numerical values of conductance variation as a function of the delay between pulses, in case of bare, POPC-functionalized and brain-SLB-functionalized OECTs (blue circles, orange squares and green triangles, respectively). **d-e** Numerical values of charge injected and retained in the transistor channel as a function of the delay between pulses, in case of bare, POPC-functionalized and brain-SLB-functionalized OECTs (blue circles, orange squares and green triangles, respectively).

Lastly, neurotransmitter-mediated synaptic plasticity was recapitulated by oxidizing DA and 5-HT at the gate terminal of the SLB functionalized OECTs. The oxidation of the neurotransmitters elicited the reduction of the polymeric channel of the device, changing its conductance as discussed previously (**Paragraph 3.2**). Several pulses and three consecutive measurements per device were employed to extract conductance variations, as discussed in **Materials and Methods 2.4.5**.

The conductance variation induced by DA 30 µM solution, before and after the formation of the SLBs is shown in Fig. **3.36-a**. Interestingly, in presence of the brain-SLB the conductance variation was increased (**Fig. 3.36-a**, green triangle), whereas no significant differences could be observed between bare and POPC-coated OECTs (**Fig. 3.36-a**, blue circle and orange square, respectively).

On the contrary, a noticeable difference based on the lipidic composition could be observed in the conductance modulation obtained when 30 µM 5-HT was present in the electrolyte (**Fig. 3.38-b**). In particular, the modulation of the POPC-coated OECT (**Fig. 3.36-b**, orange square) was lower than the bare and brain-SLB-coated ones (**Fig. 3.36-b**, blue circle and green triangle, respectively). Such difference was ascribed to the combination of two effects: bilayer fluidity and electrode fouling effect. Indeed, 5-HT oxidation was known to produce induce fouling effect[280,281] (passivation of the electrode due to the formation of an insulating layer made of the byproduct of the faradic reaction). Such fouling can be drastically reduced by a continuous refresh of the species available for the oxidation[248]. Therefore, in the presented platform, the fluid nature of the POPC-SLB could prevent from a complete washing of the electrode surface between consecutive measurements in which 5-HT was oxidized.

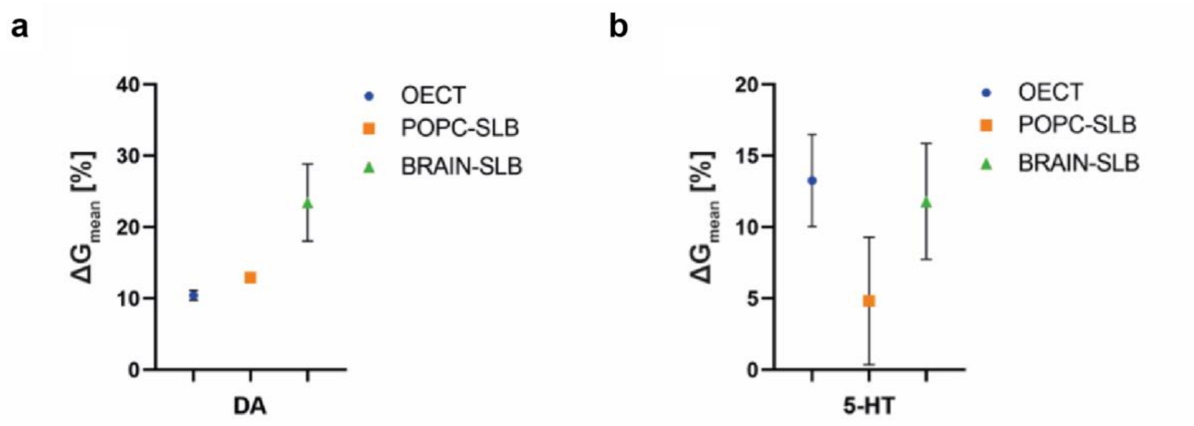

Figure 3.36 | **a**) Conductance variation induced by oxidation of DA 30 µM, in case of bare, POPC-functionalized and brain-SLB-functionalized OECTs (blue circles, orange squares and green triangles, respectively). **b**) Conductance variation induced by oxidation of 5-HT 30 µM, in case of bare, POPC-functionalized and brain-SLB-functionalized OECTs (blue circles, orange squares and green triangles, respectively).

In addition, the neurotransmitter-induced LTP was used to recapitulate Pavlovian associative learning[282] in the neuromorphic platform (**Fig. 3.37**). Here, neurotransmitters were used to achieve potentiation while H_2O_2 was used to induce depression, as discussed in **Paragraph 3.2.3**.

In the classical Pavlovian experiment, a dog was subjected to a neutral stimulus (ringing of a bell), which did not evoke any response. Subsequently, the dog underwent an unconditioned stimulus, (food) that elicited an unconditioned response (the dog started salivating). Then, the dog was repeatedly subjected to the two stimuli delivered together. After some iterations, the association was completed: the unconditioned response was expressed in response to the neutral stimulus, (the dog started salivating when the bell was ringing).

The OECT functionalized with the brain-SLB was exposed to DA 30 µM (neutral stimulus) while applying three consecutive voltage pulses at the gate terminal (**Figure 3.37**, **i**) allowing to identify the neutral stimulus response as elicited conductance variation. Then a washing procedure with H2O2 was performed to restore the initial conductance level (not shown to help visualization).

Then, the unconditioned stimulus was supplied as 5-HT µM along with three voltage pulses at the gate terminal (**Fig. 3.37**, **ii**). The minimum conductance level reached after the neurotransmitter oxidation was defined as salivation threshold: whenever the conductance of the device reached or crossed the above-defined threshold, the unconditioned response was correctly evoked. An additional washing procedure was then performed.

The association of conditioned and unconditioned stimuli was carried out by using a DA:5-HT solution as electrolyte (ratio of neurotransmitter 1:1, [30 µM:30 µM]) while applying three square voltage pulses at the gate terminal (**Fig. 3.37**, **iii**) then followed by a washing procedure. The conductance of the device was shifted towards a smaller value in a non-reversible manner as the washing procedure could not restore the initial conductance level. Therefore, associative learning was completed. Indeed, the application of the neutral stimulus (DA 30 µM) could elicit the unconditioned response, (crossing of the salivation threshold, **Fig. 3.37**, **iv**).

Further details about number of pulses, amplitudes, PWs and duration can be found in **Materials and Methods 2.6.4**.

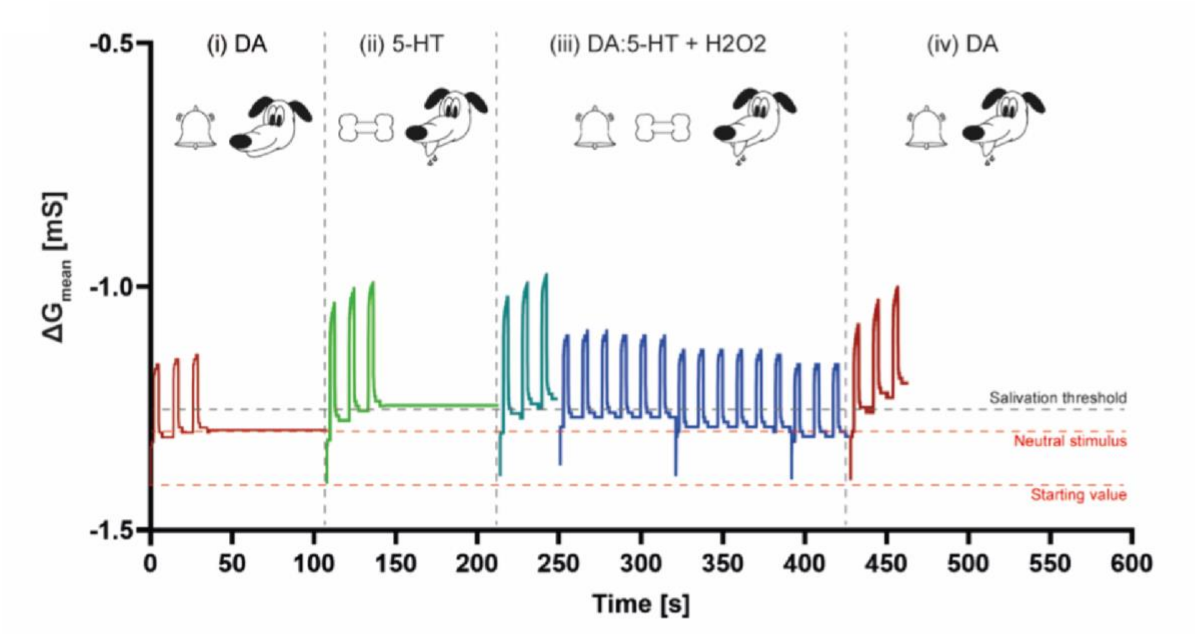

Figure 3.37 | Associative Pavlovian learning demonstrate in the neuromorphic OECTs, functionalized with a brain-SLB. **i**) Neutral stimulus supplied as DA 30 µM. A washing procedure followed the stimulation by using H_2O_2 60 mM. **ii**) Unconditioned stimulus supplied as 5-HT 30 µM, and definition of the salivation threshold, *i.e.*, unconditioned response. A washing procedure followed the stimulation by using H_2O_2 60 mM, not shown for better visualization. **iii**) Associative learning achieved through the application of both stimuli at the same time:DA:5-HT solution as electrolyte (ratio 1:1, 30 µM:30 µM). A washing procedure followed the stimulation, by using H_2O_2 60 mM. **iv**) The associative learning was tested by supplying again the neutral stimulus.

3.4. Closed-loop neuromorphic system

The last application of this thesis work focused on the emulation of the complex closed-loop circuitry that the human brain exploits to accomplish countless tasks. In particular, the learning and control of voluntary movements involve a multi-area, closed-loop circuit (known as nigrostriatal pathway) in which DA signals from the midbrain modulate the integration of descending control signals from the motor cortex in the striatum to generate motor output[92]. Here, by drawing inspiration from such closed-loop implementations of motor learning in the brain, a closed-loop neuromorphic platform based on a neuromorphic OECT was developed (**Fig. 3.38**), in which the dopaminergic signaling of the brain is exploited to drive a conventional mechatronic system like a prosthetic hand. Here the neuromorphic system learns from DA-mediated signal, mirroring what happens in the brain's motor-loop and ultimately leading to the fine control of the robotic hand. In addition, DA-mediated reinforcement learning was achieved. Importantly, the aim of this last part was to achieve bio-inspired learning in neuromorphic closed-loop system while demonstrating the possibility of interfacing such technologies with commercially available silicon platform.

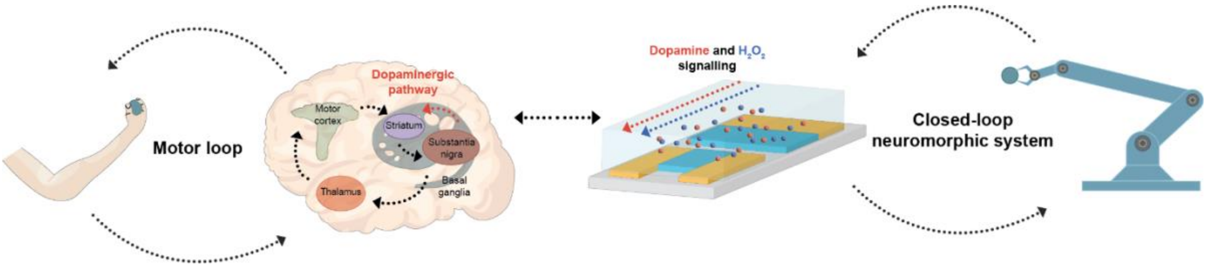

Figure 3.38 | Schematic of the closed-loop application.

The core of the closed-loop platform was a neuromorphic OECT, fabricated as discussed in **Material and Methods 2.7.1** and coupled to a microfluidic chamber made of PDMS. Closed-loop operations were carried out in cooperation with Daniela Rana, Tissue Electronics lab at the Italian Institute of Technology, Naples. Synaptic potentiation and depression were emulated (**Fig. 3.39**). In brief, the application of a square voltage pulse at the gate terminal, mirrored the arrival of an AP at the presynaptic domain. While in biological synapses neurotransmitters are released, in the artificial counterpart the ionic communication was recapitulated by DA or H_2O_2 electrolytic solutions. Lastly, conductance increase/decrease emulated synaptic depression/potentiation.

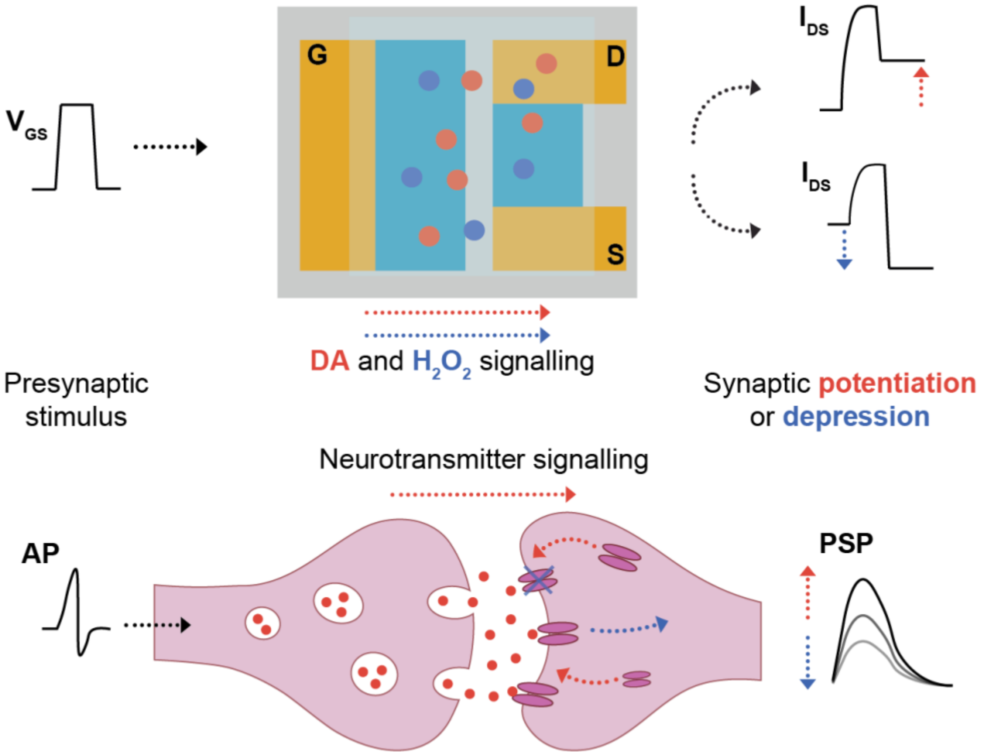

Figure 3.39 | Comparison between the synaptic transistor and a biological synapse, in which the synaptic plasticity is emulated by PEDOT:PSS oxidation/reduction.

The closed-loop neuromorphic system is shown in **Fig. 3.40** in which the neuromorphic OECT was coupled to a silicon microcontroller and a 3D-printed robotic hand to achieve a closed-loop regulation and an execution of a real-world task: opening or closing the hand. The completion of the task was mapped as a specific channel current value (a setpoint that can be arbitrarily chosen), while a control system regulated the competing flowrates of DA/H_2O_2, to decrease/increase the current level and reach such value.

At each iteration of the loop, a square voltage pulse (amp = 0.3 V, PW = 1 s, Δt = 9 s) was applied at the gate terminal, while the drain electrode was constantly biased of –0.2 V with respect to the source. The channel current was then measured (IMEAS), after the removal of the square voltage pulse, to not include the transient response of the transistor[193] (ions injected from the electrolyte to the polymeric channel during pulse ON and then migrating back to the electrolyte during pulse OFF). IMEAS was then compared to the setpoint (ISET), to compute an error *e*, *i.e.*, *e* = ISET – IMEAS. Such error e represented the input value signal of a PID controller, that computed a control law *u*, as a linear combination of *e*, its integral and its derivative with respect to time.

The control law u determined the flowrates of either DA or H_2O_2 needed to minimize the error *e*. A square voltage pulse was applied at the gate terminal, oxidizing DA (if present), changing the channel conductance and starting a new iteration. This process was repeated until the channel current reached the setpoint ($e \cong 0$). At the same time, the value of the measured current was sent to a microcontroller, which determined an input signal for some servomotors driving the 3D printed hand. By changing ISET, it was possible to decide whether the hand should open or close and thus transducing synaptic potentiation/depression into movements. Further details are discussed in **Materials and Methods 2.7.2**.

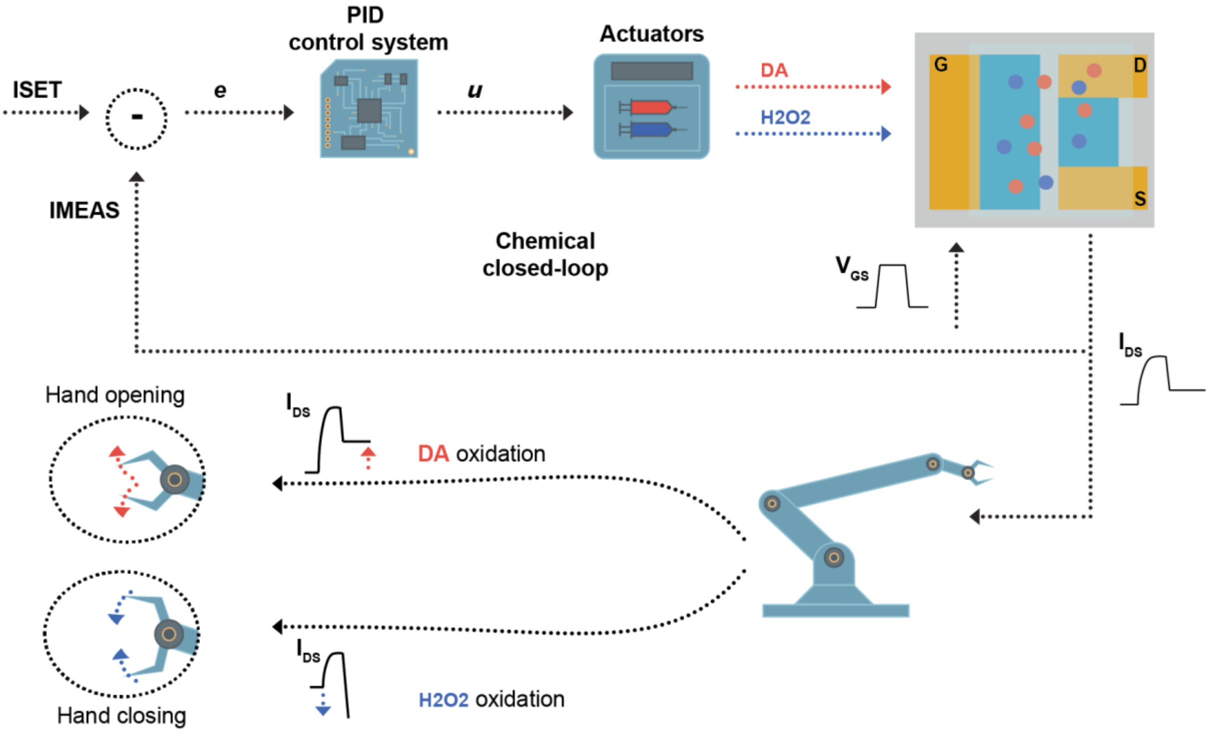

Figure 3.40 | Schematic of the closed-loop neuromorphic system. The loop is made of a PID controller (software) driving actuators to release either DA or H_2O_2 to regulate the conductance of the OECT. At the same time, the channel current is digitalized and sent to microcontroller to open/close a 3D printed robotic hand.

A neuromorphic closed-loop measurements is shown in **Fig. 3.41-a**, in which the channel current was plotted versus the number of control steps (iterations of the closed loop). Two setpoints were chosen (I_1 and I_2). Initially, the measured current was lower than the setpoint $I_1$and synaptic potentiation was required to achieve the regulation task. Indeed, DA was released inside the electrolyte of the OECT and subsequently oxidized. Such oxidation caused the reduction of the PEDOT:PSS at the channel, decreasing the absolute value of the current flowing in the channel. After a certain amount of control steps, the setpoint was reached. Simultaneously, the robotic hand was progressively opening, until full aperture occurring when channel current entered the area highlighted in yellow. Subsequently, the setpoint was changed from I_1 to I_2.

Here, the OECT required synaptic depression to complete the regulation task, as IMES was higher than ISET. The PID provided the correct control law *u* to release H_2O_2 in the electrolyte of the OECT oxidizing the channel of the transistor and increasing the current, until the setpoint was reached and the robotic hand was completely closed. The process was iterated more than once (also using different OECTs), to demonstrate reproducibility. Further details are available in **Materials and Methods 2.7.3**.

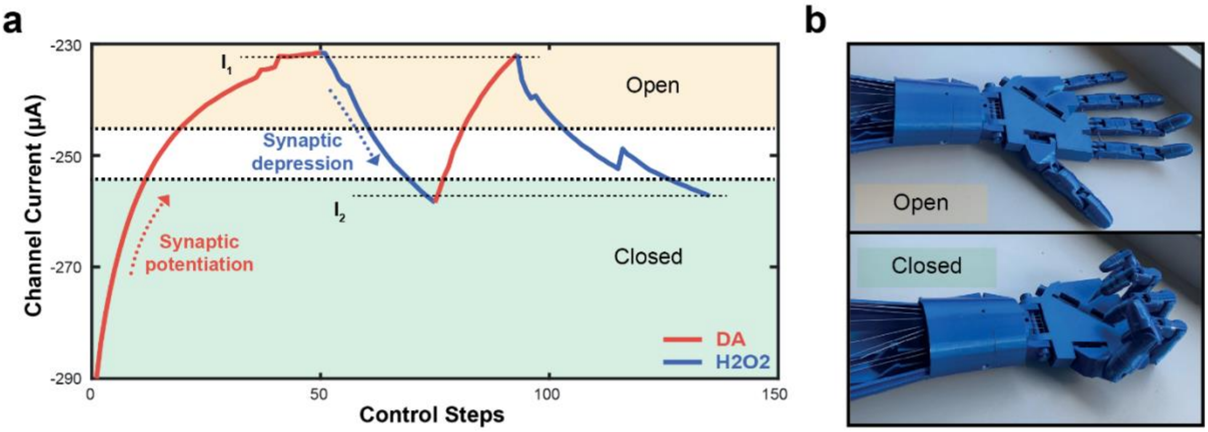

Figure 3.41 | **a**) Measurements of the closed-loop neuromorphic system, in which two setpoints are chosen (I1 and i2), and synaptic potentiation/depression were activated to complete the regulation task. **b**) At the same time a 3D printed robotic hand was controlled by a microcontroller transducing synaptic potentiation/depression into opening/closing commands. As a result, the hand was completely closed or open in the corresponding current regions (**a**, yellow and green boxes).

Furthermore, a pressure sensor was integrated into the 3D robotic hand to sense the closure of the hand. Another neuromorphic closed-loop system was developed (**Fig. 3.42**), which was able to demonstrate autonomous reinforcement learning. In this case, the robotic hand was required to accomplish a task (grasp an object). Initially, the system tried to grasp the object using the reading of the sensor to determine whether the object was grasped or not. In case of failure, a punishment signal was sent to the neuromorphic OECT (DA was introduced in the electrolyte and a square voltage pulse was applied at the gate terminal). As a result, the polymeric channel of the OECT was de-doped decreasing the channel current. Such current decrease was encoded as further hand closure. By iterating such process, the hand was able to grasp the object eliciting the release of a reward signal (V_{GS} = 0 V) and stopping the learning procedure.

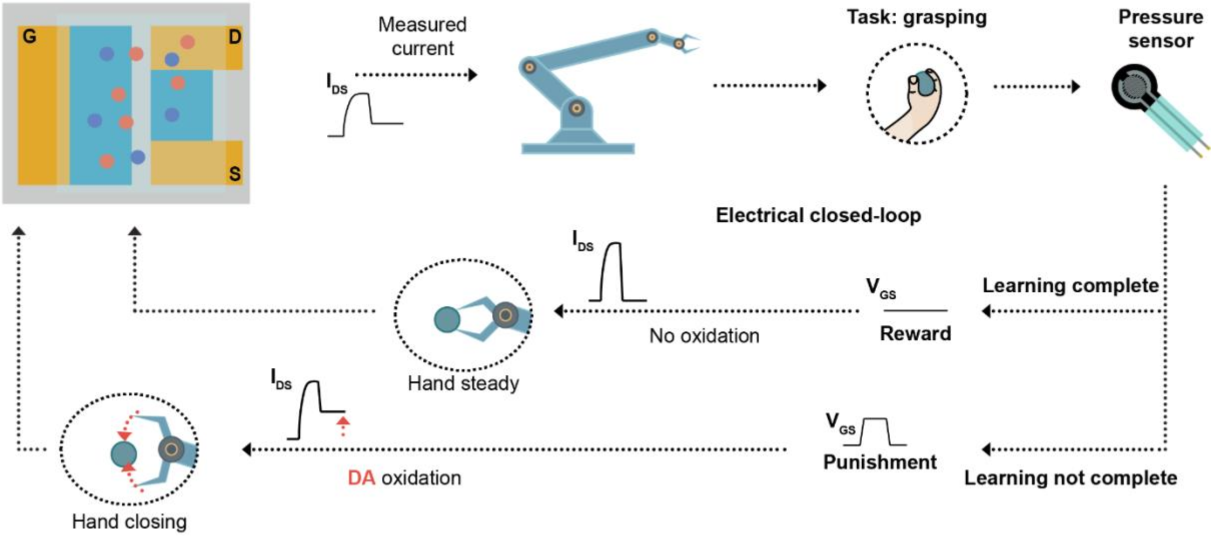

Figure 3.42 | Schematic of the neuromorphic closed-loop system for reinforcement learning. A pressure sensor is used to read the possible grasp of an object. If the grasp is failed, learning is not complete and DA is oxidized as punishment signal, to further close the hand. In case of a successful grasp, learning is complete, and the hand movements stop.

A reinforcement learning experiment is shown in **Fig. 3.43-a**, in which three quantities were reported. First, the reading of the pressure sensor that described whether the hand came into contact with the target object. Second, the angle of the servomotors driving the hand. An increase in the angle meant that the hand is furtherly closing while when the angle was constant, the hand was not moving. Third the channel current of the OECT (the learning curve of the neuromorphic OECT) determining whether punishment or reward had to be delivered. Two objects were employed: a tennis ball and a ping pong ball.

Initially, the tennis ball was employed (**Fig. 3.43-a**, **i**). As the robotic hand failed the grasping task, punishment signals were sent decreasing the amount of current and furtherly closing the hand (increasing motor angle). Eventually, the reading of the pressure sensor revealed a contact stopping the procedure (no further DA oxidation and constant motor angle). Subsequently, after the OECT learnt how to grasp the first object, the ping pong ball was introduced (**Fig. 3.43-a**, **ii**). Given that this second object was smaller in size of the first one, the hand could not complete a grasp (the pressure sensor revealed no contact). The punishment signal was sent again, furtherly decreasing IDS and closing the hand even more (increasing motor angle). Eventually, the reading of the pressure would reveal a contact with the second object, stopping the procedure again. Lastly, the former object (tennis ball) was introduced again (**Fig. 3.43-a**, **iii**). In this case the neuromorphic OECT could grab the object immediately, as it had already learned how to grasp it.

Pictures of the three steps of the learning experiments are shown in **Fig. 3.43-b**, **i**, **ii** and **iii**.

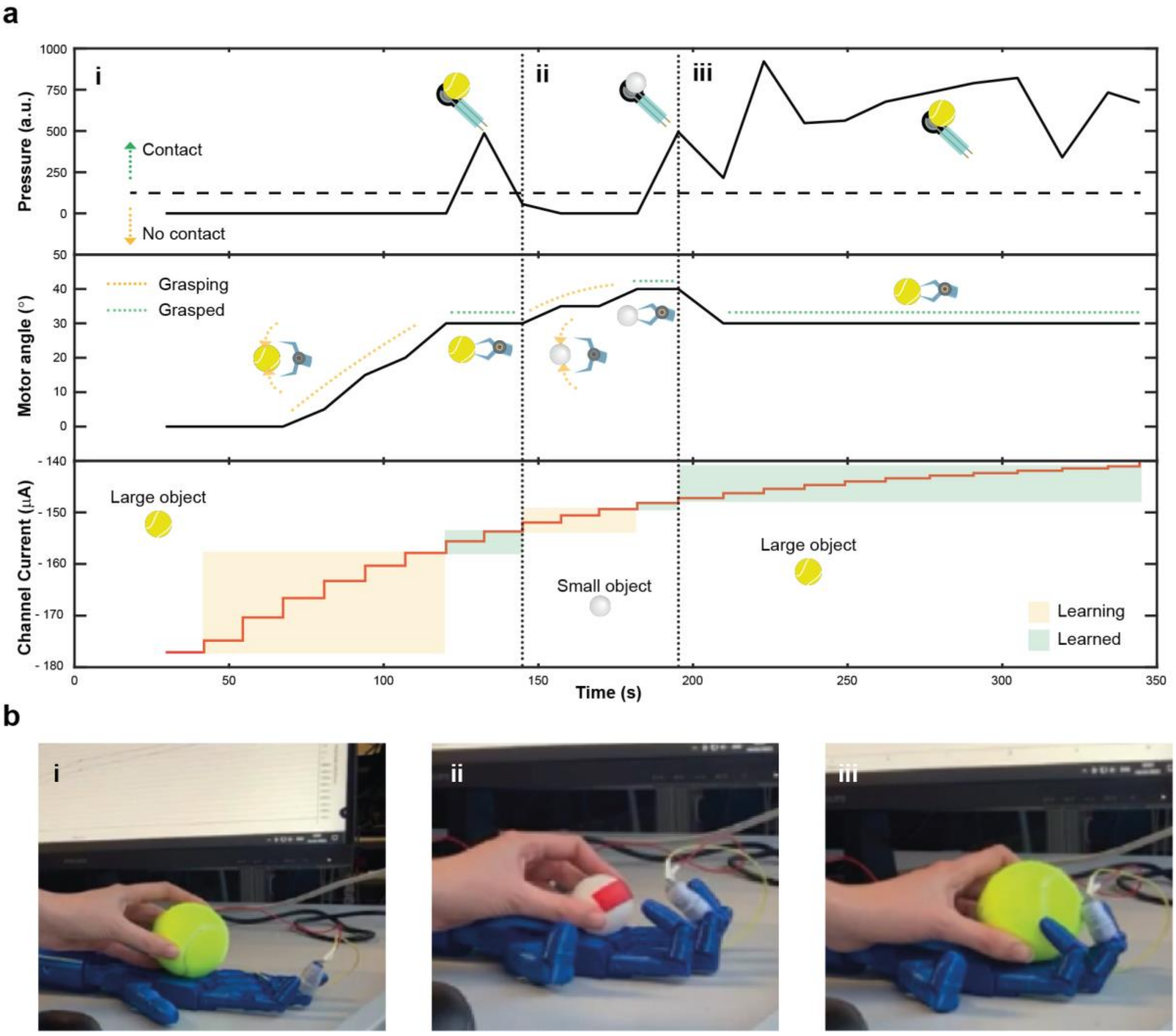

Figure 3.43 | **a**) Reinforcement learning experiment. **i**) The tennis ball is introduced. **ii**) Introduction of the ping pong ball. **iii**) The former object is introduced again. **b**) Photos of the three steps of the experiment.

Chapter 4: Conclusion

Drawing inspiration from the human brain, *i.e.*, the most efficient computer available in nature, neuromorphic engineering started to develop innovative hardware. Indeed, by leveraging on bio-inspired designs and unique features of innovative materials, several prototypes and proof of concepts of the novel generation of hardware were demonstrated.

In this framework, organic materials and conducting polymers emerged as ideal candidates to develop electronic devices able to emulate neural processing, while naturally transducing ionic current into electronic ones. Two- and three-terminal devices were developed, demonstrating learning, hardware for matrix-vector-multiplication and in-memory computing. In addition, these materials were shown to minimize the mechanical mismatch between electronic devices and biological tissue, offering a seamless integration. Indeed, OECTs were shown to bridge such diverse worlds as electronics and biology, in a biohybrid synapse in which a direct communication between a presynaptic biological terminal and a postsynaptic artificial one was established.

Here, OECTs-based platforms were designed to possibly interface with biology, while emulating the way in which the nervous system deals with information processing. Neuromorphic sensors, emulating the sense of touch and vision, were developed. The formed was able to achieve a memorization of a pressure stimulation, in a fully organic platform without the need of enforcing non-volatility with external hardware.

The sense of vision, on the other hand, was emulated by chemically synthetizing an azobenzene functionalized PEDOT:PSS, which was able to induce a faradic charge transfer upon light stimulation. As conductivity was depleted by light exposure, the OFF vertical pathway of the human retina was emulated, in which the light entering the cornea of the eye silences a group of spiking neurons projecting into the visual cortex. In addition, optoelectronic memorization was shown by characterizing a write/erase procedure by means of light and negative erasing voltage stimuli, emulating the human memory compartmentalization.

Subsequently, as redox reactions were shown to regulate conductance levels of organic conducting polymers, a 2D drift-diffusion-reaction model was developed allowing to analyse and predict the effect of reactive species on the ionic environment of the electrolyte solution of OECTs. A clear dependence of redox reactions on the conductivity of the electrolyte was simulated and experimentally confirmed.

Neurotransmitter-mediated LTP was reproduced and investigated. Indeed, when a reactive molecule as dopamine or serotonin is oxidized at the gate terminal of the transistor, a faradic charge transfer process is elicited, de-doping the polymer that covers the gate terminal. As a result, to maintain electroneutrality, de-doping of the polymeric channel occurs, changing the conductance of the device in a non-volatile manner. Such process was characterized as a function of the concentration of the neurotransmitter, also achieving co-modulation and selectivity.

The emulation of LTD was then achieved by polymer oxidation, mediated by hydrogen peroxide. Here, no dependence on the concentration was found suggesting that, unlike the neurotransmitter oxidation that de-doped the whole bulk of the polymer, such solution was only able to dope the surface of the polymer. By integrating a microfluidic system with the neuromorphic OECTs, it was possible to demonstrate real time regulation of the conductance of a neuromorphic device in a closed-loop fashion, in which a standard PID controller was employed to build a closed-loop neuromorphic system. Here, the system demonstrated the potential of organic devices to cooperate with silicon technologies to build a hybrid system, which bridges the novelty of innovative materials and the know-how of well-established engineering techniques and approaches in system design.

Indeed, the closure of 3D printed robotic hard was controlled by oxidizing or reducing the channel of an organic transistor in response to neurotransmitters released in an electrolytic environment, emulating biologically relevant processes. Furthermore, reinforcement learning was shown, endowing the system with sensor to perceive the environment (the hand could sense the contact with objects) to teach the neuromorphic device to grasp spheres of different sizes.

Lastly, the possibility of structural biomimicry was investigated by coupling OECTs with SLBs, *i.e.*, biomembranes closely emulating the biological one. Notably, embedding of these membranes in a OECT was demonstrated and characterized, surprisingly showing that the non-complete ionic permeability of such bilayer could be exploited to emulate STP in neuromorphic devices, eliciting a charge trapping mechanism.

Furthermore, by optimizing a protocol to selectively confine SLBs on the channel of the transistor, modulation of LTP was demonstrated allowing to emulate associative learning, as formulated by Pavlovian classical conditioning theory.

In conclusion, this work wants to demonstrate the flexibility of OECTs platforms that can be *ad hoc* engineered to emulate several features of the brain, from sensing to memory compartmentalization. Pivotal is the unique feature of mixed ionic-electronic conductors to effortlessly transduce ions into electrons, emerging as natural candidates in the bridging of electronical and biological systems. As a future perspective, OECTs may represent a building block toward truly hybrid system, in which neuromorphic and in-memory computation could allow for smart biointerfacing devices, that could continuously adapt to communicate with living and always evolving biological tissue, while offering a clean, stable and reliable electronic readouts for artificial computing systems.

References

1. Kandel, E. R., Schwartz, J. H., Jessell, T. M., Siegelbaum, S. A. & Hudspeth, A. J. *Principles of Neural Science*. vol. 4 (McGraw-hill New York, 2000).
2. Marković, D., Mizrahi, A., Querlioz, D. & Grollier, J. Physics for neuromorphic computing. *Nat. Rev. Phys.* **2**, 499–510 (2020).
3. Raghavan, M., Fee, D. & Barkhaus, P. E. Chapter 1 - Generation and propagation of the action potential. in *Handbook of Clinical Neurology* (eds. Levin, K. H. & Chauvel, P.) vol. 160 3–22 (Elsevier, 2019).
4. Yèagle, P. L. Lipid regulation of cell membrane structure and function. *FASEB J.* **3**, 1833–1842 (1989).
5. Cardozo, D. An intuitive approach to understanding the resting membrane potential. *Adv. Physiol. Educ.* **40**, 543–547 (2016).
6. Hodgkin, A. L. & Huxley, A. F. A quantitative description of membrane current and its application to conduction and excitation in nerve. *J. Physiol.* **117**, 500–544 (1952).
7. Ackerman, M. J. & Clapham, D. E. Ion Channels — Basic Science and Clinical Disease. *N. Engl. J. Med.* **336**, 1575–1586 (1997).
8. Jäkel, S. & Dimou, L. Glial Cells and Their Function in the Adult Brain: A Journey through the History of Their Ablation. *Front. Cell. Neurosci.* **11**, (2017).
9. Peles, E. & Salzer, J. L. Molecular domains of myelinated axons. *Curr. Opin. Neurobiol.* **10**, 558–565 (2000).
10. Mariano, A. *et al.* Advances in Cell-Conductive Polymer Biointerfaces and Role of the Plasma Membrane. *Chem. Rev.* **122**, 4552–4580 (2022).
11. Janson, I. A. & Putnam, A. J. Extracellular matrix elasticity and topography: Material-based cues that affect cell function via conserved mechanisms. *J. Biomed. Mater. Res. A* **103**, 1246–1258 (2015).
12. Wang, T., Nanda, S. S., Papaefthymiou, G. C. & Yi, D. K. Mechanophysical Cues in Extracellular Matrix Regulation of Cell Behavior. *ChemBioChem* **21**, 1254–1264 (2020).
13. Kshitiz, Afzal, J., Kim, S.-Y. & Kim, D.-H. A nanotopography approach for studying the structure-function relationships of cells and tissues. *Cell Adhes. Migr.* **9**, 300–307 (2015).
14. Cox, T. R. & Erler, J. T. Remodeling and homeostasis of the extracellular matrix: implications for fibrotic diseases and cancer. *Dis. Model. Mech.* **4**, 165–178 (2011).
15. Jansen, K. A., Atherton, P. & Ballestrem, C. Mechanotransduction at the cell-matrix interface. *Semin. Cell Dev. Biol.* **71**, 75–83 (2017).

16. van Deenen, L. L. M. Phospholipids and biomembranes. *Prog. Chem. Fats Other Lipids* **8**, 1–127 (1966).
17. Pichot, R., Watson, R. L. & Norton, I. T. Phospholipids at the Interface: Current Trends and Challenges. *Int. J. Mol. Sci.* **14**, 11767–11794 (2013).
18. Milosevic, I. *et al.* Plasmalemmal Phosphatidylinositol-4,5-Bisphosphate Level Regulates the Releasable Vesicle Pool Size in Chromaffin Cells. *J. Neurosci.* **25**, 2557–2565 (2005).
19. Di Paolo, G. & De Camilli, P. Phosphoinositides in cell regulation and membrane dynamics. *Nature* **443**, 651–657 (2006).
20. Simons, K. & Ikonen, E. Functional rafts in cell membranes. *Nature* **387**, 569–572 (1997).
21. Igarashi, M., Honda, A., Kawasaki, A. & Nozumi, M. Neuronal Signaling Involved in Neuronal Polarization and Growth: Lipid Rafts and Phosphorylation. *Front. Mol. Neurosci.* **13**, (2020).
22. Allen, J. A., Halverson-Tamboli, R. A. & Rasenick, M. M. Lipid raft microdomains and neurotransmitter signalling. *Nat. Rev. Neurosci.* **8**, 128–140 (2007).
23. Olsen, A. S. B. & Færgeman, N. J. Sphingolipids: membrane microdomains in brain development, function and neurological diseases. *Open Biol.* **7**, 170069 (2017).
24. Jędrzejewska-Szmek, J. & Blackwell, K. T. From membrane receptors to protein synthesis and actin cytoskeleton: Mechanisms underlying long lasting forms of synaptic plasticity. *Semin. Cell Dev. Biol.* **95**, 120–129 (2019).
25. Trimble, W. S. & Grinstein, S. Barriers to the free diffusion of proteins and lipids in the plasma membrane. *J. Cell Biol.* **208**, 259–271 (2015).
26. Hedin, L. E., Illergård, K. & Elofsson, A. An Introduction to Membrane Proteins. *J. Proteome Res.* **10**, 3324–3331 (2011).
27. Carruthers, A. Mechanisms for the facilitated diffusion of substrates across cell membranes. *Biochemistry* **30**, 3898–3906 (1991).
28. Dubyak, G. R. Ion homeostasis, channels, and transporters: an update on cellular mechanisms. *Adv. Physiol. Educ.* **28**, 143–154 (2004).
29. Chowdhury, S., Jarecki, B. W. & Chanda, B. A Molecular Framework for Temperature-Dependent Gating of Ion Channels. *Cell* **158**, 1148–1158 (2014).
30. Hucho, F. & Weise, C. Ligand-Gated Ion Channels. *Angew. Chem. Int. Ed.* **40**, 3100–3116 (2001).

31. Bezanilla, F. Voltage-Gated Ion Channels. in *Biological Membrane Ion Channels: Dynamics, Structure, and Applications* (eds. Chung, S.-H., Andersen, O. S. & Krishnamurthy, V.) 81–118 (Springer, New York, NY, 2007). doi:10.1007/0-387-68919-2_3.
32. Dipalo, M. *et al.* Intracellular and Extracellular Recording of Spontaneous Action Potentials in Mammalian Neurons and Cardiac Cells with 3D Plasmonic Nanoelectrodes. *Nano Lett.* **17**, 3932–3939 (2017).
33. Spira, M. E. & Hai, A. Multi-electrode array technologies for neuroscience and cardiology. *Nat. Nanotechnol.* **8**, 83–94 (2013).
34. Massobrio, G., Martinoia, S. & Massobrio, P. Equivalent Circuit of the Neuro-Electronic Junction for Signal Recordings From Planar and Engulfed Micro-Nano-Electrodes. *IEEE Trans. Biomed. Circuits Syst.* **12**, 3–12 (2018).
35. Bruno, U., Mariano, A. & Santoro, F. A systems theory approach to describe dynamic coupling at the cell–electrode interface. *APL Mater.* **9**, 011103 (2021).
36. Bechtel, T. J., Reyes-Robles, T., Fadeyi, O. O. & Oslund, R. C. Strategies for monitoring cell–cell interactions. *Nat. Chem. Biol.* **17**, 641–652 (2021).
37. Akins, M. R. & Biederer, T. Cell–cell interactions in synaptogenesis. *Curr. Opin. Neurobiol.* **16**, 83–89 (2006).
38. Rutishauser, U., Acheson, A., Hall, A. K., Mann, D. M. & Sunshine, J. The Neural Cell Adhesion Molecule (NCAM) as a Regulator of Cell-Cell Interactions. *Science* **240**, 53–57 (1988).
39. Fry, C. H. & Jabr, R. I. The action potential and nervous conduction. *Surg. Oxf.* **28**, 49–54 (2010).
40. Gallistel, C. R., Rolls, E. & Greene, D. Neuron Function Inferred from Behavioral and Electrophysiological Estimates of Refractory Period. *Science* **166**, 1028–1030 (1969).
41. Perez de Arce, K. *et al.* Topographic Mapping of the Synaptic Cleft into Adhesive Nanodomains. *Neuron* **88**, 1165–1172 (2015).
42. Ackermann, F., Waites, C. L. & Garner, C. C. Presynaptic active zones in invertebrates and vertebrates. *EMBO Rep.* **16**, 923–938 (2015).
43. Reiner, A. & Levitz, J. Glutamatergic Signaling in the Central Nervous System: Ionotropic and Metabotropic Receptors in Concert. *Neuron* **98**, 1080–1098 (2018).
44. Gwynne, R. M. & Bornstein, J. C. Synaptic Transmission at Functionally Identified Synapses in the Enteric Nervous System: Roles for Both Ionotropic and Metabotropic Receptors. *Curr. Neuropharmacol.* **5**, 1–17.

45. Citri, A. & Malenka, R. C. Synaptic Plasticity: Multiple Forms, Functions, and Mechanisms. *Neuropsychopharmacology* **33**, 18–41 (2008).
46. Magee, J. C. & Grienberger, C. Synaptic Plasticity Forms and Functions. *Annu. Rev. Neurosci. 2020* **43**, 95–117.
47. Schulz, P. E. & Fitzgibbons, J. C. Differing Mechanisms of Expression for Short- and Long-Term Potentiation. *J. Neurophysiol.* **78**, 321–334 (1997).
48. Zucker, R. S. & Regehr, W. G. Short-Term Synaptic Plasticity. *Annu. Rev. Physiol.* **64**, 355–405 (2002).
49. Jackman, S. L. & Regehr, W. G. The Mechanisms and Functions of Synaptic Facilitation. *Neuron* **94**, 447–464 (2017).
50. Munakata, Y. & Pfaffly, J. Hebbian learning and development. *Dev. Sci.* **7**, 141–148 (2004).
51. Bliss, T. V. P. & Lømo, T. Long-lasting potentiation of synaptic transmission in the dentate area of the anaesthetized rabbit following stimulation of the perforant path. *J. Physiol.* **232**, 331–356 (1973).
52. Mayer, M. L., Westbrook, G. L. & Guthrie, P. B. Voltage-dependent block by Mg2+ of NMDA responses in spinal cord neurones. *Nature* **309**, 261–263 (1984).
53. Feldman, D. E. The Spike-Timing Dependence of Plasticity. *Neuron* **75**, 556–571 (2012).
54. Song, S. & Abbott, L. F. Cortical Development and Remapping through Spike Timing-Dependent Plasticity. *Neuron* **32**, 339–350 (2001).
55. Wu, Y. K., Miehl, C. & Gjorgjieva, J. Regulation of circuit organization and function through inhibitory synaptic plasticity. *Trends Neurosci.* **45**, 884–898 (2022).
56. Shouval, H., Wang, S. & Wittenberg, G. Spike Timing Dependent Plasticity: A Consequence of More Fundamental Learning Rules. *Front. Comput. Neurosci.* **4**, (2010).
57. Sutton, R. S. & Barto, A. G. Toward a modern theory of adaptive networks: expectation and prediction. *Psychol. Rev.* **88**, 135–170 (1981).
58. Frémaux, N. & Gerstner, W. Neuromodulated Spike-Timing-Dependent Plasticity, and Theory of Three-Factor Learning Rules. *Front. Neural Circuits* **9**, (2016).
59. Fusi, S. & Abbott, L. F. Limits on the memory storage capacity of bounded synapses. *Nat. Neurosci.* **10**, 485–493 (2007).
60. Steinberg, E. E. *et al.* A causal link between prediction errors, dopamine neurons and learning. *Nat. Neurosci.* **16**, 966–973 (2013).
61. Berke, J. D. What does dopamine mean? *Nat. Neurosci.* **21**, 787–793 (2018).

62. Gu, Q. Neuromodulatory transmitter systems in the cortex and their role in cortical plasticity. *Neuroscience* **111**, 815–835 (2002).
63. Brzosko, Z., Zannone, S., Schultz, W., Clopath, C. & Paulsen, O. Sequential neuromodulation of Hebbian plasticity offers mechanism for effective reward-based navigation. *eLife* **6**, e27756 (2017).
64. Gerstner, W., Lehmann, M., Liakoni, V., Corneil, D. & Brea, J. Eligibility Traces and Plasticity on Behavioral Time Scales: Experimental Support of NeoHebbian Three-Factor Learning Rules. *Front. Neural Circuits* **12**, (2018).
65. Izhikevich, E. M. Solving the Distal Reward Problem through Linkage of STDP and Dopamine Signaling. *Cereb. Cortex* **17**, 2443–2452 (2007).
66. Raymond, J. L. & Medina, J. F. Computational Principles of Supervised Learning in the Cerebellum. *Annu. Rev. Neurosci.* **41**, 233–253 (2018).
67. Kawato, M. Internal models for motor control and trajectory planning. *Curr. Opin. Neurobiol.* **9**, 718–727 (1999).
68. Muller, S. Z., Zadina, A. N., Abbott, L. F. & Sawtell, N. B. Continual Learning in a Multi-Layer Network of an Electric Fish. *Cell* **179**, 1382-1392.e10 (2019).
69. Bell, C. C., Han, V. Z., Sugawara, Y. & Grant, K. Synaptic plasticity in a cerebellum-like structure depends on temporal order. *Nature* **387**, 278–281 (1997).
70. Marques, T., Nguyen, J., Fioreze, G. & Petreanu, L. The functional organization of cortical feedback inputs to primary visual cortex. *Nat. Neurosci.* **21**, 757–764 (2018).
71. Steward, O. & Scoville, S. A. Cells of origin of entorhinal cortical afferents to the hippocampus and fascia dentata of the rat. *J. Comp. Neurol.* **169**, 347–370 (1976).
72. Stuart, G. J. & Sakmann, B. Active propagation of somatic action potentials into neocortical pyramidal cell dendrites. *Nature* **367**, 69–72 (1994).
73. Xu, N. *et al.* Nonlinear dendritic integration of sensory and motor input during an active sensing task. *Nature* **492**, 247–251 (2012).
74. Bittner, K. C. *et al.* Conjunctive input processing drives feature selectivity in hippocampal CA1 neurons. *Nat. Neurosci.* **18**, 1133–1142 (2015).
75. Gambino, F. *et al.* Sensory-evoked LTP driven by dendritic plateau potentials in vivo. *Nature* **515**, 116–119 (2014).
76. Golding, N. L., Staff, N. P. & Spruston, N. Dendritic spikes as a mechanism for cooperative long-term potentiation. *Nature* **418**, 326–331 (2002).
77. Bittner, K. C., Milstein, A. D., Grienberger, C., Romani, S. & Magee, J. C. Behavioral time scale synaptic plasticity underlies CA1 place fields. *Science* **357**, 1033–1036 (2017).

78. Zhao, X., Wang, Y., Spruston, N. & Magee, J. C. Synaptic mechanisms of context-dependent sensory responses in the hippocampus. 624262 Preprint at https://doi.org/10.1101/624262 (2019).
79. Somjen, G. *Sensory Coding in the Mammalian Nervous System*. (Springer US, Boston, MA, 1975). doi:10.1007/978-1-4684-1707-4.
80. Harris, K. D. & Mrsic-Flogel, T. D. Cortical connectivity and sensory coding. *Nature* **503**, 51–58 (2013).
81. Adrian, E. D. & Zotterman, Y. The impulses produced by sensory nerve endings. *J. Physiol.* **61**, 465–483 (1926).
82. Gray, J. A. B. & Sato, M. Properties of the receptor potential in Pacinian corpuscles. *J. Physiol.* **122**, 610–636 (1953).
83. Wang, F. *et al.* Sensory Afferents Use Different Coding Strategies for Heat and Cold. *Cell Rep.* **23**, 2001–2013 (2018).
84. Doetsch, G. S. Patterns in the brain: Neuronal population coding in the somatosensory system. *Physiol. Behav.* **69**, 187–201 (2000).
85. Encyclopedia Britannica | Britannica. https://www.britannica.com/.
86. Marzvanyan, A. & Alhawaj, A. F. Physiology, Sensory Receptors. in *StatPearls* (StatPearls Publishing, Treasure Island (FL), 2024).
87. Kennedy, P. M. & Inglis, J. T. Distribution and behaviour of glabrous cutaneous receptors in the human foot sole. *J. Physiol.* **538**, 995–1002 (2002).
88. Haberberger, R. V., Barry, C., Dominguez, N. & Matusica, D. Human Dorsal Root Ganglia. *Front. Cell. Neurosci.* **13**, (2019).
89. Hildebrand, G. D. & Fielder, A. R. Anatomy and Physiology of the Retina. in *Pediatric Retina* (eds. Reynolds, J. & Olitsky, S.) 39–65 (Springer, Berlin, Heidelberg, 2011). doi:10.1007/978-3-642-12041-1_2.
90. Joselevitch, C. Human retinal circuitry and physiology. *Psychol. Neurosci.* **1**, 141 (20110919).
91. Boccuni, I. & Fairless, R. Retinal Glutamate Neurotransmission: From Physiology to Pathophysiological Mechanisms of Retinal Ganglion Cell Degeneration. *Life Basel Switz.* **12**, 638 (2022).
92. Lanciego, J. L., Luquin, N. & Obeso, J. A. Functional Neuroanatomy of the Basal Ganglia. *Cold Spring Harb. Perspect. Med.* **2**, a009621 (2012).

93. Wang, A. R., Groome, A., Taniguchi, L., Eshel, N. & Bentzley, B. S. The role of dopamine in reward-related behavior: shining new light on an old debate. *J. Neurophysiol.* **124**, 309–311 (2020).

94. Lewis, R. G., Florio, E., Punzo, D. & Borrelli, E. The Brain's Reward System in Health and Disease. *Adv. Exp. Med. Biol.* **1344**, 57–69 (2021).

95. Mead, C. Neuromorphic electronic systems. *Proc. IEEE* **78**, 1629–1636 (1990).

96. Boahen, K. Dendrocentric learning for synthetic intelligence. *Nature* **612**, 43–50 (2022).

97. Yang, J.-Q. *et al.* Neuromorphic Engineering: From Biological to Spike-Based Hardware Nervous Systems. *Adv. Mater.* **32**, 2003610 (2020).

98. Duan, Y., Edwards, J. S. & Dwivedi, Y. K. Artificial intelligence for decision making in the era of Big Data – evolution, challenges and research agenda. *Int. J. Inf. Manag.* **48**, 63–71 (2019).

99. Tian, Y. Artificial Intelligence Image Recognition Method Based on Convolutional Neural Network Algorithm. *IEEE Access* **8**, 125731–125744 (2020).

100. Iqbal Quraishi, Md., Pal Choudhury, J. & De, M. Image recognition and processing using Artificial Neural Network. in *2012 1st International Conference on Recent Advances in Information Technology (RAIT)* 95–100 (2012). doi:10.1109/RAIT.2012.6194487.

101. Abdel-Hamid, O. *et al.* Convolutional Neural Networks for Speech Recognition. *IEEEACM Trans. Audio Speech Lang. Process.* **22**, 1533–1545 (2014).

102. Brown, T. *et al.* Language Models are Few-Shot Learners. in *Advances in Neural Information Processing Systems* vol. 33 1877–1901 (Curran Associates, Inc., 2020).

103. Mehonic, A. & Kenyon, A. J. Brain-inspired computing needs a master plan. *Nature* **604**, 255–260 (2022).

104. Jouppi, N. P. *et al.* A domain-specific supercomputer for training deep neural networks. *Commun. ACM* **63**, 67–78 (2020).

105. Dally, W. J., Turakhia, Y. & Han, S. Domain-specific hardware accelerators. *Commun. ACM* **63**, 48–57 (2020).

106. Anthony, L. F. W., Kanding, B. & Selvan, R. Carbontracker: Tracking and Predicting the Carbon Footprint of Training Deep Learning Models. Preprint at https://doi.org/10.48550/arXiv.2007.03051 (2020).

107. News, C. H. & Network, part of the G. E. 'Tsunami of data' could consume one fifth of global electricity by 2025. *The Guardian* (2017).

108. Dally, W. J. *et al.* Hardware-Enabled Artificial Intelligence. in *2018 IEEE Symposium on VLSI Circuits* 3–6 (2018). doi:10.1109/VLSIC.2018.8502368.

109. Chua, L. Memristor-The missing circuit element. *IEEE Trans. Circuit Theory* **18**, 507–519 (1971).
110. Strukov, D. B., Snider, G. S., Stewart, D. R. & Williams, R. S. The missing memristor found. *Nature* **453**, 80–83 (2008).
111. Ielmini, D. & Wong, H.-S. P. In-memory computing with resistive switching devices. *Nat. Electron.* **1**, 333–343 (2018).
112. Waser, R. & Aono, M. Nanoionics-based resistive switching memories. *Nat. Mater.* **6**, 833–840 (2007).
113. Covi, E. *et al.* Analog Memristive Synapse in Spiking Networks Implementing Unsupervised Learning. *Front. Neurosci.* **10**, (2016).
114. Zhang, W. *et al.* Analog-Type Resistive Switching Devices for Neuromorphic Computing. *Phys. Status Solidi RRL – Rapid Res. Lett.* **13**, 1900204 (2019).
115. Valov, I., Waser, R., Jameson, J. R. & Kozicki, M. N. Electrochemical metallization memories—fundamentals, applications, prospects. *Nanotechnology* **22**, 254003 (2011).
116. Valasek, J. Piezo-Electric and Allied Phenomena in Rochelle Salt. *Phys. Rev.* **17**, 475–481 (1921).
117. Buck, D. A. *Ferroelectrics for Digital Information Storage and Switching*. https://dome.mit.edu/handle/1721.3/40244 (1952).
118. Majumdar, S., Tan, H., Qin, Q. H. & van Dijken, S. Energy-Efficient Organic Ferroelectric Tunnel Junction Memristors for Neuromorphic Computing. *Adv. Electron. Mater.* **5**, 1800795 (2019).
119. Esaki, a L., Laibowitz, R. B. & Stiles, P. J. Polar switch. *IBM Tech Discl Bull* **13**, 114 (1971).
120. Max, B., Hoffmann, M., Mulaosmanovic, H., Slesazeck, S. & Mikolajick, T. Hafnia-Based Double-Layer Ferroelectric Tunnel Junctions as Artificial Synapses for Neuromorphic Computing. *ACS Appl. Electron. Mater.* **2**, 4023–4033 (2020).
121. Mulaosmanovic, H., Chicca, E., Bertele, M., Mikolajick, T. & Slesazeck, S. Mimicking biological neurons with a nanoscale ferroelectric transistor. *Nanoscale* **10**, 21755–21763 (2018).
122. Gallo, M. L. & Sebastian, A. An overview of phase-change memory device physics. *J. Phys. Appl. Phys.* **53**, 213002 (2020).
123. Sebastian, A., Le Gallo, M., Khaddam-Aljameh, R. & Eleftheriou, E. Memory devices and applications for in-memory computing. *Nat. Nanotechnol.* **15**, 529–544 (2020).

124. Li, H. *et al.* Memristive Crossbar Arrays for Storage and Computing Applications. *Adv. Intell. Syst.* **3**, 2100017 (2021).
125. Li, C. *et al.* Analogue signal and image processing with large memristor crossbars. *Nat. Electron.* **1**, 52–59 (2018).
126. Jung, S. *et al.* A crossbar array of magnetoresistive memory devices for in-memory computing. *Nature* **601**, 211–216 (2022).
127. Shi, L., Zheng, G., Tian, B., Dkhil, B. & Duan, C. Research progress on solutions to the sneak path issue in memristor crossbar arrays. *Nanoscale Adv.* **2**, 1811–1827 (2020).
128. Study of the Selector Element for Resistive Memory - KU Leuven. https://kuleuven.limo.libis.be/discovery/fulldisplay/lirias1733031/32KUL_KUL:Lirias.
129. Zhang, Z. *et al.* Memory materials and devices: From concept to application. *InfoMat* **2**, 261–290 (2020).
130. Abderrahmane, N. & Miramond, B. Information Coding and Hardware Architecture of Spiking Neural Networks. in *2019 22nd Euromicro Conference on Digital System Design (DSD)* 291–298 (2019). doi:10.1109/DSD.2019.00050.
131. Schuman, C. D. *et al.* A Survey of Neuromorphic Computing and Neural Networks in Hardware. Preprint at https://doi.org/10.48550/arXiv.1705.06963 (2017).
132. Indiveri, G. *et al.* Neuromorphic Silicon Neuron Circuits. *Front. Neurosci.* **5**, (2011).
133. McCulloch, W. S. & Pitts, W. A logical calculus of the ideas immanent in nervous activity. *Bull. Math. Biophys.* **5**, 115–133 (1943).
134. Zendrikov, D., Solinas, S. & Indiveri, G. Brain-inspired methods for achieving robust computation in heterogeneous mixed-signal neuromorphic processing systems. *Neuromorphic Comput. Eng.* **3**, 034002 (2023).
135. Thorpe, S., Fize, D. & Marlot, C. Speed of processing in the human visual system. *Nature* **381**, 520–522 (1996).
136. Maass, W. Networks of spiking neurons: The third generation of neural network models. *Neural Netw.* **10**, 1659–1671 (1997).
137. Neuronal Dynamics - a neuroscience textbook by Wulfram Gerstner, Werner M. Kistler, Richard Naud and Liam Paninski. https://neuronaldynamics.epfl.ch/.
138. Bohte, S. M., La Poutre, H. & Kok, J. N. Unsupervised clustering with spiking neurons by sparse temporal coding and multilayer RBF networks. *IEEE Trans. Neural Netw.* **13**, 426–435 (2002).
139. Bohte, S. M. The evidence for neural information processing with precise spike-times: A survey. *Nat. Comput.* **3**, 195–206 (2004).

140. Stone, J. *Principles of Neural Information Theory: Computational Neuroscience and Metabolic Efficiency*. (2018).
141. Kasabov, N., Dhoble, K., Nuntalid, N. & Indiveri, G. Dynamic evolving spiking neural networks for on-line spatio- and spectro-temporal pattern recognition. *Neural Netw.* **41**, 188–201 (2013).
142. Izhikevich, E. M. Simple model of spiking neurons. *IEEE Trans. Neural Netw.* **14**, 1569–1572 (2003).
143. Delorme, A., Gautrais, J., van Rullen, R. & Thorpe, S. SpikeNET: A simulator for modeling large networks of integrate and fire neurons. *Neurocomputing* **26–27**, 989–996 (1999).
144. Wu, T., Zhang, L., Lyu, Q. & Jin, Y. Asynchronous spiking neural P systems with local synchronization of rules. *Inf. Sci.* **588**, 1–12 (2022).
145. Liu, Q., Pu, L. & Poo, M. Repeated cocaine exposure in vivo facilitates LTP induction in midbrain dopamine neurons. *Nature* **437**, 1027–1031 (2005).
146. Popovici, E., Bucci, A., Wiegand, R. & de Jong, E. Handbook of Natural Computing. *Handb. Nat. Comput.* (2012) doi:10.1007/978-3-540-92910-9_31.
147. Masquelier, T. & Kheradpisheh, S. R. Optimal Localist and Distributed Coding of Spatiotemporal Spike Patterns Through STDP and Coincidence Detection. *Front. Comput. Neurosci.* **12**, (2018).
148. Tavanaei, A. & Maida, A. S. A spiking network that learns to extract spike signatures from speech signals. *Neurocomputing* **240**, 191–199 (2017).
149. Bohte, S. M., Kok, J. N. & La Poutré, H. Error-backpropagation in temporally encoded networks of spiking neurons. *Neurocomputing* **48**, 17–37 (2002).
150. Wu, Y., Deng, L., Li, G., Zhu, J. & Shi, L. Spatio-Temporal Backpropagation for Training High-Performance Spiking Neural Networks. *Front. Neurosci.* **12**, (2018).
151. Lee, J. H., Delbruck, T. & Pfeiffer, M. Training Deep Spiking Neural Networks Using Backpropagation. *Front. Neurosci.* **10**, (2016).
152. Neftci, E. O., Augustine, C., Paul, S. & Detorakis, G. Event-Driven Random Back-Propagation: Enabling Neuromorphic Deep Learning Machines. *Front. Neurosci.* **11**, (2017).
153. Tanaka, G. *et al.* Recent advances in physical reservoir computing: A review. *Neural Netw.* **115**, 100–123 (2019).
154. Recurrent Neural Networks for Prediction: Learning Algorithms, Architectures and Stability | Wiley. *Wiley.com* https://www.wiley.com/en-

br/Recurrent+Neural+Networks+for+Prediction%3A+Learning+Algorithms%2C+Architectures+and+Stability-p-9780470845356.

155. Jalalvand, A., Van Wallendael, G. & Van De Walle, R. Real-Time Reservoir Computing Network-Based Systems for Detection Tasks on Visual Contents. in *2015 7th International Conference on Computational Intelligence, Communication Systems and Networks* 146–151 (2015). doi:10.1109/CICSyN.2015.35.
156. Paquot, Y. *et al.* Optoelectronic Reservoir Computing. *Sci. Rep.* **2**, 287 (2012).
157. Jaeger, H. & Haas, H. Harnessing Nonlinearity: Predicting Chaotic Systems and Saving Energy in Wireless Communication. *Science* **304**, 78–80 (2004).
158. Jaeger, H. Adaptive Nonlinear System Identification with Echo State Networks. in *Advances in Neural Information Processing Systems* vol. 15 (MIT Press, 2002).
159. Akiyama, T. & Tanaka, G. Analysis on Characteristics of Multi-Step Learning Echo State Networks for Nonlinear Time Series Prediction. in *2019 International Joint Conference on Neural Networks (IJCNN)* 1–8 (2019). doi:10.1109/IJCNN.2019.8851876.
160. Gallicchio, C., Micheli, A. & Pedrelli, L. Deep reservoir computing: A critical experimental analysis. *Neurocomputing* **268**, 87–99 (2017).
161. Qiao, J., Li, F., Han, H. & Li, W. Growing Echo-State Network With Multiple Subreservoirs. *IEEE Trans. Neural Netw. Learn. Syst.* **28**, 391–404 (2017).
162. Fernando, C. & Sojakka, S. Pattern Recognition in a Bucket. in vol. 2801 588–597 (2003).
163. Coulombe, J. C., York, M. C. A. & Sylvestre, J. Computing with networks of nonlinear mechanical oscillators. *PLOS ONE* **12**, e0178663 (2017).
164. Nakao, H. Phase reduction approach to synchronization of nonlinear oscillators. *Contemp. Phys.* **57**, 188–214 (2016).
165. Nichele, S. & Gundersen, M. S. Reservoir Computing Using Non-Uniform Binary Cellular Automata. Preprint at https://doi.org/10.48550/arXiv.1702.03812 (2017).
166. Lepri, S., Giacomelli, G., Politi, A. & Arecchi, F. T. High-dimensional chaos in delayed dynamical systems. *Phys. Nonlinear Phenom.* **70**, 235–249 (1994).
167. Brunner, D. *et al.* Tutorial: Photonic neural networks in delay systems. *J. Appl. Phys.* **124**, 152004 (2018).
168. Ortín, S. & Pesquera, L. Reservoir Computing with an Ensemble of Time-Delay Reservoirs. *Cogn. Comput.* **9**, 327–336 (2017).

169. Appeltant, L. *et al.* Information processing using a single dynamical node as complex system. *Nat. Commun.* **2**, 468 (2011).
170. Smirnova, L., Caffo, B. & Johnson, E. C. Reservoir computing with brain organoids. *Nat. Electron.* **6**, 943–944 (2023).
171. Hafizovic, S. *et al.* A CMOS-based microelectrode array for interaction with neuronal cultures. *J. Neurosci. Methods* **164**, 93–106 (2007).
172. Bracciale, M. P., Kim, C. & Marrocchi, A. 1 - Organic electronics: an overview of key materials, processes, and devices. in *Sustainable Strategies in Organic Electronics* (ed. Marrocchi, A.) 3–71 (Woodhead Publishing, 2022). doi:10.1016/B978-0-12-823147-0.00001-X.
173. Cox, P. A. *The Electronic Structure and Chemistry of Solids*. (Oxford University Press, Oxford [Oxfordshire], 1987).
174. Akamatu, H. & Inokuchi, H. On the Electrical Conductivity of Violanthrone, Iso-Violanthrone, and Pyranthrone. *J. Chem. Phys.* **18**, 810–811 (1950).
175. Horowitz, G. Organic Field-Effect Transistors. *Adv. Mater.* **10**, 365–377 (1998).
176. Torsi, L., Magliulo, M., Manoli, K. & Palazzo, G. Organic field-effect transistor sensors: a tutorial review. *Chem. Soc. Rev.* **42**, 8612–8628 (2013).
177. Kim, S. H. *et al.* Electrolyte-Gated Transistors for Organic and Printed Electronics. *Adv. Mater.* **25**, 1822–1846 (2013).
178. Sarcina, L. *et al.* A large-area organic transistor with 3D-printed sensing gate for noninvasive single-molecule detection of pancreatic mucinous cyst markers. *Anal. Bioanal. Chem.* **414**, 5657–5669 (2022).
179. Solodka, K. *et al.* Detection of Neurofilament Light Chain with Label-Free Electrolyte-Gated Organic Field-Effect Transistors. *Adv. Mater. Interfaces* **9**, 2102341 (2022).
180. Seshadri, P. *et al.* Low-picomolar, label-free procalcitonin analytical detection with an electrolyte-gated organic field-effect transistor based electronic immunosensor. *Biosens. Bioelectron.* **104**, 113–119 (2018).
181. Yuvaraja, S. *et al.* Organic field-effect transistor-based flexible sensors. *Chem. Soc. Rev.* **49**, 3423–3460 (2020).
182. Li, H. *et al.* Chemical and Biomolecule Sensing with Organic Field-Effect Transistors. *Chem. Rev.* **119**, 3–35 (2019).
183. White, H. S., Kittlesen, G. P. & Wrighton, M. S. Chemical derivatization of an array of three gold microelectrodes with polypyrrole: fabrication of a molecule-based transistor. *J. Am. Chem. Soc.* **106**, 5375–5377 (1984).

184. Rivnay, J., Owens, R. M. & Malliaras, G. G. The Rise of Organic Bioelectronics. *Chem. Mater.* **26**, 679–685 (2014).
185. Bernards, D. A. & Malliaras, G. G. Steady-State and Transient Behavior of Organic Electrochemical Transistors. *Adv. Funct. Mater.* **17**, 3538–3544 (2007).
186. Rivnay, J. *et al.* Organic electrochemical transistors. *Nat. Rev. Mater.* **3**, 17086 (2018).
187. Friedlein, J. T., McLeod, R. R. & Rivnay, J. Device physics of organic electrochemical transistors. *Org. Electron.* **63**, 398–414 (2018).
188. Koutsouras, D. A. *et al.* Impedance Spectroscopy of Spin-Cast and Electrochemically Deposited PEDOT:PSS Films on Microfabricated Electrodes with Various Areas. *ChemElectroChem* **4**, 2321–2327 (2017).
189. Tu, D., Kergoat, L., Crispin, X., Berggren, M. & Forchheimer, R. Transient analysis of electrolyte-gated organic field-effect transistors. *Proc. SPIE - Int. Soc. Opt. Eng.* **8478**, (2012).
190. Faria, G. C., Duong, D. T. & Salleo, A. On the transient response of organic electrochemical transistors. *Org. Electron.* **45**, 215–221 (2017).
191. Friedlein, J. T., Donahue, M. J., Shaheen, S. E., Malliaras, G. G. & McLeod, R. R. Microsecond Response in Organic Electrochemical Transistors: Exceeding the Ionic Speed Limit. *Adv. Mater.* **28**, 8398–8404 (2016).
192. Kaphle, V., Paudel, P. R., Dahal, D., Radha Krishnan, R. K. & Lüssem, B. Finding the equilibrium of organic electrochemical transistors. *Nat. Commun.* **11**, 2515 (2020).
193. Paudel, P. R., Skowrons, M., Dahal, D., Radha Krishnan, R. K. & Lüssem, B. The Transient Response of Organic Electrochemical Transistors. *Adv. Theory Simul.* **5**, 2100563 (2022).
194. Jo, Y. J., Kwon, K. Y., Khan, Z. U., Crispin, X. & Kim, T. Gelatin Hydrogel-Based Organic Electrochemical Transistors and Their Integrated Logic Circuits. *ACS Appl. Mater. Interfaces* **10**, 39083–39090 (2018).
195. Mannerbro, R., Ranlöf, M., Robinson, N. & Forchheimer, R. Inkjet printed electrochemical organic electronics. *Synth. Met.* **158**, 556–560 (2008).
196. Andersson Ersman, P. *et al.* All-printed large-scale integrated circuits based on organic electrochemical transistors. *Nat. Commun.* **10**, 5053 (2019).
197. Hutter, P. C., Rothlander, T., Scheipl, G. & Stadlober, B. All Screen-Printed Logic Gates Based on Organic Electrochemical Transistors. *IEEE Trans. Electron Devices* **62**, 4231–4236 (2015).

198. Sun, H. *et al.* Complementary Logic Circuits Based on High-Performance n-Type Organic Electrochemical Transistors. *Adv. Mater.* **30**, 1704916 (2018).
199. Wu, H.-Y. *et al.* Influence of Molecular Weight on the Organic Electrochemical Transistor Performance of Ladder-Type Conjugated Polymers. *Adv. Mater.* **34**, 2106235 (2022).
200. He, R.-X. *et al.* Detection of bacteria with organic electrochemical transistors. *J. Mater. Chem.* **22**, 22072–22076 (2012).
201. Fenoy, G. E., Azzaroni, O., Knoll, W. & Marmisollé, W. A. Functionalization Strategies of PEDOT and PEDOT:PSS Films for Organic Bioelectronics Applications. *Chemosensors* **9**, 212 (2021).
202. Guo, K. *et al.* Rapid single-molecule detection of COVID-19 and MERS antigens via nanobody-functionalized organic electrochemical transistors. *Nat. Biomed. Eng.* **5**, 666–677 (2021).
203. Song, J. *et al.* Organic Photo-Electrochemical Transistor-Based Biosensor: A Proof-of-Concept Study toward Highly Sensitive DNA Detection. *Adv. Healthc. Mater.* **7**, 1800536 (2018).
204. Yang, A. *et al.* Fabric Organic Electrochemical Transistors for Biosensors. *Adv. Mater.* **30**, 1800051 (2018).
205. Wustoni, S. *et al.* Membrane-Free Detection of Metal Cations with an Organic Electrochemical Transistor. *Adv. Funct. Mater.* **29**, 1904403 (2019).
206. Xie, K. *et al.* Organic electrochemical transistor arrays for real-time mapping of evoked neurotransmitter release in vivo. *eLife* **9**, e50345 (2020).
207. Li, W., Jin, J., Xiong, T., Yu, P. & Mao, L. Fast-Scanning Potential-Gated Organic Electrochemical Transistors for Highly Sensitive Sensing of Dopamine in Living Rat Brain. *Angew. Chem. Int. Ed.* **61**, e202204134 (2022).
208. Luo, Z. *et al.* Sub-thermionic, ultra-high-gain organic transistors and circuits. *Nat. Commun.* **12**, 1928 (2021).
209. Rashid, R. B. *et al.* Ambipolar inverters based on cofacial vertical organic electrochemical transistor pairs for biosignal amplification. *Sci. Adv.* **7**, eabh1055 (2021).
210. Cea, C. *et al.* Enhancement-mode ion-based transistor as a comprehensive interface and real-time processing unit for in vivo electrophysiology. *Nat. Mater.* **19**, 679–686 (2020).
211. Campana, A., Cramer, T., Simon, D. T., Berggren, M. & Biscarini, F. Electrocardiographic Recording with Conformable Organic Electrochemical Transistor Fabricated on Resorbable Bioscaffold. *Adv. Mater.* **26**, 3874–3878 (2014).

212. Lee, H. *et al.* Ultrathin Organic Electrochemical Transistor with Nonvolatile and Thin Gel Electrolyte for Long-Term Electrophysiological Monitoring. *Adv. Funct. Mater.* **29**, 1906982 (2019).

213. Spyropoulos, G. D., Gelinas, J. N. & Khodagholy, D. Internal ion-gated organic electrochemical transistor: A building block for integrated bioelectronics. *Sci. Adv.* **5**, eaau7378 (2019).

214. Khodagholy, D. *et al.* In vivo recordings of brain activity using organic transistors. *Nat. Commun.* **4**, 1575 (2013).

215. Lee, W. *et al.* Integration of Organic Electrochemical and Field-Effect Transistors for Ultraflexible, High Temporal Resolution Electrophysiology Arrays. *Adv. Mater. Deerfield Beach Fla* **28**, 9722–9728 (2016).

216. Lee, W. *et al.* Transparent, conformable, active multielectrode array using organic electrochemical transistors. *Proc. Natl. Acad. Sci.* **114**, 10554–10559 (2017).

217. Polikov, V. S., Tresco, P. A. & Reichert, W. M. Response of brain tissue to chronically implanted neural electrodes. *J. Neurosci. Methods* **148**, 1–18 (2005).

218. Williamson, A. *et al.* Localized Neuron Stimulation with Organic Electrochemical Transistors on Delaminating Depth Probes. *Adv. Mater.* **27**, 4405–4410 (2015).

219. Zhang, S. *et al.* Tuning the Electromechanical Properties of PEDOT:PSS Films for Stretchable Transistors And Pressure Sensors. *Adv. Electron. Mater.* **5**, 1900191 (2019).

220. Zhou, X. *et al.* Aerosol Jet Printing of Multi-Dimensional OECT Force Sensor with High Sensitivity and Large Measuring Range. *Adv. Mater. Technol.* **8**, 2201272 (2023).

221. Wang, X. *et al.* A Sub-1-V, Microwatt Power-Consumption Iontronic Pressure Sensor Based on Organic Electrochemical Transistors. *IEEE Electron Device Lett.* **42**, 46–49 (2021).

222. Chen, S., Surendran, A., Wu, X. & Leong, W. L. Contact Modulated Ionic Transfer Doping in All-Solid-State Organic Electrochemical Transistor for Ultra-High Sensitive Tactile Perception at Low Operating Voltage. *Adv. Funct. Mater.* **30**, 2006186 (2020).

223. Parker, D. Review of Neurotransmitters and Neuromodulators: Handbook of Receptors and Biological Effects, Oliver von Bohlen und Halbach, Rolf Dermietzel, David J Ballantyne. *Q. Rev. Biol.* **78**, 125–125 (2003).

224. Bruno, U. *et al.* From neuromorphic to neurohybrid: transition from the emulation to the integration of neuronal networks. *Neuromorphic Comput. Eng.* (2023).

225. Pan, F., Gao, S., Chen, C., Song, C. & Zeng, F. Recent progress in resistive random access memories: Materials, switching mechanisms, and performance. *Mater. Sci. Eng. R Rep.* **83**, 1–59 (2014).

226. Santos, Y. P., Valença, E., Machado, R. & Macêdo, M. A. A novel structure ZnO-Fe-ZnO thin film memristor. *Mater. Sci. Semicond. Process.* **86**, 43–48 (2018).

227. Li, S. *et al.* Synaptic plasticity and learning behaviours mimicked through Ag interface movement in an Ag/conducting polymer/Ta memristive system. *J. Mater. Chem. C* **1**, 5292–5298 (2013).

228. Wang, Y. *et al.* Near-Infrared-Irradiation-Mediated Synaptic Behavior from Tunable Charge-Trapping Dynamics. *Adv. Electron. Mater.* **6**, 1900765 (2020).

229. Zhou, Z. *et al.* Transient and flexible polymer memristors utilizing full-solution processed polymer nanocomposites. *Nanoscale* **10**, 14824–14829 (2018).

230. van de Burgt, Y., Melianas, A., Keene, S. T., Malliaras, G. & Salleo, A. Organic electronics for neuromorphic computing. *Nat. Electron.* **1**, 386–397 (2018).

231. Liu, G. *et al.* Organic Biomimicking Memristor for Information Storage and Processing Applications. *Adv. Electron. Mater.* **2**, 1500298 (2016).

232. Yang, X. *et al.* An organic terpyridyl-iron polymer based memristor for synaptic plasticity and learning behavior simulation. *RSC Adv.* **6**, 25179–25184 (2016).

233. Choi, H. Y., Wu, C., Bok, C. H. & Kim, T. W. Organic electronic synapses with pinched hystereses based on graphene quantum-dot nanocomposites. *NPG Asia Mater.* **9**, e413–e413 (2017).

234. Dai, S. *et al.* Recent Advances in Transistor-Based Artificial Synapses. *Adv. Funct. Mater.* **29**, 1903700 (2019).

235. Wang, L. *et al.* Rectification-Regulated Memristive Characteristics in Electron-Type CuPc-Based Element for Electrical Synapse. *Adv. Electron. Mater.* **3**, 1700063 (2017).

236. Yoo, E. *et al.* Bifunctional resistive switching behavior in an organolead halide perovskite based Ag/CH3NH3PbI3−xClx/FTO structure. *J. Mater. Chem. C* **4**, 7824–7830 (2016).

237. Kim, M.-K. & Lee, J.-S. Short-Term Plasticity and Long-Term Potentiation in Artificial Biosynapses with Diffusive Dynamics. *ACS Nano* **12**, 1680–1687 (2018).

238. Wan, C. *et al.* An artificial sensory neuron with visual-haptic fusion. *Nat. Commun.* **11**, 4602 (2020).

239. Lee, K. *et al.* Artificially Intelligent Tactile Ferroelectric Skin. *Adv. Sci.* **7**, 2001662 (2020).

240. Dai, S. *et al.* Intrinsically stretchable neuromorphic devices for on-body processing of health data with artificial intelligence. *Matter* **5**, 3375–3390 (2022).

241. Gong, J. *et al.* An artificial visual nerve for mimicking pupil reflex. *Matter* **5**, 1578–1589 (2022).

242. Tian, B. *et al.* A Robust Artificial Synapse Based on Organic Ferroelectric Polymer. *Adv. Electron. Mater.* **5**, 1800600 (2019).

243. Qian, C. *et al.* Artificial Synapses Based on in-Plane Gate Organic Electrochemical Transistors. *ACS Appl. Mater. Interfaces* **8**, 26169–26175 (2016).

244. van de Burgt, Y. *et al.* A non-volatile organic electrochemical device as a low-voltage artificial synapse for neuromorphic computing. *Nat. Mater.* **16**, 414–418 (2017).

245. Yang, J. J. & Xia, Q. Battery-like artificial synapses. *Nat. Mater.* **16**, 396–397 (2017).

246. Keene, S. T. *et al.* A biohybrid synapse with neurotransmitter-mediated plasticity. *Nat. Mater.* **19**, 969–973 (2020).

247. Gualandi, I. *et al.* Selective detection of dopamine with an all PEDOT:PSS Organic Electrochemical Transistor. *Sci. Rep.* **6**, 35419 (2016).

248. Matrone, G. M. *et al.* Electrical and Optical Modulation of a PEDOT:PSS-Based Electrochemical Transistor for Multiple Neurotransmitter-Mediated Artificial Synapses. *Adv. Mater. Technol.* 2201911 (2023) doi:10.1002/admt.202201911.

249. Wu, C., Kim, T. W., Choi, H. Y., Strukov, D. B. & Yang, J. J. Flexible three-dimensional artificial synapse networks with correlated learning and trainable memory capability. *Nat. Commun.* **8**, 752 (2017).

250. Erokhin, V. *et al.* Stochastic hybrid 3D matrix: learning and adaptation of electrical properties. *J. Mater. Chem.* **22**, 22881–22887 (2012).

251. Gkoupidenis, P., Koutsouras, D. A. & Malliaras, G. G. Neuromorphic device architectures with global connectivity through electrolyte gating. *Nat. Commun.* **8**, 15448 (2017).

252. Koutsouras, D. A. *et al.* An Iontronic Multiplexer Based on Spatiotemporal Dynamics of Multiterminal Organic Electrochemical Transistors. *Adv. Funct. Mater.* **31**, 2011013 (2021).

253. Cucchi, M. *et al.* Reservoir computing with biocompatible organic electrochemical networks for brain-inspired biosignal classification. *Sci. Adv.* **7**, eabh0693 (2021).

254. Harikesh, P. C. *et al.* Organic electrochemical neurons and synapses with ion mediated spiking. *Nat. Commun.* **13**, 901 (2022).

255. Harikesh, P. C. *et al.* Ion-tunable antiambipolarity in mixed ion–electron conducting polymers enables biorealistic organic electrochemical neurons. *Nat. Mater.* **22**, 242–248 (2023).
256. Sarkar, T. *et al.* An organic artificial spiking neuron for in situ neuromorphic sensing and biointerfacing. *Nat. Electron.* **5**, 774–783 (2022).
257. Krauhausen, I. *et al.* Organic neuromorphic electronics for sensorimotor integration and learning in robotics. *Sci. Adv.* **7**, eabl5068 (2021).
258. Ferhan, A. R. *et al.* Solvent-assisted preparation of supported lipid bilayers. *Nat. Protoc.* **14**, 2091–2118 (2019).
259. Park, H.-L. *et al.* Flexible Neuromorphic Electronics for Computing, Soft Robotics, and Neuroprosthetics. *Adv. Mater.* **32**, 1903558 (2020).
260. Zeng, M., He, Y., Zhang, C. & Wan, Q. Neuromorphic Devices for Bionic Sensing and Perception. *Front. Neurosci.* **15**, (2021).
261. Corrado, F. *et al.* Azobenzene-based optoelectronic transistors for neurohybrid building blocks. *Nat. Commun.* **14**, 6760 (2023).
262. Dissertation, D. & Priimagi, A. POLYMER-AZOBENZENE COMPLEXES: FROM SUPRAMOLECULAR CONCEPTS TO EFFICIENT PHOTORESPONSIVE POLYMERS. (2022).
263. Goulet-Hanssens, A. *et al.* Hole Catalysis as a General Mechanism for Efficient and Wavelength-Independent Z → E Azobenzene Isomerization. *Chem* **4**, 1740–1755 (2018).
264. Lisdat, F. & Schäfer, D. The use of electrochemical impedance spectroscopy for biosensing. *Anal. Bioanal. Chem.* **391**, 1555–1567 (2008).
265. Atkinson, R. C. & Shiffrin, R. M. The control of short-term memory. *Sci. Am.* **225**, 82–90 (1971).
266. Liu, M.-M. *et al.* Experimental and Theoretical Prediction of The Redox Potential of Dopamine and Its Supramolecular Complex With Glycine. *Int. J. Electrochem. Sci.* **10**, 235–247 (2015).
267. Bacil, R. P., Chen, L., Serrano, S. H. P. & Compton, R. G. Dopamine oxidation at gold electrodes: mechanism and kinetics near neutral pH. *Phys. Chem. Chem. Phys.* **22**, 607–614 (2020).
268. Zobel, K., Choi, S. E., Minakova, R., Gocyla, M. & Offenhäusser, A. N-Cadherin modified lipid bilayers promote neural network formation and circuitry. *Soft Matter* **13**, 8096–8107 (2017).

269. Tanaka, M. & Sackmann, E. Polymer-supported membranes as models of the cell surface. *Nature* **437**, 656–663 (2005).
270. Cui, X. *et al.* Surface modification of neural recording electrodes with conducting polymer/biomolecule blends. *J. Biomed. Mater. Res.* **56**, 261–272 (2001).
271. Inzelt, G. & Láng, G. G. Electrochemical Impedance Spectroscopy (EIS) for Polymer Characterization. in *Electropolymerization* 51–76 (John Wiley & Sons, Ltd, 2010). doi:10.1002/9783527630592.ch3.
272. Ertürk, G. & Mattiasson, B. Capacitive Biosensors and Molecularly Imprinted Electrodes. *Sensors* **17**, 390 (2017).
273. Ursell, T. S., Klug, W. S. & Phillips, R. Morphology and interaction between lipid domains. *Proc. Natl. Acad. Sci.* **106**, 13301–13306 (2009).
274. Lipid Rafts: Phase Separation in Lipid Bilayers studied with Atomic Force Microscopy. *Analytical Science News* https://analyticalscience.wiley.com/do/10.1002/micro.162/.
275. Macháň, R. & Hof, M. Lipid diffusion in planar membranes investigated by fluorescence correlation spectroscopy. *Biochim. Biophys. Acta BBA - Biomembr.* **1798**, 1377–1391 (2010).
276. Koutsouras, D. A., Torricelli, F., Gkoupidenis, P. & Blom, P. W. M. Efficient Gating of Organic Electrochemical Transistors with In-Plane Gate Electrodes. *Adv. Mater. Technol.* **6**, 2100732 (2021).
277. Lu, Z. *et al.* Understanding electrochemical properties of supported lipid bilayers interfaced with organic electronic devices. *J. Mater. Chem. C* **10**, 8050–8060 (2022).
278. Schafer, E. A., Davis, E., Manzer, Z., Daniel, S. & Rivnay, J. Hybrid Supported Lipid Bilayers for Bioinspired Bioelectronics with Enhanced Stability. *ACS Appl. Mater. Interfaces* **15**, 24638–24647 (2023).
279. Zaborowska, M., Dziubak, D., Matyszewska, D. & Bilewicz, R. Surface and electrochemical properties of lipid raft model membranes and how they are affected by incorporation of statin. *Electrochimica Acta* **386**, 138514 (2021).
280. Trouillon, R. & Gijs, M. A. M. Paper-Based Polymer Electrodes for Bioanalysis and Electrochemistry of Neurotransmitters. *ChemPhysChem* **19**, 1164–1172 (2018).
281. Dunham, K. E. & Venton, B. J. Improving serotonin fast-scan cyclic voltammetry detection: new waveforms to reduce electrode fouling. *Analyst* **145**, 7437–7446 (2020).
282. LeDoux, J. E. Emotion, memory and the brain. *Sci. Am.* **270**, 50–57 (1994).

List of publications

- Ausilio, C., Bruno, U.* et al. Concealing organic neuromorphic devices with neuronal-inspired supported lipid bilayers. Adv. Sci. Accepted.
- Corrado, F., Bruno, U.*, Prato, M. et al. Azobenzene-based optoelectronic transistors for neurohybrid building blocks. Nat Commun 14, 6760 (2023). https://doi.org/10.1038/s41467-023-41083-2
- Bruno, U., Rana. D. et al. From neuromorphic to neurohybrid: transition from the emulation to the integration of neuronal networks. Neuromorphic Computing and Engineering (2023). doi: 10.1088/2634-4386/acc683
- Matrone, G.M., Bruno, U., Forró, C., Lubrano, C., Cinti, S., van de Burgt, Y. and Santoro, F. (2023), Electrical and Optical Modulation of a PEDOT:PSS-Based Electrochemical Transistor for Multiple Neurotransmitter-Mediated Artificial Synapses. Adv. Mater. Technol., 8: 2201911. https://doi.org/10.1002/admt.202201911
- Lubrano, C., Bruno, U.*, Ausilio, C., Santoro, F., Supported Lipid Bilayers Coupled to Organic Neuromorphic Devices Modulate Short-Term Plasticity in Biomimetic Synapses. Adv. Mater. (2022). doi: 10.1002/adma.202110194
- Ruggiero, A., Criscuolo, V., Grasselli, S., Bruno, U., Ausilio, C., Bovio, C. L., Bettucci, O. & Santoro, F. Two-photon polymerization lithography enabling the fabrication of PEDOT:PSS 3D structures for bioelectronic applications. Chem. Commun. (2022). Doi: 10.1039/d2cc03152c
- Mariano, A., Lubrano, C., Bruno, U., Ausilio, C., Dinger, N. B. & Santoro, F. Advances in Cell-Conductive Polymer Biointerfaces and Role of the Plasma Membrane. Chem. Rev. (2021). doi: 10.1021/acs.chemrev.1c00363
- Bruno, U., Mariano, A. & Santoro, F. A systems theory approach to describe dynamic coupling at the cell–electrode interface. APL Materials. (2021). doi: 10.1063/5.0025293

* co-first authorship

Annex A: Continuity equation of non-charged particles

The continuity equation to be solved is:

$$\frac{dJ}{dx} = q\frac{dn}{dt} = qR(n) \tag{A.1}$$

Where *J* is the current density, *q* is the elementary charge, *n* is the particle density and *R* is the generation/recombination rate of the particles.

Then, a first order approximation is then introduced, yielding:

$$\left(\frac{dJ}{dx}\right)_i = \frac{J_{i+1/2} - J_{i-1/2}}{(h_i + h_{i+1})/2} \tag{A.2}$$

Where h_i indicated the distance (in space) between the i-th point and the previous one, *i.e.*, $h_i = x_i - x_{i-1}$. In addition, *qR(n)* was omitted to simplify the notation.

To derive the expression of the current density $J_{i+1/2}$, one can start from the current equation, without any drift contribution, as the particle under discussion is non-charged, yielding for a single diffusion-related term:

$$J_{i+1/2} = qD_n\frac{dn}{dx} \tag{A.3}$$

Where D_n is the diffusion constant of the particle.

Let it be:

$$x_i = n_i \tag{A.4}$$

$$x_{i+1} = n_{i+1} \tag{A.5}$$

$$x_{i+1} - x_i = x_i + h_{i+1} \tag{A.6}$$

It is possible to integrate equation (A.3) from x_i to x_{i+1}, as follows:

$$\int_{x_i}^{x_{i+1}} J_{i+1/2} dx = qD_n \int_{x_i}^{x_{i+1}} \frac{dn}{dx} dx \tag{A.7}$$

Considering $J_{i+1/2}$ constant in the interval [x_i; x_{i+1}], equation (A.7) can be easily solved as:

$$J_{i+1/2}[x]_{x_i}^{x_{i+i}} = qD_n[n]_{x_i}^{x_{i+i}} \tag{A.8}$$

Substituting (A.4) and (A.5), it simplifies to:

$$J_{i+1/2}(x_{i+1} - x_i) = qD_n(n_{i+i} - n_i) \tag{A.9}$$

Furtherly substituting (A.6):

$$J_{i+1/2}h_{i+1} = qD_n(n_{i+i} - n_i) \tag{A.10}$$

Finally leading to:

$$J_{i+1/2} = \frac{qD_{n,i+1/2}}{h_{i+1}}(n_{i+i} - n_i) \tag{A.11}$$

Analogously, one can compute $J_{i-1/2}$, by iterating the calculations shown in (A.7)-(A.10) in the integration interval [x_{i-1};x_i], yielding:

$$J_{i-1/2} = \frac{qD_{n,i-1/2}}{h_i}(n_i - n_{i-1}) \tag{A.12}$$

Substituting (A.11) and (A.12) in (A.2), it leads to:

$$\left(\frac{dJ}{dx}\right)_i = \frac{\frac{qD_{n,i+\frac{1}{2}}}{h_{i+1}}(n_{i+i} \; - n_i) - \frac{qD_{n,i-1/2}}{h_i}(n_i \; - n_{i-1})}{(h_i + h_{i+1})/2} \tag{A.13}$$

Then, trivially executing the multiplications of the numerator and then extracting the common factors n_{i-1}, n_i and n_{i+1}, (A.13) becomes:

$$\left(\frac{dJ}{dx}\right)_i = \frac{\frac{qD_{n,i-1/2}}{h_i} n_{i-1} - \left(\frac{qD_{n,i+\frac{1}{2}}}{h_{i+1}} - \frac{qD_{n,i-\frac{1}{2}}}{h_i}\right) n_i - \frac{qD_{n,i+\frac{1}{2}}}{h_{i+i}} n_{i+1}}{(h_i + h_{i+1})/2} \tag{A.14}$$

Then, dividing in simple fractions and recovering the generation/recombination factor *qR(n)*, it leads to:

$$\begin{gathered} \frac{2D_{n,i-1/2}}{(h_i)(h_i + h_{i+1})} n_{i-1} - \left(\frac{2D_{n,i+\frac{1}{2}}}{(h_{i+1})(h_i + h_{i+1})} + \frac{2D_{n,i-\frac{1}{2}}}{(h_i)(h_i + h_{i+1})}\right) n_i \\ + \frac{2D_{n,i+\frac{1}{2}}}{(h_{i+1})(h_i + h_{i+1})} n_{i+1} = R(n) \end{gathered} \tag{A.15}$$

Notably the charge *q* was removed in all the expression. In addition, it is possible to write (A.15) using matrices, by defining as $A_{i,i-1}$ the coefficient of n_{i-1}, $A_{i,i}$ the coefficient of n_i and $A_{i,i+1}$ the coefficient of n_{i+1}. Lastly, it is possible to define b_i the elements on the right-hand side of (A.15), yielding:

$$\begin{bmatrix} A_{1,1} & A_{1,2} & \dots & \dots & \dots & \dots & \dots \\ A_{2,1} & A_{2,2} & A_{2,3} & \dots & \dots & \dots & \dots \\ \dots & \dots & \dots & \dots & \dots & \dots & \dots \\ \dots & \dots & A_{i,i-1} & A_{i,i} & A_{i,i+1} & \dots & \dots \\ \dots & \dots & \dots & \dots & \dots & \dots & \dots \\ \dots & \dots & \dots & \dots & \dots & A_{n-2,n-2} & A_{n-2,n-1} \\ \dots & \dots & \dots & \dots & A_{n-1,n-3} & A_{n-1,n-2} & A_{n-1,n-1} \end{bmatrix} \begin{bmatrix} n_1 \\ \dots \\ \dots \\ n_i \\ \dots \\ \dots \\ \dots \\ n_{n-1} \end{bmatrix} = \begin{bmatrix} b_1 \\ \dots \\ \dots \\ b_i \\ \dots \\ \dots \\ \dots \\ b_{n-1} \end{bmatrix} \tag{A.16}$$